

9-14-2017

Characterization of Jet Fuel Combustion Emissions During a C-130 Aeromedical Evacuation Engines Running Onload

Michelle L. Page

Follow this and additional works at: <https://scholar.afit.edu/etd>

Part of the [Environmental Engineering Commons](#), and the [Occupational Health and Industrial Hygiene Commons](#)

Recommended Citation

Page, Michelle L., "Characterization of Jet Fuel Combustion Emissions During a C-130 Aeromedical Evacuation Engines Running Onload" (2017). *Theses and Dissertations*. 778.
<https://scholar.afit.edu/etd/778>

This Thesis is brought to you for free and open access by the Student Graduate Works at AFIT Scholar. It has been accepted for inclusion in Theses and Dissertations by an authorized administrator of AFIT Scholar. For more information, please contact richard.mansfield@afit.edu.



**DYNAMICS OF CHEMICAL DEGRADATION IN WATER USING
PHOTOCATALYTIC REACTIONS IN AN ULTRAVIOLET LIGHT EMITTING
DIODE REACTOR**

DISSERTATION

John E. Stubbs, Lieutenant Colonel, USAF
AFIT-ENV-DS-17-S-052

**DEPARTMENT OF THE AIR FORCE
AIR UNIVERSITY**

AIR FORCE INSTITUTE OF TECHNOLOGY

Wright-Patterson Air Force Base, Ohio

DISTRIBUTION STATEMENT A. APPROVED FOR PUBLIC RELEASE;
DISTRIBUTION UNLIMITED.

The views expressed in this thesis are those of the author and do not reflect the official policy or position of the United States Air Force, Department of Defense, or the United States Government. This material is declared a work of the U.S. Government and is not subject to copyright protection in the United States.

**DYNAMICS OF CHEMICAL DEGRADATION IN WATER USING
PHOTOCATALYTIC REACTIONS IN AN ULTRAVIOLET LIGHT EMITTING
DIODE REACTOR**

DISSERTATION

Presented to the Faculty

Graduate School of Engineering and Management

Air Force Institute of Technology

Air University

Air Education and Training Command

in Partial Fulfillment of the Requirements for the

Degree of Doctor of Philosophy

John E. Stubbs, BS, MS

Lieutenant Colonel, USAF

September 2017

**DISTRIBUTION STATEMENT A. APPROVED FOR PUBLIC RELEASE;
DISTRIBUTION UNLIMITED.**

DYNAMICS OF CHEMICAL DEGRADATION IN WATER USING PHOTOCATALYTIC
REACTIONS IN AN ULTRAVIOLET LIGHT EMITTING DIODE REACTOR

John E. Stubbs, BS, MS
Lieutenant Colonel, USAF

Committee Membership:

Willie F. Harper, Jr., PhD
Chairman

LTC Douglas R. Lewis, USA, PhD
Member

Matthew L. Magnuson, PhD
Member

Michael E. Miller, PhD
Member

ADEDJI B. BADIRU, PhD
Dean, Graduate School of Engineering and Management

Abstract

Water scarcity and contamination are challenges to which the United States homeland is not shielded and policies and technologies that support a “Net Zero” water use posture will become increasingly critical. This work examined ultraviolet (UV) light emitting diodes (LED) and hydrogen peroxide in an advanced oxidation process in support of a USAF net zero water initiative. A UV LED reactor was used for degradation of soluble organic chemicals. Linear relationships were observed between input drive current, optical output power, and apparent first order degradation rate constants. When drive current was varied, apparent first order degradation rates depended on chemical identities and the drive current. When molar peroxide ratios were varied, kinetic profiles revealed peroxide-limited or radical-scavenged phenomena. Accounting for molar absorptivity helped explain chemical removal profiles. Observed degradation kinetics were used to compare fit with molecular descriptors from published quantitative structure property relationship (QSPR) models. A new QSPR model was built using zero point energy and molar absorptivity as novel predictors. Finally, a systems architecture was used to describe a USAF installation net zero water program and proposed areas where UV LED reactors might be integrated. Facility-level wastewater treatment was found to be the most feasible near-term application. This research is the first UV LED-based AOP study to identify linear power-kinetics relationships, determine optimum molar peroxide ratios, and reveal the complexity of molar absorptivity in shaping treatment profiles.

AFIT-ENV-DS-17-S-052

To God, my family, and the betterment of future generations.

Acknowledgments

I am forever grateful to my research advisor, Dr. Willie Harper, for his wisdom, patience, and guidance. To my research committee members, Dr. Michael Miller, Dr. Douglas Lewis, and Dr. Matthew Magnuson, thank you for your critical review and willingness to give your time and expertise to the process. Thanks also to Dr. Daniel Felker for countless hours of laboratory support and analytical method development, Lt Col David Kempisty for lending an ear when needed, Ms. Kandace Bailey for helping with subtle secrets of the lab, and Mr. Morgan Russell for sharing lab space, equipment, and time.

Most importantly, thanks to God and my family. This would not have been possible without a solid spiritual grounding and the support of my wife and children.

John E. Stubbs

Table of Contents

	Page
Abstract	iv
Acknowledgments.....	vi
List of Figures	ix
List of Tables	xii
I. Introduction	1
1.1. Motivation	1
1.2. Problem.....	3
1.3. Research Objectives and Scope.....	4
1.4. Contributions	6
1.5. Document Outline	8
II. The Effect of Operating Parameters on Kinetics in an UV LED/H ₂ O ₂ Advanced Oxidation Process	9
2.1. Introduction	10
2.2. Materials and Methods	19
2.3. Results and Discussion	34
2.4. Conclusions	58
III. Quantitative Structure Property Relationship Models for Predicting Degradation Kinetics for a Ultraviolet Light Emitting Diode/Peroxide Advanced Oxidation Process	60
3.1. Introduction	61
3.2. Materials and Methods	68
3.3. Results and Discussion	72
3.4. Conclusions	100
IV. UV LED AOP Application in a USAF Net Zero Water Program – A Systems Architecture View	101

4.1. Introduction	102
4.2. Background.....	103
4.3. Net Zero Water System Model.....	109
4.4. Discussion.....	118
4.5. Conclusions	127
V. Conclusions	129
5.1 Discussion.....	129
5.2 Future Work.....	132
VI. Appendix A.....	135
VII. Appendix B.....	184
Bibliography	214
Vita	223

List of Figures

Figure	Page
Figure 1. Complete UV LED reactor assembly showing pairing of central cylinder and spherical end caps with heat sinks.	23
Figure 2. View of an end cap removed from the reactor showing LED placement.	24
Figure 3. Schematic depicting complete experimental setup.....	27
Figure 4. View of reactor endcap removed showing stir bar in middle of tube and LED at distal end.	28
Figure 5. Comparison of optical output power achieved from input drive current.	36
Figure 6. Linear relationship between apparent degradation rate constant and drive current. Three example linear fits are shown.	38
Figure 7. The effect of drive current on Erythrosine B removal.	44
Figure 8. The effect of drive current on the degradation of dyes.	46
Figure 9. The effect of molar peroxide ratio on Brilliant Blue FCF removal at 200 mA.	51
Figure 10. The effect of molar peroxide ratio on Erythrosine B removal at 80 mA.	52
Figure 11. The effect of molar peroxide ratio on TBA removal at 120 mA.....	53
Figure 12. Relationship between CSTR model fit and molar absorptivity.....	57
Figure 13. Actual versus predicted degradation rate constants utilizing Wang et al. descriptors with the full data set.....	74
Figure 14. Actual versus predicted degradation rate constants utilizing Wang et al. descriptors with the dye data set.	75
Figure 15. Actual versus predicted degradation rate constants utilizing Wang et al. descriptors with the achromatic chemical data set.	76

Figure 16. Actual versus predicted degradation rate constants utilizing Jin et al. descriptors with the full data set.....	78
Figure 17. Actual versus predicted degradation rate constants utilizing Tang descriptors with the full data set.	81
Figure 18. Actual versus predicted degradation rate constants utilizing Tang descriptors with the dye data set.	82
Figure 19. Actual versus predicted degradation rate constants utilizing Tang descriptors with the achromatic chemical data set.	83
Figure 20. Actual versus predicted degradation rate constants utilizing Kusic et al. descriptors with the full data set.....	86
Figure 21. Actual versus predicted degradation rate constants utilizing Kusic et al. descriptors and omitting malathion and Allura Red AC.....	87
Figure 22. Actual versus predicted degradation rate constants utilizing Kusic et al. descriptors with the dye data set.	88
Figure 23. Actual versus predicted degradation rate constants utilizing Sudhakaran and Amy, 2012 descriptors with the full data set.....	90
Figure 24. Actual versus predicted degradation rate constants utilizing Sudhakaran and Amy, 2013 descriptors with the full data set.....	92
Figure 25. Actual versus predicted degradation rate constants utilizing Sudhakaran and Amy, 2013 descriptors with the dye data set.	93
Figure 26. Actual versus predicted degradation rate constants utilizing Sudhakaran and Amy, 2013 descriptors with the achromatic chemical data set.	94

Figure 27. Actual versus predicted degradation rate constants utilizing Zero Point Energy as a descriptor with the full data set.	98
Figure 28. Actual versus predicted degradation rate constants utilizing Zero Point Energy and molar absorptivity as descriptors with the full data set.	99
Figure 29. Capability taxonomy for a USAF installation net zero water program.	110
Figure 30. Hybrid systems view of a net zero water program at a USAF installation with boundaries at the installation and facility level.	113
Figure 31. Operational activity lanes for four areas of potential UV LED/H ₂ O ₂ advanced oxidation treatment within a net zero water program.	115
Figure 32. Mass balance relationships between facility influent, recycle, and effluent flows; Q ₂ /Q ₁ represents a recycle ratio in water reuse scenarios.	123
Figure 33. The effect of facility size and recycle ratio on the required first order rate constant.	124

List of Tables

Table	Page
Table 1. Basic information and properties pertaining to dyes and achromatic chemicals used in experiments.....	21
Table 2. Output characteristics of UV LEDs utilized in reactor experiments.	35
Table 3. Calculated photon production rate for each drive current level.....	40
Table 4. Molecular descriptors utilized in QSPRs built from traditional mercury lamp AOP data.	71
Table 5. Parameters and tests of statistical significance for new models built with zero point energy and molar absorptivity.	97

DYNAMICS OF CHEMICAL DEGRADATION IN WATER USING PHOTOCATALYTIC REACTIONS IN AN ULTRAVIOLET LIGHT EMITTING DIODE REACTOR

I. Introduction

1.1. Motivation

The United States Air Force (USAF) *Energy Strategic Plan* identifies water as a critical asset and incorporates water into a strategy seeking to balance resource consumption, production, and conservation (US Air Force 2013). It sets a foundation for all Airmen to make energy and water conservation a part of operational considerations. The USAF generally consumes around 27 billion gallons of water per year at an annual cost of \$150 million, and energy utilized in water treatment and delivery contributes to an overall \$9 billion annual energy cost. The plan establishes energy priorities of improved resilience, reduced demand, assured supply, and fosters an energy aware culture. This culture should lead the way toward a future state where the USAF identifies and integrates energy and water efficiency throughout business and planning processes, promotes integration of new technologies to reduce costs and increase effectiveness, and leverages investments in a constrained resource environment. In the near term, the USAF has established a “Net Zero Initiative” where an installation consumes no more energy than is generated on the installation, and potable water demand is reduced by capturing and reusing, repurposing, or recharging an amount of water that is greater than or equal to the volume of water the installation uses. The initiative is designed to achieve a federal

zero net energy goal by 2030 for new facility construction and alterations (US Air Force 2013).

Furthermore, the US military has been engaged globally since World War I with forces deployed worldwide supporting a spectrum of operations from humanitarian crises to wartime contingencies. The reach of the military has continued to grow in recent decades with a need for simultaneous peacetime and wartime operations, and it is inevitable that the need for global engagement will continue in coming decades. An adequate supply of clean, safe drinking water is critical to the success of US forces carrying out missions in support of these operations. Water is necessary for hydration, food preparation, medical treatment, hygiene, construction, decontamination, maintenance, and many additional tasks. Water supply functions enable freedom of action, extend operational reach, and prolong operational endurance (US Army 2015). Water supply to both large, established bases and forward-deployed personnel is one of the largest logistics requirements of the military; however, water is also a limited resource that can cause disruptions and instability in numerous regions across the world. Conserving energy and water not only results in savings to the USAF, it can also mitigate increased competition in water-scarce regions that provoke potential conflicts (US Air Force 2013):

“Optimizing energy and water use not only saves resources and money, but is also a force multiplier that allows the Air Force to apply resources and airpower more efficiently and effectively.”

1.2. Problem

In an operational context that seeks to balance fiscal constraint with sustained global operations, the USAF needs to consider emerging technologies for water treatment that provide necessary water supply while simultaneously reducing energy costs and striving for net zero consumption. Once such technological advancement is recent development of energy efficient ultraviolet (UV) light emitting diodes (LED) as a replacement for high energy consuming mercury vapor lamps in advanced oxidation processes (AOP) utilizing hydrogen peroxide (H_2O_2). UV LED based water treatment is now possible. However, little data is available on the use of UV LED/ H_2O_2 for the destruction of soluble organics (Duckworth, et al. 2015; Scott, et al. 2016). There is a need to expand understanding of organic chemical destruction work to a greater number of chemicals to improve the fundamental understanding of this process. This study seeks to expand upon UV LED AOP treatment for the degradation of soluble organic compounds.

There is also a general need to assess tools that can be used to predict chemical degradation in UV AOPs in general, and particularly UV LED-based processes. Quantitative structure-property relationships (QSPR) can provide such a tool. The advantage of the QSPR approach, once an acceptable model is developed, is the ability to predict removal relative to baseline conditions strictly on the basis of the compound structure without further laboratory testing. Several previous studies have developed QSPRs relating chemical structure to degradability (Sudhakaran, et al. 2012; Chen, et al. 2007; Kusic, et al. 2009; Lee and von Gunten 2012; Meylan and Howard 2003;

Minakata, et al. 2009; Ohura, et al. 2008; Sudhakaran and Amy 2013; Wang, et al. 2009).

QSPRs have not been evaluated for UV LED-based reactors.

1.3. Research Objectives and Scope

1.3.1. Objectives

1.3.1.1. The first objective is to determine the effect of key reactor operating parameters on the reaction mechanisms associated with the advanced oxidation of soluble organic compounds with UV LEDs. The supporting tasks are:

- Determine the effect of peroxide stoichiometry on typical soluble organic chemical degradation profiles
- Determine the effect of LED output power on soluble organic chemical degradation profiles
- Evaluate optimality of degradation rate/input power/H₂O₂ combinations

Hypothesis #1 is that reactions with chemicals involving chain-terminating steps (i.e., those that stop the propagation of hydroxyl radicals) are expected to slow down at a faster rate as the availability of light and H₂O₂ is decreased, as compared to chemicals not involving chain-terminating steps. These chain-terminating steps cause peroxide to become consumed, which in turn prevents the regeneration of hydroxyl radicals.

Chemicals that involve chain-terminating steps include tert-butyl alcohol.

1.3.1.2. The second objective is to evaluate QSPRs for the advanced oxidation of soluble organic compounds with UV LEDs. The supporting tasks are:

- Determine apparent first order degradation rate constants for test chemicals

- Determine molecular descriptors for test chemicals
- Assess apparent first order degradation rate constant fit to molecular descriptors used in existing QSPRs in the literature
- Utilize multivariate methods to develop and test new basic QSPRs

Hypothesis #2 is that the observed reaction rate can be best predicted using frontier electron density (FED). The rationale for this is as follows. FED is a part of electronic theory, where the reactivity of a chemical can be explained by the distribution of electrons in a molecule (Fukui 1981). FED theory involves determining the highest occupied molecular orbital (HOMO) and the lowest unoccupied molecular orbital (LUMO) interaction. For electrophilic reactions, HOMO densities govern reaction pathways, while for nucleophilic reactions, the LUMO densities govern reaction pathways. Additionally, Koopman's theorem states that ionization energy (or ionization potential) of a molecule is equal to the negative of the HOMO energy. Following this hypothesis, the observed reaction rates should be greatest where the HOMO-based FED is highest (or conversely, the ionization energy is lowest).

1.3.1.3. The third objective is to use systems engineering principles to propose appropriate applications of UV LED-based reactors in support of specific water quality applications. The supporting tasks include:

- Identify the scope of near term water quality challenges in USAF
- Identify opportunities to couple AOP with other existing and emerging technologies (e.g. microbial fuel cells)

- Build a conceptual systems architecture view illustrating areas of potential UV LED/H₂O₂ technology integration within a “Net Zero” water program

Hypothesis #3 is that the most promising near term UV LED applications will involve those that leverage existing technologies to treat low flow waste streams to remove chemicals that do not include chain terminating steps.

1.3.2. Scope

The scope of this research is limited to degradation of six dyes and five achromatic chemicals by UV LED/H₂O₂ AOP. In this work, achromatic is used explicitly to denote the chemicals are without color (e.g. they do not have a visible spectrum). The scope is also constrained to the specific reactor and associated reactor parameters utilized in the experiments; however, the results of this study may be more broadly applicable to optimizing reactor design and operating parameters. Degradation rate constants derived from an experiment are limited in scope to the conditions under which the experiment was conducted (e.g. flow, volume, chemical concentrations, UV intensity, etc.). Additionally, QSPR development is limited to the domain of applicability of the test compounds used to develop the model. Development of a systems architecture view is hypothetical in nature and must be customized to specific installation requirements.

1.4. Contributions

This research effort expands significantly upon prior UV LED AOP studies. The initial emphasis was on creating a reactor platform that allowed for comparative

UV/H₂O₂ AOP degradation analysis of multiple dyes and achromatic chemicals across varying H₂O₂ concentrations and light intensities. Reactor operating parameters were adjusted to assess models of optimal efficiency and gain insight into hydroxyl radical production and associated degradation rates. Molecular descriptors of the dyes and achromatic chemicals used were assessed for their predictive capability and molecular descriptors used in existing QSPRs were assessed for their fit to the UV LED domain.

Several specific contributions to the existing body of knowledge come from this research:

1. A comparison of degradation kinetics for six dyes and five achromatic chemicals reacted in the same well-mixed, flow through reactor platform under the same reaction conditions.
2. An understanding of any relationships between degradation kinetics and molecular descriptors for six dyes and five achromatic chemicals and development of a novel QSPR.
3. An assessment of the adequacy of existing QSPR models relating molecular descriptors to apparent first order degradation rate constants.
4. An understanding of the impact of molar absorptivity of a dye at peak LED output wavelength on overall reaction kinetics.
5. A comparative analysis of the efficiency tradeoffs between optical output power, H₂O₂ concentration, and apparent first order degradation rate constants.

1.5. Document Outline

This dissertation contains five chapters. Chapter I provided the motivation, problem statement, research questions, scope, and tasks. Chapters II-IV are presented in scholarly format where each chapter can stand alone and be made ready for publication in journals/conference proceedings, although currently their level of detail is designed for this dissertation. Chapter II addresses research objective 1 and presents the results of reactor operating parameter effects on degradation kinetics and analyzes comparative kinetics of the various test compounds. Chapter III addresses research objective 2 in assessing suitability of molecular descriptors used in existing QSPR models and their fit to the UV LED domain. Chapter III also discusses efforts to build new basic QSPRs from the apparent first order degradation rate constants and molecular descriptors relevant to the test compounds. Chapter IV reviews near term water challenges for the USAF and introduces a proposed “Net Zero” systems architecture view, integrating UV LED AOP with other treatment technologies. Finally, Chapter V offers concluding discussion and suggestions for future work.

II. The Effect of Operating Parameters on Kinetics in an UV LED/H₂O₂ Advanced Oxidation Process

Keywords

Ultraviolet (UV), light emitting diode (LED), advanced oxidation process (AOP), hydrogen peroxide (H₂O₂)

Abstract

A bench-scale reactor utilizing UV LEDs as an energy source in a UV/H₂O₂ advanced oxidation process was used for the degradation of 6 dye and 5 achromatic organic compounds. As individual LEDs provide significantly less total output power as compared to mercury lamps, it is important to understand parameters that impact the production and efficient utilization of the available photons. There was a linear relationship between the input drive current, optical output power, and the apparent first order degradation rate constant, consistent with first principles from quantum mechanics. When the drive current was systematically varied, the apparent first order degradation rate constants depended on the identity of the test compound and the drive current, and were between 0.003 min⁻¹ - 1.078 min⁻¹. There was also a linear relationship between the drive current and the degradation extent. When the molar peroxide ratio was systematically varied, the kinetic profiles revealed either peroxide-limited or radical-scavenged phenomena, consistent with existing literature. The optimum molar peroxide ratios were at or near 500 mole H₂O₂/mole test compound for most of the dyes, but for erythrosine B (EB), the best molar peroxide ratios tested were in the range of 2500-3000 mole H₂O₂/mole EB, likely because of its relatively high molar absorptivity ratio. Accounting for molar absorptivity also helped to explain the shape of the removal profiles associated with EB and tartrazine, as well as the regression coefficients associated with the model fitting of experimental data. In contrast, the optimal molar peroxide ratios were at or near 100 mole H₂O₂/mole test compound for achromatic chemicals with the lowest molar absorptivity. This research is the first UV LED-based AOP study to identify linear power-kinetics relationships, determine optimum molar peroxide ratios, and reveal the complex role of molar absorptivity in shaping the speed and extent of treatment.

2.1. Introduction

Advanced oxidation processes are important to the water treatment community, because they can degrade a wide range of toxic chemical compounds (Crittenden et al. 2012). This study is focused on the UV/H₂O₂-based AOP and seeks to implement UV/H₂O₂ AOPs with light emitting diodes (LEDs) as an alternative to conventional mercury lamps. Hydroxyl radicals are produced when hydrogen peroxide absorbs UV light at a wavelength < 280 nm, resulting in the rapid and non-selective degradation of many soluble organic compounds and their byproducts (Minakata, et al. 2009) (Andreozzi, et al. 1999). UV light must be available at an energy level high enough to achieve oxygen-to-oxygen bond cleavage in the peroxide molecule, resulting in the production of two hydroxyl radicals (Benjamin and Lawler 2013; Luo 2007). Reactions with hydroxyl radicals are among the fastest aqueous phase reactions known (Dorfman and Adams 1973).

UV LEDs exhibit several advantages over mercury lamps including small size, light weight, physical durability, and lack of hazardous components (Ibrahim, et al. 2014). UV LEDs may also have a comparative disadvantage currently as the output power of an individual LED is significantly lower than traditional lamps; however, manufacturing improvements are continually increasing the comparative output power of LED sources (Gallucci 2016). Presently available UV LED models provide optical output power in the milliwatt (mW) range, whereas low pressure mercury lamps have output of 30-600 watts (W) and medium pressure lamps between 1-12 kilowatts (kW) (Atlantium Technologies 2017). However, given their compact size and point source configuration, UV LEDs can be placed more flexibly and can be arranged in multi-LED

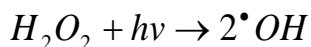
arrays to achieve increased overall output power. UV LEDs may have another comparative advantage in the ability to select LEDs with specific desired output wavelengths, whereas low pressure lamps are limited to a single 254 nm wavelength and medium pressure lamps emit a broad spectrum covering 200-320 nm.

The success of the UV LED/H₂O₂ AOP depends on the structure of the chemical compound, the amount of peroxide in solution, and the LED output power. These factors can be systematically tested in an attempt to understand the more general trends that impact chemical degradation. The objective of this study is to evaluate the effect of reaction stoichiometry, molecular structure, and optical output power on the UV LED/H₂O₂ process.

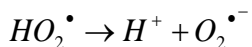
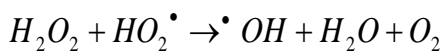
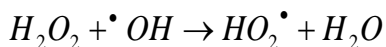
2.1.1. General Characteristics of the UV/H₂O₂ Advanced Oxidation Process

UV-peroxide advanced oxidation processes produce hydroxyl radicals through a photocatalytic reaction initiated when H₂O₂ absorbs UV light at a wavelength (λ) < 280 nm. Critical to the initiation of this process is ensuring adequate exposure to UV light at an energy high enough to achieve cleavage of the O-O bond in the H₂O₂ molecule. This cleavage leads to the formation of two hydroxyl radicals (Benjamin and Lawler 2013). A representative published value for the energy required to activate O-O bond dissociation is 210.66 ± 0.42 kJ/mol (Luo 2007). Energy per unit time provided by the UV LEDs and residence time of solution within the light distribution will together determine whether there is sufficient energy for cleavage to occur. Compared to medium pressure and low pressure mercury UV lamps, individual LEDs produce significantly less optical output power making this a critical comparison and design factor.

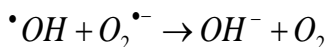
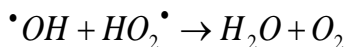
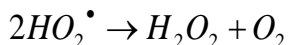
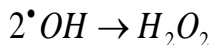
The equations governing the generation, interaction, and termination of hydroxyl radicals are well-researched and documented in the literature (Chang, et al. 2010; Crittenden, et al. 1999; Edalatmanesh, et al. 2008; Ghafoorim, et al. 2014; Grcic, et al. 2014; Mariani, et al. 2013; Wols and Hofman-Caris 2012). When the H_2O_2 molecule absorbs sufficient UV energy at the proper wavelength, the initiated reaction produces two hydroxyl radicals as shown below:



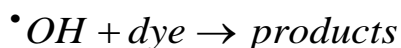
The hydroxyl radicals further propagate through the following reactions:



Radical products are then terminated through the following reactions:



During this process, the hydroxyl radicals will rapidly and non-selectively react with organic compounds they encounter. Subsequent radical production in the chain can continue to attack the organic material until it is mineralized. As an example in the context of this research, the hydroxyl radicals will react with a dye and mineralize it as seen below:



Hydroxyl radicals can also react with each other. These fast reactions result in short lifetimes of the hydroxyl radicals (Gligorovski, et al. 2015; Benjamin and Lawler 2013). Therefore, mixing and proper UV fluence is critical to the effectiveness of hydroxyl radicals as oxidants (USEPA 1999).

Hydroxyl radicals can react with the organic compounds by one of three mechanisms: 1) hydrogen abstraction (H removal), 2) hydroxylation (OH addition), or 3) oxidation without transfer of atoms (Buxton, et al. 1988). In general, hydrogen abstraction is likely to occur in saturated molecules (those with no double bonds) and hydroxylation is likely to occur in unsaturated molecules (those with double bonds); however, this is not always the case and oxidation without atom transfer can occur (Benjamin and Lawler 2013).

2.1.2. Effect of Reactant Concentrations and Solution pH

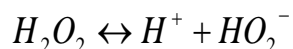
Prior studies suggest that starting molar ratios of H_2O_2 to dye must be considered to avoid creating a condition that is limited by one of the reactants. In a study that degraded Basic Violet 16 dye with UV/ H_2O_2 , varying the starting dye concentration while holding H_2O_2 constant had a pronounced impact on reducing degradation rate as dye concentration increased beyond a critical point. Additionally, increasing concentration of H_2O_2 improved degradation to a critical point, thereafter additional H_2O_2 decreased the reaction rate due to H_2O_2 self-scavenging of hydroxyl radicals (Rahmani, et al. 2012). The first point is supported in other studies related to UV/ H_2O_2 degradation of dyes (Chang, et al. 2010; Narayansamy and Murugesan 2014). The second point is also supported elsewhere in literature, indicating that too low a level of H_2O_2 appears to limit

generation of hydroxyl radicals, while too much H₂O₂ appears to scavenge hydroxyl radicals (Sharma 2015; Muruganandham and Swaminathan 2004; Oancea and Meltzer 2013).

An additional flaw in selecting incorrect starting quantities of reactants is the potential to violate assumptions underlying a pseudo-first order kinetic reaction model. In a pseudo-first order model, a fundamental requirement is that one of the reactants is available in abundance over the other reactant so that it may be essentially treated as a constant. Violating this assumption with stoichiometric adjustments may create a bias in the model (Hartog, et al. 2015).

A point regarding stoichiometry can also be made with the relationship between H₂O₂, the quantity of hydroxyl radicals produced, and the quantity of hydroxyl radicals actually available for reaction. General chemistry principles indicate the generation of two moles of hydroxyl radicals from each mole of hydrogen peroxide. However, it has been found that in aqueous solutions, a solvent “cage effect” can trap up to 50% of the hydroxyl radicals, reducing the number available for oxidation (Oppenlander 2003).

Another consideration in the AOP process is the effect that the solution’s pH may have on the efficiency of hydroxyl radical production. H₂O₂ has a pK_a of 11.8 and dissociation will increase as the solution becomes more basic as shown below:



There is literature to suggest that changing pH can affect the efficacy of hydroxyl radical degradation of dyes when other parameters are held constant. In one such study, the azo dye Reactive Orange 4 was degraded using H₂O₂/UV. The effect of varying pH

over a range of 2-8 and changing the amount of H_2O_2 between 5-25 mmol were studied. Maximum degradation was achieved at $\text{pH} = 3$ with sharp decline as pH was adjusted higher. Degradation increased along with increasing H_2O_2 addition from 5-20 mmol and then declined when moving from 20-25 mmol, suggesting a hydroxyl radical quenching effect (Muruganandham and Swaminathan 2004). Similar findings were made in experiments with tartrazine, where negative correlation was found between degradation rate and increasing pH (range 6-9), and $\text{pH} 6$ was found to be most preferable (Stewart 2016).

2.1.3. Prior UV LED AOP Chemical Degradation Studies

Prior UV LED reactor experiments have been conducted to investigate the degradation of chemical compounds; however, the scope has been limited, including three organic dye compounds: methylene blue, Brilliant Blue FCF, and tartrazine. Experiments with methylene blue were conducted in a flow through stainless steel reactor with seven 240 nm UV LEDs operating with 20 mA drive current. The primary goal of that research was to evaluate the effect of continuous or pulsed current operating modes on resultant degradation. Results indicated that both operating modes were successful in generating hydroxyl radicals, but continuous drive current was more effective. Degradation rates were found to increase exponentially with increased duty cycle. An anomaly was also noted in which a cationic/anionic interaction between the dye and quartz lens of the LED caused staining of the lens and reduced optical output power over time. (K. Duckworth 2014)

In a second study utilizing the same stainless steel reactor and LED parameters, Brilliant Blue FCF was utilized as a witness dye. Similar to the earlier study, effects of varied UV LED duty cycles on degradation rates were studied. Experiments showed that Brilliant Blue FCF worked well as an indicator dye in the AOP and did not exhibit the lens sorbance issues experienced with methylene blue. Additionally, experiments showed that when degradation rate constants were normalized to duty cycle, lower duty cycles were more efficient and optimal efficiency was reached at the lowest duty cycle of 5%. (R. W. Scott 2015)

A third study using the same stainless steel reactor design with seven 240 nm UV LEDs explored tartrazine as a witness dye. Pulsed drive current was again used to test the effect of duty cycle on degradation rate constants. Results showed that tartrazine was relatively resistant to AOP degradation, achieving only 18% removal after a 300 minute detention time. Comparatively, the Brilliant Blue FCF study reported more rapid degradation with apparent first order degradation rate constants eight to fifteen times greater (R. W. Scott 2015); however, upon further analysis, it must be noted that starting molar concentrations of tartrazine were 5 times greater than those of Brilliant Blue FCF, which likely accounted for some of the difference. Positive correlation was found with the first order rate constants, but negative correlation was observed with the normalized rate constants accounting for duty cycle. (Mudimbi 2015)

An additional study was conducted with tartrazine utilizing the same stainless steel reactor setup in which the effects of solution pH on degradation rate constants was assessed. Starting pH values were adjusted between 6 and 9 at varying LED duty cycles. Degradation rate constants were positively correlated with duty cycle and negatively

correlated with pH, with greatest degradation rates typically observed at pH 6.

Byproduct analysis indicated that hydrogen abstraction, OH addition, and electron transfer without molecule transfer were all plausible reaction mechanisms. Six byproducts were identified and two were potentially novel, indicating the tartrazine molecule may have been cleaved. (Stewart 2016)

A final study utilizing tartrazine in a new, smaller flow through reactor design investigated the effects of construction material and LED output power on degradation rate constants. Two low power, one diode UV LEDs were compared to two higher power, seven diode UV LEDs with reactor walls constructed of either stainless steel or Teflon with one of three wall thicknesses. Teflon of medium thickness was found to have a statistically significant higher rate constant than the other reactor wall thicknesses when utilizing low power UV LEDs. Experiments with high power UV LEDs produced rate constants ten times higher than experiments with low power UV LEDs, but showed no significant difference with regard to reactor construction materials. (Gallucci 2016)

2.1.4 Additional UV/H₂O₂ Advanced Oxidation Processes with Chemicals

A vast number of studies involving degradation of chemicals in UV/H₂O₂ AOPs are available in the literature. In one such study, AOPs were investigated for the removal of organophosphorus pesticides in wastewater by selecting and optimizing oxidation processes (Fenton reaction, UV/H₂O₂, and photo-Fenton process) and adjusting parameters (starting pH, chemical oxygen demand/H₂O₂ ratios, and Fe(II)/H₂O₂ ratios. Effects of parameter adjustments were observed and optimums were identified, finding the photo-Fenton reaction to be the most effective and economic treatment process under

acidic conditions (Badawy, et al. 2006). Similarly, degradation of salicylic acid in simulated wastewater was assessed by UV alone, UV/ H₂O₂, UV/Ozone, and photo-Fenton processes. The experiments were carried out in a batch reactor, and operating variables (pH, ratio of H₂O₂/chemical oxygen demand, varying concentrations) were compared with degradation rate achieved. UV/ H₂O₂ oxidation achieved greater degradation than UV light alone (Mandavgane and Yenkie 2011). Additional approaches have sought to compare the effect of different UV LED wavelengths (255, 265 and 280 nm) on the degradation of phenol (Vilhunen and Sillanpaa 2009), along with the effect of adjusting starting H₂O₂ and contaminant concentrations on the degradation of 2,4-dichlorophenoxyacetic acid (Murcia, et al. 2015).

Studies have also been conducted to assess AOP use in degradation of pharmaceutical compounds. In research utilizing a batch reactor with a low pressure UV lamp, comparisons were made between UV photolysis alone, peroxide alone, and UV/H₂O₂ oxidation of 14 pharmaceutical compounds and 2 personal care products. Seven compounds were found to have > 96 % removal by ultraviolet photolysis alone. For the majority of compounds, H₂O₂ addition to UV photolysis was not beneficial as removal did not increase significantly, and large fractions (> 85 %) of the added hydrogen peroxide remained. The authors hypothesized the residual peroxide was due to small fluence of the lamp being used, small molar absorption for hydrogen peroxide at 254 nm, and acidic pH of reaction solution. (Giri, et al. 2011) However, it is also plausible the residual may actually be due to H₂O₂ regeneration in the reaction chain.

The experimental design aspects of the previous study may explain why additional studies of pharmaceutical and personal care product degradation differ from

the above findings. One found that adding H_2O_2 during UV treatment could be effective in improving degradation in 30 pharmaceutical and personal care products, with >90% degradation achieved after 30 mins. The combination of H_2O_2 with UV light was noted to reduce the overall UV dose required as compared to photodegradation alone. (Kim, et al. 2009). Similarly, Rosario-Ortiz et al. evaluated UV/ H_2O_2 treatment of pharmaceuticals in wastewater, observing > 90% removal of several compounds, and concluding that UV/ H_2O_2 removal of pharmaceuticals was a function of hydroxyl radical reactivity. UV absorptivity of the treated effluent at 254 nm was found to be a viable method of assessing pharmaceutical removal efficiency. (Rosario-Ortiz, et al. 2010) Additionally, Shu et al. investigated the degradation of emerging micropollutants, including pharmaceuticals, using a UV/ H_2O_2 AOP catalyzed by a medium pressure UV lamp. Pseudo first-order rate constants were found to be dependent on initial compound concentrations and H_2O_2 concentration. UV dose required for 50% and 90% removal was measured at varying H_2O_2 levels and varied significantly across the compounds. Input energy efficiency was measured for each compound by observing the electrical energy (in kWh) required to reduce a pollutant concentration by 90%. (Shu, et al. 2013)

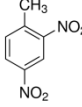
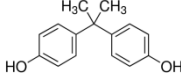
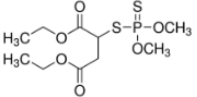
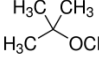
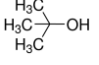
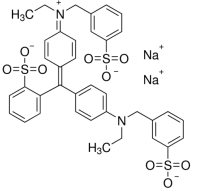
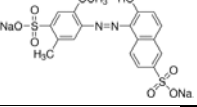
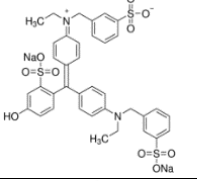
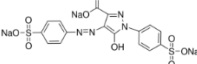
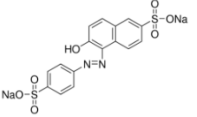
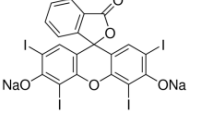
2.2. Materials and Methods

2.2.1. Apparatus

Experiments were conducted utilizing six dye and five achromatic chemical compounds with diverse molecular structures, with each being tested individually (e.g. no mixtures).

Table 1 lists the test compounds used along with basic properties and manufacturer information. Previous research indicated that methylene blue dye caused staining of the quartz LED lenses due to a cationic/anionic attraction between the dye and the quartz (K. Duckworth 2014). For this research, anionic dyes were selected in order to avoid the lens staining effect. Solutions for each AOP experiment were prepared by mixing hydrogen peroxide (30% in water, Fisher Scientific) and one of the test compounds in deionized (DI) water. Each experimental solution was prepared to a well-mixed concentration of 0.01 millimolar (mM) test compound and 5 mM H₂O₂ in a 250 mL volumetric flask.

Table 1. Basic information and properties pertaining to dyes and achromatic chemicals used in experiments.

Compound & (Abbreviation)	Manufacturer & Lot	Formula	Molecular Weight	Structure	Dye Peak Absorptivity Wavelength
2,4-Dinitrotoluene (DNT)	Sigma Aldrich Lot: MKAA0690V	$C_7H_6N_2O_4$ or $CH_3C_6H_3(NO_2)_2$	182.135 g/mol		N/A
Bisphenol A (BPA)	Sigma Aldrich Lot: MBH2096V	$C_{15}H_{16}O_2$ or $(CH_3)_2C(C_6H_4OH)_2$	228.291 g/mol		N/A
Malathion (MAL)	Pfaltz and Bauer Lot: 122029-1	$C_{10}H_{19}O_6PS_2$	330.35 g/mol		N/A
Methyl tert-butyl ether (MTBE)	Fisher Scientific Lot: 6810PHM90003392	$C_5H_{12}O$ or $(CH_3)_3COCH_3$	88.15 g/mol		N/A
Tert-butyl Alcohol (TBA)	Fluka Chemical Lot: FJ456J477	$C_4H_{10}O$ or $(CH_3)_3COH$	74.123 g/mol		N/A
Brilliant Blue FCF (BB)	Dr. Ehrenstorfer GmbH Lot: 41030	$C_{37}H_{34}Na_2N_2O_9S_3$	792.85 g/mol		630 nm
Allura Red AC (AR)	TCI America Lot: GJ01-AGBL	$C_{18}H_{14}N_2Na_2O_8S_2$	496.42 g/mol		504 nm
Fast Green FCF (FG)	Fisher Scientific Lot: 162339	$C_{37}H_{34}N_2O_{10}S_3Na_2$	808.85 g/mol		625 nm
Tartrazine (TT)	Sigma Aldrich Lot: MKBQ1073V	$C_{16}H_9N_4Na_3O_9S_2$	534.36 g/mol		427 nm
Sunset Yellow FCF (SY)	TCI America Lot: GSAXJ-OD	$C_{16}H_{10}N_2Na_2O_7S_2$	452.37 g/mol		482 nm
Erythrosine B (EB)	TCI America Lot: TSP5N-LB	$C_{20}H_6I_4Na_2O_5$	879.86 g/mol		527 nm

AOP experiments were conducted by flowing solutions through a cylindrical reactor with a central tube constructed of 2 mm thick polytetrafluoroethylene (PTFE) that fits securely into end caps of a half-sphere design, also constructed of PTFE. The central cylinder has an internal diameter of 22.1 mm with a length of 80.52 mm, and the internal diameter of each of the half-sphere end caps is 22.1 mm. Overall design of the interior reactor volume is capsule-shaped when assembled. The reactor was oriented horizontally with flow entering through the top side wall of one end cap, progressing horizontally through the cylinder, and out the top side wall of the opposite end cap. One LED was mounted through the center of each end cap such that the lens of the LED was flush and in contact with the test solution. A copper fin assembly was attached to each end cap in thermal contact with the back of the LED to dissipate heat from the LEDs. Total interior volume of the assembled reactor was 36.53 mL. Figure 1 shows the complete reactor assembly. Figure 2 shows a representative LED mounted in an end cap.

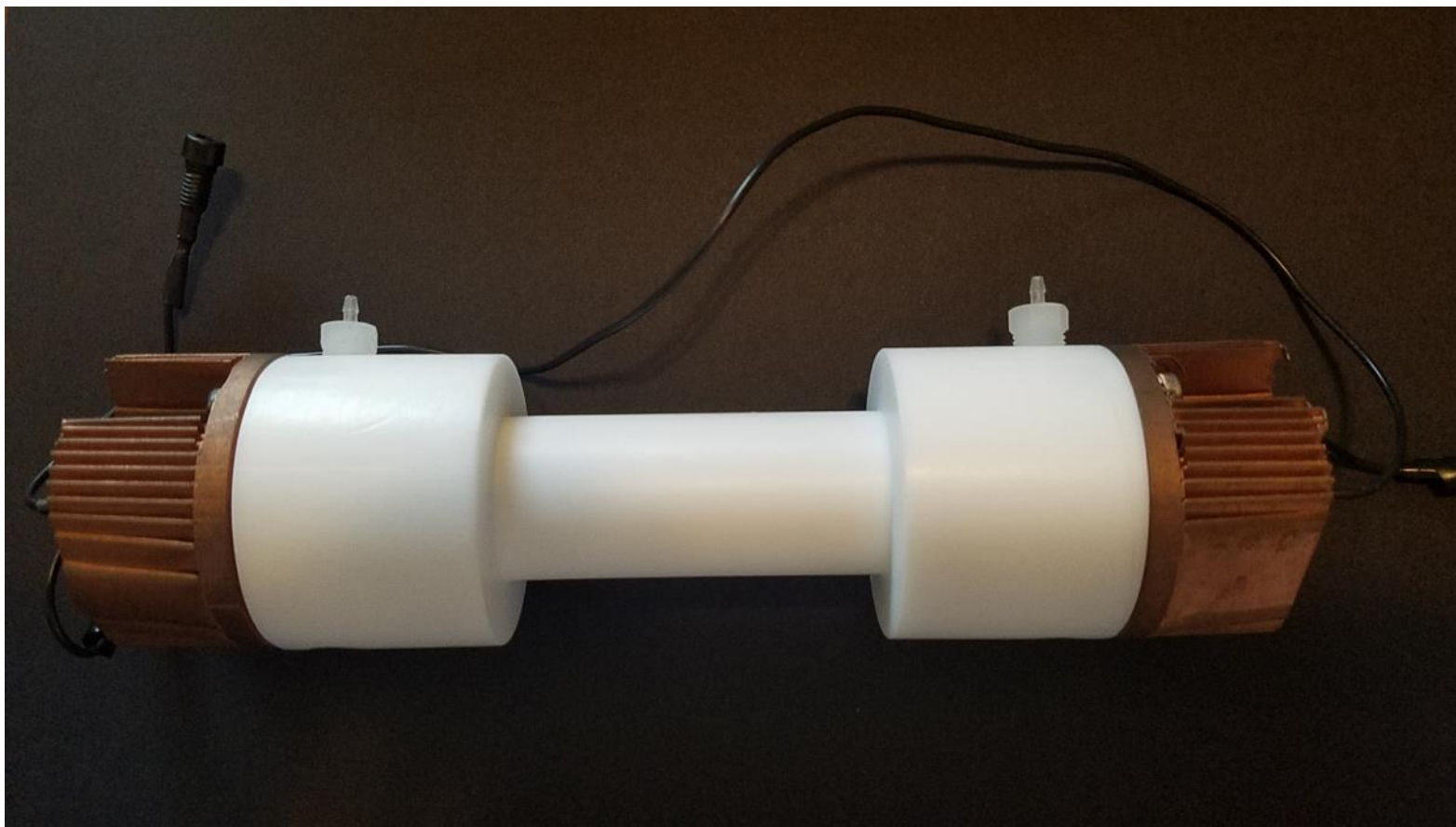


Figure 1. Complete UV LED reactor assembly showing pairing of central cylinder and spherical end caps with heat sinks.

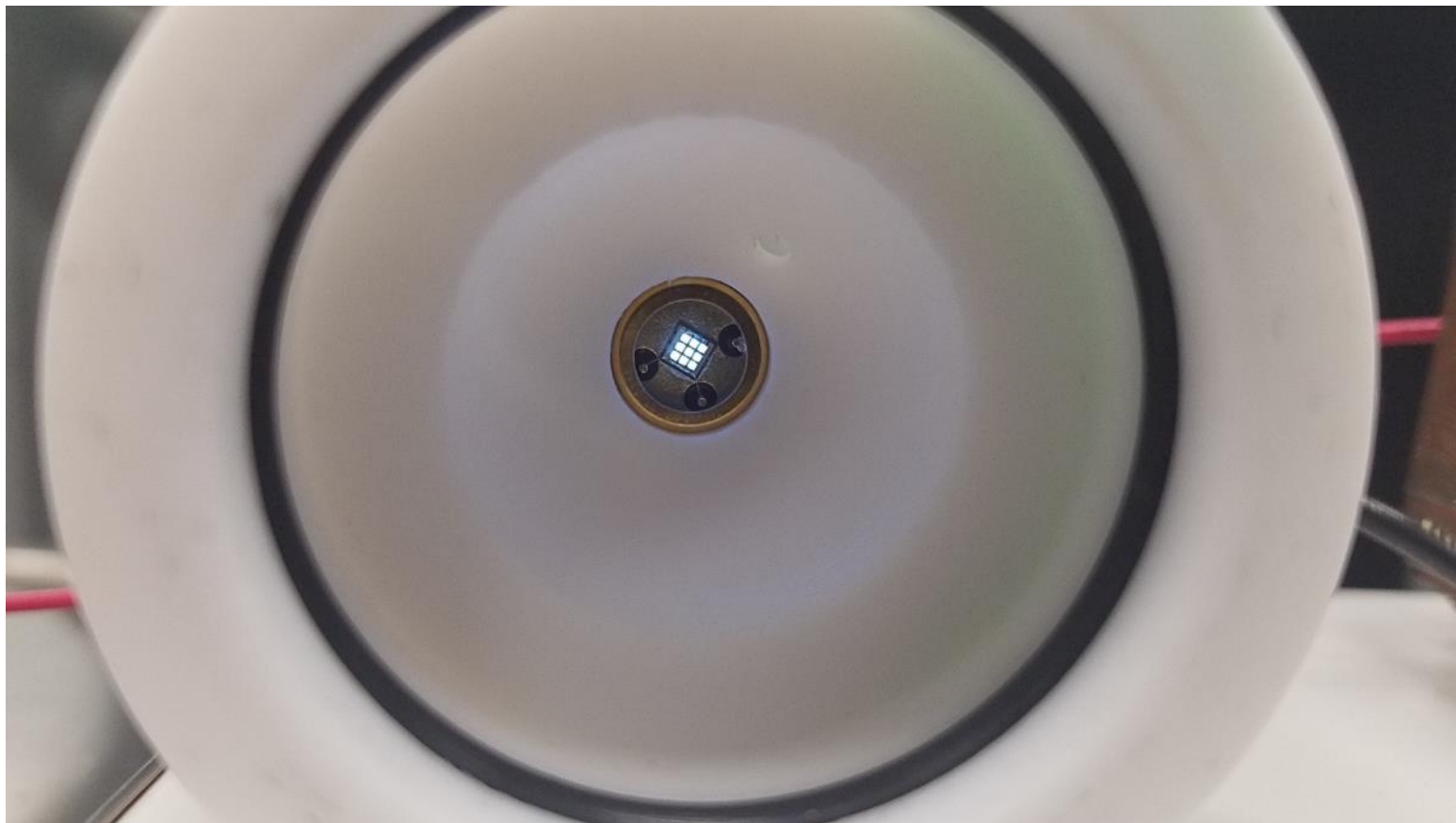


Figure 2. View of an end cap removed from the reactor showing LED placement.

Flow of test solutions through the reactor assembly was controlled by a MasterFlex Console Drive 77521-50 peristaltic pump and MasterFlex 14 tubing (Cole Parmer, Vernon Hills, Illinois). Flow rates were set at 2 mL/min for all experiments, which resulted in approximately 17.5 mins of residence time in the reactor. Magnetic stir plates and PTFE coated stir bars were used to ensure mixing in the volumetric flask of test solution and also within the reactor tube to ensure well mixed model assumptions were met during each experiment. When accounting for the volume displaced by the stir bar inside the reactor, useable volume was reduced to approximately 35 mL. An injection tracer test was conducted and results indicated the reactor with stirring produced near ideal continuous flow stirred tank reactor (CSTR) behavior. Two models of UV LEDs (UV-TOP and UV-CLEAN) procured from Sensor Electronic Technology Incorporated (SETi, Columbia, South Carolina) were utilized throughout this research. Both models provide a typical peak output wavelength at approximately 265 nm. The UV-TOP models consist of one diode and were utilized for low power tests with drive currents of 20 and 40 mA. The UV-CLEAN models consist of nine diodes and were utilized for high power tests with drive currents of 80, 120, 160, and 200 mA. LEDs were driven by circuit boards consisting of 20mA LUXdrive 4006 series semi-conductor resistors (LEDdynamics, Randolph, Vermont). The circuit boards were powered by a KEYSIGHT E3620A digital power supply (Keysight Technologies, Santa Rosa, California).

A Labsphere integrating sphere calibrated with a D2 Deuterium lamp was used to measure optical power of the UV LEDs at each drive current of interest. Output data from the integrating sphere was processed in Illumia Pro software (Labsphere, Inc, North

Sutton, New Hampshire) to acquire total power and peak wavelength data on each LED at all drive current levels evaluated.

Figure 3 depicts the overall orientation of the reactor setup and flow scheme. Figure 4 shows the reactor with one end cap removed to illustrate the orientation of a magnetic stir bar and one of the LEDs within the reactor.

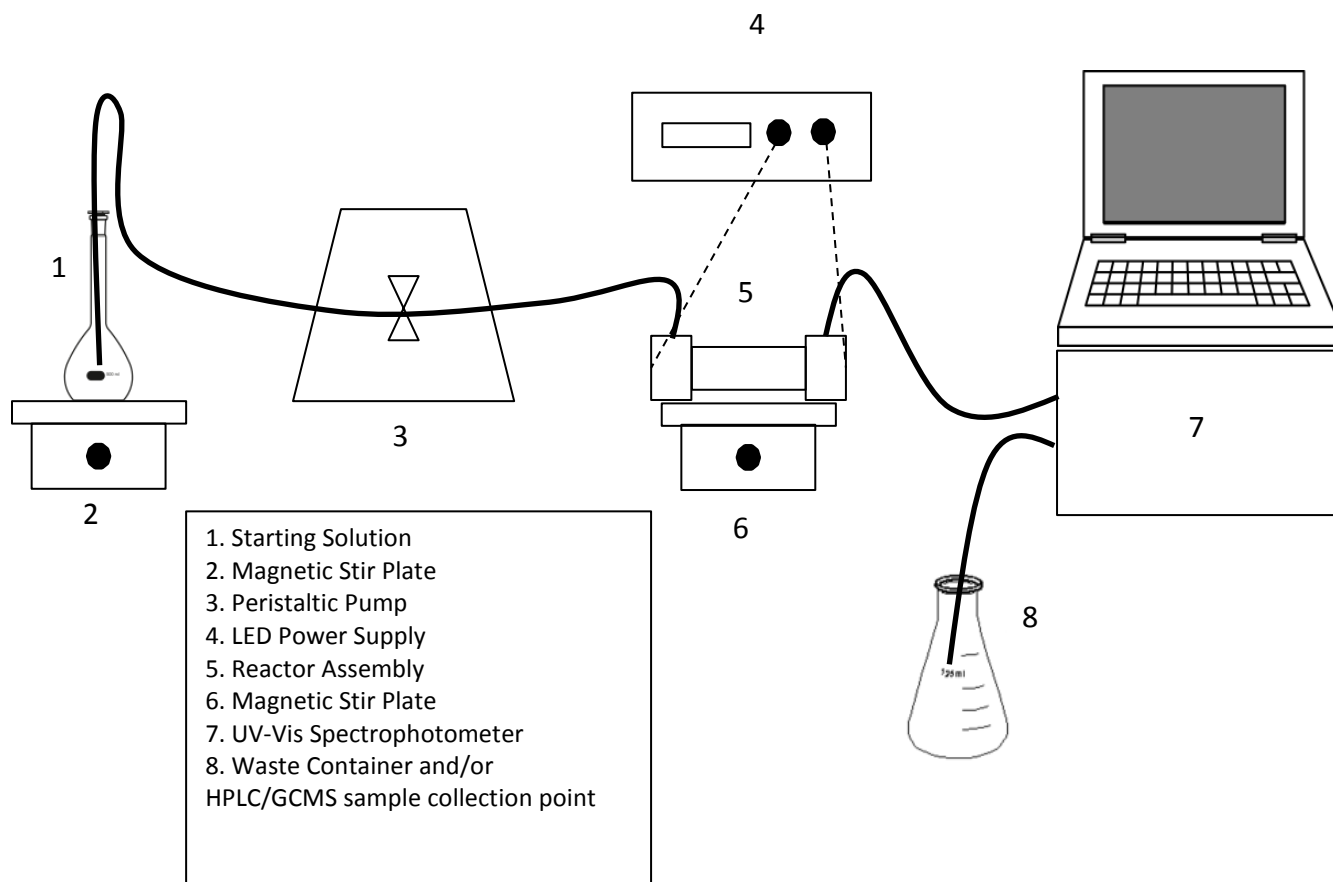


Figure 3. Schematic depicting complete experimental setup.



Figure 4. View of reactor endcap removed showing stir bar in middle of tube and LED at distal end.

An Agilent Technologies Cary 60 UV-Vis spectrophotometer (Agilent Technologies, Santa Clara, California) was used to measure the change in absorbance of dyes over time at a peak wavelength specific to each dye as listed in

Table 1. For example, the Brilliant Blue FCF dye used in this study has a peak wavelength at 630 nm. Over the course of an AOP experiment, reduction in absorbance values with time at 630 nm was measured as an indicator of degradation.

The spectrophotometer was not suitable or practical in the measurement of the achromatic chemical compounds that were weaker chromophores than the dyes (dyes are designed to be very strong chromophores). An Agilent Technologies 6130 quadrupole high-performance liquid chromatography (HPLC) system was used to analyze BPA via fluorescence detector, DNT via diode array detector, and MAL via mass spectrometer. An Agilent Technologies 7000C triple quad gas chromatography-mass spectrometry (GCMS) system paired with an Agilent Technologies 7697A headspace sampler (Agilent Technologies, Santa Clara, California) was used to analyze TBA and MTBE. In the case of HPLC analyses, samples were manually collected in amber vials at predetermined time increments during each experiment. Samples for GCMS headspace analysis were collected manually in clear headspace vials, 1 g of sodium chloride (Thermo Fisher Scientific, Waltham, Massachusetts) was added to each vial (to “salt out” the analyte from solution and force it into the headspace), and the vial was immediately capped.

2.2.2. Experimental Procedure

Initial UV LED/ H₂O₂ AOP experiments were conducted to assess the comparative differences in degradation of the 11 compounds. The solutions for all experiments were prepared to starting concentrations of 5 mM hydrogen peroxide and 0.01 mM test compound in 250 mL of DI water. This resulted in solutions with a 500 to 1 molar ratio of H₂O₂ to test compound. Stock solutions were prepared at predetermined concentrations in a base of deionized water and stored in appropriate conditions to maintain the integrity of the solutions for use over multiple experiments. Hydrogen peroxide procured for this research is certified at 31.9% (w/w) H₂O₂ content per the certificate of analysis and was stored refrigerated at 5°C. At 5°C, the density of 31.9% (w/w) H₂O₂ in water is expected to be 1.1278 g/mL. One mL of refrigerated stock H₂O₂ was weighed on a microbalance and compared to the certificate of analysis content. The density of the H₂O₂ was used to determine a pipette volume of 126.2 microliters was necessary to achieve the desired 5 mM concentration.

For each experiment, a precise volume of test compound stock solution was pipetted into a 250 mL volumetric flask prefilled halfway with DI water, followed by pipetting a precise volume of H₂O₂ into the flask and approximately one minute of mixing on a vortex mixing unit. The flask was then brought to 250 mL volume with DI water and was then capped and mixed by hand for approximately 5 minutes, a magnetic stir bar was inserted, and the solution was further mixed on a magnetic stir plate for an additional 15 minutes. For dye experiments, the spectrophotometer was zeroed with DI water and set to measure absorbance values +/- 5 nm around the peak wavelength for the

dye being studied. Absorbance measurements were taken every one minute over a total 75 minute time period, equal to just over four reactor bed volumes to reach near steady state final concentration. For achromatic chemicals, 2 mL samples were collected in either amber vials or clear headspace vials at 0, 2, 4, 6, 8, 10, 12, 15, 20, 25, 30, 35, 45, 60, and 75 min increments and immediately transferred to the HPLC or GC-MS for analysis. Initial experiments utilized the low power UV-TOP LEDs operating at 40mA to initiate the AOP reaction.

As each experimental solution was mixing, the pump was turned on to allow for warm up. After mixing, the pump was briefly turned off, and a 60 mL Becton Dickinson syringe was used to load the reactor with the starting solution, the reactor stir plate was started, and the pump was started again to initiate solution flow through the reactor (flow was assessed at the beginning and end of each experiment to ensure the desired 2 mL/min rate was achieved and maintained). In the case of dyes, the spectrophotometer data collection was started simultaneous to the LED power being activated, and the experiment was allowed to progress for 75 minutes. Five absorbance values representing 0%, 25%, 50%, 75%, and 100% starting dye concentrations were also obtained for each experiment to generate a degradation calibration curve and assess accurate operation of the spectrophotometer.

Subsequent experiments were conducted with various levels of UV LED drive current. Experiments were first repeated with the lower power UV-TOP LEDs operating at 20 mA versus the original 40mA. The higher power UV-CLEAN LEDs were then installed in reactor end caps and experiments were repeated at 80 mA, 120 mA, 160 mA, and 200 mA drive current. This portion was designed to assess quantum yield effect on

AOP optimization and hydroxyl radical production. Theoretically, higher drive current should result in higher optical output power and, subsequently, increased hydroxyl radical production.

Further experiments were conducted in which the molar ratio of H_2O_2 to test compound was varied. Starting test compound concentrations remained constant at 0.01 mM; however, H_2O_2 concentrations were adjusted above and below the starting 5mM value until optimal degradation rate or degradation extent was achieved. The starting concentrations represented a 500:1 H_2O_2 :test compound ratio. This ratio was then adjusted in increments of 100:1 above and below 500:1 (e.g. 100:1, 200:1, 300:1, 400:1, 600:1, 700:1; 800:1, 900:1) to assess if a point or range of optimality exists. This was designed to identify ratios where the reaction becomes rate limited by either inefficient hydroxyl radical production or by potential hydroxyl radical scavenging by H_2O_2 when too much H_2O_2 is present in solution.

Control experiments were conducted with the test compound and H_2O_2 solutions mixed and passed through the reactor for a period of 75 minutes without exposure to UV light to assess whether the specific compound is subject to degradation by reaction with H_2O_2 alone. Similarly, experiments were conducted with test compound solutions containing no H_2O_2 passing through the reactor with UV light exposure for a period of 75 minutes to assess whether the specific dye is subject to photodegradation by exposure to UV light alone. It was assumed that if a compound did not show degradation at a 200 mA drive current, then optical output from lower drive currents would not cause degradation.

Finally, solutions of 0.01 mM concentrations of each test compound in DI water with no H₂O₂ were scanned in the spectrophotometer to determine the absorbance value for each at the LED peak output wavelength of 265 nm. These values were then used to calculate molar extinction coefficients and assess any impact that molar absorptivity may have on reaction kinetics.

2.2.3. Data Analysis

Data was plotted in Microsoft Excel (Microsoft, Redmond, Washington) to show the normalized change in effluent concentration (C/C_0) of dye or chemical over time as measured by the spectrophotometer, HPLC, or GC-MS. Absorbance values for dyes were exported directly from the Cary 60 software, and Agilent Technologies ChemStation software was used to integrate peaks of resultant chromatograms from the HPLC and GC-MS analyses. The data was then modeled using the following mass balance relationship for a completely mixed reactor with flow (Duckworth et al., 2015):

$$\frac{C}{C_0} = \frac{\tau k_S e^{-\left(t\left(k_S + \frac{1}{\tau}\right)\right)} + 1}{\tau k_S + 1} \quad (1)$$

Where

C : concentration of dye at time t

C_0 : starting dye concentration at time 0

τ : residence time of solution in reactor

k_s : apparent first order degradation rate constant

Residence time, τ , was computed by dividing the volume of the reactor (35 mL, accounting for volume lost to stir bar) by the flow (2 mL/min), resulting in $\tau = V/Q = 17.5$

min. An apparent degradation rate constant, k_s , was calculated for each experiment using the Microsoft Excel Solver Add-In to optimize the best overall k_s that minimizes the sum of square difference between actual and model C/C_0 values. Any deviations from the fitted model indicate deviation from CSTR conditions or deviations from first-order reaction kinetics.

With known molar concentrations and known cuvette optical path length, Equation 2 below was utilized to calculate the molar extinction coefficient for each compound at the peak LED output wavelength (265 nm).

$$\varepsilon = \frac{A}{cl} \quad (2)$$

Where

ε : molar extinction coefficient

A : absorptivity as measured by spectrophotometer

c : concentration of species in solution

l : path length of light through solution

2.3. Results and Discussion

2.3.1. The Effect of Drive Current on Power Output

Following measurements in the integrating sphere and processing of optical output power measurements in the Illumia Pro software, the two UV-TOP LEDs and two UV-CLEAN LEDs with the highest total output power measurements were chosen for installation in the reactor. Table 2 shows results of integrating sphere analysis for the

LEDs selected. Figure 5 shows a linear relationship ($R^2 = 0.9914$) between applied drive current and total additive output power for LED pairs (e.g. UV-TOP pair and UV-CLEAN pair). A slight transition can be seen in the figure between 40 mA and 80 mA with the change in LED models. Peak output wavelengths occurred at 265 nm and total output power ranged from 1.31 mW at 20 mA for a UV-TOP model to 12.47 mW at 200 mA for a UV-CLEAN model.

Table 2. Output characteristics of UV LEDs utilized in reactor experiments.

LED Model	Serial #	Drive Current (mA)	Total Output Power (mW)	Peak Output Wavelength (nm)
UV-TOP	P53	20	1.343	265
UV-TOP	R54	20	1.310	265
UV-TOP	P53	40	2.464	265
UV-TOP	R54	40	2.442	265
UV-CLEAN	U9	80	5.702	265
UV-CLEAN	V5	80	5.700	265
UV-CLEAN	U9	120	8.328	265
UV-CLEAN	V5	120	8.340	265
UV-CLEAN	U9	160	10.7	265
UV-CLEAN	V5	160	10.24	265
UV-CLEAN	U9	200	12.26	265
UV-CLEAN	V5	200	12.47	265

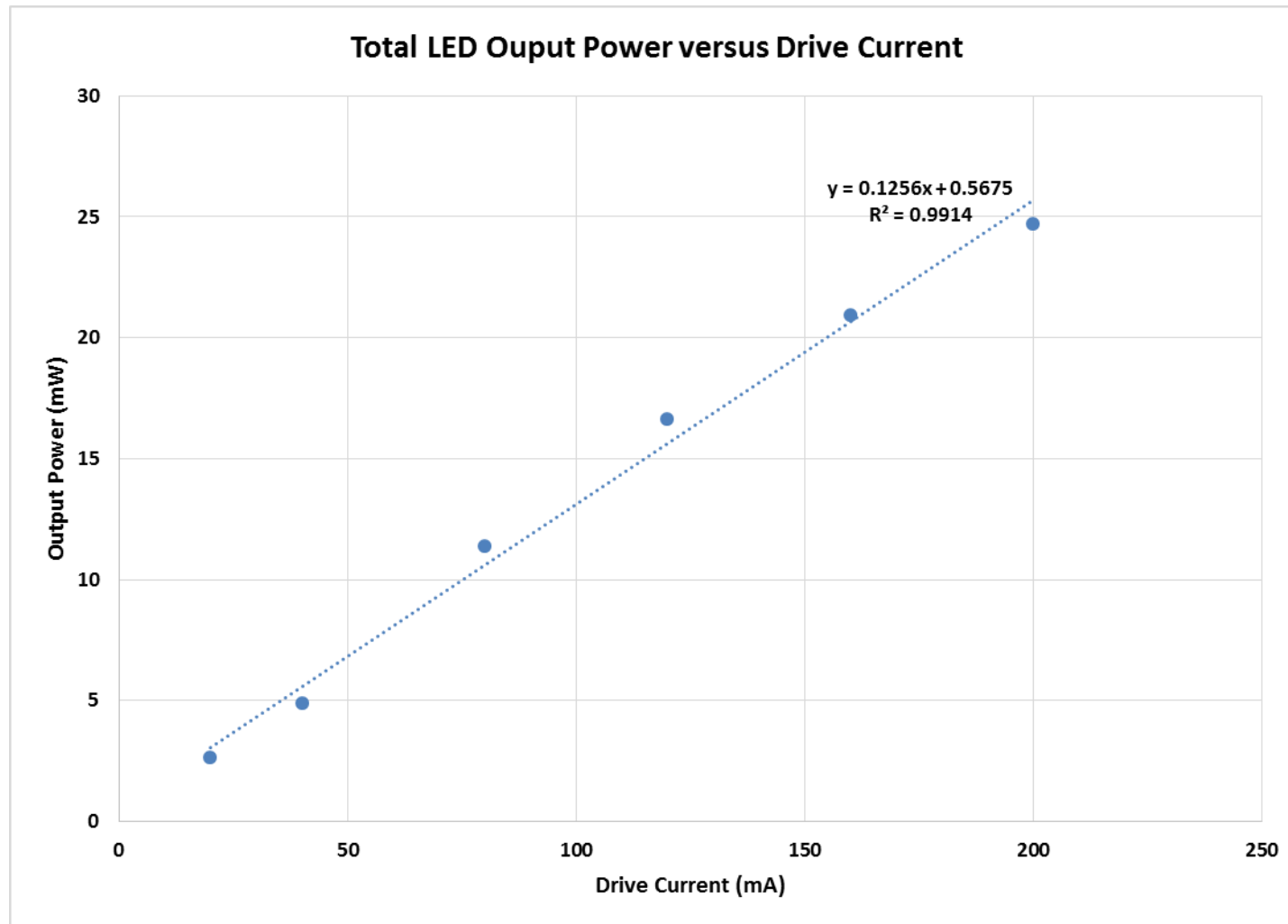


Figure 5. Comparison of optical output power achieved from input drive current.

2.3.2. The Effect of Drive Current on the Removal of Organic Compounds

Figure 6 presents k_s versus drive current data in a graphical format for each compound and drive current level tested with the molar peroxide ratio at 500 mole H_2O_2 /mole test compound. Some degree of degradation was observed for all dyes and achromatic chemicals under all drive current conditions. Of interest in the figure is a linear increase in k_s with increase in drive current for each compound. For example, the k_s for MAL increased from 0.144 min^{-1} at 20 mA drive current to 1.078 min^{-1} at 200 mA drive current. The lowest k_s values were associated with EB, but the linear relationship was also observed in this case, as the k_s increased linearly from 0.003 min^{-1} at 20 mA drive current to 0.255 min^{-1} at 200 mA drive current. Exponential relationships were observed between the drive current and degradation extent where an initial sharp linear phase between 20 – 80 mA begins to taper, and the benefit to overall degradation extent begins to flatten between 120 - 200 mA (Figure A1, Appendix A). If percent removal is a priority goal over rate of removal in a real world application, such a relationship suggests that there may not be significant added benefit in applying additional energy to the system beyond a critical point (e.g. approximately the same percent removal may be achieved at 120 mA when compared to 200 mA--in some cases in a comparable timeframe). This may be particularly true of systems that are operating at or near steady state conditions. Summary apparent first order degradation rate constants and percent removal for all test compounds tested at all drive current levels with a molar peroxide ratio of 500 mole H_2O_2 /mole test compound are provided in Tables A1 and A2 and Figures A2 through A5 (Appendix A).

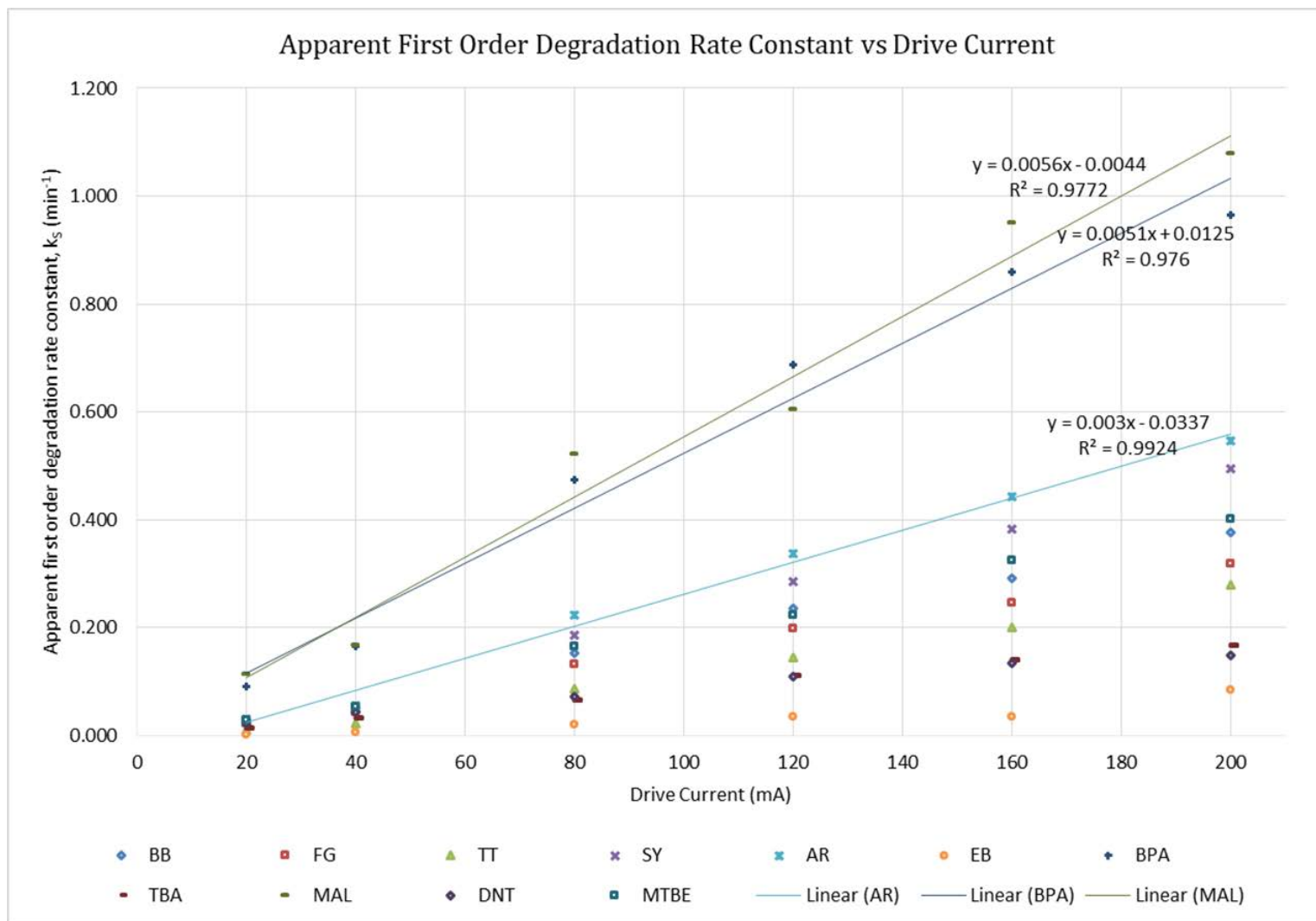


Figure 6. Linear relationship between apparent degradation rate constant and drive current. Three example linear fits are shown.

These linear relationships are expected first principles of electromagnetic radiation. However, one underlying question is if there are any phenomena occurring in the experimental apparatus which would cause a deviation from theory—e.g., non-linear output from the LEDs when applied in the reactor, fundamentals of hydroxyl reactions, competitive reactions, etc. These are explored in more detail below. First, it is useful to review the theory: the energy of an individual photon can be described by Planck's equation:

$$E = hc/l \quad (3)$$

Where

E : Energy (J)

h : Planck's constant = 6.626×10^{-34} J's

c : Speed of light = 3×10^8 m/s

l : Wavelength of light (m)

In the case of the 265 nm peak output of the LEDs utilized in this study, this results in an energy of 7.5×10^{-19} J (or 4.68 eV) per photon. We can then use this to determine the number of photons produced per unit time by considering the relationship to optical output power in the following equation:

$$\text{Photon production rate (photons/sec)} = P/E \quad (4)$$

Where

P : Optical Output Power (W)

E : Energy of a photon from Equation 3 (J)

Therefore, the optical output power is linearly related to the photon production rate, which, in turn, generates a linear increase in hydroxyl radicals because a photon is required for production of hydroxyl radicals from hydrogen peroxide (according to the equations on page 12)

and, therefore, the apparent first order degradation rate constants. The linear relationship of such a plot can be used to predict degradation rates achievable with varying current levels. Such an approach could be useful in fiscal decisions if implemented at full scale.

As a Watt is equivalent to a Joule/s, the units on Equation 4 become $(J/s)/(J/photon)$ and reduce to *photons/second*. Based on Equation 4, Table 3 summarizes the total number of photons/second calculated to be produced in the reactor under each drive current level using total output powers from Table 2. The estimated total number of photons/second increases linearly with power output. Note that these absolute values are likely an overestimate given that the calculations are assuming the output light is monochromatic at 265 nm. LEDs do not produce truly monochromatic light, and 265 nm is the peak output with other neighboring wavelengths contributing to the total output power. However, for purposes of understanding the linear nature of the relationship between photon production rate and LED output power, assuming a single wavelength is useful.

Table 3. Calculated photon production rate for each drive current level.

	20mA	40mA	80mA	120mA	160mA	200mA
Photon production (s⁻¹) X 10¹⁶	0.354	0.654	1.52	2.22	2.79	3.3

The theoretical linear relationship between drive current and the apparent first order degradation rate constant also has two implications for understanding the action of the hydroxyl radical when present in a solution containing an organic chemical, H₂O₂, and other hydroxyl radicals. First, hydroxyl radicals are known to react with a wide range of constituents present in solution (Buxton, et al. 1988). Reactions with other hydroxyl radicals are most thermodynamically favorable because the activation energies (8 kJ/mol, Buxton, et al. 1988) that

are required are lower than those associated with hydroxyl-peroxide reactions (14 kJ/mol, Buxton, et al. 1988) and common achromatic water pollutants (typically 14 - 20 kJ/mol, Buxton, et al. 1988). As the drive current is increased, more hydroxyl radicals are produced, but this does not lead to a disproportionate (nonlinear) proportion of hydroxyl-hydroxyl reactions. The energetic favorability of the hydroxyl-hydroxyl radical reaction does not lead to nonlinear relationships between power output and the apparent first order degradation rate constants. The second implication of the linear relationships observed here is related to how hydroxyl radicals attack organic compounds. The three oxidative modes are 1) hydrogen abstraction (i.e. removing a hydrogen atom from a saturated hydrocarbon), 2) hydroxylation (i.e. adding the hydroxyl group to an unsaturated hydrocarbon), or 3) oxidation without transfer of atoms. The kinetics associated with these mechanisms are different because the shape of the pre-reactive (i.e. transition state) complexes are different. The linear power-kinetics relationships observed in this study (Figure 6) imply that the relative contribution of these reaction mechanisms does not change as a function of the drive current. These two implications merit further study.

While Equations 3 and 4 relate to the relative contribution to the reaction mechanism, they do not directly speak to the specifics of the reaction mechanism and kinetics. For example, Erythrosine B exhibited notable behavior with respect to degradation kinetics (Figure 7). When the drive current was 20 or 40 mA, the apparent first order degradation constants were 0.003 and 0.006 min⁻¹ respectively, and the EB degradation curves exhibited smooth, nonlinear profiles, consistent with first order degradation in a CSTR, and showing less than 10% total EB removal. However, at 80 mA an interesting transition occurred wherein degradation did not appear to reach a steady state, instead tending to continue a linear degradation pattern until the end of the run. At 120 mA, unexpectedly unique kinetics were observed, and an inflection point appeared

as EB was approximately 40% degraded. After the inflection point, a secondary degradation profile appears to begin, and degradation proceeds at a faster rate until EB is nearly 100% degraded. Inflection points were also observed at 160 mA and 200 mA, but they were reached more rapidly. At 200 mA, the transition at the inflection point is less pronounced as the overall degradation proceeds at a faster rate with an apparent first order degradation rate constant of 0.255 min^{-1} .

Rather than reflecting a deviation from the theory discussed above, these results could suggest the presence of multiple processes relevant to degradation. Namely, Erythrosine B was the only dye to exhibit direct photodegradation from UV light alone. Exposure at 20, 40 and 200 mA drive currents over 75 minute UV control runs resulted in 1%, 2.1% and 21 % degradation, respectively. However, photodegradation does not completely explain the results. The photodegradation of EB is related to its structure, but the results in Figure 7 may involve more complex mechanisms. As noted in Table A3 and Figure A4 – A5 (Appendix A), EB has the highest molar absorptivity at the 265 nm output wavelength of the LEDs, and it absorbs almost 5.5 times more strongly than 5 mM H_2O_2 at that wavelength, perhaps reducing the amount of hydroxyl radicals available to oxidatively degrade EB. Further, there may be a change in the relative importance of photodegradation compared to oxidative degradation as the reaction proceeds. Initially, direct photodegradation is breaking down EB molecules, which in turn begins to reduce the photon absorbance competition at 265 nm. Simultaneously, H_2O_2 molecules benefit from this reduction in EB concentration, and hydroxyl radical production increases due to increased photon interaction. It is possible that the inflection point marks a transition where enough degradation has occurred and more photon energy is available for hydroxyl radical production. At higher drive current levels, more photons are available to reach and flatten this

transition more rapidly. This finding led to a hypothesis that EB may benefit from greater initial H_2O_2 concentrations in order to give H_2O_2 a higher likelihood of competing for photons in the vicinity of the LED lens.

The literature is silent on the degradation phenomena evident in Figure 7, and pseudo-first order kinetics have generally been utilized in different types of UV AOPs. Bairagi and Ameta studied the degradation of EB in a UV/ TiO_2 reactor. Degradation values were reported in a tabular format; however, when plotted it appears that a subtle inflection point may be present, though the authors report pseudo-first order kinetics (Bairagi and Ameta 2016). Similarly, in a study by Apostol et al., EB was degraded via UV/ TiO_2 . The resultant degradation was presented in a graphical format using overlaid spectrophotometer curves. When the approximate absorbance values from these curves is plotted, an inflection point can be seen, though the authors did not specifically mention the result (Apostol, et al. 2015). Though these studies utilized TiO_2 , and not H_2O_2 as in the present study, the same competition for UV absorbance and changes in competition over time would be expected. TiO_2 requires photons to produce hydroxyl radicals just as H_2O_2 does. As the EB degrades, more photons would become available to the TiO_2 substrate.

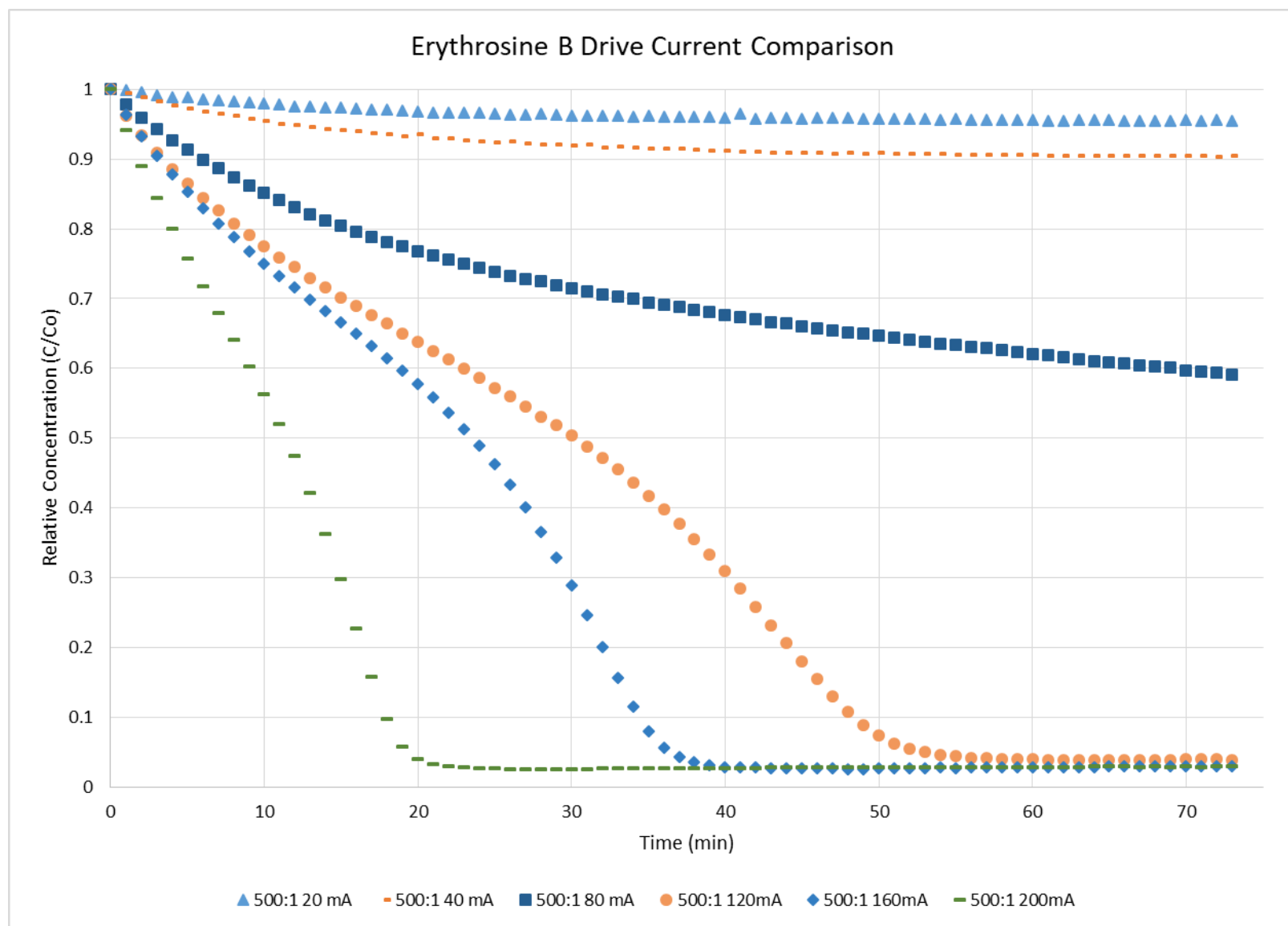


Figure 7. The effect of drive current on Erythrosine B removal.

Another deviation from theoretical behavior predicated by Equations 3 and 4 is revealed in Figure 8, which shows removal profiles for BB, FG, and TT as a function of drive current. Of particular interest in this figure is the transition that TT makes relative to the other dyes as the drive current increases. Initially at 20 and 40 mA, the order of degradation rates and extents are aligned between the dyes where the order of each follows $BB > FG > TT$. Overall degradation extent for TT lags significantly at these two drive current levels as evidenced by TT degradation extent at 40 mA being approximately equal to BB degradation extent with half the drive current at 20 mA. At 80 mA, a transition is observed where TT begins to surpass BB and FG in overall degradation extent, though the degradation rate is still slower. This transition continues at 120, 160, and 200 mA as TT continues to reach a greater degradation extent than BB and FG and the degradation rates continue to move closer to parity. As with EB, Table A3 and Figure A6 (Appendix A) show that TT exhibits the second highest molar extinction at 265 nm and absorbs 3.9 times more strongly than H_2O_2 , though it exhibited no direct photodegradation at its starting concentration. It is likely that this non-destructive UV absorbance by TT competes with H_2O_2 for the available photons, and higher drive current levels begin to more rapidly mitigate this competition as more photons are made available. Kinetics indicate that TT degradation starts out hampered by absorbance competition resulting in a slower initial observed degradation rate and less removal, but ultimately catches up as TT degradation proceeds and the TT absorbance competition decreases. Comparatively, BB and FG have lower molar absorptivity at 265 nm and tended to follow first order behavior without shifts.

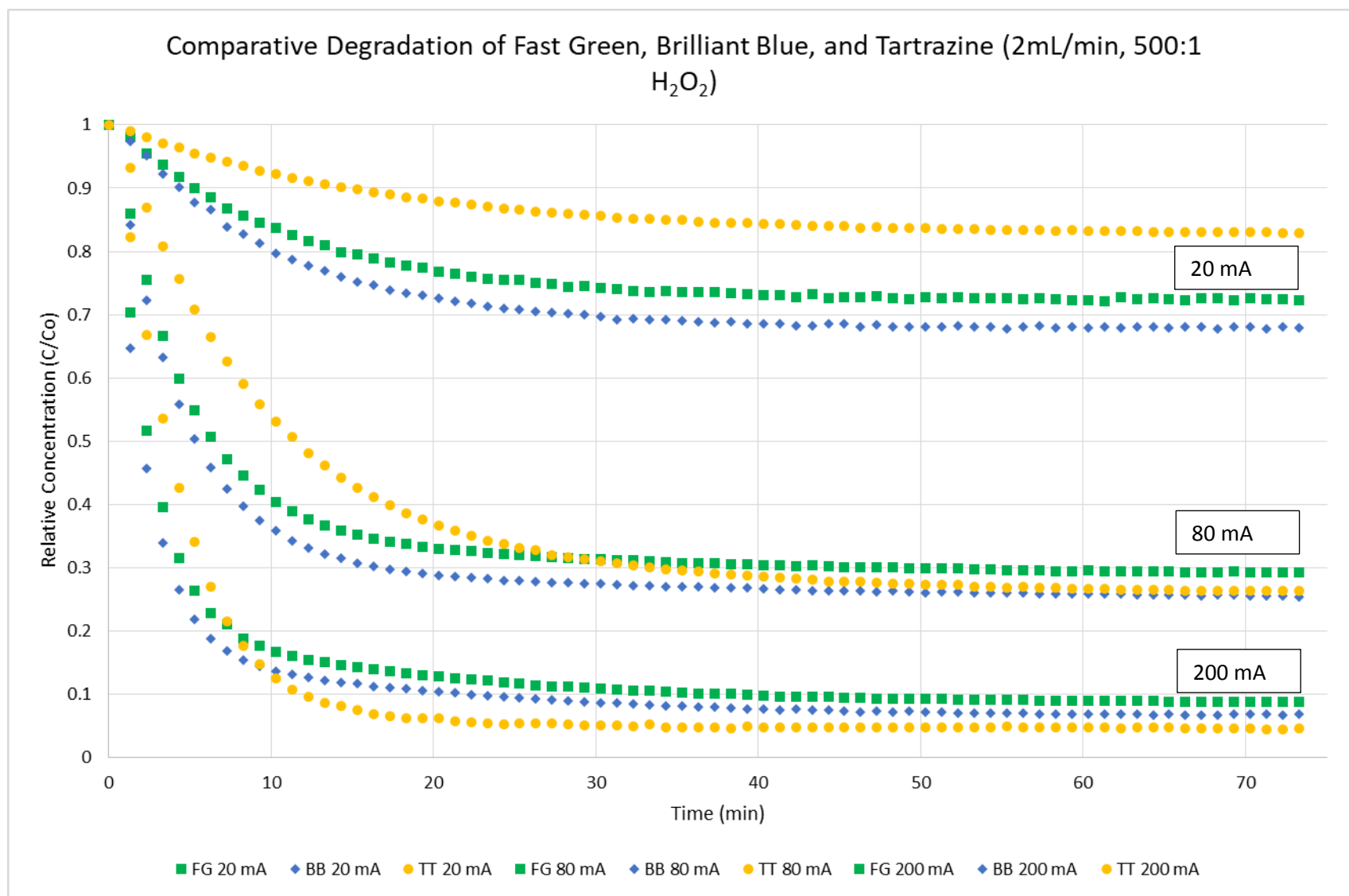


Figure 8. The effect of drive current on the degradation of dyes.

As compared to degradation shifts observed with TT during dye experiments, degradation profiles for chemicals with weaker chromophores generally proceeded as expected with respect to first order kinetics and followed the same rank order of degradation rate and extent throughout experiments. DNT was a notable exception, where an immediate removal was observed in the first minute of reaction under all drive current conditions. This was also true of UV control experiments where immediate removal occurred in the first minute followed by no additional removal over 75 minutes. Similar removal was observed in the 20 mA experiment with H₂O₂ where immediate removal in the first minute is subsequently followed by little removal at a slow rate over the remainder of the experiment. Pre and post HPLC control samples ruled out any anomalies in analysis. There appears to be a possible loss to another mechanism such as adsorption to a component of the reactor assembly; however, adsorption would not be expected to occur so rapidly and adsorption sites would be expected to fill over time. Experimental design and constraints did not allow for identification of the mechanism.

MAL exhibited similar behavior in a UV control sample where there was immediate removal followed by no removal over the remainder of a 75 minute experiment; however, MAL exhibits a greater overall degradation rate during the AOP, and this potential loss mechanism is masked in the other experiments. BPA exhibited 26% degradation in a UV control at 200 mA. MTBE and TBA did not exhibit direct degradation in UV controls. TBA is a known hydroxyl radical chain terminator and, as initially hypothesized, it was in line with DNT with the lowest overall degradation rate and extent. TBA is also a byproduct of MTBE degradation and prior literature suggests that the oxidation pathway of MTBE may result in 10-15% TBA formation (Stefan, et al. 2000). It is plausible that formation and subsequent degradation of TBA during MTBE experiments likely resulted in chain termination to a lesser extent there as well. Lower

comparative degradation rates and extents for DNT, TBA, and MTBE agree well with prior published work suggesting that smaller molecules ($MW < 200$), in general, having electron withdrawing substituents have lower hydroxyl radical reactivity (Lee and von Gunten 2012). Additional supplementary plots of drive current experiments are provided in Appendix A as Figures A8 - A30.

2.3.3. The Effect of Molar Peroxide Ratio on the Removal of Organic Compounds

Results in this section present the comparative degradation of dyes and achromatic chemicals at varying molar ratios of H_2O_2 to test compound. No direct degradation from peroxide alone was observed in control experiments for any dyes. Representative figures are shown to demonstrate ratios where reactions were peroxide limited or where H_2O_2 scavenging of hydroxyl radicals likely occurred. With one exception, optimal molar peroxide ratios for the dye compounds did not deviate from the starting ratio of 500 moles H_2O_2 /mole dye. There was very little discernible difference until extreme points were reached, such as those exhibited in the Figure 9 plot showing BB molar peroxide ratios at 100:1, 500:1, and 1000:1, where the apparent first order degradation rate constants were 0.187, 0.476, and 0.387 min^{-1} for each molar peroxide ratio, respectively. Final normalized BB concentrations for 100:1, 500:1, and 1000:1 molar peroxide ratio experiments were 0.236, 0.068, and 0.102, respectively. The figure shows peroxide-limited reaction at 100:1 with significantly slower degradation rate and less removal, optimality at 500:1 with the fastest rate and largest removal, and slowed degradation rate and less removal at 1000:1, perhaps due to radical scavenging.

Among the most interesting results in peroxide ratio experiments with the dyes are those of EB. As hypothesized following drive current experiments, EB reaction kinetics benefited

significantly from increased molar peroxide ratios. Optimality was achieved at ratios in the range of 2500-3000 moles H_2O_2 /mole EB. Extensive peroxide ratio tests were conducted with EB at all drive current levels with the exception of 20 mA. An especially notable point appears in Figure 10, which shows EB molar peroxide ratio tests at 80 mA. When moving incrementally from molar ratios of 500:1 to 3000:1, the inflection point noted during drive current experiments gradually starts to appear and transition. Curves for higher drive currents with higher molar peroxide ratios begin to move closer to a first order profile. Additionally, the 99% EB removal at the end of the 3000:1 molar peroxide ratio at 80 mA surpasses the 97% removal achieved at 500:1 at 160 mA and 200 mA. The apparent first order degradation rate achieved at 3000:1 molar peroxide ratio at 80 mA (0.182 min^{-1}) exceeds the degradation rate at 500:1 at 160 mA (0.144 min^{-1}) and approaches the rate of 500:1 at 200 mA (0.255 min^{-1}) in Figure 7. A review of the literature found no prior publications that have discovered the pronounced effect of drive current and molar peroxide ratio on EB removal kinetics.

As with the dye compounds, no achromatic chemicals showed direct degradation from H_2O_2 alone in peroxide control experiments. In general, the achromatic chemical compounds exhibited different behavior than the dyes with regard to optimal molar peroxide ratios. TBA, MTBE, and MAL exhibited optimal kinetics around a 100:1 peroxide ratio. MAL trials were conducted as low as 25:1 and 50:1 ratios, and degradation rate and extent were comparable to 100:1. Comparatively, DNT and BPA were optimized in the 500:1 range, which might be attributable to the molar extinction data exhibited in Table A3 and Figure A6 (Appendix A illustrations). Among the chemical compounds, DNT and BPA have the highest molar absorptivity at 265 nm and also require a higher molar peroxide ratio to optimize hydroxyl radical production. In contrast, TBA and MTBE have the lowest molar absorptivity at 265 nm

with less competition for photon absorbance and were optimized at much lower peroxide concentrations at a 100:1 ratio.

Another notable result from molar peroxide ratio experiments was observed with TBA. It was initially hypothesized that TBA would benefit from greater peroxide ratios due to the expected and documented chain termination mechanism and that higher concentrations of H_2O_2 would be required to offset the loss to that process. However, results in Figure 11 show that likely hydroxyl radical scavenging by excess peroxide exceeds any detriment of chain termination. Final normalized concentrations of TBA were 0.194, 0.308, and 0.439 at 100:1, 500:1, and 1000:1 molar peroxide ratios, respectively. Apparent first order degradation rates achieved under each condition were 0.190, 0.111, and 0.067 min^{-1} , respectively, for the 100:1, 500:1, and 1000:1 molar peroxide ratio experiments. The concentration of H_2O_2 used in the 100:1 molar peroxide ratio experiments is equivalent to 34 mg/L. The findings in the current work are in agreement with a prior study on modeling and treatment system design for TBA removal that utilized 10 – 20 mg/L H_2O_2 concentrations, and the authors note that at that level, the negative effects of hydroxyl radical scavenging by excess H_2O_2 is not observed (Li et al, 2008). It is possible that a point of optimality below the 100:1 molar peroxide ratio used in this study may be achievable and would require further investigation. Additional supplementary plots of peroxide ratio experiments are provided in Appendix A as Figures A31-A45.

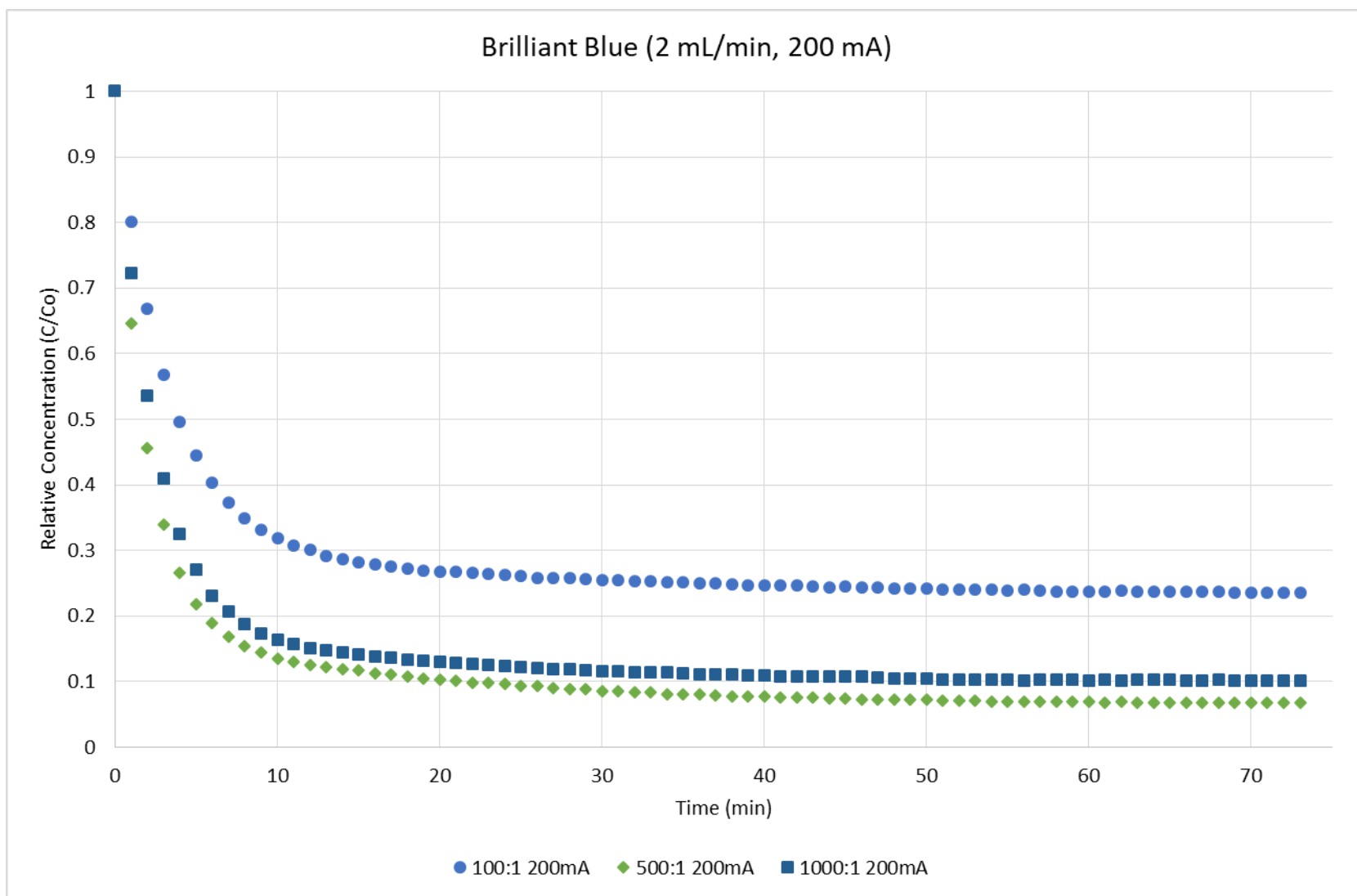


Figure 9. The effect of molar peroxide ratio on Brilliant Blue FCF removal at 200 mA.

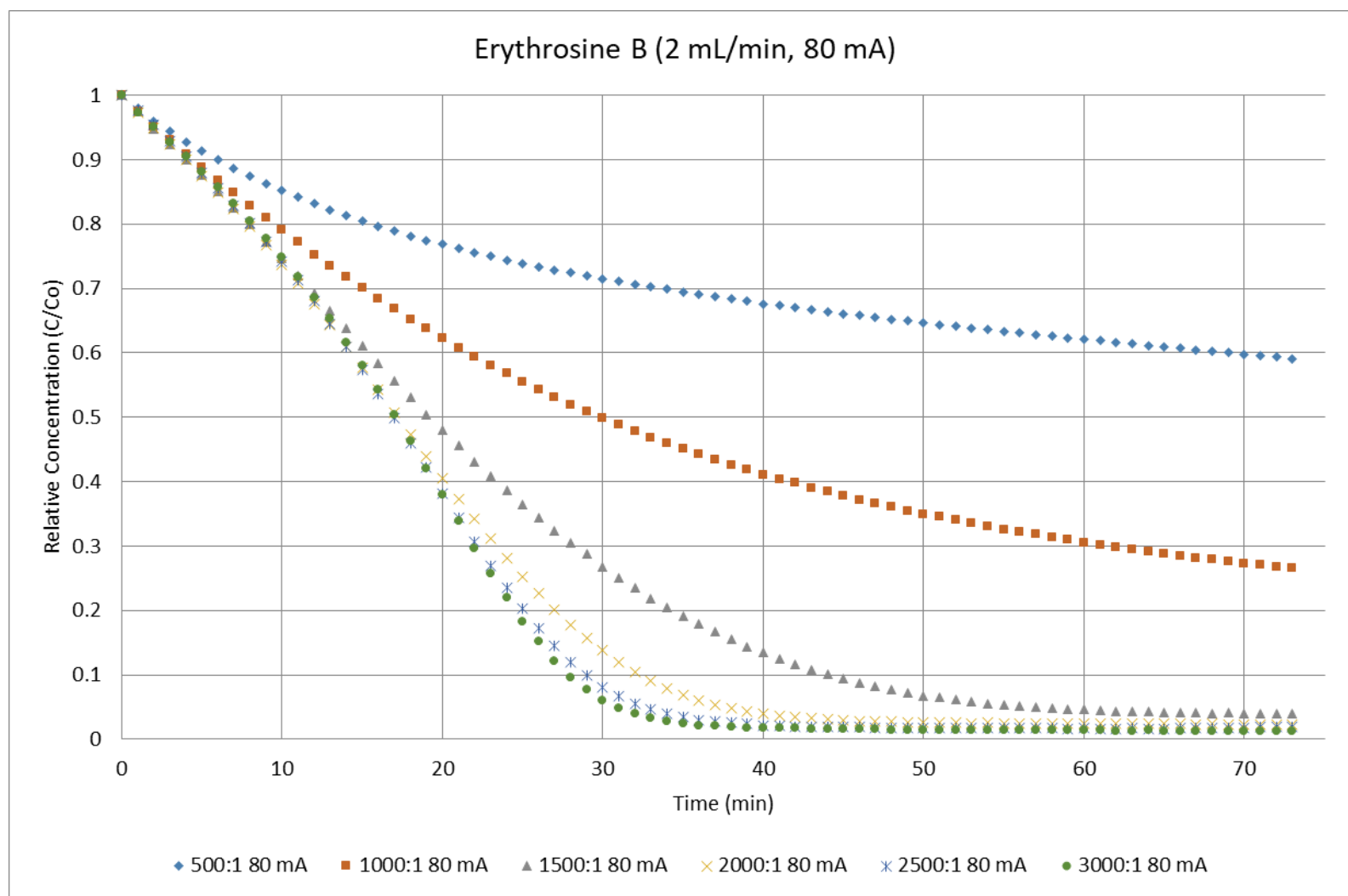


Figure 10. The effect of molar peroxide ratio on Erythrosine B removal at 80 mA.

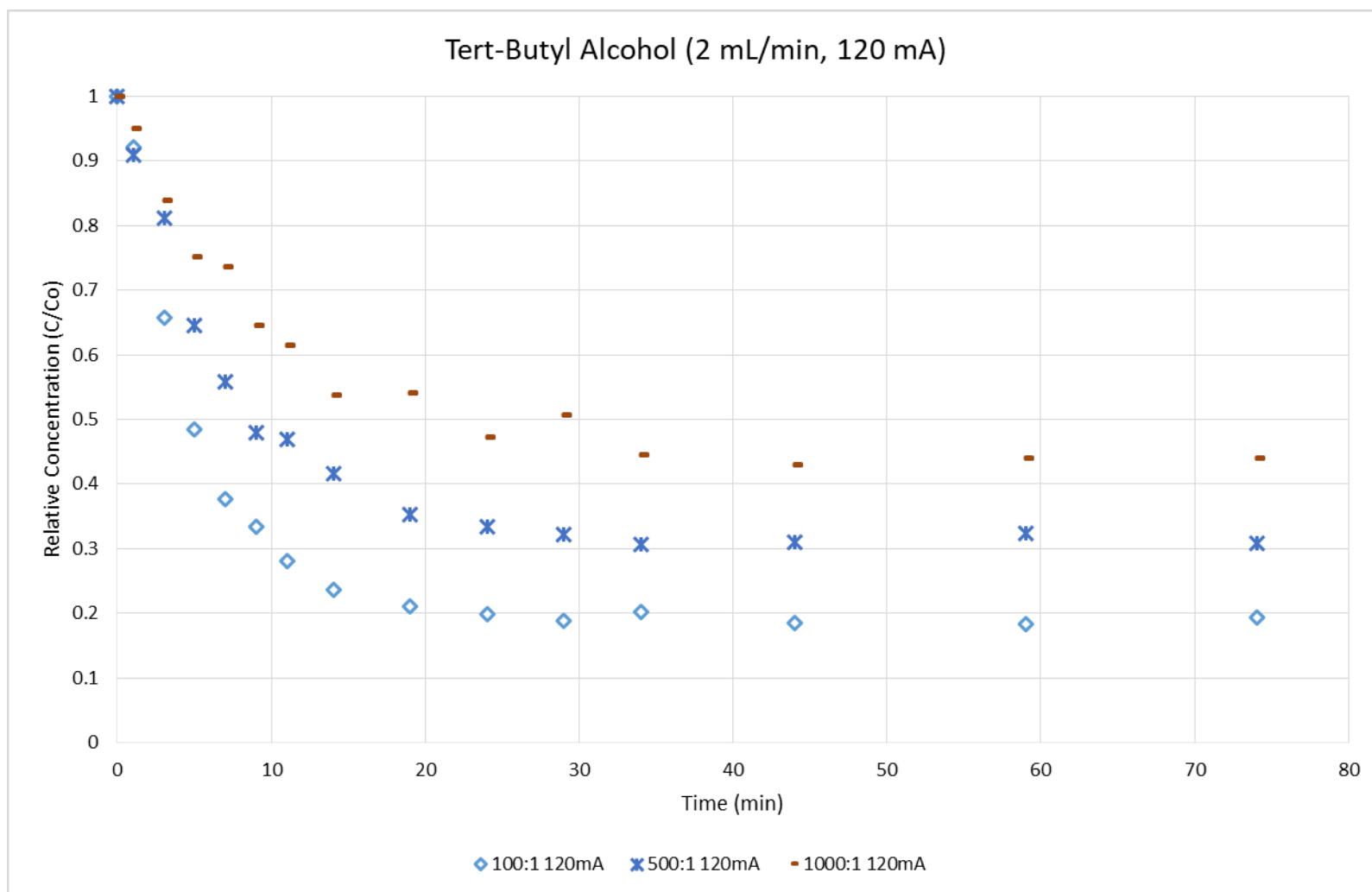


Figure 11. The effect of molar peroxide ratio on TBA removal at 120 mA.

2.3.4. Summary of the Effect of Molar Absorptivity on Chemical Removal

As alluded to above, molar light absorbance near the 265 nm LED peak output wavelength range creates the potential for an organic compound to compete for absorbance with H_2O_2 for the photons available to generate hydroxyl radicals. This is of particular interest in the LED domain as the optical output power and resultant photon production is significantly less than mercury lamps, as discussed previously and as shown in Tables 2 and 3. UV light can excite the electrons present in organic chemical compounds. This is a fundamental reason why molar absorptivity is expected to be important in water treatment applications involving UV light. It is therefore necessary to address the role of molar absorptivity in UV LED-based AOPs.

Previous UV LED-based AOP studies have degraded chemicals with relatively high molar extinction coefficients, but to date, there has been no previous effort to account for UV absorbance in the interpretation or modeling of the removal profiles (Duckworth, et al. 2015; Stewart 2016; Gallucci 2016; Mudimbi 2015; Scott, et al. 2015). However, in the current work, accounting for molar absorptivity has helped explain the presence of inflection points observed during EB degradation (Figure 7) and why drive current has a notable effect on the apparent first order degradation rate constant and the degradation extent for TT (Figure 8). There is also previously published experimental data that can be better understood by accounting for the molar light absorbance of EB (Apostol, et al. 2015; Bairagi and Ameta 2016).

Figure A7 (Appendix A) shows a full range UV-Visible scan of all dyes (0.01 mM) compared to H_2O_2 at 100:1 (1 mM) and 500:1 (5 mM) ratios. Figure A6 (Appendix A) isolates absorbance values for each dye at the 265 nm wavelength. The molar extinction coefficient values for all dyes and achromatic chemicals are presented in Table A3 (Appendix A) along with absorbance ratio (background corrected to DI water) as compared to a 500:1 molar peroxide ratio

(e.g. molar absorptivity of test compound at 265 nm divided by molar absorptivity of 5 mM H_2O_2 at 265 nm). The overall range of absorbance ratios was 0.03 to 5.45. As expected, the dyes had a higher absorbance ratio than the achromatic chemicals. The only chemical with notable absorbance comparable to the lowest absorbing dyes was DNT, followed by BPA. These observations demonstrate the range of molar light absorbance that is associated with the organic chemicals in this study.

There is also evidence to suggest that molar absorptivity at 265 nm is an important factor in explaining deviations from CSTR model fit for individual chemicals. When plotting model versus observed data for dyes, visual fit to the model was good for all compounds at 20 and 40mA; however, moving to 80 mA and beyond began to produce widening gaps in model fit for some dyes. BB and FG experimental data continued to track the model relatively well, whereas TT experimental data would notably proceed initially at a rate slower than the model predictions and eventually cross and overshoot the model, finishing with greater than predicted degradation extent. It is hypothesized that the deviations from model fit are again related to the molar extinction of the dyes and the effect that the competition for absorbance has on the underlying kinetics. The deviation at 20 and 40 mA is less significant because the reaction is more photon limited under those conditions and impact of competing absorbance is less significant than the overall lack of photon energy to catalyze the reaction. Table A4 (Appendix A) shows the comparative R^2 values between model and experimental data fit to Equation 1 for all dyes and drive current levels at 500:1 peroxide ratios. Deviation from ideal model fit (where $R^2 = 1$) is positively correlated with higher molar absorptivity at 265 nm (e.g. model fit R^2 is negatively correlated with molar absorptivity at 265 nm). Figure 12 shows a comparison of model fit R^2 versus molar absorptivity for all dyes at each drive current level. In the figure, molar

absorptivity values at 0.1, 0.101, 0.158, 0.169, 0.274, and 0.371 represent BB, FG, AR, SY, TT, and EB, respectively. From a qualitative viewpoint, we observe that for 80-200 mA data series, there is a relationship where higher R^2 values are associated with lower molar absorptivity values. In general, Figure 12 reflects a variety of complex and competing mechanisms that make data interpretation challenging, underscoring the value and need for predictive tools.

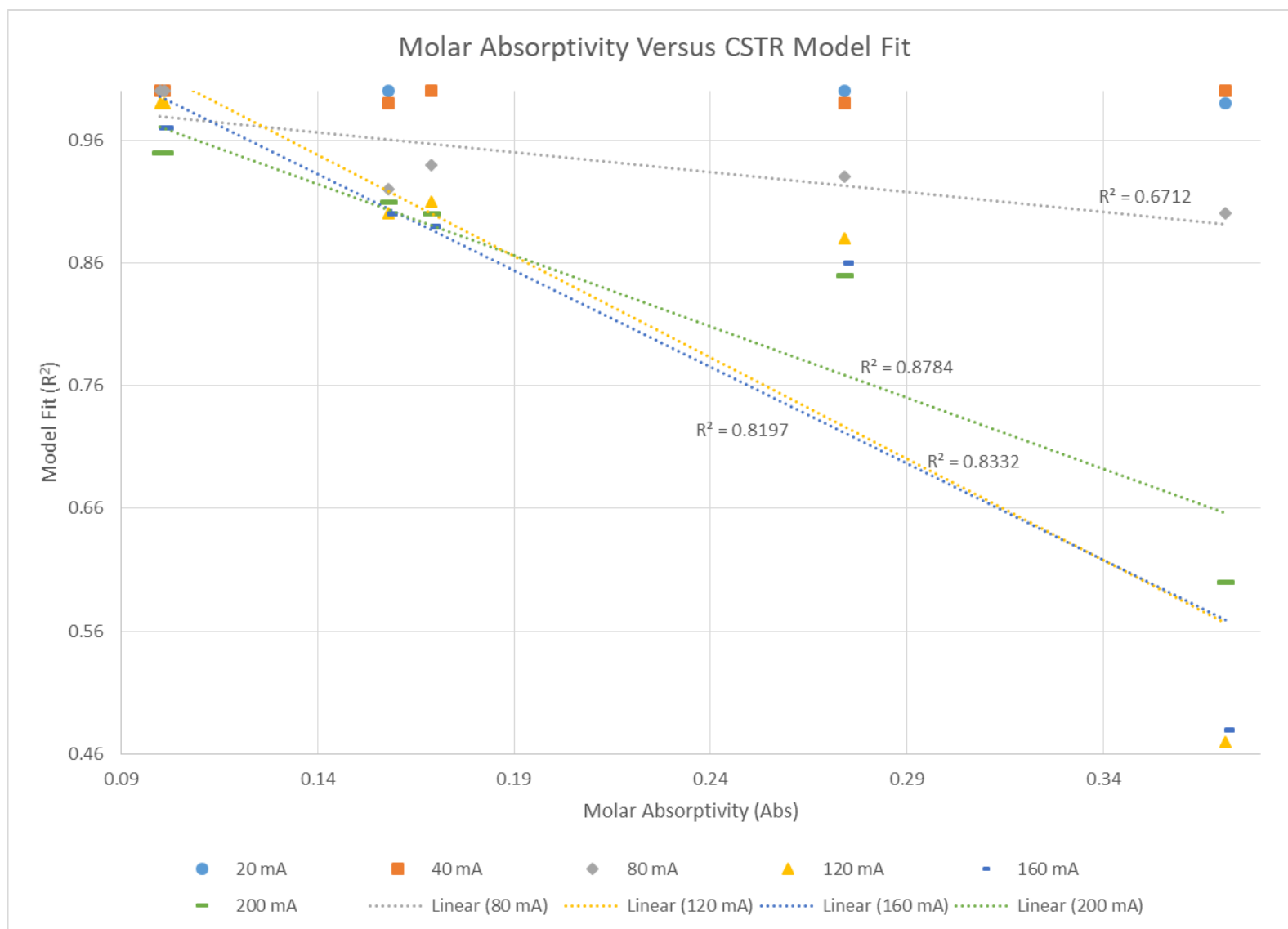


Figure 12. Relationship between CSTR model fit and molar absorptivity.

2.4. Conclusions

This research analyzed the impact of input drive current and molar peroxide ratios on the kinetics of UV LED-driven AOP at bench scale. There was a linear relationship between the input drive current, optical output power, and the apparent first order degradation rate constant for the removal of each test compound. When the drive current was 20 mA and the molar peroxide ratio was 500 mole H_2O_2 /mole test compound, the apparent first order degradation rate constants were between $0.011 - 0.033 \text{ min}^{-1}$ for the dyes and between $0.013 - 0.114 \text{ min}^{-1}$ for achromatic chemicals. When the drive current was 200 mA and the molar peroxide ratio was 500 mole H_2O_2 /mole test compound, the apparent first order degradation rate constants were between $0.255 - 0.785 \text{ min}^{-1}$ for the dyes and between $0.149 - 1.0748 \text{ min}^{-1}$ for achromatic chemicals. There was also a linear relationship between the drive current and the degradation extent. Data suggested both peroxide-limited and radical-scavenged kinetics. The optimum molar peroxide ratio for most chemicals exhibiting moderate molar absorptivity at the LED output wavelength was at or near 500 moles H_2O_2 /mole chemical. This observation varied at extremes where achromatic chemicals exhibiting lower molar absorptivity were optimized at a molar peroxide ratio of 100 moles H_2O_2 /mole chemical and EB, with the strongest molar absorptivity, was optimized at a molar peroxide ratio of 2500-3000 moles H_2O_2 /mole EB. Accounting for molar absorptivity and its photodegradation rate successfully helped to explain the molar peroxide requirement for EB, the presence of inflection points in EB removal profiles, as well as the relationship between drive current and the apparent first order degradation rate constants for TT removal. The regression coefficients associated with the CSTR model fitting of data also did not correlate well with molar absorptivity. These results are particularly notable because full scale

applications would involve the treatment of a variety of chemicals, each with unique light absorbing features.

III. Quantitative Structure Property Relationship Models for Predicting Degradation Kinetics for a Ultraviolet Light Emitting Diode/Peroxide Advanced Oxidation Process

Keywords

QSAR, QSPR, Ultraviolet (UV), light emitting diode (LED), advanced oxidation process (AOP), hydrogen peroxide (H_2O_2)

Abstract

This study utilized the observed degradation kinetics of 6 dye and 5 achromatic chemical compounds in a UV-LED/ H_2O_2 advanced oxidation process to evaluate QSPRs for predicting degradation rates. Prior to this study, QSPRs had not been evaluated for UV LED-based reactors, with published QSPRs reported for traditional mercury lamp AOP data, which has different spectral characteristics and reactor design. Overall fit to descriptors used in all of the existing QSPR models compared was relatively poor for the complete data set of compounds studied with the UV LED AOP reactor. The resultant R^2 values were 0.024, 0.116, 0.157, 0.312, 0.481, and 0.864; however, several of the descriptors producing the model with the R^2 of 0.864 failed to pass tests of statistical significance. When breaking the larger data set into smaller subsets of dyes and achromatic chemicals, improvement was seen with R^2 values between 0.033 – 0.996, but most models and individual parameters failed tests of statistical significance. Statistical robustness was also compromised due to smaller data set sizes compared to numbers of predictors included in models. A new model was constructed for predicting the dye and achromatic chemical degradation rates utilizing zero point energy (ZPE) combined with molar absorptivity of the chemical compound at the output wavelength of the LEDs (265 nm). Overall, ZPE and molar absorptivity at 265 nm produces a QSPR model with $R^2 = 0.951$. The model and each of the model parameters were statistically significant at a 95% confidence interval. This represents the first known use of ZPE and molar absorptivity in the construction of a QSPR model in the UV/ H_2O_2 AOP domain.

3.1. Introduction

Advanced oxidation processes (AOP) using UV/H₂O₂ reactions have proven to be a powerful method of generating hydroxyl radicals, which subsequently react rapidly and non-selectively with organic compounds at near diffusion controlled rates. AOPs utilizing UV/H₂O₂ have proven to be highly effective at oxidizing many chemical compounds; however, the energy requirements for UV/H₂O₂ AOP treatment using traditional mercury lamps has proven to be substantially higher than other AOPs in many cases (Katsoyiannis, Canonica and von Gunten 2011). UV LEDs may be a suitable replacement for high energy consuming mercury vapor lamps in AOPs utilizing H₂O₂. UV LED based water treatment is now possible; however, little data has been available on the use of UV LED/H₂O₂ for the destruction of soluble organic compounds that may threaten our water supply. Recent research at the Air Force Institute of Technology has expanded this work to a greater number of soluble organic compounds to improve the fundamental understanding of the AOP as it relates to LEDs.

There is also a general need to assess tools that can be used to predict chemical degradation in UV LED-based processes. Quantitative structure-property relationships (QSPR) can provide such a tool. The advantage of the QSPR approach, once an acceptable model is developed, is the ability to predict removal relative to baseline conditions strictly on the basis of the compound structure without further laboratory testing. Several previous studies have developed QSPRs relating chemical structure to degradability (Sudhakaran, et al. 2012; Chen, et al. 2007; Kusic, et al. 2009; Lee and von Gunten 2012; Meylan and Howard 2003; Minakata, et al. 2009; Ohura, Amagai and Makino 2008; Sudhakaran and Amy 2013; Wang, et al. 2009; Tang 2004). QSPRs have not been evaluated for UV LED-based reactors.

Many existing QSPRs have been built upon degradation rate constants mined from the literature. This approach is straightforward as there is no time or cost associated with conducting experiments; however, there is no control over the quality of the underlying experiments from which the kinetic data was derived. Furthermore, experimental conditions (batch vs CSTR, varying reactant concentrations, varying UV light sources, varying retention times, etc) under which the rate constants were measured are often very disparate. There is risk in using large, low quality data sets, as they may offer a misleading impression with respect to the relative importance of model parameters. The present study sought to investigate the use of a smaller, high quality data set built from degradation experiments of 6 dye and 5 weaker chromophore compounds tested in the same bench-scale UV LED reactor under identical operating conditions. Apparent first order degradation rate constants for the 11 compounds were used to investigate molecular descriptors that are most significant to the UV LED-based AOP by first assessing significance of molecular descriptors used in existing QSPRs developed with traditional mercury lamp AOP data and then using multiple linear regression (MLR) to assess potential new QSPR models.

3.1.1. Overview of QSPR and Molecular Descriptors

Quantitative structure-property relationship (QSPR) models seek to relate structural features of a chemical compound to physicochemical activity (Yee and Wei 2012). Fundamental to the successful development and application of QSPR models is the selection of molecular descriptors (MD) that adequately represent the important parameters affecting the observed property of interest. QSPR methods have been used historically in the design of pharmaceuticals that target specific diseases or medical conditions; however, use of the methodology for

prediction in environmental applications has increased significantly in recent decades (Singh, et al. 2014). MDs are numerous and diverse with various software packages capable of calculating anywhere from 200 to over 3000 unique descriptors for a single chemical compound (Hong, et al. 2012). There is an art and a science to selecting the most important subset of MDs relevant to the goals and mechanisms of each study. Doing so can improve prediction accuracy, facilitate interpretation of a model, and prevent potential over-fitting of data (Singh and Gupta 2014).

In general, MDs are classified into five categories: 1) physicochemical (e.g. octanol-water partition coefficient, Log P, density, melting point, half-life in water/air, persistence time), 2) constitutional (e.g. numbers of atoms and bonds, molecular weight, hydrogen percent, carbon percent, hydrogen bond donors, hydrogen bond acceptors, etc.), 3) geometrical (e.g. maximum Z-length, molecule surface area, etc.), 4) topological (e.g. connectivity and valence connectivity indexes, etc.), and 5) quantum-chemical (polarizability, electric dipole moment, total energy, electron density, etc) (Servien, et al. 2014; Singh, et al. 2013). Numerous software packages are available for the calculation of MDs, with some specializing only in subsets of these categories. Options range from freeware to commercial software packages, and capabilities range from calculating hundreds of descriptors to several thousand descriptors, depending on the software selected.

3.1.2 Use of QSPR and Molecular Descriptors in AOPs and Similar Domains

QSPRs have been utilized to predict degradation rates in numerous environmental applications including atmospheric reactions, direct UV photolysis in aqueous and non-aqueous solutions, and reactions in AOPs used for water treatment. Methodology and descriptor selection varies broadly. One study focused on developing a QSPR to model the removal of organic micropollutants (primarily pharmaceuticals, personal care products, and pesticides) in four

different river water sources (Colorado River, Passaic River, Ohio River, and Suwannee synthetic water) via ozonation AOP. QSPR models were built using bench scale data from experiments with the source waters. An initial set of 40 molecular descriptors potentially influencing AOP were selected using MLR and ranged from simple atom counts to complex quantum-chemical properties. An artificial neural network (ANN) was created with a compilation of molecular descriptors of pollutants from the four water sources. The ANN identified the following relevant molecular descriptors for inclusion in QSPR models: LUMO–HOMO energy difference, electron affinity, number of halogen atoms, number of ring atoms, weakly polar component of the solvent accessible surface area, and oxygen to carbon ratio (Sudhakaran, et al. 2012). The same research group used a different approach in developing additional QSPRs using ozone and hydroxyl radical degradation rate constants as dependent variables. Molecular descriptors selected were double bond equivalence, ionization potential, electron affinity, and weakly-polar component of solvent accessible surface area. As opposed to ANN used to construct the prior QSPR models, MLR was used to build the additional models (Sudhakaran and Amy 2013). In both cases, models were validated with internal and external data sets and showed high goodness of fit.

In another study related to hydroxyl radical reactions in water, a QSPR was built using MLR on quantum chemical descriptors to predict degradation rate constants. The molecular descriptors found to be significant were the HOMO energy, average net H atom atomic charges, molecular surface area (MSA), and dipole moment. Degradation rate constants were positively correlated with increasing HOMO energy and molecular surface area and negatively correlated with increasing H atom atomic charge and dipole moment. Particular emphasis was placed on following QSPR development guidelines set forth by the Organization for Economic

Cooperation and Development (OECD; <http://www.oecd.org/env/ehs/oecdquantitativestructure-activityrelationshipsprojectqsars.htm>), including validation, domain of applicability, and mechanistic interpretation. (Wang, et al. 2009)

A similar methodology was used to develop a QSPR to predict hydroxyl radical degradation rate constants for 78 aromatic compounds in water. A genetic algorithm (heuristic method) was used to select relevant descriptors and multiple linear regression was used to build the QSPR models. The DRAGON software package was used to calculate molecular descriptors. A final model consisting of 4 molecular descriptors (HOMO, molecular path count of order 8, Geary auto-correlation-2/lag weighted by polarizabilities, leverage weighted autocorrelation of lag 7/weighted by atomic polarizabilities) was found to be ideal without overfitting and HOMO energy was the main contributor to the resultant degradation rate. (Kusic, et al. 2009)

Jin et al. developed a QSPR model for the prediction of hydroxyl radical degradation rates for emerging micro pollutants. The model building data set included 118 emerging micro pollutants, including some from the literature and some experimentally collected. DRAGON was used to calculate 951 descriptors. MLR was used to build and refine a final model which includes the mean atomic Sanderson electronegativity, the number of double bonds, the number of primary alkyl halide functional groups, number of hydrogen bond acceptors, Moran autocorrelation of lag 2 weighted by mass, Balaban V index, and signal 27 weighted by polarizability. (Jin, et al. 2015)

Huang et al. built a QSPR model based on ten sulfonamide compounds (SAs) degraded in TiO₂ photocatalytic systems. Partial least squares regression was used to build optimal QSAR models. Degradation of SAs was found to be strongly related to the highest occupied molecular

orbital, the maximum values of nucleophilic attack ($f(+)x$), and the minimum values of the most negative partial charge on a main-chain atom ($q(C)_{\min}$). (Huang, et al. 2015)

Borhani et al. developed a QSPR for predicting the hydroxyl radical rate constant for a dataset of 457 water contaminants spanning 27 chemical classes. A constricted binary particle swarm optimization and MLR (BPSO-MLR) technique was used to fit an optimal model with eight molecular descriptors including sphericity, R autocorrelation of lag 1/unweighted, Broto-Moreau autocorrelation of a topological - lag 2/weighted by atomic van der Waals volumes, highest eigenvalue of Burden matrix/weighted by atomic Sanderson electronegativities, spectral moment 05 from edge adjacent matrix weighted by edge degrees, number of terminal primary C, number of aromatic hydroxyls, and number of sulfur atoms. (Borhani, et al. 2016)

Tang investigated the use of LUMO as a sole descriptor in a predictive model for degradation in a UV/H₂O₂ AOP. The descriptor produced models with strong R^2 values ranging from 0.9094 – 0.9876 for separate chemical classes of alkane, benzene, halide, and phenol compounds. Separate models were built for each chemical class with only $n=3$ compounds employed in each model. Each class resulted in vastly different coefficients and a model with all classes combined would have likely resulted in a poor model fit. LUMO showed less fit to individual models built with alkenes, aromatic hydrocarbons, carboxylic acids, and sulfonic acids with lower R^2 values ranging from 0.06 – 0.77. (Tang 2004)

Additional QSPR models have been developed for predicting degradation rates for the direct photodegradation of compounds in either aqueous or non-aqueous solutions. One such model was built to predict degradation of polybrominated diphenyl ethers in water/methanol or methanol solutions. Partial least squares regression was used to build the model and the following descriptors were found to be significant: LUMO–HOMO energy gap, most positive

Mulliken atomic charges on a hydrogen atom, $\log k$, molecular weight, average molecular polarizability, and average Mulliken atomic charges on bromine atoms (Chen, et al. 2007). Other QSPRs have been built to predict photodegradation of compounds on aerosol surfaces (Ohura, et al. 2008) and oxidation of compounds in the atmosphere (Meylan and Howard 2003) using similar model building techniques.

A different model building technique employed by Minakata et al. involved the development of a group contribution method (GCM) to predict hydroxyl radical degradation rate constants by predicting rate constants for individual reaction mechanisms: 1) hydrogen abstraction, 2) hydroxyl radical addition to alkenes, 3) hydroxyl radical addition to aromatic compounds, and 4) hydroxyl radical interaction with compounds containing sulfur, nitrogen, or phosphorus. The GCM is predicated on the idea that the experimental degradation rate constant for a given organic compound is the combined rate of all elementary hydroxyl radical reactions. A total of 66 group rate constants and 80 group contribution factors are included in the GCM. Degradation rate constants were mined from the literature with 310 compounds used for calibration and 124 compounds used for prediction. Genetic algorithms were used to determine the group rate constants and contribution factors. The best results for calibrations and predictions were within 0.5-2 times experimental values. (Minakata, et al. 2009) Though the GCM is a robust methodology, it also requires a large data set for proper calibration and prediction (Minakata, et al. 2014).

3.2. Materials and Methods

3.2.1 Data Set and Generation of Molecular Descriptors

A set of experimental data (including observed degradation rate constants, degradation extent, and molar absorptivity values) was collected as previously described for 6 dye and 5 achromatic chemical compounds studied in a UV LED/H₂O₂ AOP reactor described in Chapter 2. The scope of the data set and associated degradation rate constants are constrained to the specific reactor and associated reactor parameters utilized in the experiments (e.g. flow, volume, chemical concentrations, UV intensity, etc.). Experimental procedures such as competition kinetics were not utilized to link the apparent first order degradation rate constants to second order hydroxyl radical rate constants commonly reported in the literature.

A freeware package from the US Food and Drug Administration called MOLD² was used to generate 777 molecular descriptors for each test compound (US Food and Drug Administration 2015). MOLD² requires loading of a structure data file (SDF) for each compound and performs computations based on parameters contained in the SDF. The requisite SDF for each compound was available and was downloaded from the National Institutes of Health PubChem data repository (National Institutes of Health 2016). Additional chemical properties were also selected for each dye and chemical from information published directly on the PubChem website (National Institutes of Health 2016). As MOLD² does not have quantum chemistry capabilities, two additional software packages were used to produce those descriptors, MOPAC (Stuart Computational Chemistry 2016) and Spartan '16 (Wavefunction 2017). In order to use MOPAC, the SDFs from PubChem had to be converted to MOPAC format (.mop). This was completed in open source software called Babel (O'Boyle, et al. 2011) that converts descriptor input files across multiple computational platforms. Conversions were completed for

all compounds and quantum values were successfully computed in MOPAC. Spartan software also requires input files specifically formatted for the platform; however, it can directly import SDF files and convert them internally. Several of the chemical compound structures were available in a Spartan database, whereas dye molecules were imported and manually verified for structural accuracy following conversion from 2D to 3D format. A full listing of MOLD² and PubChem descriptors is provided in Appendix B.

3.2.2. QSPR Model Development

The JMP statistical software package was used to test multivariate QSPR model candidates through linear regression by regressing degradation rate constants on one or more molecular descriptors. Regression techniques are among the most popular methods in the literature and a basic model takes the form of Equation 5:

$$y_i = \beta_0 + \beta_1 x_{i1} + \beta_2 x_{i2} + \cdots + \beta_n x_{in} + \varepsilon_i \quad (5)$$

Where

y_i : property being predicted (degradation rate constant in this case)

β_0 : constant

$\beta_1, \beta_2, \cdots, \beta_n$: regression coefficients

$x_{i1}, x_{i2}, \cdots, x_{in}$: predictor variables of compound i (molecular descriptors in this case)

Two approaches were taken to QSPR model development. In the first approach, relevant models and their associated descriptors were mined from the literature. QSPR models from the literature predicting hydroxyl radical rate constants cannot be compared directly due to the limitations noted in Section 3.2.1; however, the molecular descriptors utilized in building those models are certainly relevant for comparison and tests of statistical significance. Models were

built using the same descriptors or comparable descriptors employed in models discussed (summarized in Table 4) and standard least squares regression was used to fit the best possible model with those descriptors. In the second approach, MLR was used to build new models from the descriptors calculated, as described in Section 3.2.1. A stepwise procedure was used to down-select the descriptors by which variables are added to the model one at a time until the descriptor with the best fit (R^2) is found. The procedure then moves forward to find the next descriptor that continues to improve the R^2 when added to the model. The p-value threshold stopping rule was used with default probability to enter and exit of 0.25 and 0.1, respectively. Because the overall data set is small (6 dyes and 5 achromatic chemicals), caution was taken not to include more than 1-2 descriptors in final models in order to avoid overfitting. Assessment of model fit was completed by evaluating coefficient of determination (R^2), adjusted R^2 (R^2_{adj}), root mean square error (RMSE), Fisher criterion (F), standard error of the estimate (SE), and p-value tests for significance of predictors. Evaluation of R^2_{adj} is of particular interest as it accounts for the inclusion of additional predictors and compares the improvement that inclusion of an individual predictor has on model fit to the improvement that would be expected by chance.

Table 4. Molecular descriptors utilized in QSPRs built from traditional mercury lamp AOP data.

QSPR Model/Reference	Descriptors Used	Parameters/Notes
1. Wang, et al. 2009 model	<ul style="list-style-type: none"> - E_{HOMO} (HOMO) - Avg net atomic charges on H (Q_{H}) - Molecular surface area (MSA) - Dipole Moment (DM) 	Domain of applicability for original model was phenols, alkanes, and alcohols. Unable to obtain Q_{H} values with MOPAC/Spartan/MOLD ² .
2. Jin, et al 2015 model	<ul style="list-style-type: none"> - Mean atomic Sanderson negativity - # double bonds (DB) - # primary alkyl halides (nCH₂RX) - # hydrogen acceptors (HA) - # Moran autocorrelation lag 2 weighted by mass (MATS2m) - Balaban V index (BV) - Signal 27 weighted by polarizability (Mor27p) 	Applied to a large data set of micro pollutants. Unable to obtain Mor27p values with MOPAC/Spartan/MOLD ² .
3. Tang 2004 model	E_{LUMO} (LUMO)	Applied to alkane, benzene, halide, and phenol classes
4. Kusic, et al. 2009 model	<ul style="list-style-type: none"> - HOMO - Molecular path count of order 8 - Geary autocorrelation of lag 2/weighted by polarizabilities - Leverage weighted autocorrelation lag 7/weighted by polarizabilities 	Found E_{HOMO} to be the main contributor.
5. Sudhakaran and Amy 2012 model	<ul style="list-style-type: none"> - HOMO-LUMO energy gap - Electron affinity (EA) - # halogen atoms - # ring atoms - Weakly polarizable surface (WPSA) - Oxygen to carbon ratio (OtoC) 	Electron affinity and WPSA not available in MOPAC/Spartan/MOLD ² . Negative of the LUMO approximates electron affinity.
6. Sudhakaran and Amy 2013 model	<ul style="list-style-type: none"> - Double bond equivalence (DBE) - Weakly polarizable surface area (WPSA) - Ionization potential (IP) - Electron affinity (EA) 	Electron affinity and WPSA not available in MOPAC/Spartan/MOLD ² . Negative of the LUMO approximates electron affinity. Negative of the HOMO approximates ionization potential.

3.3. Results and Discussion

3.3.1. Assessment of Existing QPSR Models

Three models were built with each set of descriptors from Table 1 using a combined data set of dyes and achromatic chemicals (n=11), a data set of dyes alone (n=6), and a data set of achromatic chemicals alone (n=5). The rationale for this approach is to assess domains of applicability as the dye structures in general are much larger, more complex, and contain different atoms and functional groups than the achromatic chemicals. A summary of parameter estimates and statistics is provided in Table A5 (Appendix A).

3.3.1.1. Wang, *et al.* 2009 Model

As noted in Table 4, the Wang, *et al.* model consisted of 4 molecular descriptors. Three of the descriptors (energy of the highest occupied molecular orbital (HOMO), molecular surface area (MSA), and dipole moment (DM)) were available in the software packages used in this study; however, average net atomic charges on H could not be obtained directly. When evaluating the three available descriptors using MLR and putting in the form of Equation 1, the following model was obtained.

$$K_{pred} = 1.4985277 + 0.120925(HOMO) + 0.0009508 (MSA) - 0.023057 (DM)$$

Overall, the model is a poor fit to the full n=11 data set as evidenced by weak R^2 and R^2_{adj} values of 0.157 and -0.204, respectively. Figure 13 presents a plot of measured versus predicted apparent first order degradation rate constants. The solid line represents ideal fit where $k_{pred}/k_{meas} = 1$. Thinner dashed lines demark regions where k_{pred}/k_{meas} values are less than 0.5 or greater than 2. Similar plots are provided for all remaining model evaluations. Tests of significance fail for the full model and all individual parameters.

When looking at the data set of n=6 dyes alone, the fit of the model begins to shift with R^2 of 0.801; however, the R^2_{adj} value remains low at 0.50, indicating likelihood of chance parameter fit (Figure 14). Lack of statistical significance remains evident in the full model and all parameters. The resultant model is as follows.

$$K_{pred} = -4.029688 - 0.596527(HOMO) - 0.001318(MSA) + 0.0351431(DM)$$

The data set of n=5 achromatic chemicals shows significant improvement in model fit in terms of both R^2 and R^2_{adj} and results in the model below. The overall R^2 fit improves to 0.983, whereas R^2_{adj} is 0.933 (Figure 15). However, tests of statistical significance continue to fail for the full model and all individual parameters.

$$K_{pred} = 22.060342 + 2.2074904(HOMO) - 0.020181(MSA) + 0.5241355(DM)$$

Overall results indicate that these three molecular descriptors together may be useful in predicting the degradation of the achromatic chemical compounds as evidenced by the high adjusted coefficient of determination; however, caution should be taken given the lack of statistical significance in conjunction with the small data set size. The descriptors are also predictive to a lesser extent for the dye compounds. When grouping the dyes and achromatic chemicals into a combined data set, it is evident that there are structural diversities that likely shift the domain of applicability of the QSPR.

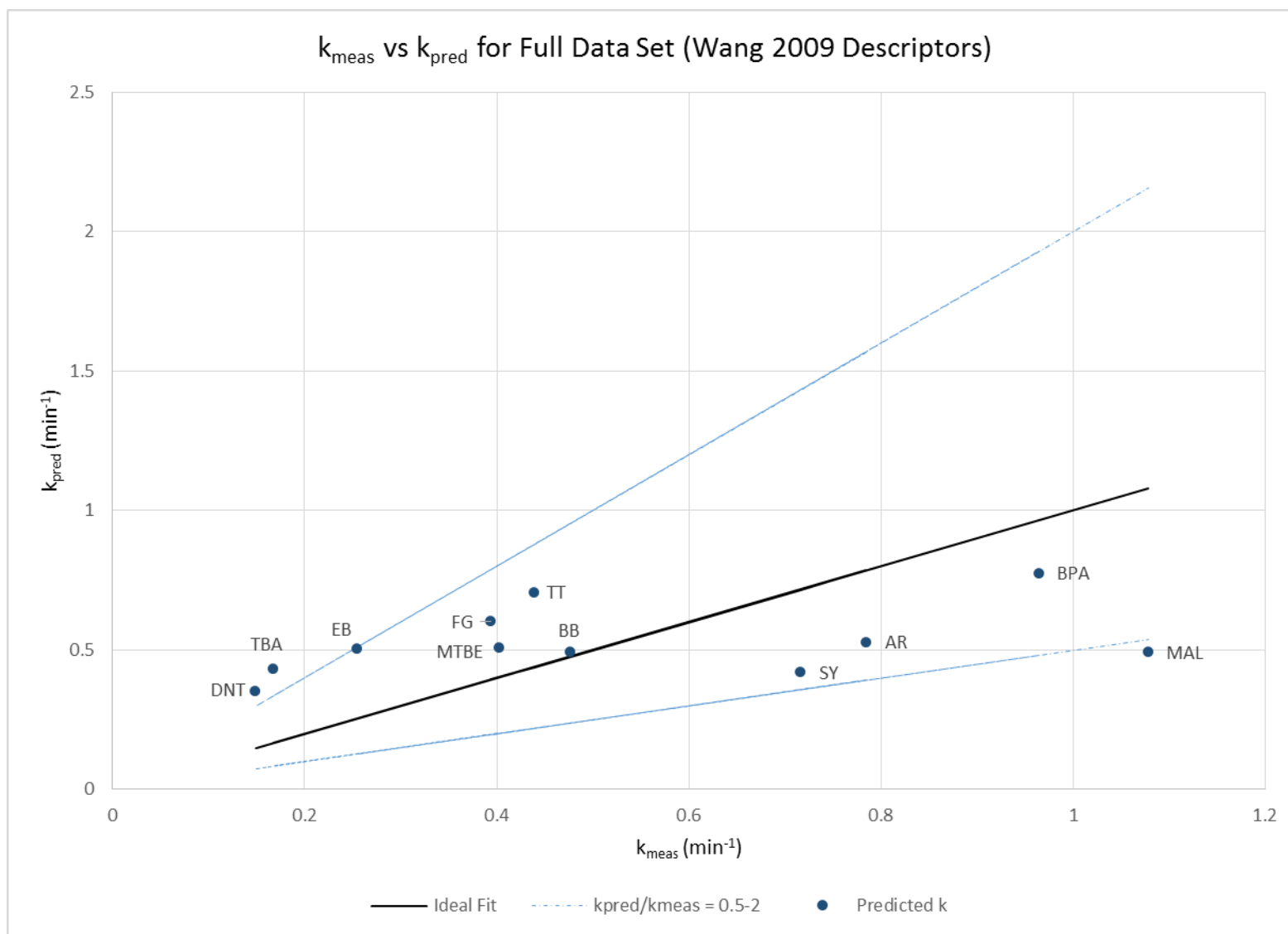


Figure 13. Actual versus predicted degradation rate constants utilizing Wang et al. descriptors with the full data set.

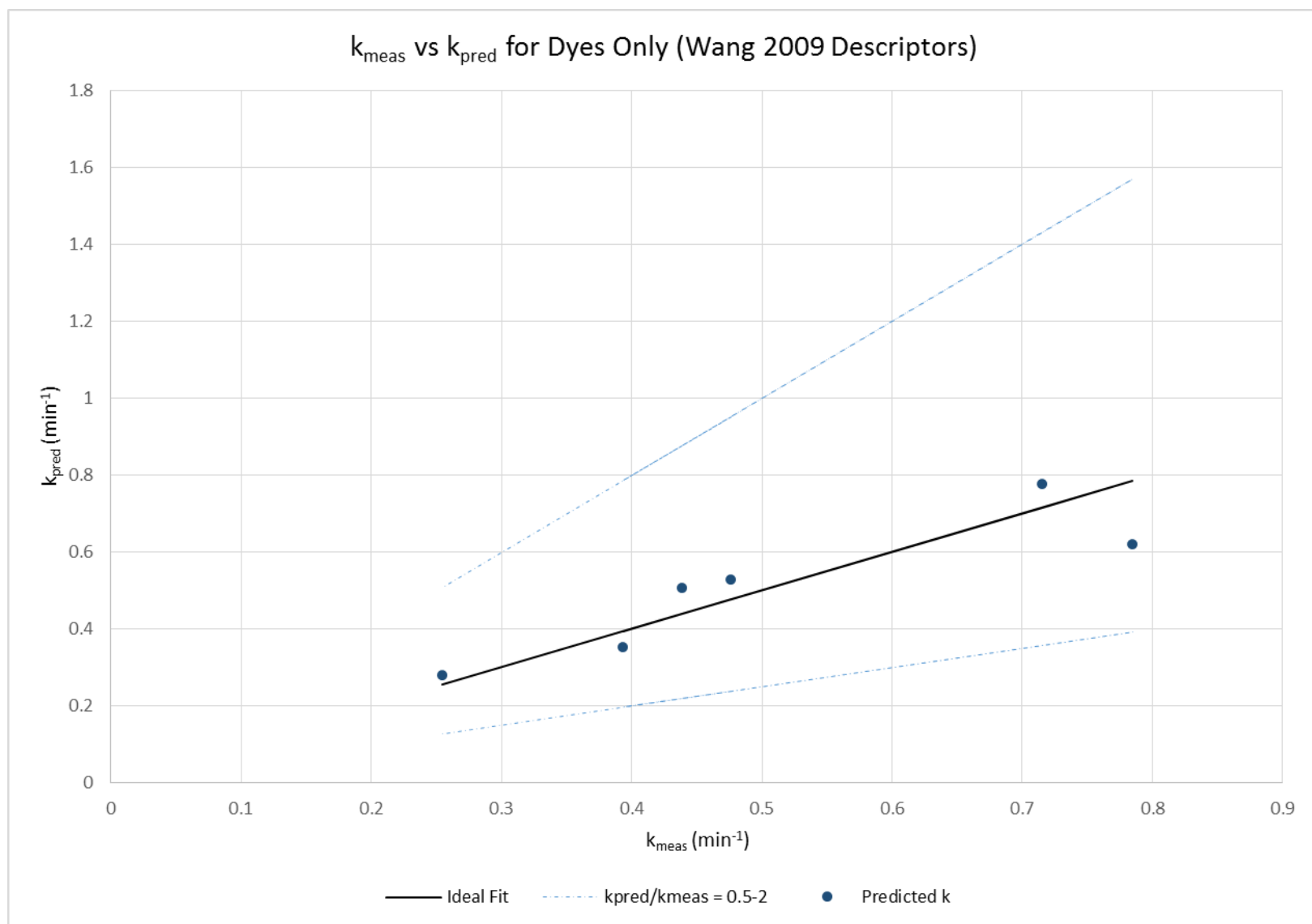


Figure 14. Actual versus predicted degradation rate constants utilizing Wang et al. descriptors with the dye data set.

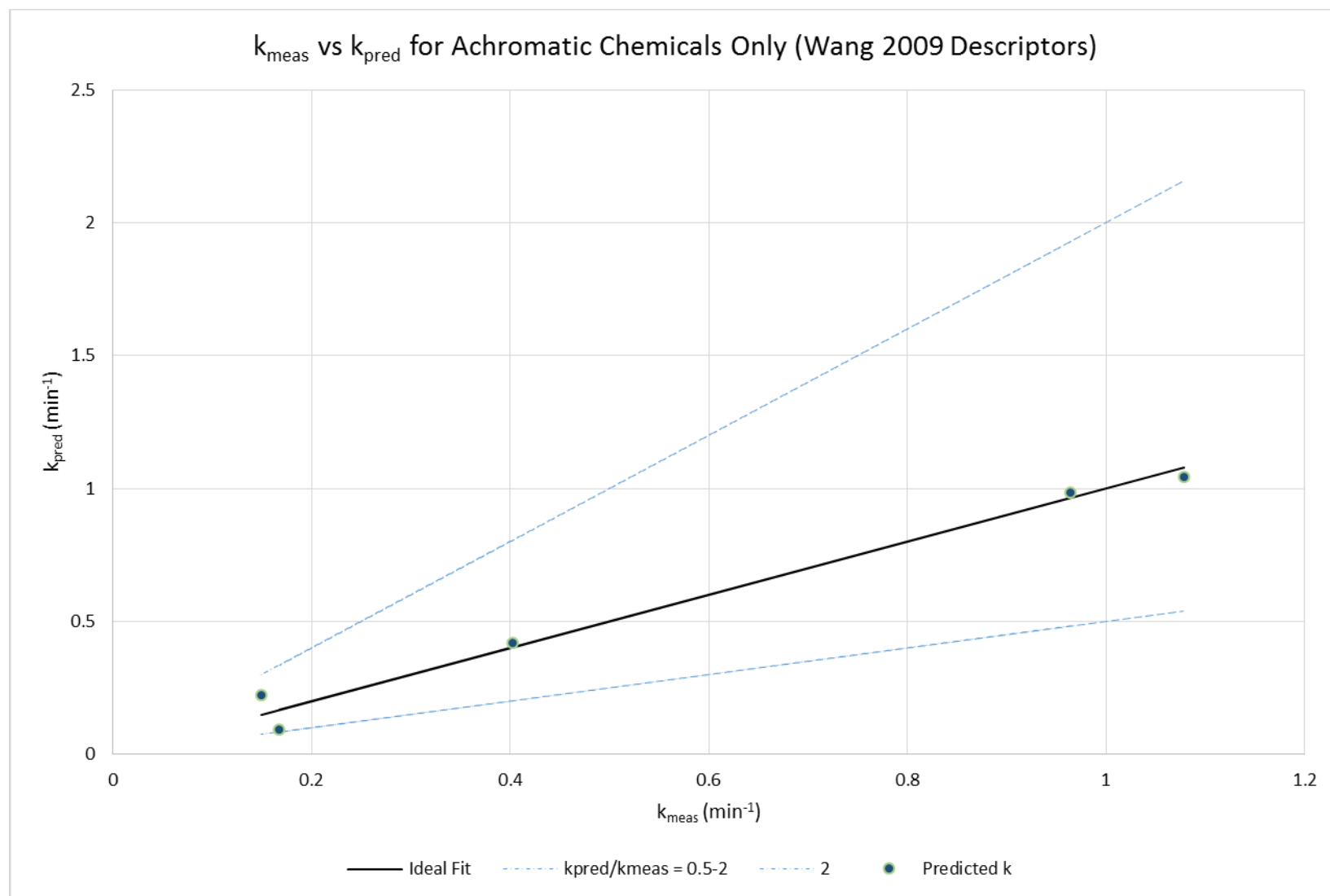


Figure 15. Actual versus predicted degradation rate constants utilizing Wang et al. descriptors with the achromatic chemical data set.

3.3.1.2. Jin, *et al.* 2015 Model

The Jin, *et al.* model consists of 7 molecular descriptors, including mean atomic Sanderson negativity (MASN), number of double bonds (DB), number of primary alkyl halides (CH2RX), number of hydrogen bond acceptors (HBA), Moran autocorrelation lag 2 weighted by mass (MAL2m), Balaban V index (BV), and signal 27 weighted by polarizability (Mor27p). Six of the seven descriptors were able to be produced; however, Mor27p was not directly available in the software packages utilized. The model below produced with the full n=11 data set results in a weak coefficient of determination of 0.481 and even weaker R^2_{adj} of -0.297 (Figure 16). The full model and all parameters failed tests of statistical significance.

$$K_{\text{pred}} = 6.2253693 + 0.2855091(\text{HBA}) - 1.433525(\text{BV}) - 0.247911(\text{DB}) - 5.817407(\text{MASN}) - 0.565174(\text{MAL2m}) - 0.076636(\text{CH2RX})$$

Fitting these parameters to n=6 dyes alone or n=5 achromatic chemicals alone is not possible due to degrees of freedom violation and bias in the model caused by the comparatively large number of descriptors. Overfitting is apparent and the resultant R^2 is 1 in both cases. Jin *et al.* found that the Balaban V index and the number of hydrogen bond acceptors showed the best correlation to the degradation rate constant in their model. When using only those two descriptors, no better model fit can be obtained with the full data set or data subsets. We can conclude that the Jin, *et al.* descriptors do not fit the dye and chemical data set used in this study.

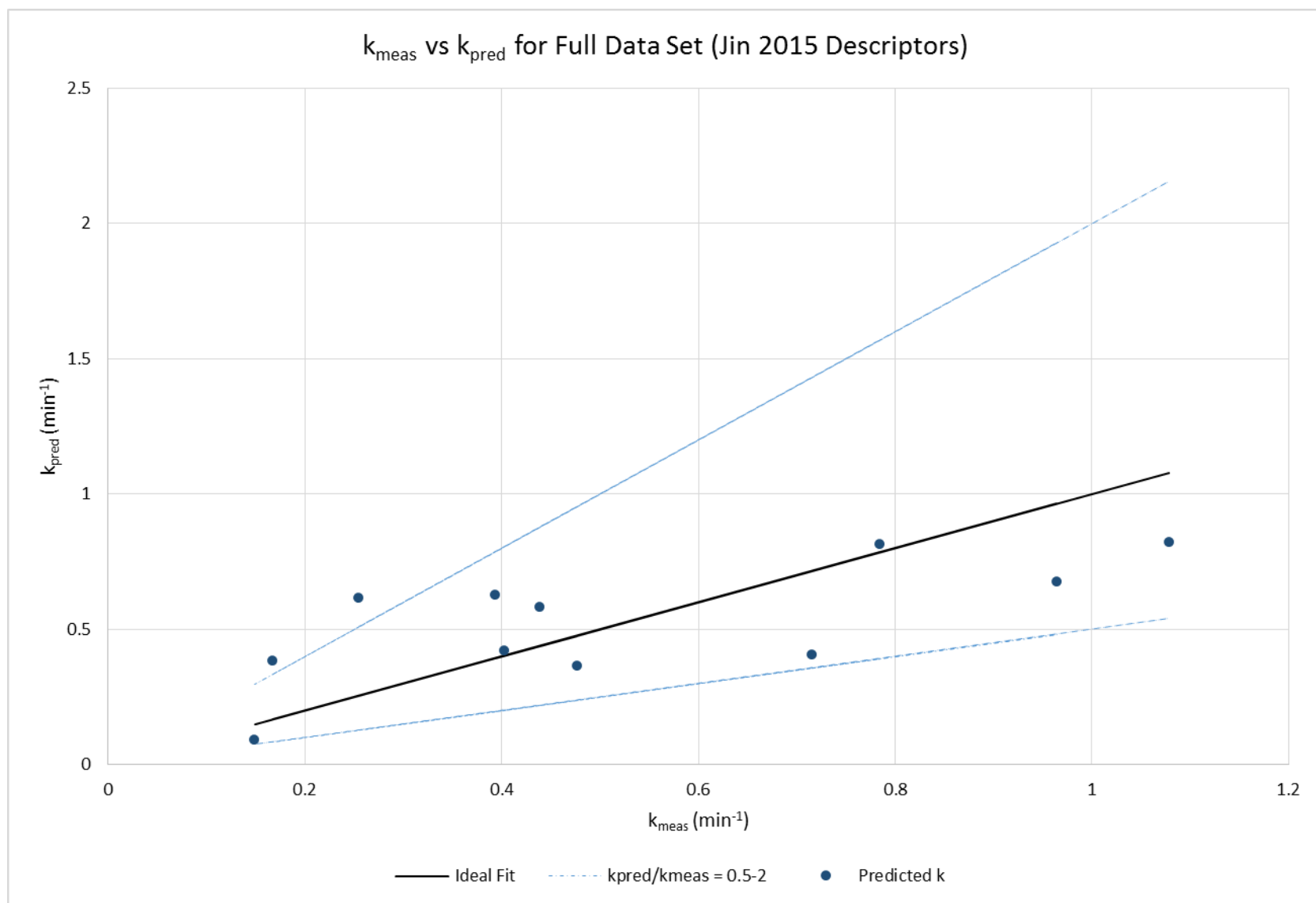


Figure 16. Actual versus predicted degradation rate constants utilizing Jin et al. descriptors with the full data set.

3.3.1.3. Tang 2004 Model

The Tang model is the least complex of all models evaluated as it consists of only one molecular descriptor, energy of the lowest unoccupied molecular orbital (LUMO). Producing a model using LUMO for the full n=11 data set results in extremely poor fit evidenced by an R^2 of 0.02 and poor statistical parameters. Only the model intercept shows significance as a parameter. Figure 17 illustrates the poor fit with a horizontal trend of the predicted k values, indicating no correlation between the measured and predicted k values, which is precisely what the R^2 value tells us. The resultant model equation is below.

$$K_{pred} = .54867 - 0.023898(E_{LUMO})$$

When looking at the data set of n=6 dyes alone, the fit of the model improves (Figure 18), but is still poor overall with an R^2 of 0.39 and an R^2_{adj} of 0.24 and all tests of statistical significance fail. The model produced is as follows.

$$K_{pred} = .4636993 - 0.148431(E_{LUMO})$$

The data set of n=5 achromatic chemicals also returns poor fit with return to a horizontal trend and an overall R^2 of 0.032 (Figure 19). Overall analysis across the full data set and two subsets indicates that LUMO alone has poor predictive power in this particular data set.

In the original work produced by Tang, individual models were built for individual chemical classes with LUMO as a descriptor. Each of these models was built with a data set of only n=3 compounds and the resultant models for each class of chemicals was vastly different from the next. Producing a model with the full Tang data set would have resulted in a poorly parameterized model. Similarly, the full data set utilized in this study produced poor fit to LUMO as a sole descriptor. Individual sets of n=3 dye or achromatic chemical data points may

have produced models of good fit, but such small data sets produce results with poor statistical relevance.

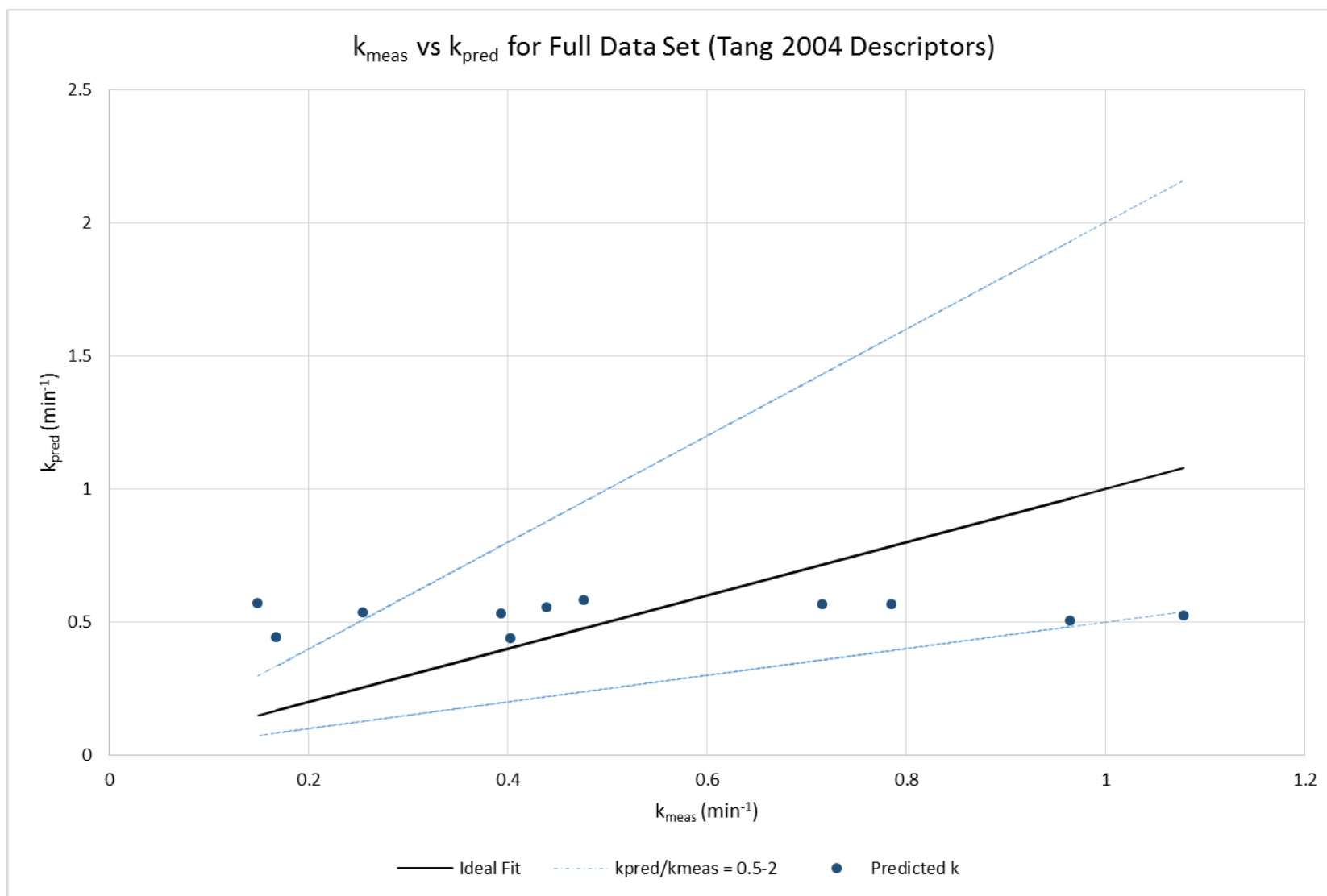


Figure 17. Actual versus predicted degradation rate constants utilizing Tang descriptors with the full data set.

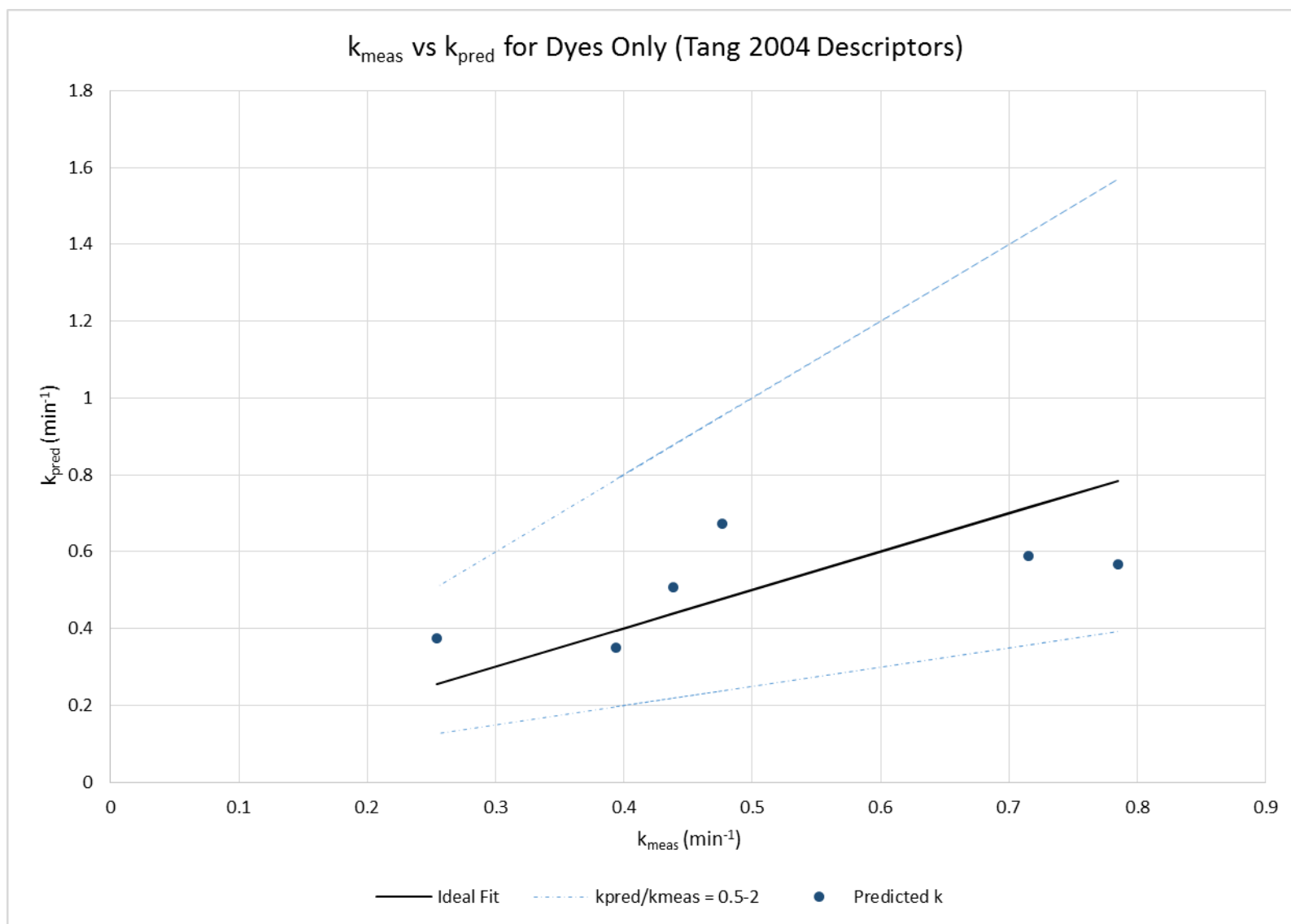


Figure 18. Actual versus predicted degradation rate constants utilizing Tang descriptors with the dye data set.

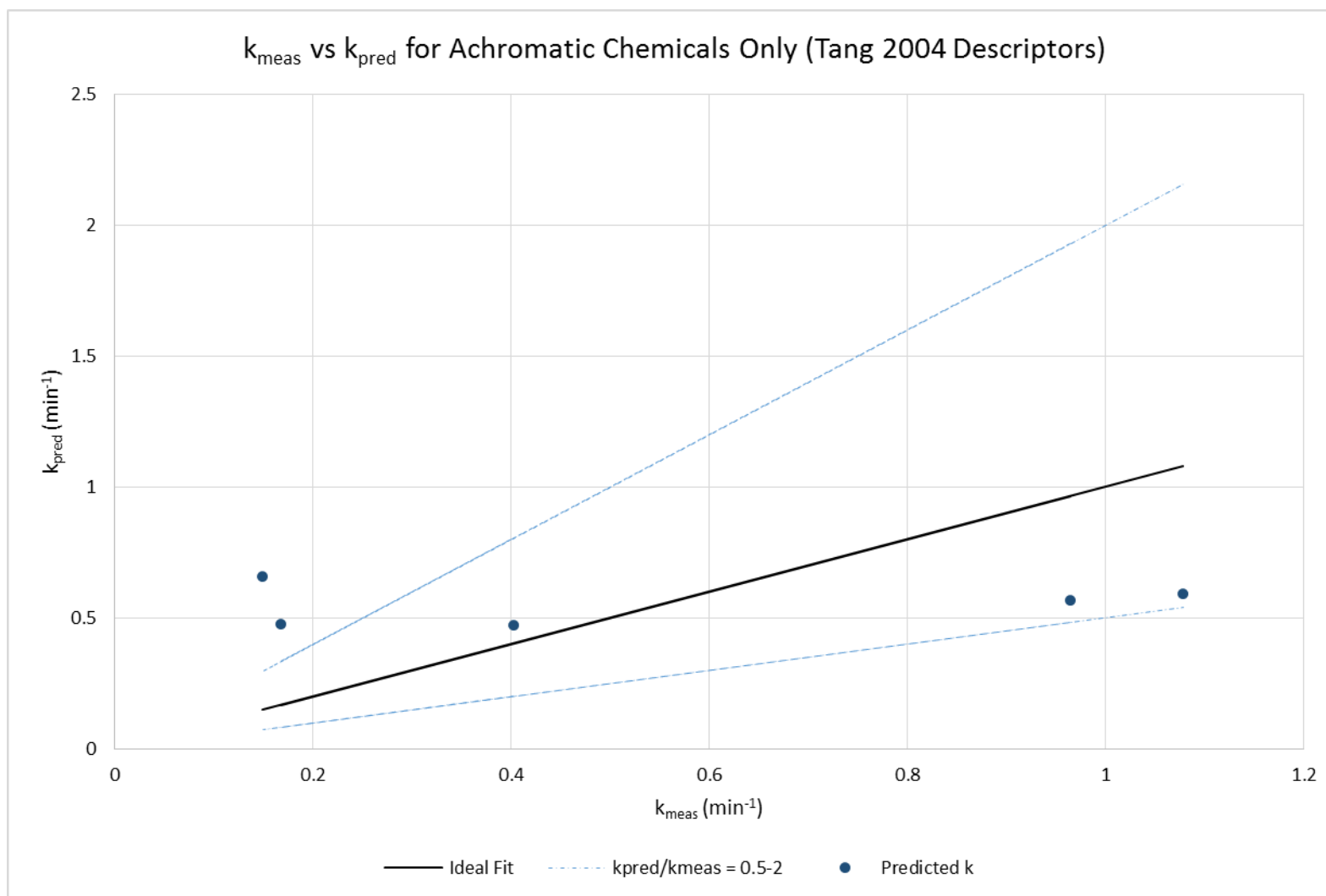


Figure 19. Actual versus predicted degradation rate constants utilizing Tang descriptors with the achromatic chemical data set.

3.3.1.4. Kusic, et al. 2009 Model

The Kusic, et al. model consists of 4 molecular descriptors including E_{HOMO} , molecular path count of order 8 (PC8), Geary autocorrelation of lag 2/weighted by polarizabilities (GACL2wP), and autocorrelation lag 7/weighted by polarizabilities (AL7wP). All the descriptors were reproducible in this study. The full $n=11$ data set produces a poor model fit with R^2 of 0.311 and R^2_{adj} of -0.147.

$$K_{pred} = 5.5068128 + 0.4620056(E_{HOMO}) - 0.001947(AL7wP) - 0.760255(GACL2wP) - 0.009211(PC8)$$

When reviewing the plot of actual versus predicted k (Figure 20), the two data points representing malathion and Allura Red AC deviate from the trend followed by the remaining data points. In general, it is not good practice to remove data points unless there is sound reasoning for why outliers may exist. In this case, we would review the structures and assess the domain of applicability of the two outliers. In the case of malathion, it is unique in that it is the only compound that contains phosphorous. However, there are no immediate differences that can be discerned for Allura Red AC; it is an azo dye just as Sunset Yellow FCF and Tartrazine and has a similar molecular structure. In principle, there is no immediately obvious reason to remove Allura Red AC; however, it is interesting to remove both compounds to assess the impact on model fit. With reduction to a data set of $n=9$, model fit is substantially enhanced (Figure 21) to an R^2 of 0.985 and R^2_{adj} of 0.971 with the following resultant model. The full model and all parameters are also statistically significant.

$$K_{pred} = 7.3060112 + 0.6488038(E_{HOMO}) - 0.002917(AL7wP) - 0.996798(GACL2wP) - 0.01186(PC8)$$

The data set of n=6 dyes alone (including return of Allura Red to the set) produces strong model fit as observed by R^2 of 0.992 and R^2_{adj} of 0.961 (Figure 22); however, in contrast to the prior model, the full model and all parameters fail tests of statistical significance. The resultant model is as follows.

$$K_{pred} = 2.7587428 + 0.3297615(E_{HOMO}) - 0.004671(AL7wP) - 2.5296858(GACL2wP) - 0.0013733(PC8)$$

The set of n=5 achromatic chemicals cannot produce a model without bias due to number of data points versus predictors. In general, descriptors utilized by Kusic, *et al.* may be useful in predicting the observed degradation rates of dyes; however, we must be cautious of the potential for overfitting with the small sample size and lack of statistical significance. The descriptors may also be useful to the overall data set if we have valid reason to exclude one dye and one achromatic chemical as outliers, though there is no immediately apparent reason to do so.

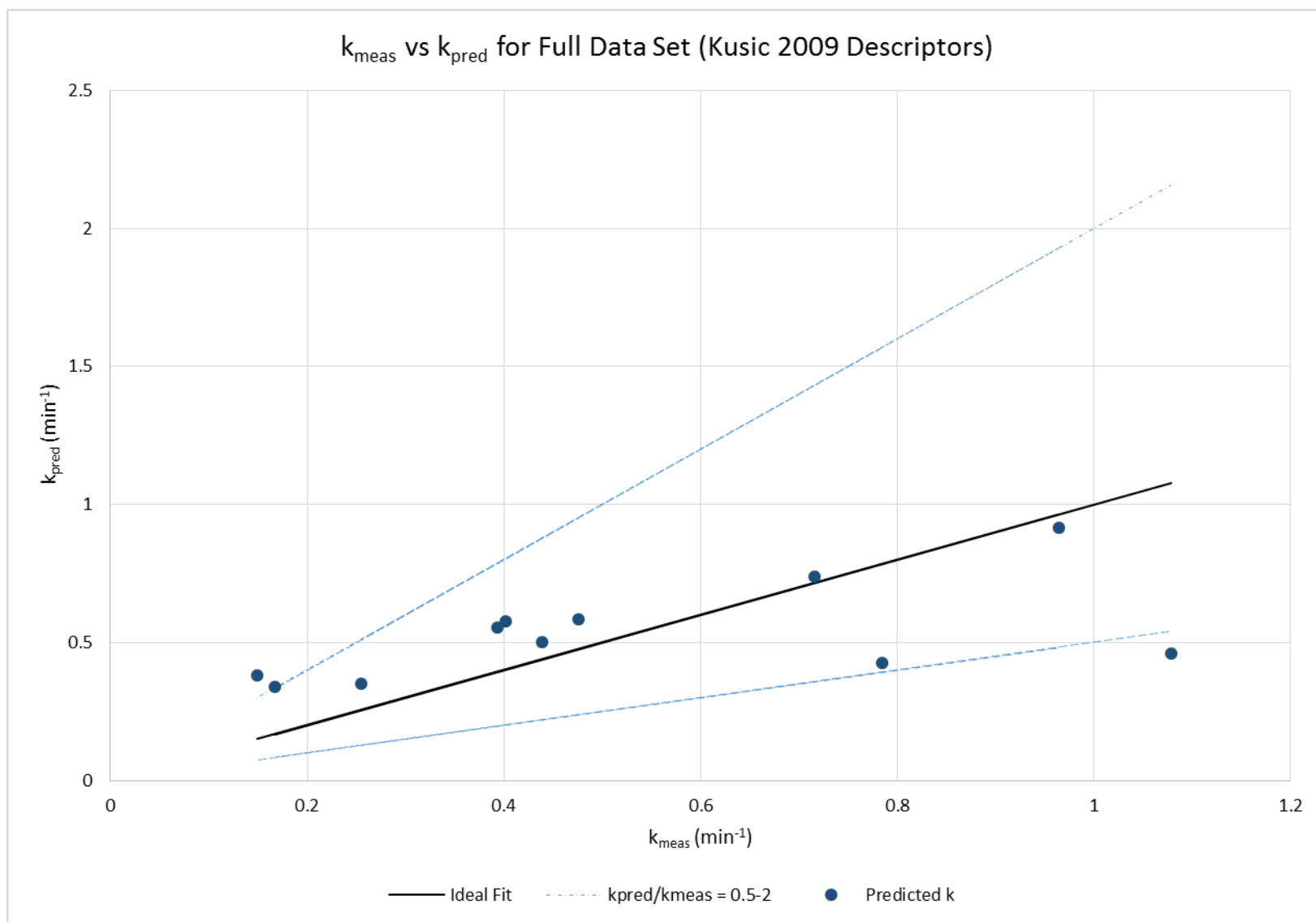


Figure 20. Actual versus predicted degradation rate constants utilizing Kusic et al. descriptors with the full data set.

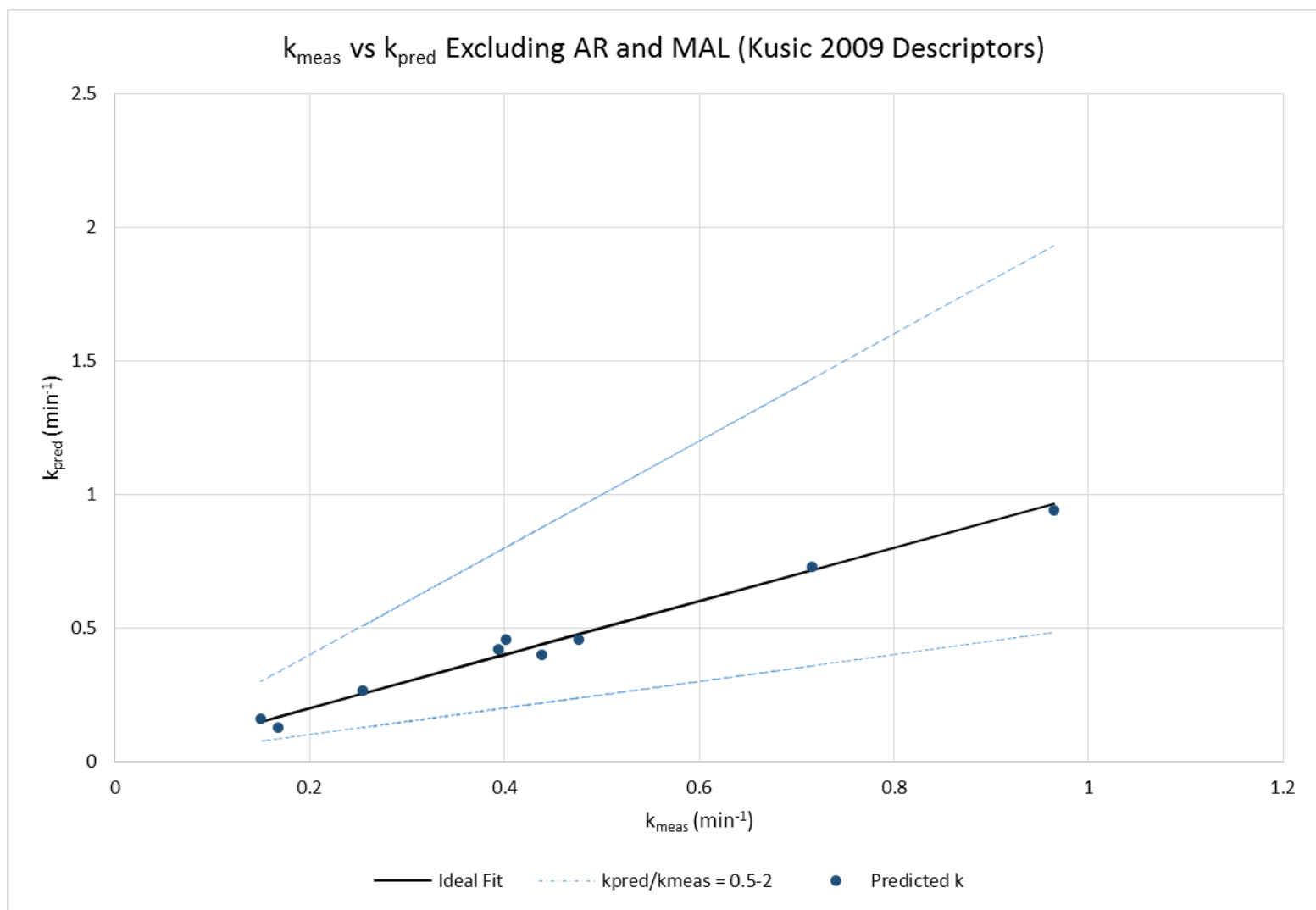


Figure 21. Actual versus predicted degradation rate constants utilizing Kusic et al. descriptors and omitting malathion and Allura Red AC.

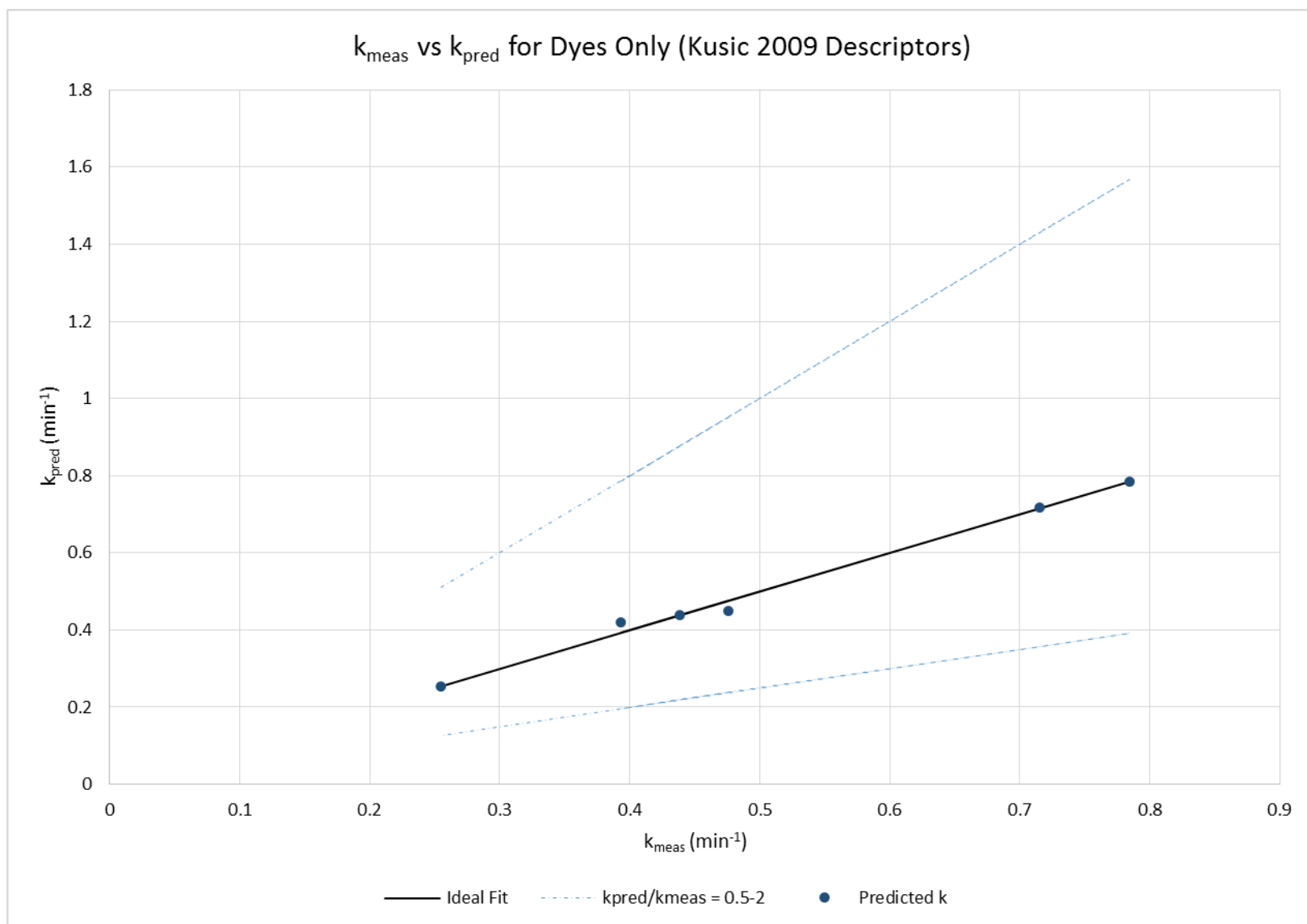


Figure 22. Actual versus predicted degradation rate constants utilizing Kusic et al. descriptors with the dye data set.

3.3.1.5. Sudhakaran and Amy 2012 Model

The first set of Sudhakaran and Amy descriptors consists of the HOMO-LUMO energy gap, electron affinity (EA), number of halogen atoms, number of ring atoms, weakly polarizable component of the solvent accessible surface area (WPSA), and oxygen to carbon ratio (OtoC). There was no direct method for obtaining WPSA in the software utilized in this study, but the remainder were obtained directly or through mathematical manipulation of existing descriptors. The descriptors fit to the full n=11 data set results in an R^2 of 0.86 and R^2_{adj} of 0.72 (Figure 23). Statistical parameters show mixed results. The overall model is statistically significant; however, the individual parameters of “Halogen” and “OtoC” fail to pass the p-value test.

$$K_{pred} = 7.0584708 - 0.57937(EA) + 0.6832793(HOMO-LUMO) - 0.09306(Halogen) - 0.063115(Ring\ Atoms) - 0.0192175(OtoC)$$

Parameter estimates for subsets of dyes and achromatic chemicals alone cannot be obtained due to bias caused by the number of predictors (e.g. more predictors than data points). Overall analysis indicates that this model is likely not a good fit to this data set and results in a coefficient of determination that is likely due primarily to chance overfitting as evidenced by the lower R^2_{adj} .

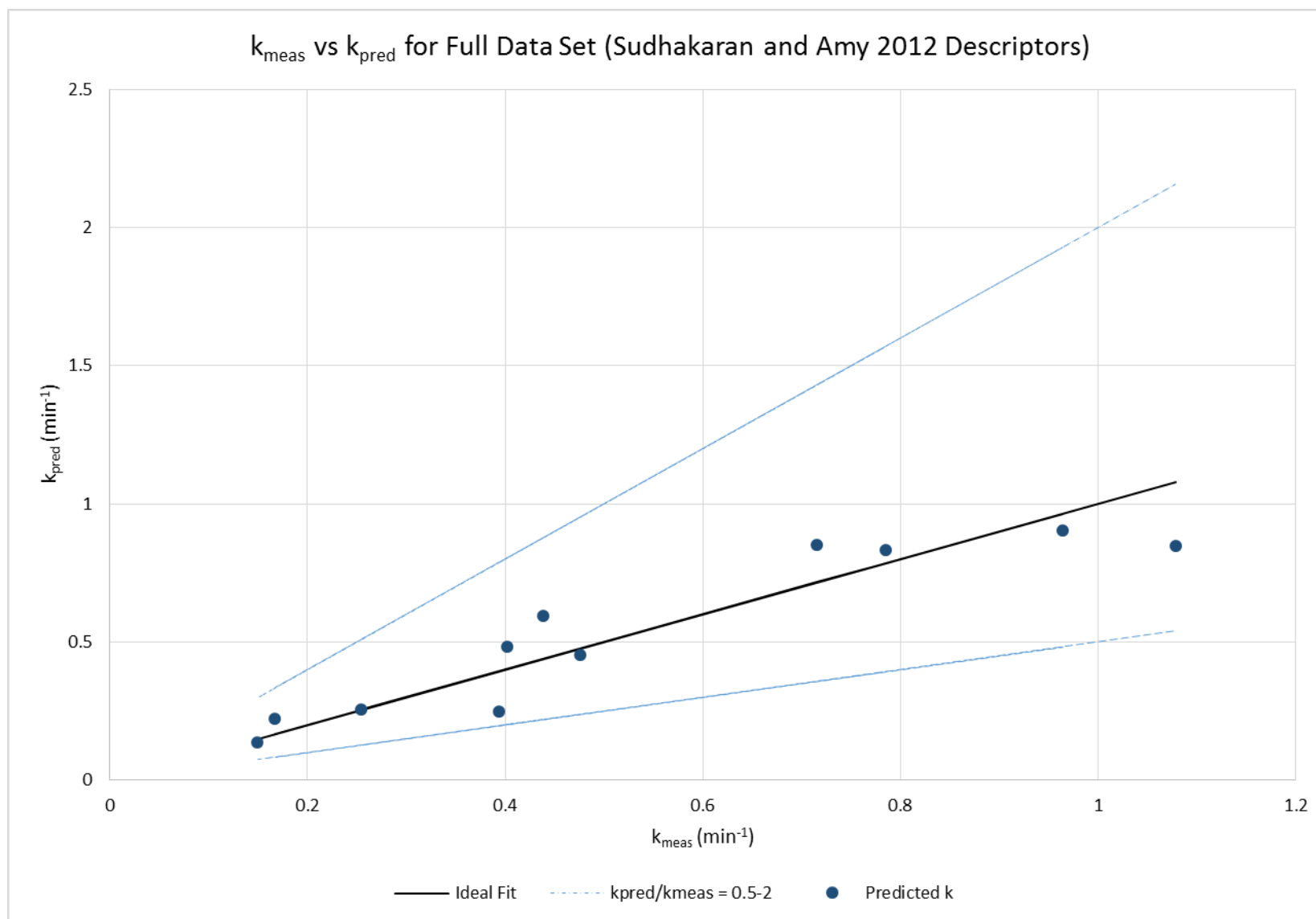


Figure 23. Actual versus predicted degradation rate constants utilizing Sudhakaran and Amy, 2012 descriptors with the full data set.

3.3.1.6. Sudhakaran and Amy 2013 Model

The second set of Sudhakaran and Amy descriptors consists of double bond equivalence (DBE), weakly polarizable component of the solvent accessible surface area (WPSA), ionization potential (IP), and electron affinity (EA). As before, there was no direct method for obtaining WPSA in the software utilized in this study. Double bond equivalence was calculated from the number of rings and double bonds, electron affinity was estimated as the opposite of the LUMO, and ionization potential was estimated as the opposite of the HOMO. The full n=11 data set fit to the three descriptors results in a model with no statistical significance and an R^2 of 0.116 (Figure 24). All parameters also show lack of significance.

$$K_{pred} = 1.7360915 - 0.033767(DBE) + 0.0586533(EA) - 0.117716(IP)$$

When building a model with the n=6 dyes subset, the R^2 improves to 0.568, however R^2_{adj} is poor at -0.081, indicating high likelihood of chance improvement (Figure 25). All parameters and the full model also show lack of statistical significance.

$$K_{pred} = -0.769738 - 0.01624(DBE) + 0.1155415(EA) + 0.1923857(IP)$$

The final model for the subset of n=5 achromatic chemicals results in a model with an R^2 of 0.995 and an R^2_{adj} of 0.982 (Figure 26); however, all parameters and the full model again show lack of statistical significance. Caution must be taken given the small sample size and lack of significance.

$$K_{pred} = 0.6893163 + 0.6937853(DBE) - 0.389132(EA) - 0.23356(IP)$$

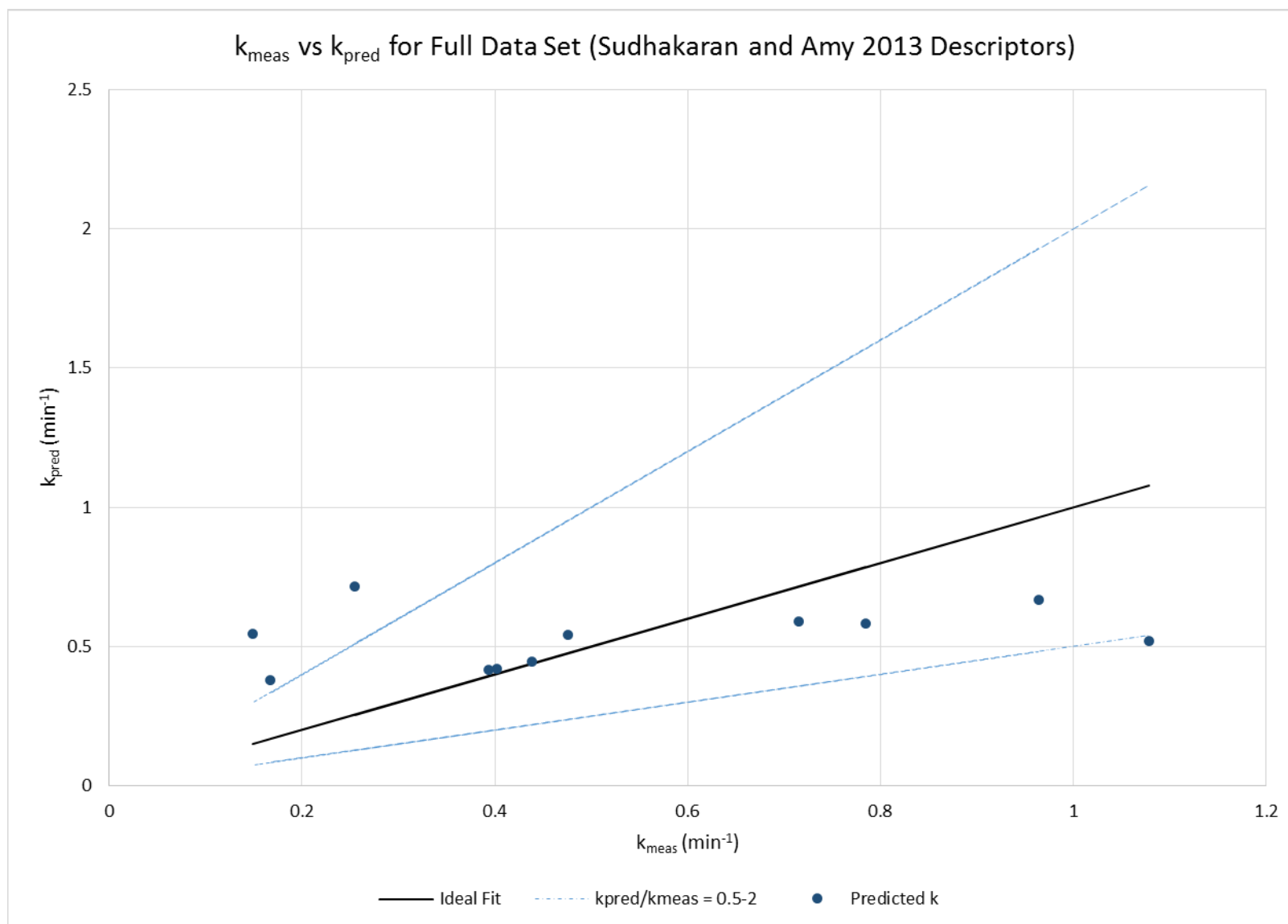


Figure 24. Actual versus predicted degradation rate constants utilizing Sudhakaran and Amy, 2013 descriptors with the full data set.

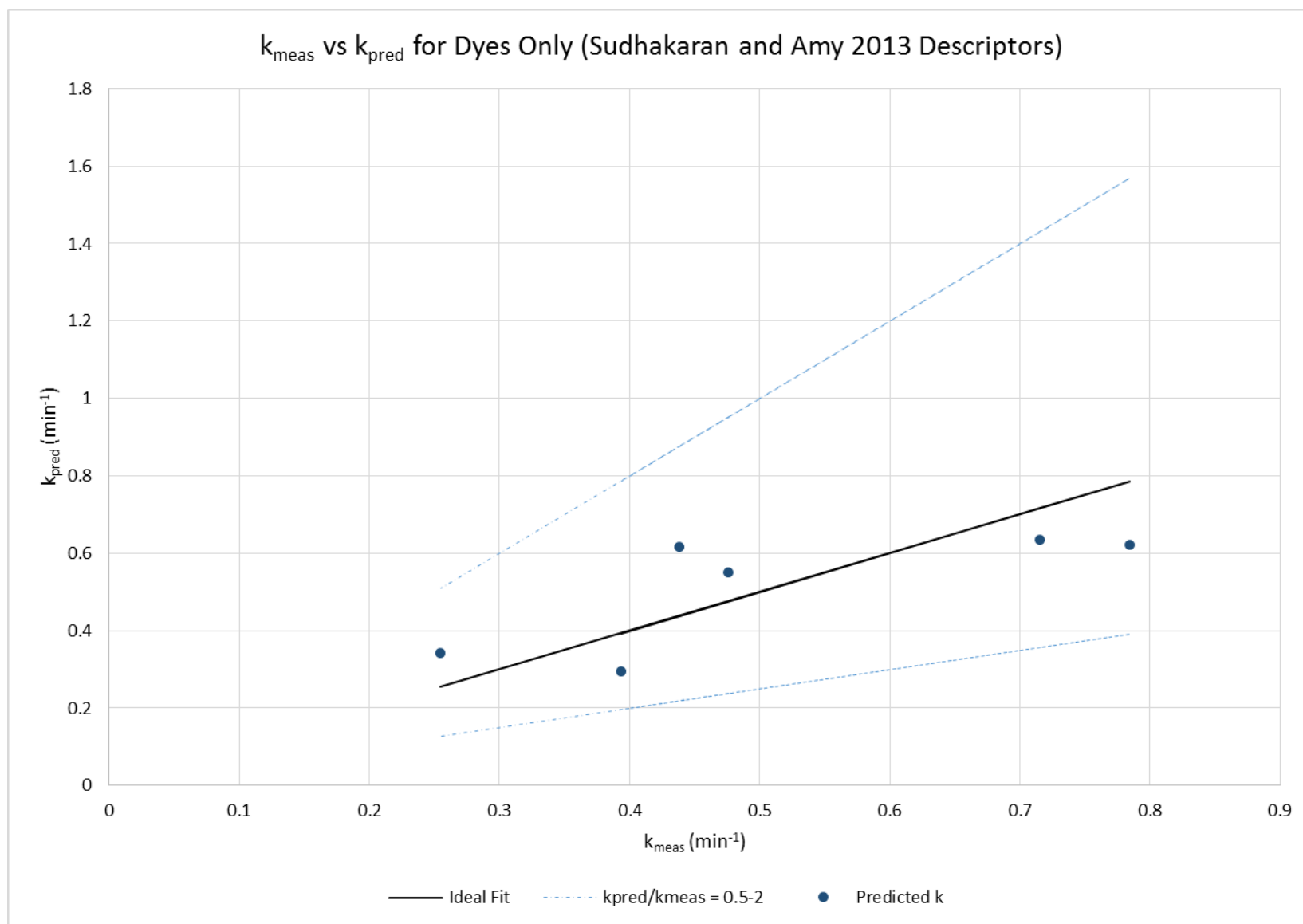


Figure 25. Actual versus predicted degradation rate constants utilizing Sudhakaran and Amy, 2013 descriptors with the dye data set.

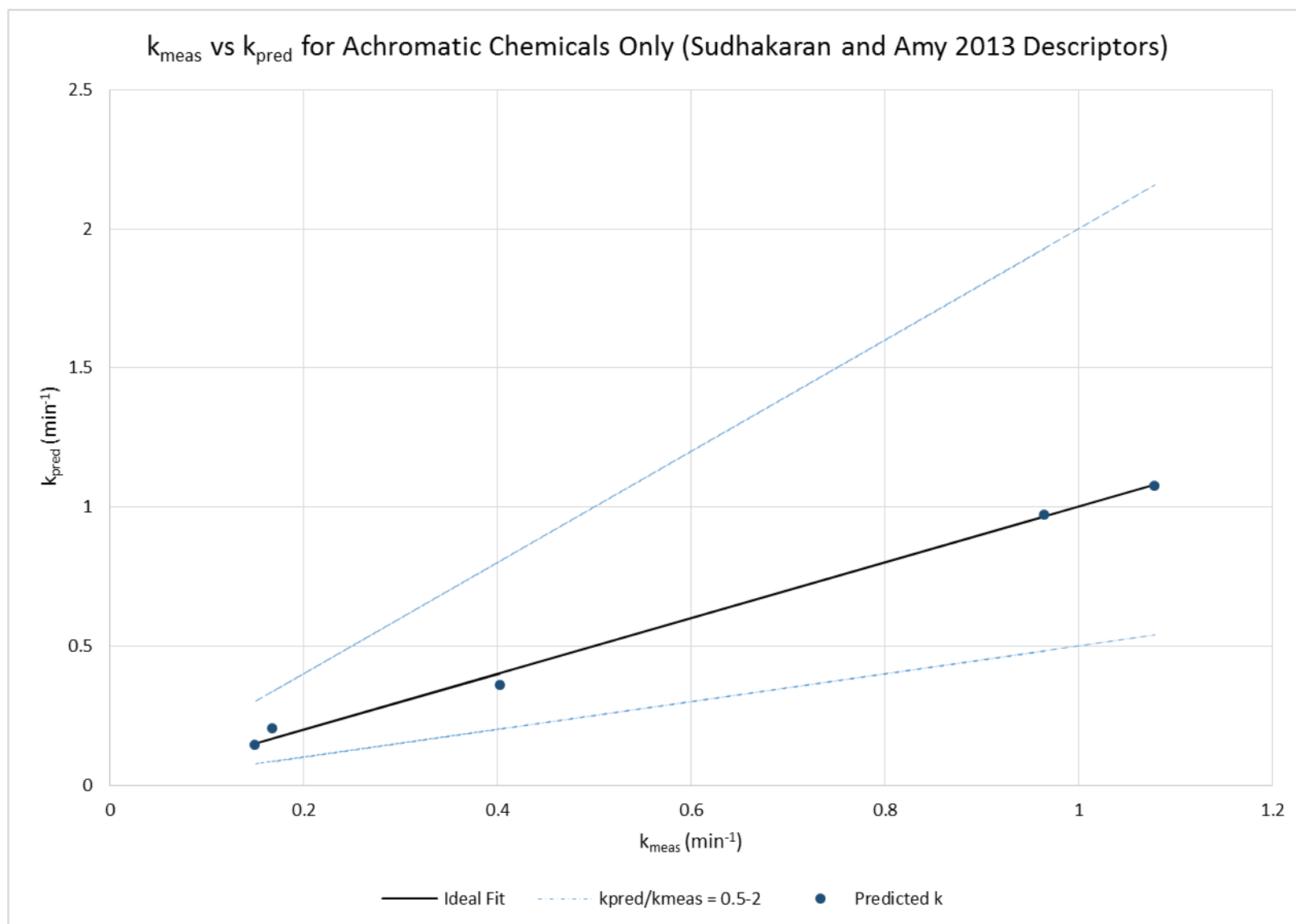


Figure 26. Actual versus predicted degradation rate constants utilizing Sudhakaran and Amy, 2013 descriptors with the achromatic chemical data set.

3.3.2. Construction of a New QSPR Model

The full set of molecular descriptors listed in Appendix B was utilized to conduct forward stepwise regression using p-value entry/exit parameters, as previously described. In general, stepwise regression will continue to add terms to a model to seek improvements in R^2 . This can quickly lead to chance overfitting, especially with small sample sizes. The initial pass through the stepwise procedure produced a list of seven descriptors that are significant in the model. However, as noted, seven descriptors as compared to a small sample size can easily over fit the data simply due to chance values of the predictors being fit. Of the seven descriptors, a model with zero point energy (ZPE) alone results in a model with $R^2 = 0.792$:

$$K_{pred} = -0.465407 + 0.0016863(ZPE)$$

The model excluded Brilliant Blue FCF and Fast Green FCF dyes as they failed to converge in Spartan geometry optimization for ZPE calculations following over 300 hours of computational time and eventual memory faults. This is due to the complexity of the molecules and the complexity of the basis sets used in the density functional theory calculations. Overall R^2 and R^2_{adj} are relatively good at 0.79 and 0.76, respectively (Figure 27). The overall model and all parameters are statistically significant with the exception of the intercept term. A plot of predicted k versus residuals in JMP shows desired randomness.

To improve the R^2 value, the additional six parameters were examined in the forward stepwise approach and found not to individually improve R^2 meaningfully. A plot of measured versus predicted k was examined. From this plot, an observation is that Tartrazine and Erythrosine B fall the furthest from the ideal fitted line (Figure 27). As previously reported

elsewhere (Chapter 2), those two dyes in particular showed a high molar absorptivity at the 265 nm wavelength (the peak output wavelength of the LEDs being used in the study), and it was hypothesized elsewhere (Chapter 2) that competition with H₂O₂ for UV absorbance likely affected the kinetics of the AOP. Absorbance at 265 nm was added as a predictor to the model to see what effect it may have. Adding the term tightens the model significantly, resulting in R² and R²_{adj} values of 0.951 and 0.934, respectively, and the full model and all parameters show significance (Table 5 and Figure 28). A predicted k versus residual plot produced in JMP also shows randomness with no pattern, as desired. The resultant model and associated parameters are as follows.

$$K_{pred} = -0.404717 + 0.0018182(ZPE) - 1.093331(Abs265)$$

3.3.3. Physical significance of newly constructed QSPR model

Parameters in the model show a positive correlation between degradation rate and ZPE and a negative correlation between degradation rate and absorbance at 265. The ZPE is a value that comes from thermodynamic calculations in Spartan. Both of these correlations make intuitive sense when considering reaction kinetics. The theory behind ZPE is that even at 0 degrees Kelvin, molecules will still have some level of vibrational energy.

This represents the first known use of ZPE in a QSPR model; however, larger data sets should be tested to further assess the utility of this novel parameter. It was hypothesized in Chapter 1 that descriptors related to frontier electron density, particularly HOMO, would be significant model parameters. This was not the case, as models incorporating HOMO, LUMO, and HOMO-LUMO performed relatively poorly and ZPE emerged as an important descriptor for this data set.

Table 5. Parameters and tests of statistical significance for new models built with zero point energy and molar absorptivity.

Model	Data Set	Rsquare	Rsquare Adj	RMSE	F Ratio	Prob > F	Parameter	Parameter Estimate	Prob > t
<i>New Model with ZPE</i>	Omit BB and FG (n=9)	0.792	0.762	0.169	26.63	0.0013	Intercept	-0.465407	0.0572
							ZPE	0.0016863	0.0013
<i>New Model with ZPE and Abs</i>	Omit BB and FG (n=9)	0.951	0.935	0.089	58.3	0.0001	Intercept	-0.404717	0.0096
							ZPE	0.0018182	<0.0001
							Abs265	-1.093331	0.0045

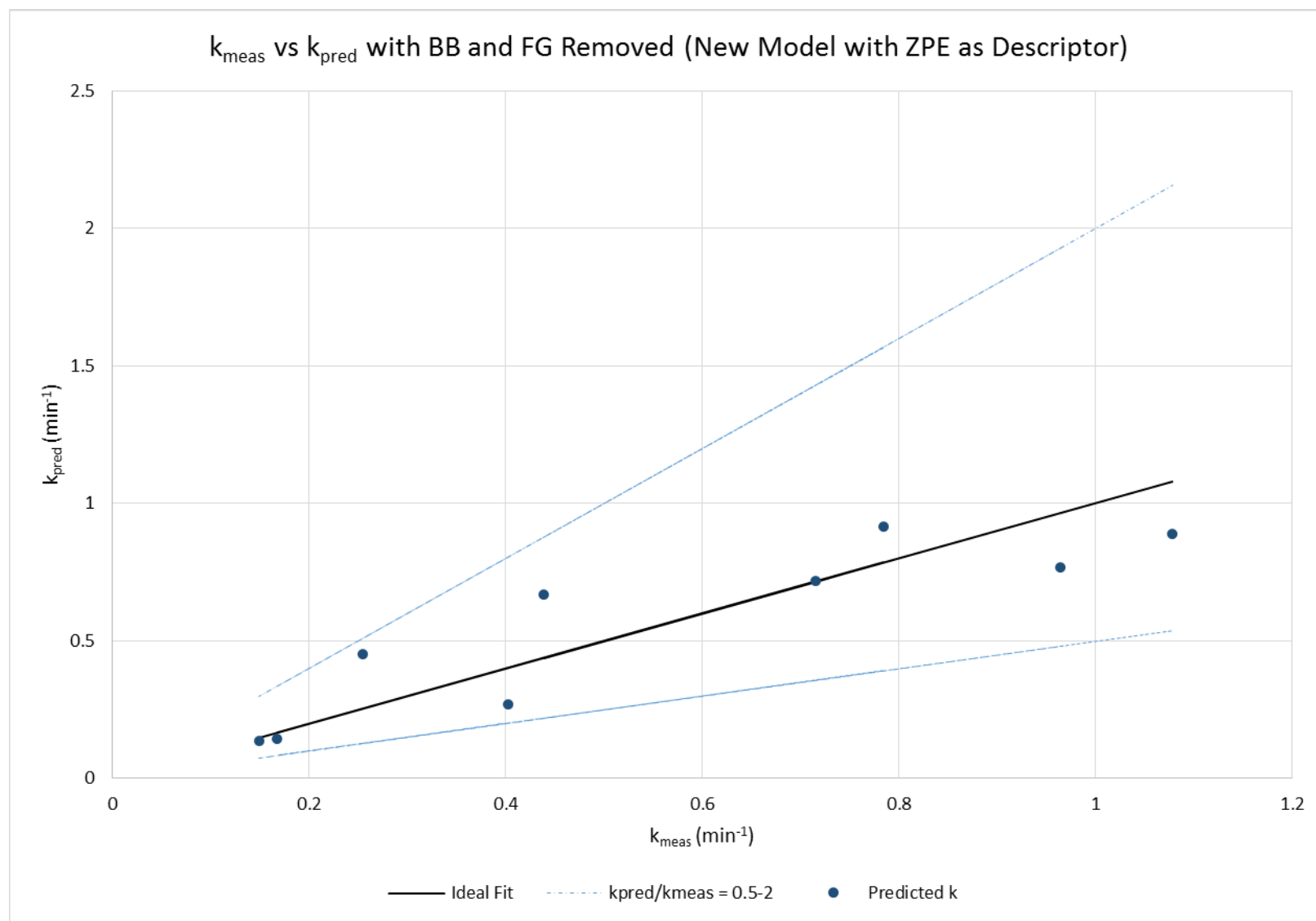


Figure 27. Actual versus predicted degradation rate constants utilizing Zero Point Energy as a descriptor with the full data set.

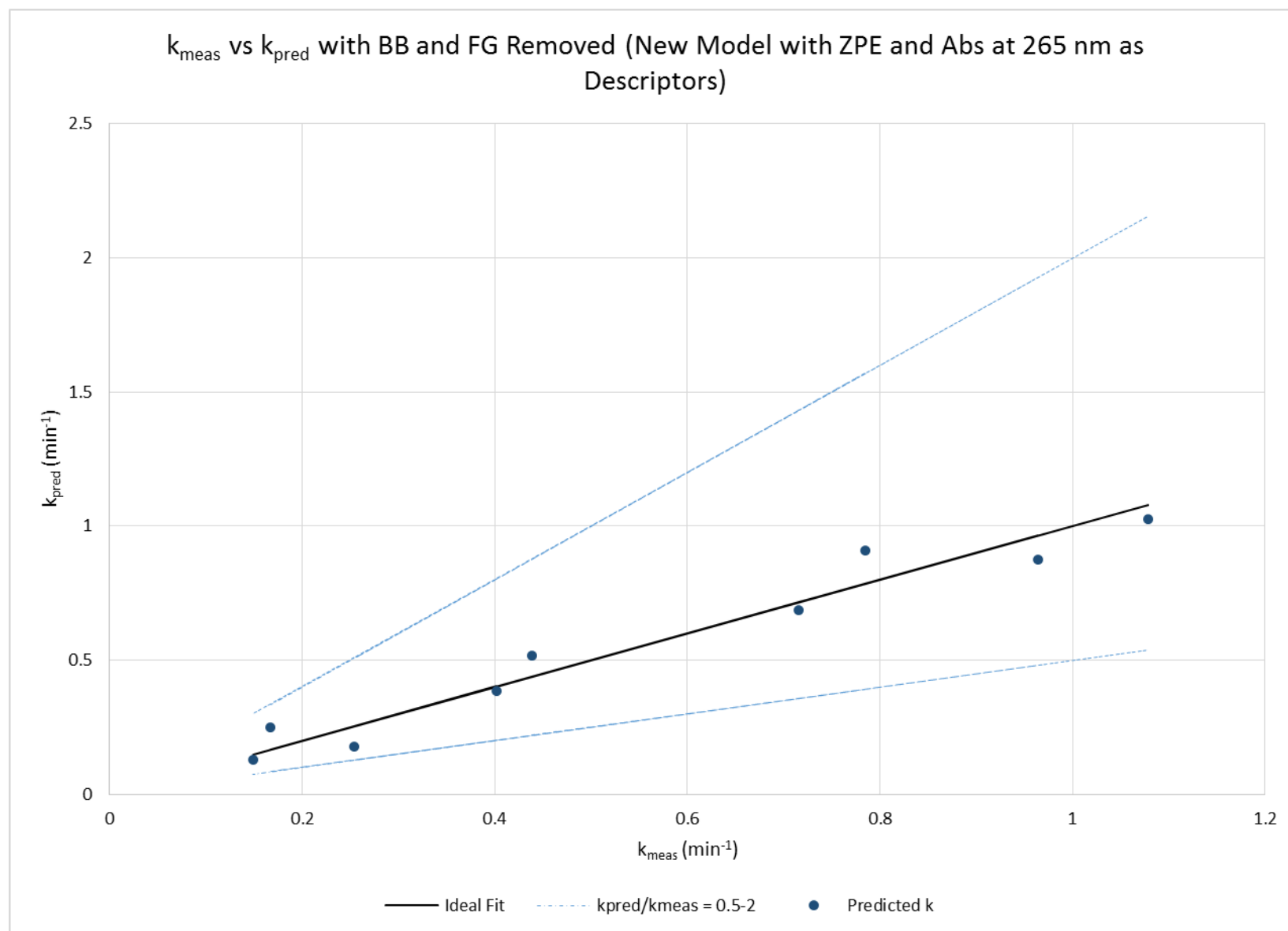


Figure 28. Actual versus predicted degradation rate constants utilizing Zero Point Energy and molar absorptivity as descriptors with the full data set.

3.4. Conclusions

This study sought to utilize a small, high quality data set of the observed degradation kinetics of 6 dye and 5 achromatic chemical compounds tested in a bench-scale UV LED reactor to compare fit with molecular descriptors in published QSPRs developed with traditional mercury lamp AOP data and also to use MLR methodology to construct a new QSPR model. Prior to this study, QSPRs had not been evaluated for UV LED-based reactors. Overall fit to descriptors used in all the existing QSPR models compared was relatively poor for the overall data set of dyes and achromatic chemicals combined. The resultant R^2 values were 0.024, 0.116, 0.157, 0.312, 0.481, and 0.864; however, several of the descriptors producing the model with the highest R^2 of 0.864 failed to pass tests of statistical significance. When breaking the larger data set into smaller subsets of dyes and achromatic chemicals, improvement was seen with R^2 values between 0.033 – 0.996, but most models and individual parameters failed tests of statistical significance. Statistical robustness was also compromised due to smaller data set sizes compared to numbers of predictors included in models.

In construction of a new model for predicting the dye and achromatic chemical apparent first order degradation rates, ZPE emerged as a statistically significant parameter. Model fit with ZPE was further enhanced by including UV absorbance competition at the peak output wavelength of the LEDs. Overall, ZPE and molar absorptivity at 265 nm result in a QSPR with $R^2 = 0.951$ with statistical significance in the model and all parameters at the 95% confidence interval. This represents the first known use of ZPE and molar absorptivity in the construction of a QSPR model for the UV/H₂O₂ AOP in both the traditional mercury lamp and UV LED domains.

IV. UV LED AOP Application in a USAF Net Zero Water Program – A Systems Architecture View

Keywords

Ultraviolet, light emitting diode, advanced oxidation process, net zero water, systems architecture

Abstract

Water scarcity and contamination are challenges to which the United States homeland is not shielded. With increased demand for water and threats to the existing supply, policies and technologies that support a “Net Zero” water use posture will become increasingly critical. The United States Air Force has established its own Net Zero initiative through an *Energy Strategic Plan* that identifies water as a critical asset and seeks potable water demand reduction by capturing and reusing, repurposing, or recharging an amount of water that is greater than or equal to the volume of water the installation uses. The present study uses a systems architecture view to describe a net zero water program at a hypothetical USAF installation and proposes areas within the program where advanced oxidation processes utilizing ultraviolet light emitting diodes and hydrogen peroxide might be paired with other technologies to treat water. Focus is placed on delineating treatment operations at the installation level and the facility level. Facility-level treatment for recycling of wastewater was found to be the most feasible application for the near term as flow rates and volumes of water treated at decentralized facilities are comparatively favorable to the current state of UV LED technology. An approach is also presented to enable comparison of the required apparent first order degradation rate constant to facility size and desired recycle ratio. Required degradation rates for a 55 gallon UV LED/H₂O₂ AOP reactor at 0.1-0.9 recycle ratios show desirable overlap with the apparent first order degradation rate constants measured for eleven representative compounds tested under quality assured conditions. Thus, the apparent first order degradation rate constant can be used as a design criteria in the overall design of a UV LED reactor and the associated operating parameters. Furthermore, if paired with the predictive capability of the previously developed QSPR model, the design criteria can extend to future contaminants as they emerge and impact the USAF.

4.1. Introduction

Water scarcity is becoming a more prevalent global reality to which the United States homeland is not shielded. As populations continue to grow, so does the demand for clean, safe drinking water. At the same time, water supplies once taken for granted are becoming depleted in some geographical regions. One need not look further than the western United States to understand the evolving situation that is a real and current crisis in some areas, such as those municipalities with water supplies originating in the Colorado River basin and specifically Lake Mead and Lake Powell (Rajagopalan, et al. 2009; Gober 2017). Other areas of the US will likely not be immune to this reality as climatic changes, increased demands, and water governance policies evolve (Sullivan, et al. 2017). Additionally, municipalities have been threatened by contaminants and forced to seek alternate supply sources, as was the case in Flint, Michigan following lead leaching into municipal drinking water distribution lines (Morckel 2017). The USAF is not immune to the reality of water scarcity and the need for conservation, because there is a tightly linked, symbiotic relationship between USAF installations and the municipalities they neighbor. Furthermore, the USAF has also been implicated as a source of water contamination in some specific cases that have threatened municipal supplies. With increased demand for water and threats to the existing supply, policies and technologies that support a “Net Zero” water use posture will become increasingly critical. The US Environmental Protection Agency (USEPA) defines net zero water as “limiting the consumption of water resources and returning it back to the same watershed so as not to deplete the resources of that region in quantity or quality over the course of the year.” (USEPA 2016)

The USAF has established its own Net Zero initiative through an *Energy Strategic Plan* that identifies water as a critical asset and seeks a balance of resource consumption, production,

and conservation. An installation is to consume no more energy than is generated on the installation, and potable water demand is reduced by capturing and reusing, repurposing, or recharging an amount of water that is greater than or equal to the volume of water the installation uses. The strategic plan places priority on reducing demand, integrating energy and water efficiency throughout business and planning processes, and promoting integration of new technologies in a constrained resource environment. The initiative is designed to achieve a federal zero net energy goal by 2030 for new facility construction and alterations. The USAF generally consumes around 27 billion gallons of water per year at an annual cost of \$150 million, and energy utilized in water treatment and delivery is closely tied to an overall \$9 billion annual energy cost (US Air Force 2013). In an operational context that seeks to balance fiscal constraint with sustained global operations, the USAF needs to consider emerging technologies for water treatment that provide necessary water supply while simultaneously reducing energy costs and striving for net zero consumption.

4.2. Background

Primary water challenges facing the USAF in the near term are twofold, availability and quality. The USAF has installations on three continents, and active, guard, or reserve installations are located in all 50 states of the US homeland (US Air Force 2017). Many of these installations are in arid environments, areas with high population density, and areas that have faced extensive drought conditions over multiple years (US Geological Survey 2017). Drought conditions in the face of continued water demand has drawn down raw water supply levels (Famiglietti 2014) and has forced local municipalities, as well as USAF installations, to implement emergency water restrictions either on a temporary basis or, in some cases, enduring restrictions which have become pseudo-standard practice. Additionally, in some coastal areas,

freshwater supplies are beginning to see saltwater intrusion due to rising sea levels (Ferguson and Gleeson 2013). One need not look further than examples in California and Florida to understand the extent and history of these issues. The South Florida Water Management District issued water emergency declarations as recently as April 2017 (SFWMD 2017). California was under a perpetual drought state of emergency from January 2014 through April 2017, with several jurisdictions still affected beyond that time. These two states alone have 13 USAF installations and support activities that are likewise impacted by these types of declarations (US Air Force 2017). Concerns were raised in the US Department of Defense (DoD) 2014 *Quadrennial Defense Review* which notes climate change and the associated effect water scarcity may have on future missions and undermine capacity of homeland installations to support training activities. The document also underscores a need to increase water security and invest in efficiency, new technologies, and renewable energy sources (US DoD 2014). Those concerns were more recently echoed by the National Intelligence Council in a report titled *Implications for US National Security of Anticipated Climate Change*. In particular, the document notes that areas where populations continue to grow in coastal areas, water-stressed regions, and expanding cities will be most vulnerable to crises such as water shortages (USODNI 2016). Traditionally, focus has been placed on water security and scarcity in overseas operations; however, it is becoming increasingly imperative that focus be placed on preserving stateside water resources as well.

Traditional potable water cycles consist of withdrawing from a ground or surface raw water source, treating the water, conveying treated water to users, conveying used water to wastewater treatment plants, treating the wastewater, and discharging the treated wastewater. The point of treated wastewater discharge is dependent on the locality and availability of options.

In some cases, municipalities have practiced indirect potable reuse (either intentionally or unintentionally) by discharging treated wastewater back to surface water streams that may be used downstream as a raw water source or to environmental buffer areas that will eventually filter to and recharge aquifers used as raw water sources. Retention times in the streams, aquifers, or environmental buffer areas allow for further purification through natural processes (Rodriguez, et al. 2009). In some coastal areas, it has been common practice to discharge to oceans, breaking the potable reuse cycle as the fresh water is lost to the salt water system.

Given the aforementioned increases in population and potable water demand contrasted with threatened and diminishing supply due to drought and climatic changes, waste in the potable water cycle is undesirable and unsustainable. Net zero water programs that embrace reduction, reuse, and repurposing will likely become increasingly necessary and prevalent. Some municipalities are beginning to turn to direct potable reuse where highly treated wastewater is immediately reintroduced without the benefit of an environmental buffer (Texas Water Development Board 2016). The underlying concepts of water reuse in a net zero construct are not new, with some of the earliest examples practiced by municipalities over thirty years ago. Initial implementation was primarily limited to areas with insufficient water supply and smaller service populations; however, advancements in technology and economics underlying such systems are making net zero programs feasible for virtually any municipal system (Englehardt, et al. 2016). In addition to returning wastewater to use as a potable water source, it can also be repurposed for non-potable use (potentially with less extensive treatment), as long as the water is segregated from potable sources. There are numerous case studies where this repurposed water is conveyed in an easy to identify “purple pipe” system and is used for alternative purposes such as landscape irrigation, toilet water supply, or supply to building cooling towers. The savings in

such systems is not limited to water, as there is also potential for energy savings in the reduction of energy used in water treatment cost and conveyance over long distances.

USAF installations essentially operate like small municipalities within a protected fence line. The source of potable water and wastewater services to the USAF varies by installation. Some operate water treatment and wastewater treatment plants on site (either operated by government employees or under contract), whereas others rely on neighboring municipalities to provide both services. With regards to wastewater treatment, a 2012 study conducted for the Strategic Environmental Research and Development Program (SERDP)/Environmental Security Technology Certification Program (ESTCP) found a strong correlation between the size and location of a military installation and whether it treated wastewater onsite or offsite; geographically isolated bases and bases with large service populations tended to treat waste on site. Overall, slightly less than 40% of USAF installations were found to have onsite wastewater treatment (Barry 2012).

There are examples of USAF installations that have implemented some degree of water reuse and/or recycling programs for several years. As early as 1997, Luke AFB began maintaining a wastewater reclamation permit allowing for reuse of over 500,000 gallons per day of wastewater effluent for irrigation. During the summer months, Luke reclaimed 100% of the effluent, making it a “zero discharge” facility; during winter months of less water demand, excess was discharged to resupply a neighboring river (Pro-Act 2000). In 2005, Los Angeles AFB won a “Customer of the Year” award from the WaterReuse Association for purchasing recycled water from a local municipality. New construction projects and renovations made dual piping systems (potable vs recycled) feasible, and over 50% of installation water consumption was sourced from the recycled supply (Gillis 2006). As of 2013, Joint Base San Antonio

(JBSA)-Randolph and JBSA-Lackland also practiced similar recycled water purchases from local municipalities. Furthermore, the installations implemented water recycling programs at wash racks and captured rainwater and air conditioner condensate for irrigation (Salinas 2013). Hurlburt Field in Florida was recognized as a Department of Energy award winner in 2014 for a water reuse project that greatly expanded gray water recycling and reuse on the installation. Hurlburt added more than 40,000 feet of water reuse pipelines and a 500,000 gallon storage tank. The reuse water was directed to irrigation, aircraft/vehicle wash racks, fire training, and facility cooling towers. Excess water beyond Hurlburt's demand can be returned to the local community for reuse. Hurlburt was able to reduce potable water consumption by 13 million gallons annually (US Department of Energy 2015).

In addition to and closely related to concerns over water availability and the need for conservation and reuse is the concern over quality of available raw and recycled water. This topic poses a "double edge sword" for the USAF as both a consumer of water and a potential source of pollution to water supplies. Recent findings and news regarding perfluorinated chemicals (PFCs), specifically perfluorooctanoic acid (PFOA) and perfluorooctane sulfonate (PFOS), serve as an evolving example. PFOA and PFOS were added to the USEPA's Third Unregulated Contaminant Monitoring Rule (UCMR 3) in 2012, requiring monitoring for the contaminants during 2013-2015. The UCMR and an associated Contaminant Candidate List (CCL, <https://www.epa.gov/ccl>) from which contaminants are selected are allowed under 1996 amendments to the Safe Drinking Water Act to monitor for contaminants that are suspected of being in drinking water, but for which no current regulation exists. Following addition to the UCMR list in 2012, the USEPA issued a health advisory for PFOS and PFOA in 2016, and a non-regulatory concentration limit of 70 parts per trillion was recommended for both

compounds. PFOS and PFOA are constituents of firefighting foams used extensively in the USAF beginning in the 1950's. The chemicals were released during events such as fire training exercises, real world aircraft firefighting events, and inadvertent discharges of aircraft hangar fire control systems. Sampling on and near USAF installations indicates that the compounds migrated to some drinking water supply sources and several installations have reported levels exceeding the health advisory recommendations and are taking remedial actions, including closing wells, installing granular activated carbon filter systems, and providing bottled water (Air Force Civil Engineer Center 2017). Total tangible costs associated with sampling and mitigation and intangible costs associated with public relations are yet to be seen. PFOS and PFOA are current news, but not the first news regarding groundwater contamination. As another example, widespread groundwater contamination with trichloroethylene (TCE) has previously been reported at USAF installations, followed by many years of remediation efforts (Anderson, Anderson and Bower 2012). These and other examples arise because the USAF is a large, industrial complex with an extensive history of chemical use. Much of the issue surrounding contamination events with chemicals such as PFCs and TCE comes from a history of chemical use, handling, and disposal that has evolved along with more stringent and informed environmental policy.

As the USAF looks to the future, focus should be placed on developing best practices to stay ahead of environmental policy versus recovering from practices of the past. Regular review of the UCMR and CCL, understanding linkages the USAF has to the chemical compounds included in the UCMR and CCL, and maintaining a proactive posture will be a priority focus area. A net zero water construct with emphasis on both centralized and decentralized containment and utilization of emerging technologies for water treatment can play a significant

role in such a vision. One such technological advancement is the use of energy efficient ultraviolet (UV) light emitting diodes (LED) as a replacement for high energy consuming mercury vapor lamps in advanced oxidation processes (AOP) utilizing hydrogen peroxide (H_2O_2). Mercury lamp-based AOPs are a proven technology in water treatment, but UV LED-based treatment is now possible as evidenced by results in Chapter 2 and previous work using UV LEDs as an energy source in a UV/ H_2O_2 advanced oxidation process (Duckworth, et al. 2015) (Gallucci 2016) (Mudimbi 2015) (R. W. Scott 2015) (Stewart 2016). While LEDs require less input power, individual LEDs also provide significantly less total output power as compared to mercury lamps, and it is important to understand the suitability for implementation at full scale.

4.3. Net Zero Water System Model

This section utilizes a reference systems architecture representation with hybrid views to conceptualize a net zero water system at a hypothetical USAF installation and assess points in the system where UV LED-based treatment might be considered in conjunction with other technologies in support of specific water quality applications. All figures were produced using Enterprise Architect software (Sparx Systems, Australia). Figure 1 presents a capability taxonomy that the architecture supports. The underlying capabilities align with those capabilities required to enable the goals of the *USAF Energy Strategic Plan*. The top level capability of the architecture is delivery of a Net Zero Water System. That overarching capability is supported by three subordinate capabilities of Water Capture & Reuse, Water Repurposing, and Water Recharge. Those three capability branches are then further decomposed as can be seen in the figure.

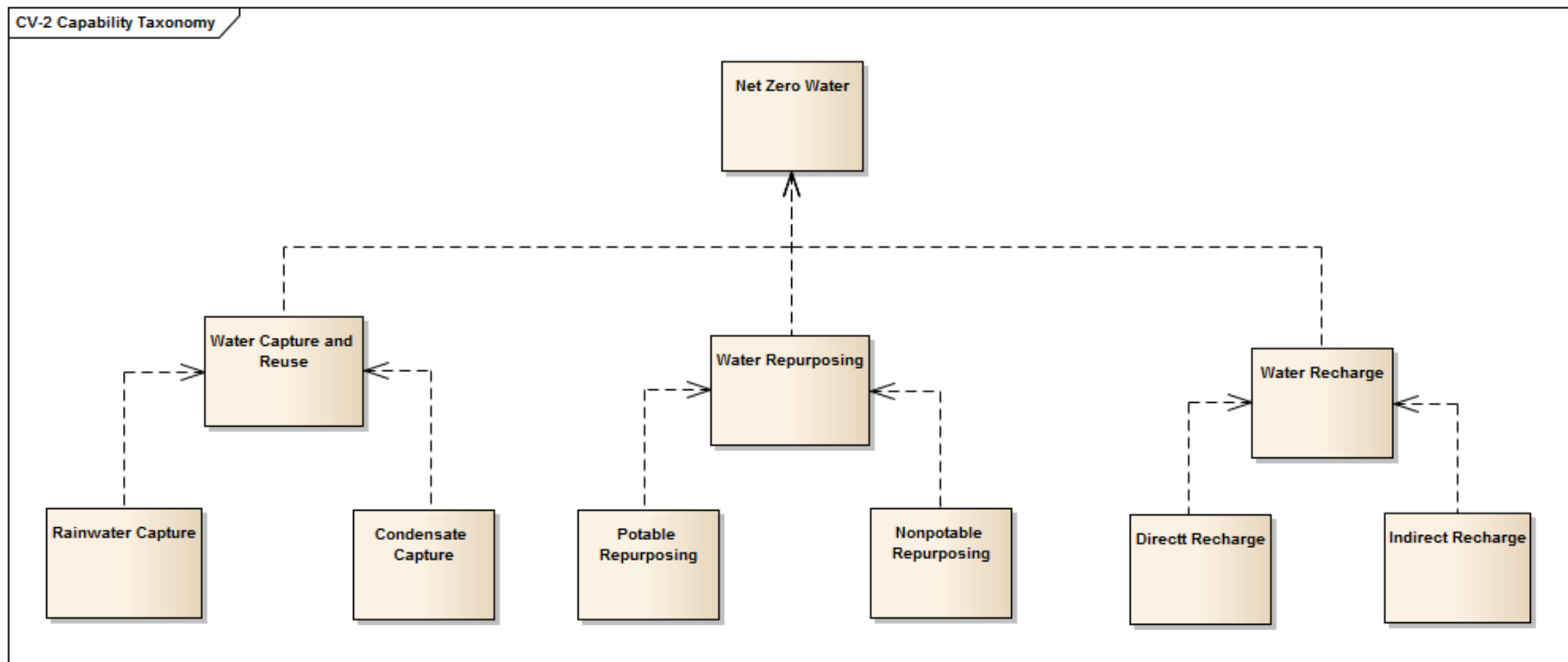


Figure 29. Capability taxonomy for a USAF installation net zero water program (figure produced in Enterprise Architect).

4.3.1. System Context and Boundaries

In order to conceptualize the full scope and potential interactions of components in a net zero water system, a hybrid services resource flow view is presented in Figure 30. The figure is designed as an all-encompassing view with implicit redundancy. Where an installation does not have access to a component of the architecture (e.g. no municipal water/wastewater treatment sources), those components and linkages would be removed. Within the figure, there are two major boundary regions defined at the installation level and the facility level. The architecture presents only one representative facility boundary, but numerous facilities would be connected to the system in practice. An understanding of these boundaries is important to the overall net zero water construct.

The installation level boundary (represented by the outer bold black box) depicts points where raw water is consumed/recharged, potable water/recycled water/wastewater services are purchased from municipal sources, and recycled water is potentially returned back to municipal sources. All these possible points of entry and exit are critical factors in calculating the total balance of water consumption. The installation boundary also depicts a transition between government and private use of water resources and serves as a reminder that containment and treatment of contaminants mitigates potential for future public exposure. The facility boundary (shown as an inner bold blue box) represents both a transition to treated water consumption and a potential transition point between centralized and decentralized water and wastewater treatment as the facility level is where water capture and reuse is most applicable. Of interest in the figure are four areas of potential water treatment where UV LED/H₂O₂ AOP technology may be applicable and merit further discussion. These areas are shaded purple and include Installation Potable Water Treatment, Facility Captured Water Treatment, Facility Recycled Water

Treatment, and Installation Wastewater Treatment. Important linkages occur between these areas of treatment that allows for a continual recycling, blending, and reuse where applicable.

All possible linkages are depicted in the figure; however, as before, those that are not applicable to a given installation or facility would be removed. As an example, the Installation Wastewater Treatment node shows up to five potential effluent linkages. The first is to the Municipal Recycled Water Supply node where the USAF may supply highly treated effluent water to the local municipality for introduction directly to its own recycled water supply. The second linkage shows return to an Environmental Recharge Buffer node, which subsequently recharges the same surface water or groundwater supply source from which the raw water originated. The third linkage shows return of treated wastewater to the start of the Installation Potable Water Treatment node for additional treatment before it is introduced into potable distribution. Similarly, the fourth linkage shows direct introduction of highly treated wastewater effluent to the Potable Water Distribution node without further treatment. Finally, the fifth linkage shows introduction of the treated effluent to the Recycled Water Distribution node, a segregated recycled water system for non-potable use. Considerations such as federal and state regulations on viable reuse options, USAF technical orders guiding use of water in industrial processes, and other unique requirements of an individual installation must be reviewed on a case-by-case basis to determine which nodes and linkages are relevant.

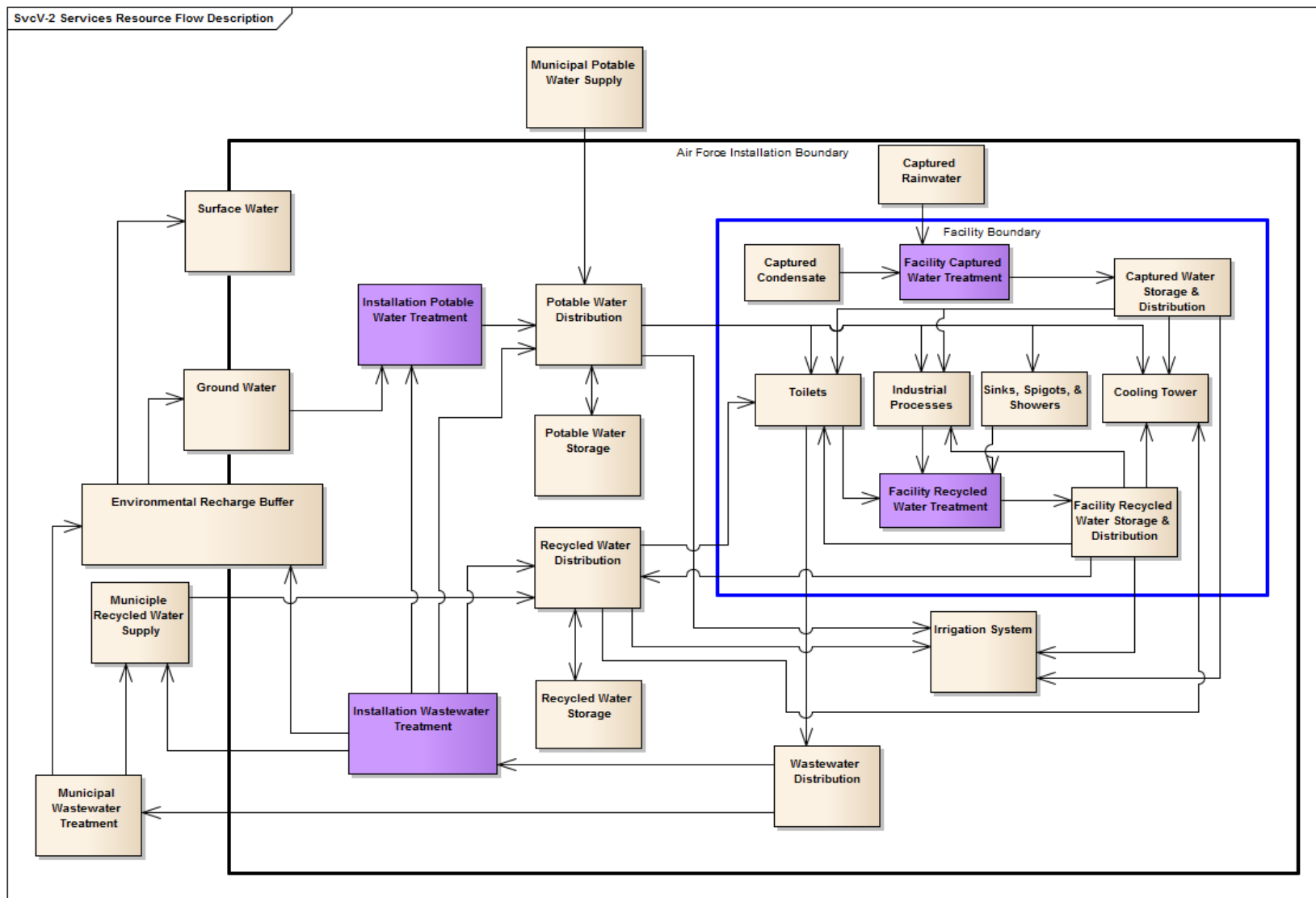


Figure 30. Hybrid systems view of a net zero water program at a USAF installation with boundaries at the installation and facility level (figure produced in Enterprise Architect).

4.3.2. Treatment Nodes

The four aforementioned treatment nodes shaded purple in Figure 30 merit further discussion with regard to potential for UV LED/H₂O₂ AOP technology integration. Figure 31 decomposes each of the nodes into activity diagrams that are representative of possible treatment trains. Throughout Figure 30 and Figure 31, technologies for the online monitoring of conditions such as flow, volume, and basic water quality parameters (e.g. pH, chlorine, temperature, turbidity, conductivity, etc) should be considered and will not be discussed further.

Technologies for measuring such parameters exist and are commercially available, and additional smart sensors for remote monitoring have shown promise as an emerging technology (Cloete et al., 2016). These technologies can regularly inform a central function of the overall health and status of the water system and can also assist in automatically balancing flow between potable, recycled, and reuse water sources based on the current status and demand for each.

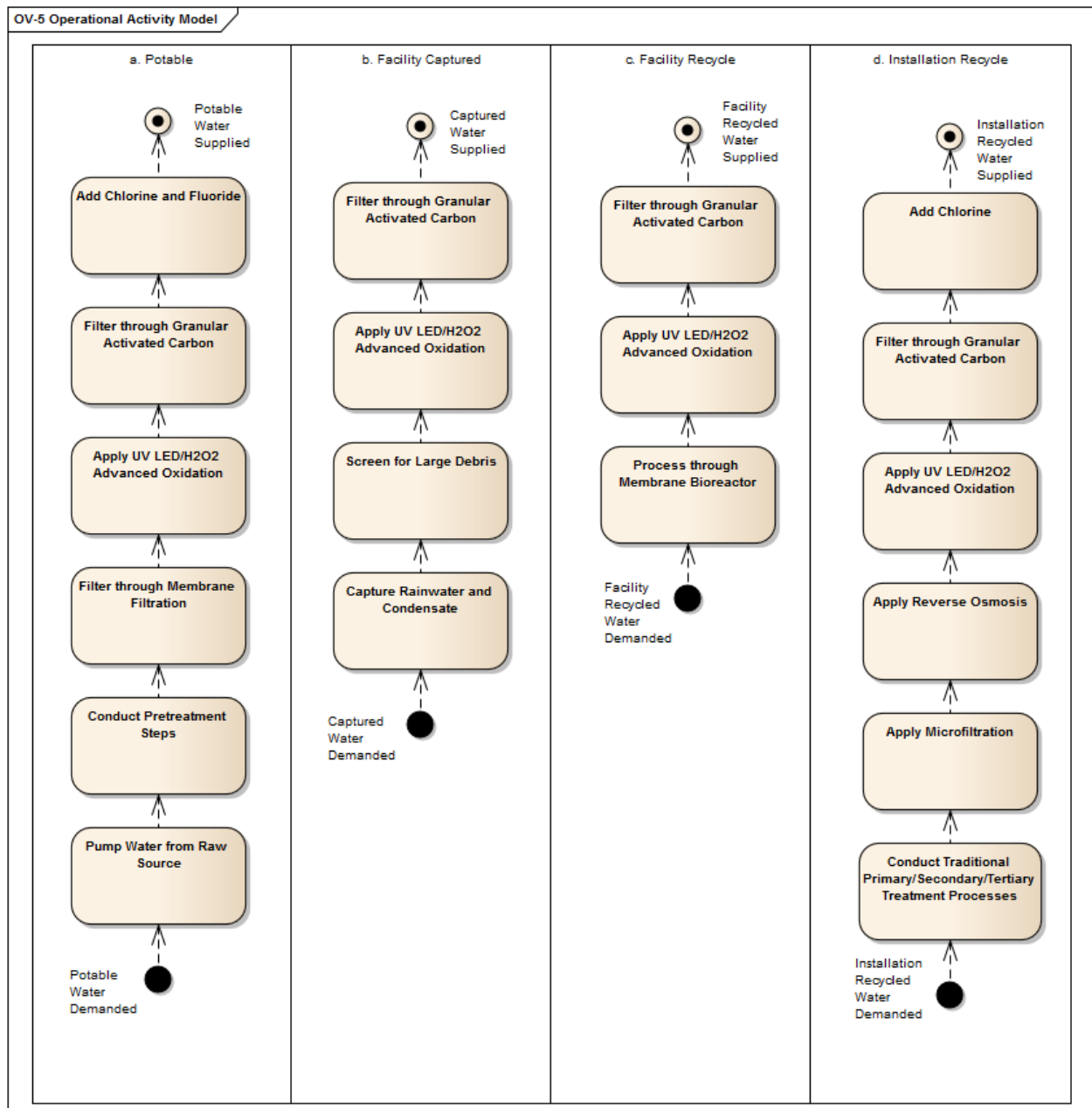


Figure 31. Operational activity lanes for four areas of potential UV LED/H₂O₂ advanced oxidation treatment within a net zero water program (figure produced in Enterprise Architect).

4.3.2.1. Installation Potable Water Treatment

Installations that treat raw water on site for introduction to the potable water distribution system will typically follow one of two treatment schemes, centralized or decentralized. In centralized treatment, raw water sources (either ground or surface) converge at a single water treatment plant that manages all treatment steps. In decentralized treatment, individual wells will pull from a ground water source at multiple locations, and water treatment is then applied at each well individually. As examples, Whiteman AFB in Missouri utilizes a central treatment plant operation, whereas Wright-Patterson AFB in Ohio and McChord Field in Washington treat directly at individual wells. Figure 31a depicts an activity model of a straightforward potable water treatment train using UV LED/H₂O₂ in conjunction with other technologies. The Conduct Pretreatment step refers to traditional coagulation, flocculation, softening, etc., dependent on the influent water source and quality. In the example train, membrane filtration is utilized immediately before UV LED/H₂O₂ advanced oxidation and could be used in place of all pretreatment steps if the source water is of sufficient initial quality. Following the UV LED/H₂O₂ step, granular activated carbon (GAC) filtration is conducted, followed by chlorination and fluoridation.

4.3.2.2. Facility Captured Water Treatment

Captured water sources within the span of control of an individual facility account for water obtained from rainwater harvesting systems and collection of climate control system condensate. These captured water sources should be relatively clean with some exceptions. Early capture of rainwater from roof surfaces and other surfaces (asphalt, concrete, etc.) may contain bird feces and some other biological contaminants. Additionally, if rainwater is

collected from parking lot runoff, chemical contaminants from sources such as leaking petroleum products or antifreeze could be present in trace amounts. Figure 31b shows an activity model for a potential captured water treatment train. The initial step includes coarse screening to catch particulate matter, leaves, and any other debris. The next step is UV LED/H₂O₂ advanced oxidation, followed by GAC filtration. There is no chlorination or fluoridation included in this particular treatment train, as there is no intent to introduce the treated water to the potable water system in a decentralized manner.

4.3.2.3. Facility Recycled Water Treatment

Facility recycled water treatment refers to the capturing of a portion (up to 100%) of spent water that would traditionally be discharged to the sewer system, and instead processing it through a facility-level treatment train to repurpose the water for additional use within the facility's span of control. Just as with captured water treatment, the intent is to repurpose the water for non-potable uses only. Such reuse purposes include toilet water supply, industrial process water, cooling tower water, and irrigation. The particular treatment train shown in Figure 31c includes a membrane bioreactor as a form of decentralized wastewater (including black water) treatment. The membrane bioreactor is followed by UV LED/H₂O₂ advanced oxidation and GAC filtration, sequentially.

4.3.2.4. Installation Wastewater Treatment

The installation wastewater treatment activities are depicted in Figure 31d. The node where these activities occur is responsible for processing all graywater, black water, and industrial wastewater that is not recycled at the facility level. Given this blending of waste

streams in larger volumes from multiple facilities, there is a higher propensity for pathogens and numerous chemical contaminants to be present in the influent water. The treatment train begins with traditional primary, secondary, and tertiary treatment steps. These steps would typically include processes such as sedimentation, activated sludge, sand filtration and nutrient removal. The next steps are microfiltration and reverse osmosis treatment to remove ions and larger particles prior to entry to the UV LED/H₂O₂ AOP. Final steps include GAC filtration and chlorination before potential return to either the installation recycled water supply or potable water supply.

4.4. Discussion

With regard to the treatment nodes in Section 4.3.2., treatment trains (unit treatment processes linked in sequence) are often necessary and, in some cases, can provide secondary benefits. Such is the case with GAC, which is prevalent throughout all nodes in Figure 31. Not only can GAC capture and remove some recalcitrant chemicals which are resistant to the UV LED/H₂O₂ AOP, such as PFCs, it can also serve as an effective quenching agent to remove H₂O₂ from the treated water before it is recycled or repurposed. Other technologies used in removing peroxide include those that use free chlorine or catalase as quenching agents. The amount of peroxide to be removed and rate of removal will vary, dependent upon the concentration of peroxide initially supplied, other constituents in the water matrix that may potentially consume the peroxide, and the overall flow of the treatment system.

As shown in this study and prior published studies, the optimal dose of H₂O₂ required in the AOP will vary based on the identity of compounds in the matrix and the concentration of each. The cost of H₂O₂ in the treatment process has also been cited as prohibitive and

disadvantageous in some cases. There are, however, some emerging technologies seeking to produce H_2O_2 by novel means that could reduce supply costs significantly. One such technology utilizes a three-chamber electrochemical reactor where oxygen flows into an initial chamber, passes into a second chamber where a catalyst reduces the oxygen gas to H_2O_2 , and in the third chamber another catalyst helps convert water back to oxygen gas to start the cycle all over again. The system has proven successful at bench scale and only requires around 1.6 volts, making it ideal for decentralized use and capable of using alternative power supplies (Chen et al., 2017). Other emerging technologies are being researched to produce H_2O_2 from microbial fuel cells paired with primary sludge processes (Ki et al., 2017). Both technologies have been proven with small scale, low volume throughput. Scale up to support volumes and concentrations of H_2O_2 production necessary to support real world water treatment application is being developed.

The feasibility of real world water treatment application is tightly linked to the volume and rate of water demand. In turn, the feasible application of UV LED/ H_2O_2 AOP must be placed in the context of the installation and facility level water demand. As previously noted, Wright-Patterson AFB (WPAFB) provides decentralized treatment at each of 10 individual water wells. The 2016 water quality report for WPAFB notes that approximately 1 billion gallons of water are supplied annually. For illustrative purposes, if we assume steady production 24 hours per day and 7 days per week equally distributed between all 10 wells, a constant 192.5 gallons per minute (gpm) is required at each well. If this level of production were instead centralized at a single treatment facility, an illustrative rate of around 2000 gpm would be expected (not accounting for water spent in the treatment process). Comparatively, the apparent first order degradation rate constants reported for representative contaminants measured in Chapter 2 were achieved at a flow of 2 mL/min with 2 LEDs. The number of LEDS required to treat

installation-level water or wastewater demand would be prohibitive with currently available technology. Though UV LEDs offer flexible placement alternatives, there could be negatives associated with current costs of individual UV LEDs and with lack of existing UV LED arrays or UV LEDs with more diodes that are closer to matching the optical output power of traditional mercury bulbs. Furthermore, individual UV LEDs represent individual points of potential failure; therefore, wiring more individual LEDs into a system to achieve higher output power, simultaneously increases complexity in diagnosing performance issues with an individual LED. As manufacturing processes improve, costs drop, and prepackaged arrays of UV LEDs with higher output power arrive, this issue may be mitigated. However, in the near term, it is more feasible that UV LED/H₂O₂ AOP technology be considered for implementation in reuse and recycling programs at the facility level where total water volume and flow are much lower.

Figure 32 depicts a UV LED/H₂O₂ AOP reactor at the facility level. Two volumetric flow rates, Q1 and Q2, are represented in the figure. Q1 is the flow of potable water supply initially entering the facility. Q2 is the flow of recycled water to be treated via the UV LED/H₂O₂ AOP and reused within the facility. Q2 is an adjustable rate where the ratio of Q2/Q1 can range from 0-1, meaning 0% to 100% recycle. Though basic in form, this figure can provide meaningful insight into applicability of UV LEDs in real world reuse scenarios. Metcalf and Eddy's *Wastewater Engineering: Treatment and Reuse* provides a range of per capita estimates for wastewater production and chemical oxygen demand (COD) loading rates. Wastewater flowrates for industrial buildings ranges from 15-35 gallons per employee per day. Estimates for COD range from 110-295 grams per person per day. To further illustrate example pairing with Figure 32 recycle scenarios, we will assume a UV LED/H₂O₂ AOP reactor of 55 gallon volume, wastewater flowrate of 30 gal/person/day and an average COD loading of 200 g/person/day. If

we further assume that the system in Figure 32 is operating at steady state, then we must achieve an apparent first order degradation rate constant, k_s , that is related to the residence time in the reactor as $k_s = 1/\tau$. We can use this relationship to suggest the necessary apparent first order degradation rate constants that are required to treat the wastewater at varying facility sizes and recycle ratios. An example of this relationship is provided in the plot in Figure 33. The figure provides k_s curves for facilities ranging from 500 – 2000 personnel and recycle ratios from 0.1-0.9. Inherent in this plot is an assumption that the COD loading is approximately equal to total organic carbon (TOC) loading, meaning approximately all of the wastewater being treated is primarily comprised of organic compounds. Of importance in this figure is the observation that the required apparent first order degradation rate constants overlap the apparent first order degradation rate constants measured in Chapter 2. At 200 mA, measured apparent first order degradation rate constants ranged from 0.084 – 1.078 min⁻¹. As an example, we can look at a facility with 500 personnel with a desired recycle ratio of 0.9, and the required k_s is 0.170 min⁻¹. Comparing this to the dyes and achromatic chemicals, we note that the k_s values for TBA, DNT, and EB are below this cutoff value and the desired level of degradation could not be achieved without moving to a larger reactor or otherwise optimizing the reactor, although optimizing the reactor is possible. Figure 33 also addresses hypothesis #3 from Chapter 1 in that the required apparent first order degradation rate constant is lower for smaller facilities, indicating that smaller facilities offer the most promising opportunity for UV LED/H₂O₂ AOP application. Though this example pertains to facilities with large numbers of personnel, similar relationships can be made with industrial wastewater from industrial facility processes involving chemicals without respect to personnel. Instead of per capita COD or TOC loading rates, real values of

minimum, maximum, and average TOC loading and volumetric flow from industrial process wastewater sampling can be used to establish similar relationships.

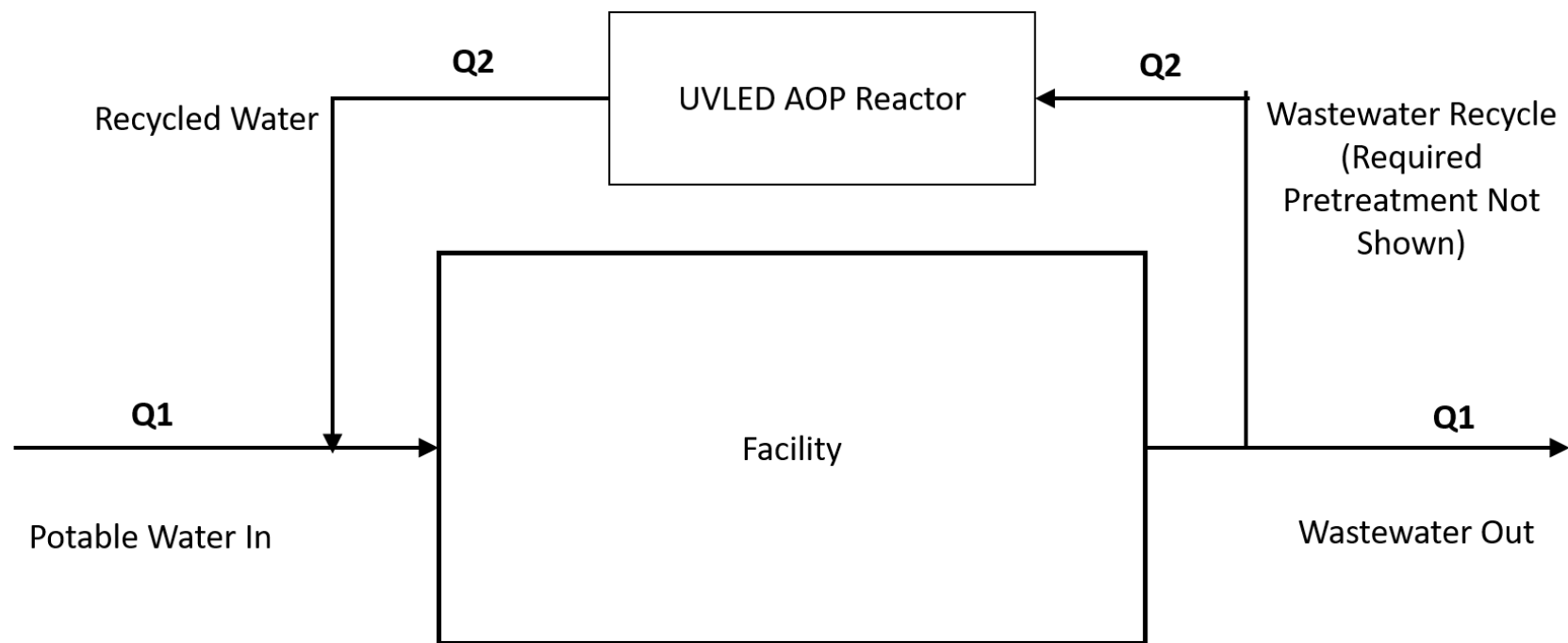


Figure 32. Mass balance relationships between facility influent, recycle, and effluent flows; Q_2/Q_1 represents a recycle ratio in water reuse scenarios.

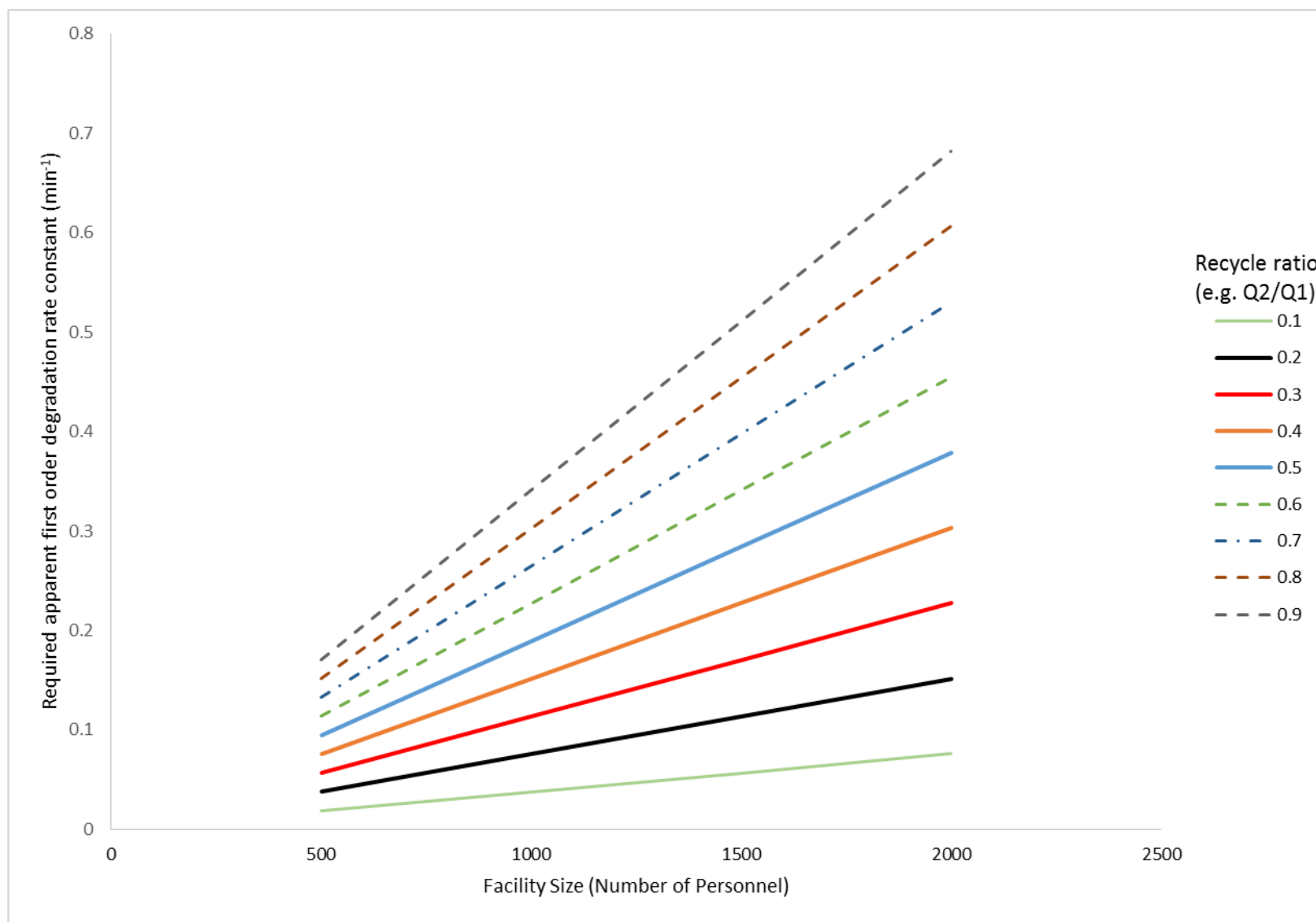


Figure 33. The effect of facility size and recycle ratio on the required first order rate constant.

The facility sizes captured in Figure 33 are relatively large, and the majority of facilities on a typical installation will fall somewhere between 0 to 500 personnel. Larger facilities of the type captured in the figure would typically consist of non-industrial functions such as headquarters facilities, dormitories, lodging facilities, education and training functions, and other organizations performing primarily office tasks. Food dyes such as those used in the study in Chapter 2 are expected to be prevalent in waste streams of these types (and to a lesser extent in industrial facilities). Actions such as pouring a colored beverage down a sink drain or rinsing food containers with traces of food dye remaining are common, expected examples. The dyes tested in this study are representative of the full range of apparent first order degradation rate constants that would be expected from this group of compounds, as they are representative of the most prevalent dyes used in United States foodstuffs.

Medical facilities on an installation vary greatly in size and scope from small clinics with no inpatient care to large medical centers with a full range of advanced care and inpatient beds. Medical waste streams will certainly include the aforementioned dyes, but will also likely include higher concentrations of prescription and non-prescription pharmaceuticals and compounds such as antibacterial hand sanitizing agents and isopropyl alcohol. Though care is taken to properly dispose of medications, it is inevitable that a portion will eventually reside in wastewater through lack of metabolism and eventual excretion by the body and the potential for direct flushing or rinsing of medications. Numerous studies have been conducted on the effectiveness of advanced oxidation processes at removing pharmaceutical compounds from wastewater. One such study investigated the removal of nine pharmaceutical compounds, including ibuprofen, carbamazepine and diazepam, from wastewater via ozonation and AOP. Results indicated that the selected compounds reacted with hydroxyl radicals at a rate 2-3 times

faster than did MTBE (Huber, et al. 2003). This comparison indicates that the UV LED/H₂O₂ AOP should be highly effective against a range of pharmaceuticals.

TBA and MTBE were selected in Chapter 2 as relevant and representative test compounds from historic fuel operations and because both were expected to exhibit some level of hydroxyl radical chain termination and comparatively lower degradation rates. Though most fuel contaminants would be anticipated to occur from aquifer infiltration or surface water discharges following accidental spills, there is opportunity for low levels of these contaminants to enter wastewater flow through rinsing of storage vessels and transfer devices and cleaning of residual amounts from personnel. Larger quantities may also be intentionally contained in industrial wastewater catchment systems and require subsequent treatment or disposal. Buxton et al reported a hydroxyl radical rate constant of $6.0 \times 10^8 \text{ M}^{-1}\text{s}^{-1}$ for TBA (Buxton, et al. 1988). Other constituents that may show up to some extent in USAF fuel system include ethanol, methanol, and 2-propanol. Representative hydroxyl radical rate constants for those compounds are 1.2×10^9 , 7.5×10^8 , and $1.2 \times 10^9 \text{ M}^{-1}\text{s}^{-1}$, respectively (Buxton, et al. 1988). The values indicate that methanol would be expected to degrade at only a slightly faster rate than TBA in the UV LED/H₂O₂ AOP, whereas ethanol and 2-propanol would degrade at a rate twice as fast.

MAL is an acetylcholinesterase inhibitor and shares structural similarities with other organophosphate pesticides. It was used as a representative surrogate for USAF pesticide processes and may be found in storm water collection systems. Because MAL is also used as a treatment for head lice, it would be found in wastewater associated with hospitals, family housing, and dormitories. A study on the removal of several pesticides and herbicides from water matrices investigated the viability of the UV/H₂O₂ treatment process as an option. Compounds tested included atrazine, isoproturon, diuron, alachlor, pentachlorophenol, and chlorfenvinphos

hydroxyl radical rate constants ranged from $0.8\text{--}18.5 \times 10^9 \text{ M}^{-1}\text{s}^{-1}$. The lowest degradation rate is associated with isoproturon and it would be expected to degrade at a relatively slow rate similar to TBA. Degradation rates of the other compounds were 6 – 23 times faster. (Sanches, et al. 2010)

DNT is representative of explosives byproducts and munitions propellants that may be found at ammunition manufacturing facilities, explosives ordinance disposal facilities, security forces training facilities, and special operations facilities. DNT exists as six isomers of which 2,4-DNT (utilized in this study) and 2,6-DNT are categorized as priority pollutants by the USEPA (USEPA, 2014). In kinetics studies, DNT was consistently on track with TBA as one of the two compounds most resistant to the UV LED/H₂O₂ AOP. A representative hydroxyl radical rate constant for 2,6-DNT from the literature is $7.5 \times 10^8 \text{ M}^{-1}\text{s}^{-1}$, putting it in close proximity to the slower observed degradation of 2,4-DNT (Beltran, et al. 1998). Another representative compound used as a secondary explosive in the manufacture of US military munitions is hexahydro-1,3,5-trinitro-1,3,5-triazine, better known as RDX (USEPA, 2014). Rates of hydroxyl radical degradation of RDX are comparatively more than twice as fast as DNT at $1.6 \times 10^9 \text{ M}^{-1}\text{s}^{-1}$, indicating that it should be more susceptible to the UV LED/H₂O₂ AOP.

4.5. Conclusions

Water challenges for the USAF in the near term include water scarcity due to drought conditions and population demands as well as water quality related to both internal and external contamination events and preparation for future emerging contaminants. Net zero water systems designed with a goal to capture, reuse, and repurpose water are imperative to help mitigate those challenges. This study has presented a reference systems architecture view with a focus on delineating installation and facility level points of application where UV LED/H₂O₂ AOP

technologies may be inserted alone or in conjunction with other technologies to achieve specific water treatment goals. Treatment trains were presented as an optimal solution to both facilitate removal of recalcitrant compounds and quench excess hydrogen peroxide remaining in the AOP effluent. Facility-level treatment for recycling of wastewater was found to be the most feasible application for the near term as the decentralized flow rates and volumes of water treated are comparatively favorable to the current state of UV LED technology. An approach was also presented to enable comparison of the required apparent first order degradation rate constant to facility size and desired recycle ratio. Required degradation rates for a 55 gallon UV LED/H₂O₂ AOP reactor at 0.1-0.9 recycle ratios show desirable overlap with the apparent first order degradation rate constants reported in Chapter 2. At 200 mA, measured apparent first order degradation rate constants ranged from 0.084 – 1.078 min⁻¹. At a desired recycle ratio of 0.9, the required k_s is 0.170 min⁻¹ for a facility with 500 personnel. From measured kinetic experiment data, 8 out of 11 dye and achromatic chemicals exceed that required degradation rate. The remaining three, TBA, DNT, and EB, would require a larger reactor volume or other optimizations. This approach can be used with any combination of facility size and effluent parameters. Furthermore, if paired with a predictive tool such as the QSPR model presented in Chapter 2, the design criteria can extend to future contaminants as they emerge and impact the USAF.

V. Conclusions

5.1 Discussion

The first objective in this work sought to determine the effect of key UV LED/H₂O₂ AOP reactor operating parameters on the degradation kinetics of soluble organic compounds. To accomplish this objective, six dyes and five achromatic chemicals were reacted in the same well mixed, flow through reactor platform under the same reaction conditions. This research is the first UV LED-based AOP study to identify linear power-kinetics relationships, determine optimum molar peroxide ratios, and reveal the complex role of molar absorptivity in shaping the speed and extent of treatment. The effect of LED output power on the chemical degradation profiles was investigated and a linear relationship was observed between the input drive current, optical output power, and the apparent first order degradation rate constant. When the drive current was systematically varied, the apparent first order degradation rate constants depended on the identity of the test compound and the drive current, and were between 0.003 min⁻¹ - 1.078 min⁻¹. A relationship was also observed between the drive current and the degradation extent with an exponential tapering at higher drive current levels. The effect of peroxide stoichiometry on the chemical degradation profiles was also investigated. When the molar peroxide ratio was varied, the kinetic profiles showed evidence of peroxide-limited conditions when too little peroxide was present or radical-scavenged phenomena when too great a concentration of peroxide was present. The optimum molar peroxide ratios were at or near 500 mole H₂O₂/mole test compound for the dyes, with the exception of EB. The optimal molar peroxide ratios tested for EB were in the range of 2500-3000 mole H₂O₂/mole EB, likely because of its relatively high molar absorbance ratio. Accounting for molar absorptivity also helped to explain the shape of the removal profiles associated with EB and tartrazine and the regression coefficients associated

with the model fitting of experimental data. In contrast, the optimal molar peroxide ratios were at or near 100 mole H_2O_2 /mole test compound for achromatic chemicals with the lowest molar absorptivity.

The second objective of this research sought to evaluate QSPRs for the advanced oxidation of soluble organic compounds with UV LED by using molecular descriptors relevant to the 11 compounds tested in the first objective to build and assess predictive models. Molecular descriptors used in existing mercury lamp AOP QSPRs from the literature were assessed for their fit to the LED domain and the 11 test compounds. This research represents the first known use of QSPR evaluation for UV LED-based reactors. Linear fit of existing QSPR model descriptors was relatively poor. Resultant R^2 values for the combined data set of dyes and achromatic chemicals were 0.024, 0.116, 0.157, 0.312, 0.481, and 0.864 for the descriptors used in the six models from the literature. When breaking the larger data set into smaller subsets of dyes and achromatic chemicals, improvement was seen with R^2 values between 0.033 – 0.996, but most models and individual parameters failed tests of statistical significance. Statistical robustness was also lost in some cases, due to smaller data set sizes compared to the numbers of predictors included in models. A new model was constructed for predicting the dye and achromatic chemical degradation rates utilizing ZPE combined with molar absorptivity. Overall, ZPE and molar absorptivity at 265 nm produces a QSPR model with $R^2 = 0.951$ with statistical significance in the model and all parameters at a 95% confidence interval. This research represents the first known use of ZPE and molar absorptivity in the construction of a QSPR model in the UV/ H_2O_2 AOP domain.

The final objective was to use systems engineering principles to propose appropriate applications of UV LED-based reactors in support of specific water quality applications. Water

scarcity and contamination were identified as near term challenges to which the USAF must be prepared. Policies and technologies that support a “Net Zero” water use posture will become increasingly important. The USAF *Energy Strategic Plan* identifies water as a critical asset and seeks potable water demand reduction by capturing and reusing, repurposing, or recharging an amount of water that is greater than or equal to the volume of water the installation uses. This study presented a systems architecture view to describe a net zero water program at a hypothetical USAF installation. Four areas within the system boundary were identified where advanced oxidation processes utilizing ultraviolet light emitting diodes and hydrogen peroxide might be paired with other technologies in order to treat water. Treatment operations at the installation level and the facility level were delineated and facility-level treatment for recycling of wastewater was found to be the most feasible application for the near term as the decentralized flow rates and volumes of water treated are comparatively favorable to the current state of UVLED technology. An approach was also presented to enable comparison of the required apparent first order degradation rate constant to facility size and desired recycle ratio. Required degradation rates for a 55 gallon UVLED/H₂O₂ AOP reactor at 0.1-0.9 recycle ratios show desirable overlap with the apparent first order degradation rate constants measured for the 6 dye and 5 achromatic chemical compounds at 200 mA (0.084 – 1.078 min⁻¹). At a recycle ratio of 0.9, the comparable required k_s is 0.170 min⁻¹. From the measured experimental data, 8 out of 11 dye and achromatic chemicals exceed that required degradation rate and the remaining 3 would require longer retention times or other optimizations. Comparisons with test compounds were also made to other compounds likely to present at a sampling of representative USAF facilities.

5.2 Future Work

- Scale up reactor volume and optimize geometry. Research to date at AFIT has focused on two basic cylindrical reactor geometries and modifying operational parameters within those reactors. Future work should seek to explore larger reactor volumes and more optimal reactor geometries that enhance UV distribution.
- Utilize higher power LEDs and/or LED arrays. Studies to date have solely utilized two LED models from one manufacturer. An updated sourcing study should be done to ascertain the full scope of currently available models and the available output wavelengths and powers. Higher power models should be investigated in conjunction with updated reactor designs and considered for installation. Short of newer LED models, creative arrays of LED placement should be considered to optimize photon distribution throughout the reactor geometry.
- Investigate peroxide production technology. A more complete review of the literature should be conducted on the current state of H₂O₂ production methods. Opportunities for partnering with institutions on linking the technology with the UV LED reactor should be explored.
- Further investigate the degradation phenomena associated with EB through additional experimental design objectives. EB elicited novel degradation kinetics and the scope and timeline associated with this research did not allow for full analysis under all conditions. There is likely much more data that can continue to

tell a story based on unique EB data but also applicable to other compounds that are subject to photodegradation and hydroxyl radical oxidation.

- Further explore ZPE. ZPE emerged as a statistically significant factor in predicting the degradation rates associated with the test compounds utilized in this study. ZPE should continue to be tested against additional compounds and compounds from other chemical classes, as well as with published data developed for other UV light sources.
- Expand QSPR models to include prediction of optimal peroxide dosing based on the molecular descriptors of a compound.
- Conduct bench-scale studies on mixtures of chemical compounds to assess impact on optimal molar peroxide ratios.
- Utilize technologies to measure peroxide and hydroxyl radical concentration changes in time. Microsensors hold the promise of allowing observation of phenomena occurring inside of a reactor without disturbing the reaction. Sensors capable of providing real time measurement of H_2O_2 and hydroxyl radical concentrations within a reactor could provide useful information regarding the underlying kinetics.
- Utilize treatment trains for conditioning the water matrix and quenching peroxide when needed. With regards to the systems application, understand when peroxide quenching is needed, and explore options for peroxide quenching including GAC and catalase matrices. With regards to GAC, assess the impact that H_2O_2 has on the ability of GAC to remove other recalcitrant chemicals.

- Utilize competition kinetics to measure hydroxyl radical rate constants. Future UV LED reactor experiments should consider some type of competition kinetics measurements in order to allow current experiments to be compared directly to published hydroxyl radical rate constants.

VI. Appendix A

Supplementary figures

Table A1. Summary of apparent degradation rate constants, k_s (min^{-1}), for all drive currents.

	20mA	40mA	80mA	120mA	160mA	200mA
AR	0.033	0.064	0.308	0.483	0.635	0.785
BB	0.028	0.049	0.156	0.256	0.342	0.476
TT	0.011	0.025	0.119	0.220	0.310	0.438
EB	0.003	0.006	0.029	0.103	0.143	0.255
SY	0.027	0.056	0.242	0.397	0.560	0.716
FG	0.022	0.041	0.131	0.217	0.284	0.393
BPA	0.091	0.165	0.474	0.687	0.860	0.964
DNT	0.023	0.044	0.073	0.110	0.134	0.149
MAL	0.114	0.167	0.522	0.604	0.950	1.078
MTBE	0.030	0.054	0.166	0.224	0.325	0.402
TBA	0.013	0.032	0.065	0.111	0.141	0.167

Table A2. Summary of degradation extent (% removal) for all drive currents.

	20mA	40mA	80mA	120mA	160mA	200mA
AR	37.3	55.2	89.6	94.6	96.5	97.8
BB	32.0	45.7	74.5	84.0	88.4	93.2
TT	17.0	31.9	73.7	86.6	91.5	95.4
EB	4.5	9.6	40.9	96.1	97.0	97.1
SY	32.7	50.9	85.5	92.4	96.1	97.1
FG	27.7	41.7	70.7	81.7	86.6	91.2
BPA	59.9	75.0	93.4	96.3	97.6	98.4
DNT	24.3	36.3	55.4	65.9	72.7	74.8
MAL	61.9	73.8	95.2	92.1	95.8	97.9
MTBE	31.1	50.0	74.6	78.8	87.4	89.3
TBA	17.8	37.8	56.2	69.2	78.0	78.0

Table A3. Absorbance and molar extinction coefficient comparisons at 265 nm wavelength.

Chemical	Absorbance at 265 nm	Molar Extinction Coefficient ($M^{-1}cm^{-1}$)	Absorptivity Ratio Relative to 500:1 H_2O_2
100:1 Peroxide	.011	1070	N/A
500:1 Peroxide	.063	6310	N/A
BB	.074	7350	1.16
FG	.074	7400	1.17
TT	.247	24700	3.91
SY	.142	14200	2.25
AR	.131	13100	2.07
EB	.344	34400	5.45
BPA	.045	4450	0.70
TBA	.002	180	0.03
MAL	.028	2830	0.45
DNT	.106	10550	1.67
MTBE	.002	210	0.03

Table A4. Comparison of deviation of model fit (R^2) with molar absorptivity

	20 mA	40 mA	80 mA	120 mA	160 mA	200 mA	Abs at 265 nm
AR	1	0.99	0.92	0.9	0.9	0.91	0.158
BB	1	1	1	0.99	0.97	0.95	0.1
EB	0.99	1	0.9	0.47	0.48	0.6	0.371
FG	1	1	1	0.99	0.97	0.95	0.101
SY	1	1	0.94	0.91	0.89	0.9	0.169
TT	1	0.99	0.93	0.88	0.86	0.85	0.274

Table A5. Parameters and tests of statistical significance for models built with molecular descriptors of existing QSPR models from the literature.

Model	Data Set	Rsquare	Rsquare Adj	RMSE	F Ratio	Prob > F	Parameter	Parameter Estimate	Prob > t
<i>Wang et al., 2009</i>	Full Set (n=11)	0.157	-0.204	0.345	0.435	0.7351	Intercept	1.4985277	0.3779
							HOMO	0.120925	0.4981
							MSA	0.0009508	0.5066
							DM	-0.023057	0.3424
<i>Wang et al., 2009</i>	Dyes (n=6)	0.801	0.504	0.142	2.69	0.2825	Intercept	-4.029688	0.1607
							HOMO	-0.596527	0.1218
							MSA	-0.001318	0.1994
							DM	0.0351431	0.1734
<i>Wang et al., 2009</i>	Achromatic (n=5)	0.983	0.933	0.114	19.58	0.1643	Intercept	22.060342	0.3894
							HOMO	2.2074904	0.3831
							MSA	-0.020181	0.4658
							DM	0.5241355	0.4163
<i>Jin et al., 2015</i>	Full Set (n=11)	0.481	-0.297	0.358	0.619	0.715	Intercept	6.2253693	0.315
							HBA	0.285091	0.3606
							BV	-1.433525	0.7217
							DB	-0.247911	0.4398
							MASN	-5.817407	0.2934
							MAL2m	-0.565174	0.6373
							CH2RX	-0.076636	0.6321
<i>Tang et al., 2004</i>	Full Set (n=11)	0.024	-0.084	0.327	0.2215	0.6491	Intercept	0.54867	0.0006
							LUMO	-0.023898	0.6491
<i>Tang et al., 2004</i>	Dyes (n=6)	0.393	0.241	0.175	2.588	0.183	Intercept	0.4636993	0.0039
							LUMO	-0.148431	0.183
<i>Tang et al., 2004</i>	Achromatic (n=5)	0.033	-0.29	0.501	0.101	0.7715	Intercept	0.6263486	0.1484
							LUMO	-0.034497	0.7715
<i>Kusic et al., 2009</i>	Full Set (n=11)	0.312	-0.147	0.337	0.679	0.6313	Intercept	5.5068128	0.1342
							HOMO	0.4620056	0.1613
							AL7wP	-0.001947	0.3283
							GACL2wP	-0.760255	0.4659
							PC8	-0.009211	0.2437
<i>Kusic et al., 2009</i>	Omit MAL and AR (n=9)	0.985	0.971	0.045	67.5	0.0006	Intercept	7.3060112	<.0001
							HOMO	0.6488038	<.0001
							AL7wP	-0.002917	0.0003
							GACL2wP	-0.996798	0.0016
							PC8	-0.01186	0.0003
<i>Kusic et al., 2009</i>	Dyes (n=6)	0.992	0.961	0.04	32.05	0.1316	Intercept	2.7587428	0.2193
							HOMO	0.3297615	0.2006
							AL7wP	-0.004671	0.0779
							GACL2wP	2.5296858	0.0888
							PC8	0.0013733	0.5318
<i>Suhakaran and Amy, 2012</i>	Full Set (n=11)	0.864	0.728	0.164	6.3625	0.0317	Intercept	7.0584708	0.0024
							EA	-0.57937	0.0101
							HOMO-LUMO	0.6832793	0.0037
							Halogen	-0.09306	0.1246
							Ring Atoms	0.063115	0.006
							OtoC	0.0192175	0.9749
<i>Sudhakaran and Amy, 2013</i>	Full Set (n=11)	0.116	-0.263	0.353	0.3065	0.8202	Intercept	1.7360915	0.2755
							DBE	-0.033767	0.4552
							EA	0.0586533	0.4949
							IP	-0.117716	0.4759
<i>Sudhakaran and Amy, 2013</i>	Dyes (n=6)	0.568	-0.081	0.209	0.8753	0.5723	Intercept	-0.769738	0.6858
							DBE	-0.01624	0.6962
							EA	0.1155415	0.4495
							IP	0.1923857	0.4894
<i>Sudhakaran and Amy, 2013</i>	Achromatic (n=5)	0.996	0.983	0.058	76.94	0.0836	Intercept	0.6893163	0.4127
							DBE	0.6937853	0.0665
							EA	-0.389132	0.0785
							IP	-0.23356	0.1143

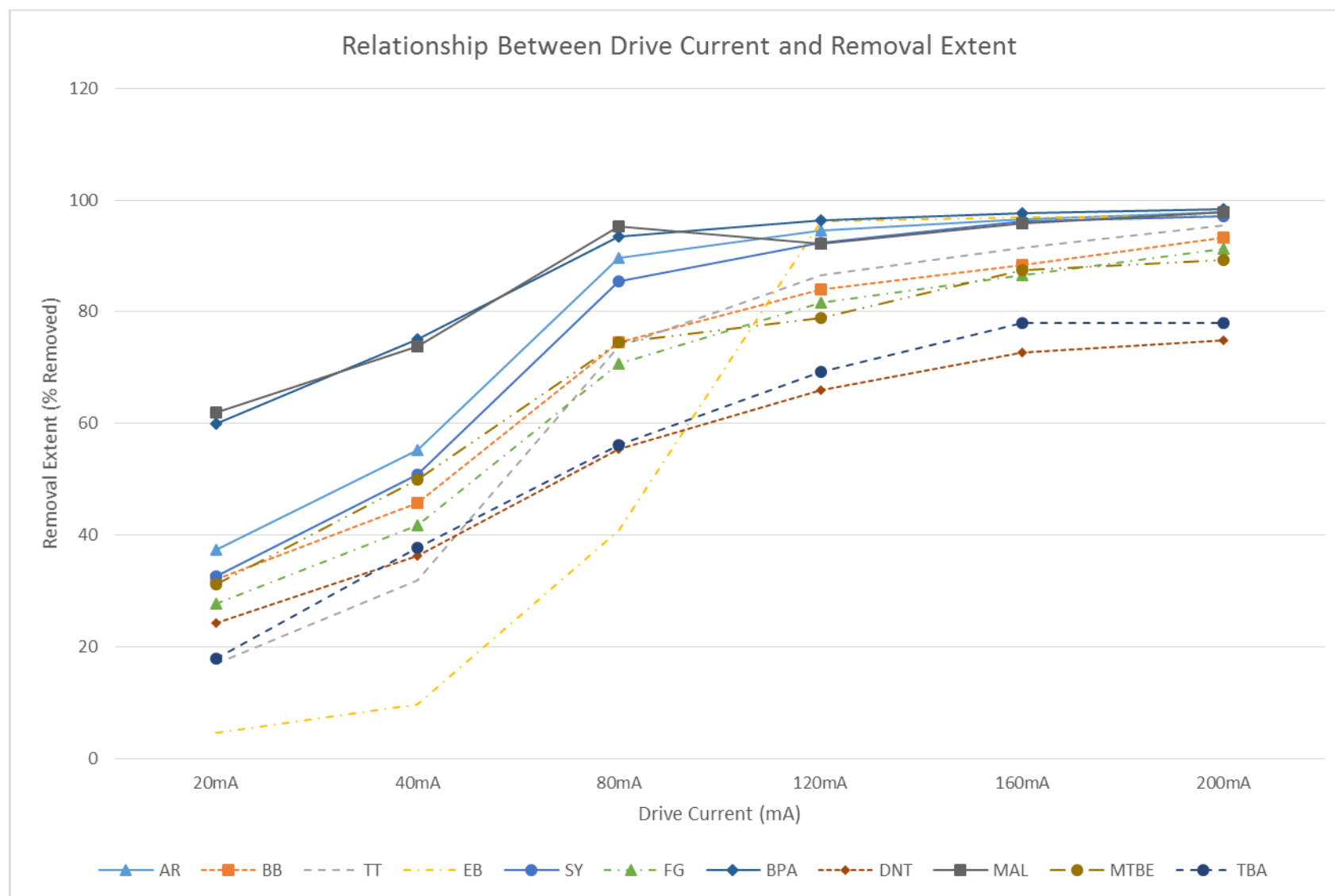


Figure A1. Effect of LED drive current on dye and achromatic chemical removal extent.

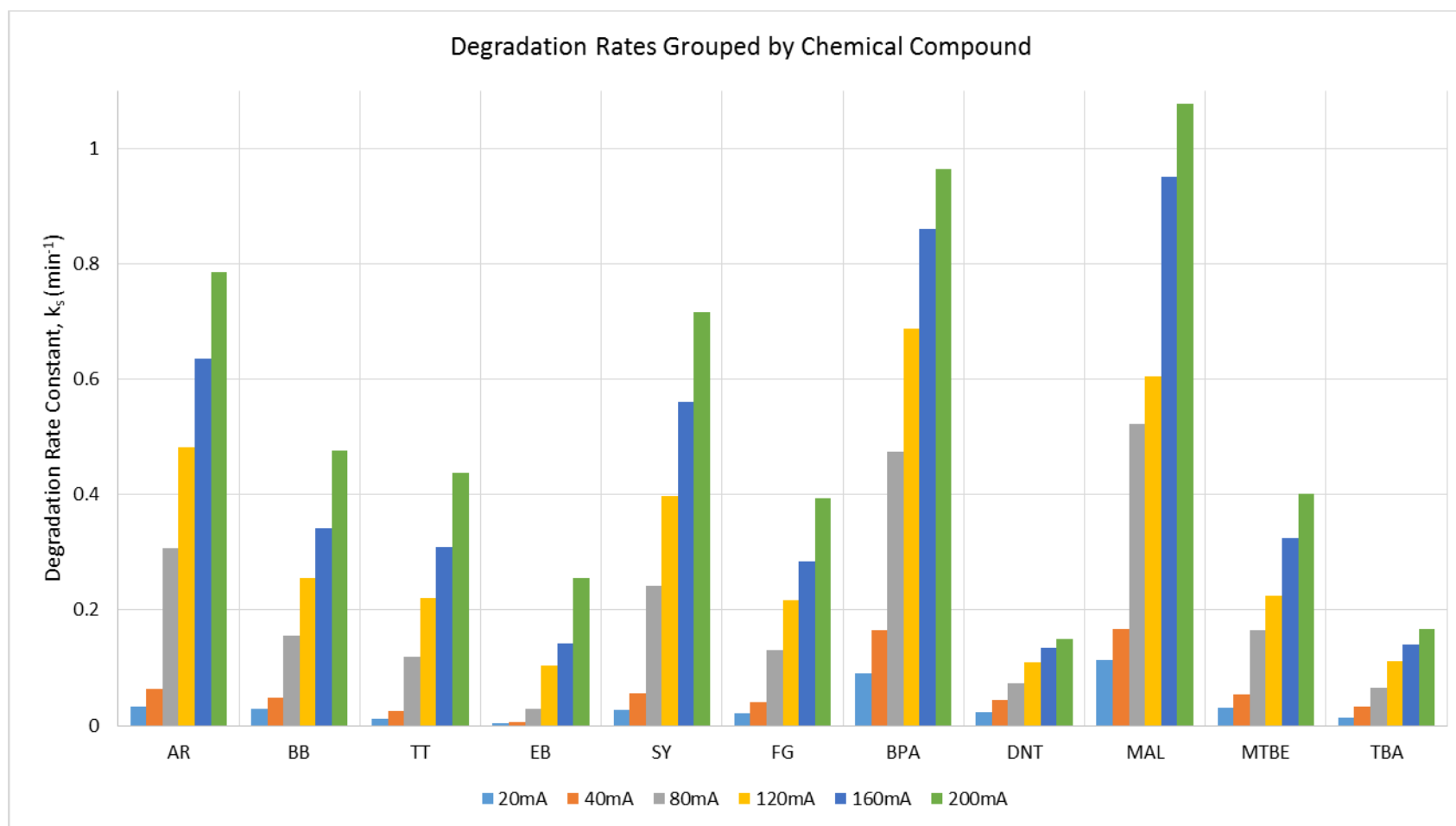


Figure A2. Comparative degradation rates across drive currents, grouped by chemical compound.

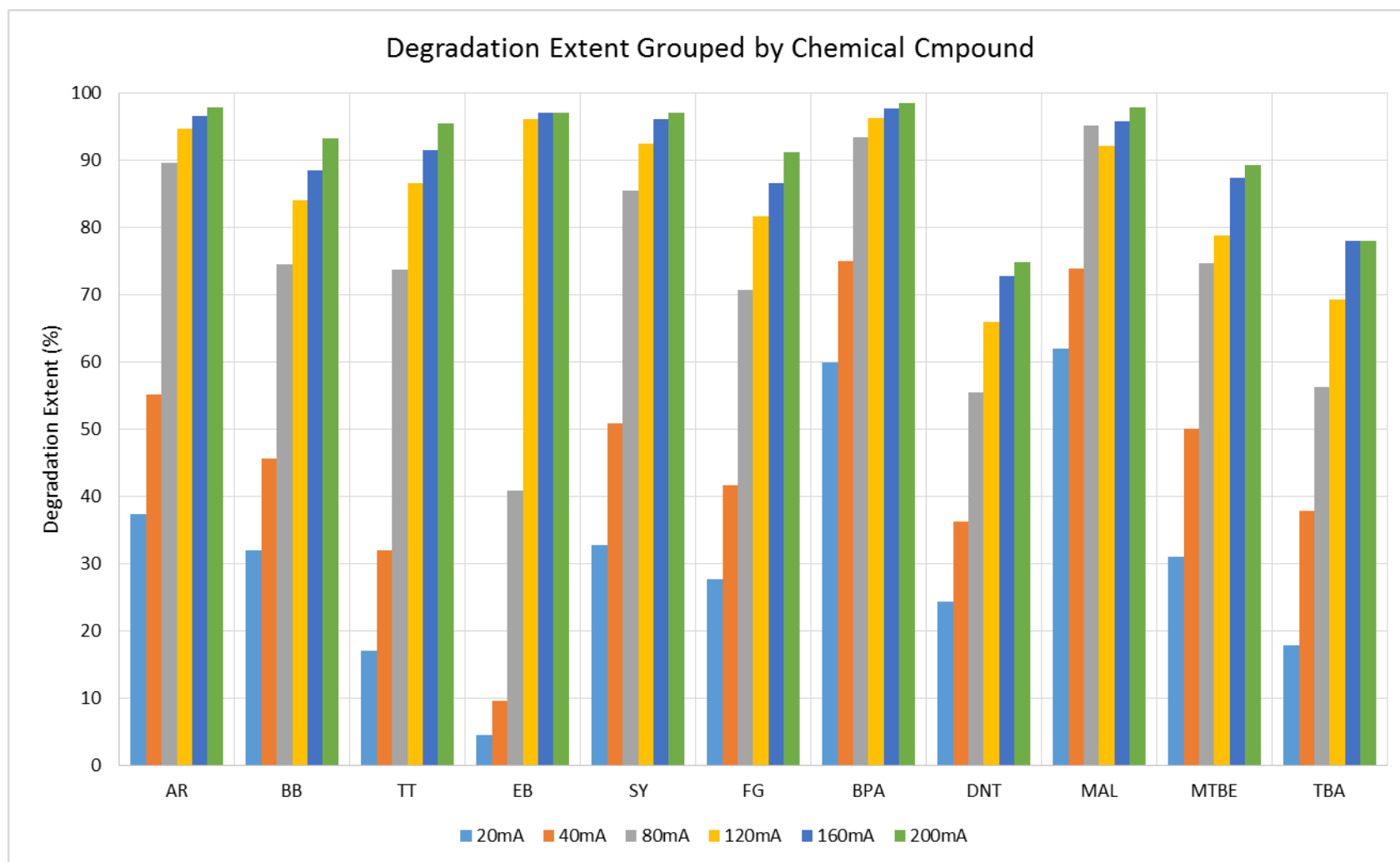


Figure A3. Comparative degradation extent across drive currents, grouped by chemical compound.

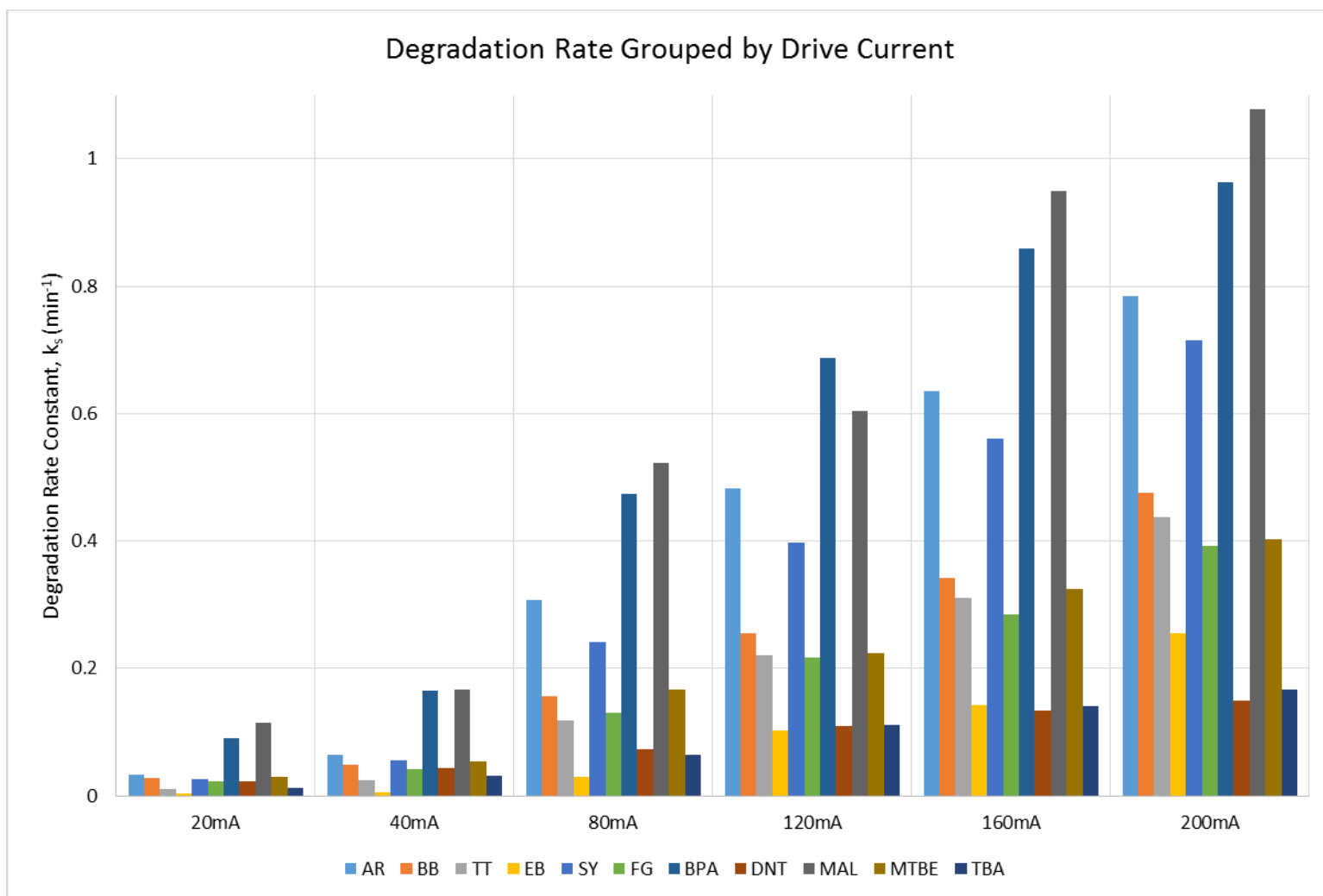


Figure A4. Comparative degradation rates across chemical compounds, grouped by drive current.

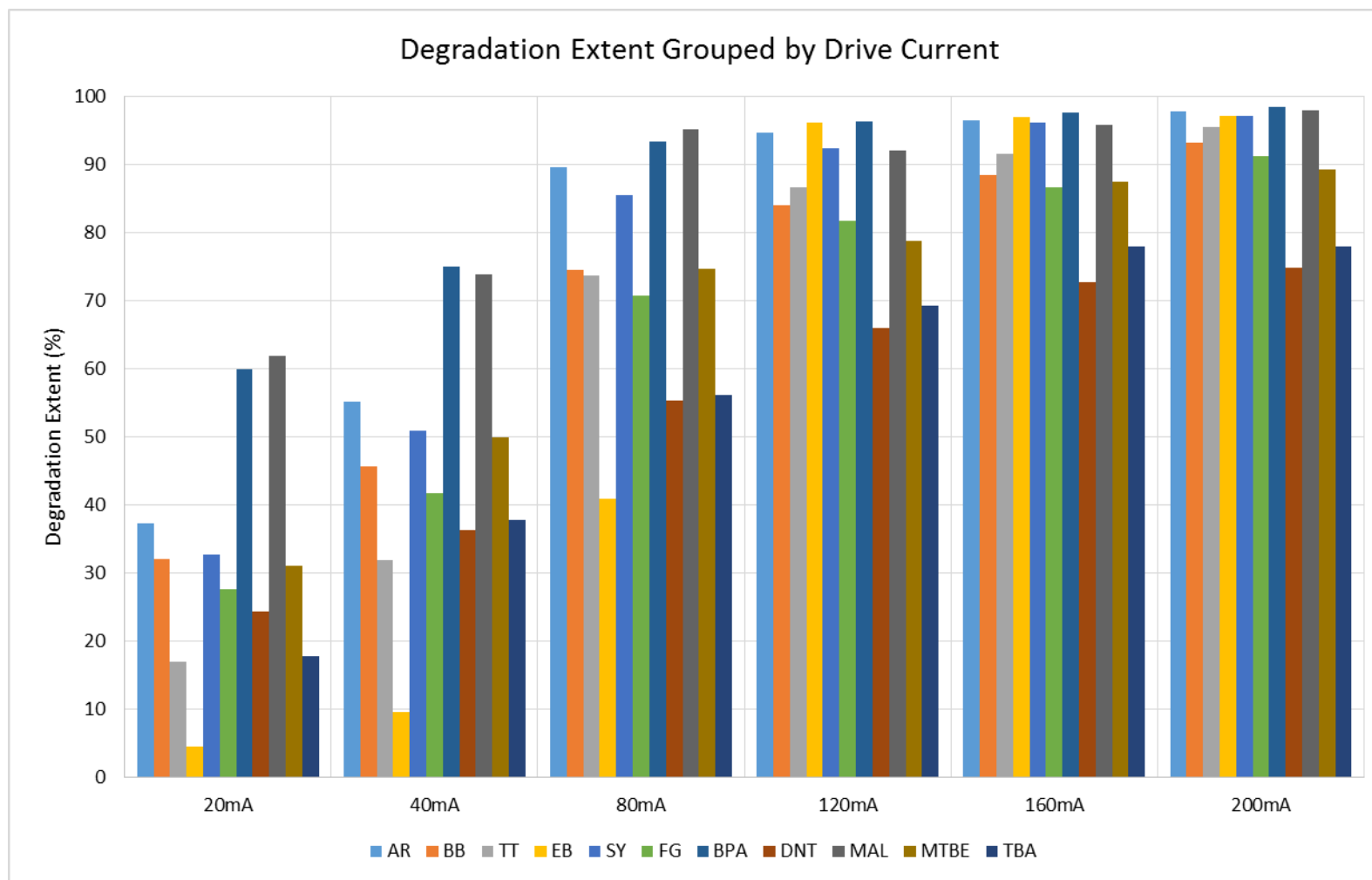


Figure A5. Comparative degradation extent across chemical compounds, grouped by drive current.

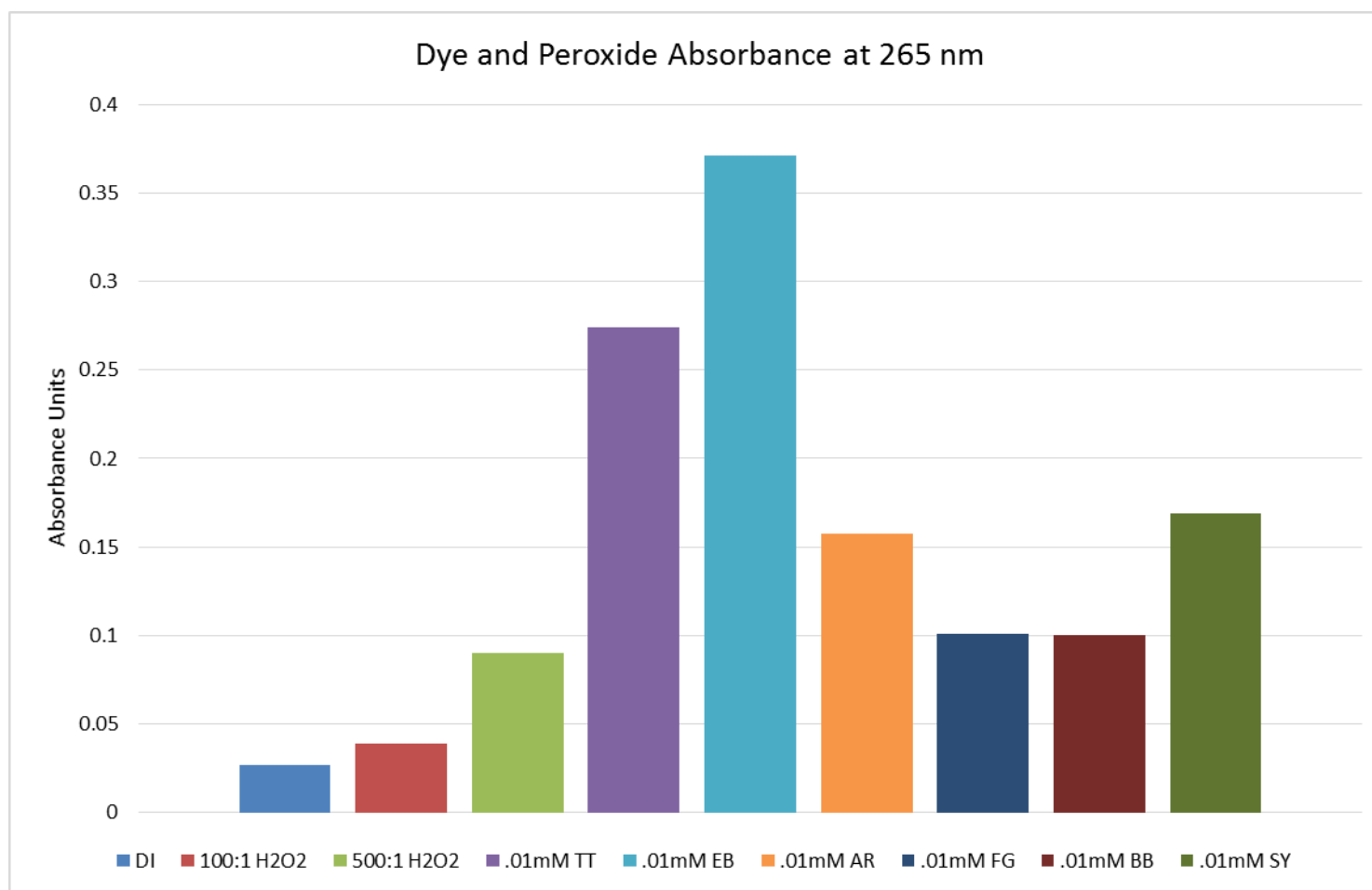


Figure A6. Spectrophotometer measurements comparing absorptivity of DI water, peroxide and dyes at 265 nm

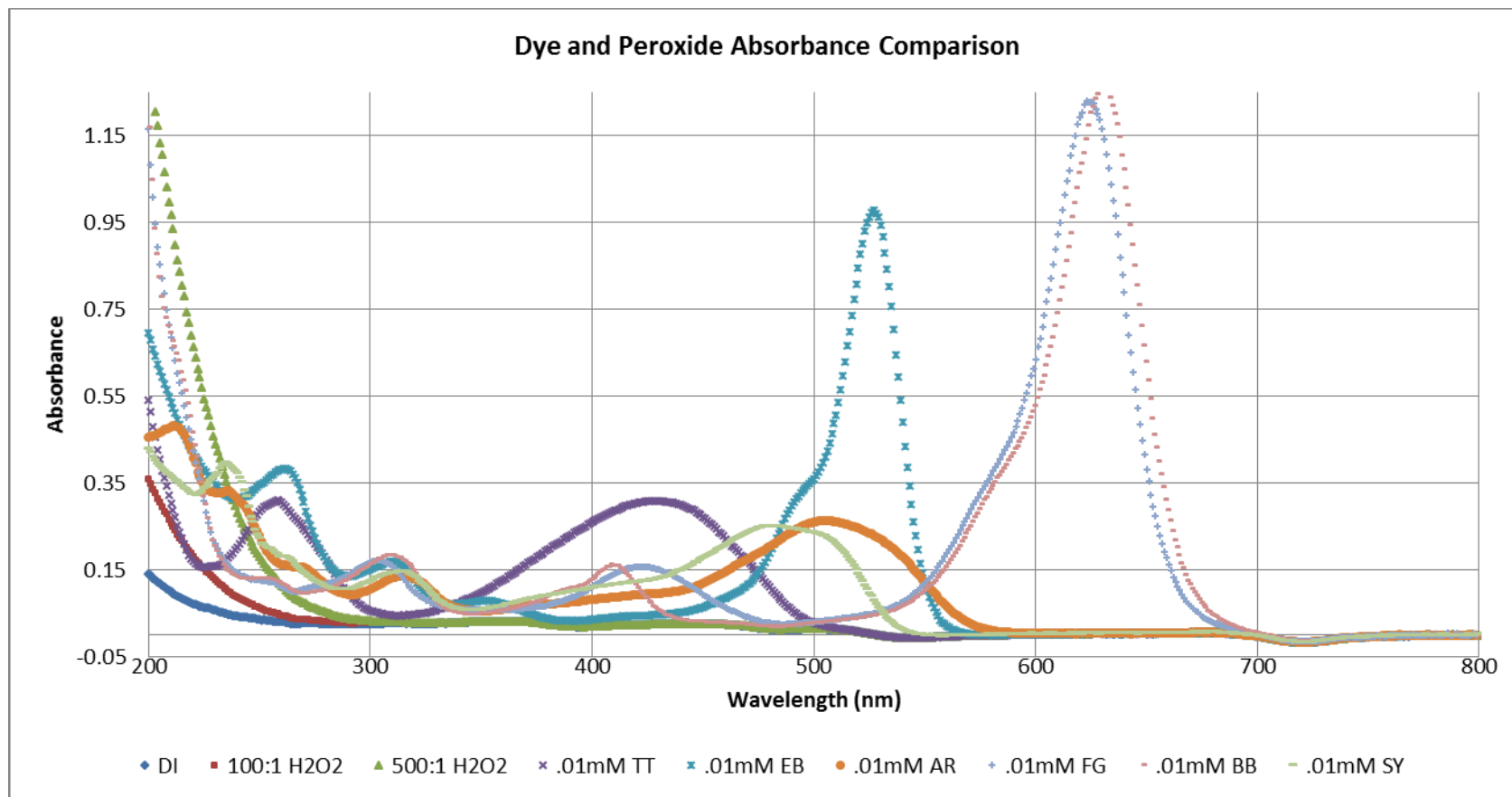


Figure A7. Spectrophotometer scan comparing absorptivity of DI water, peroxide, and dyes.

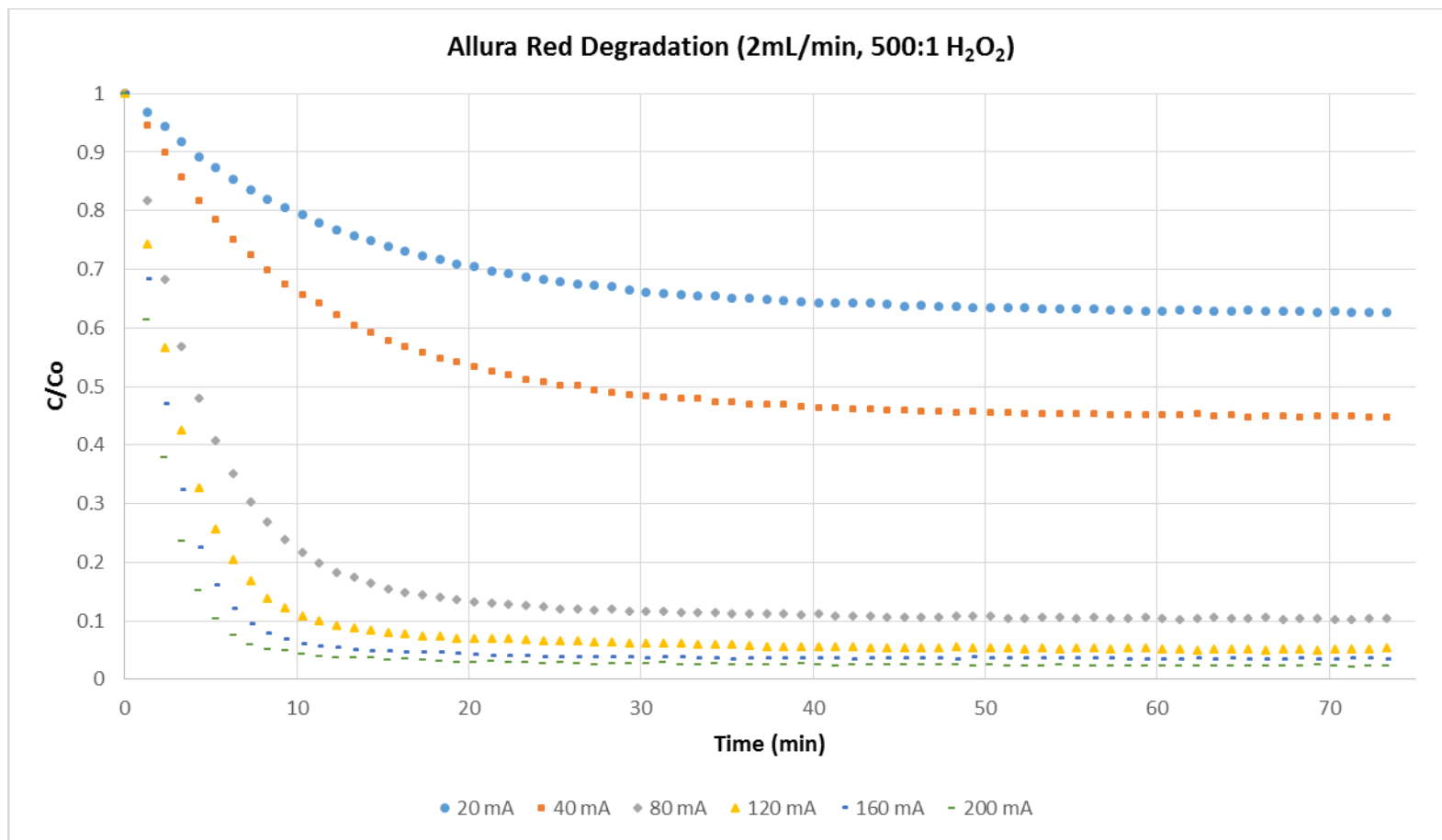


Figure A8. Allura Red degradation as a function of drive current.

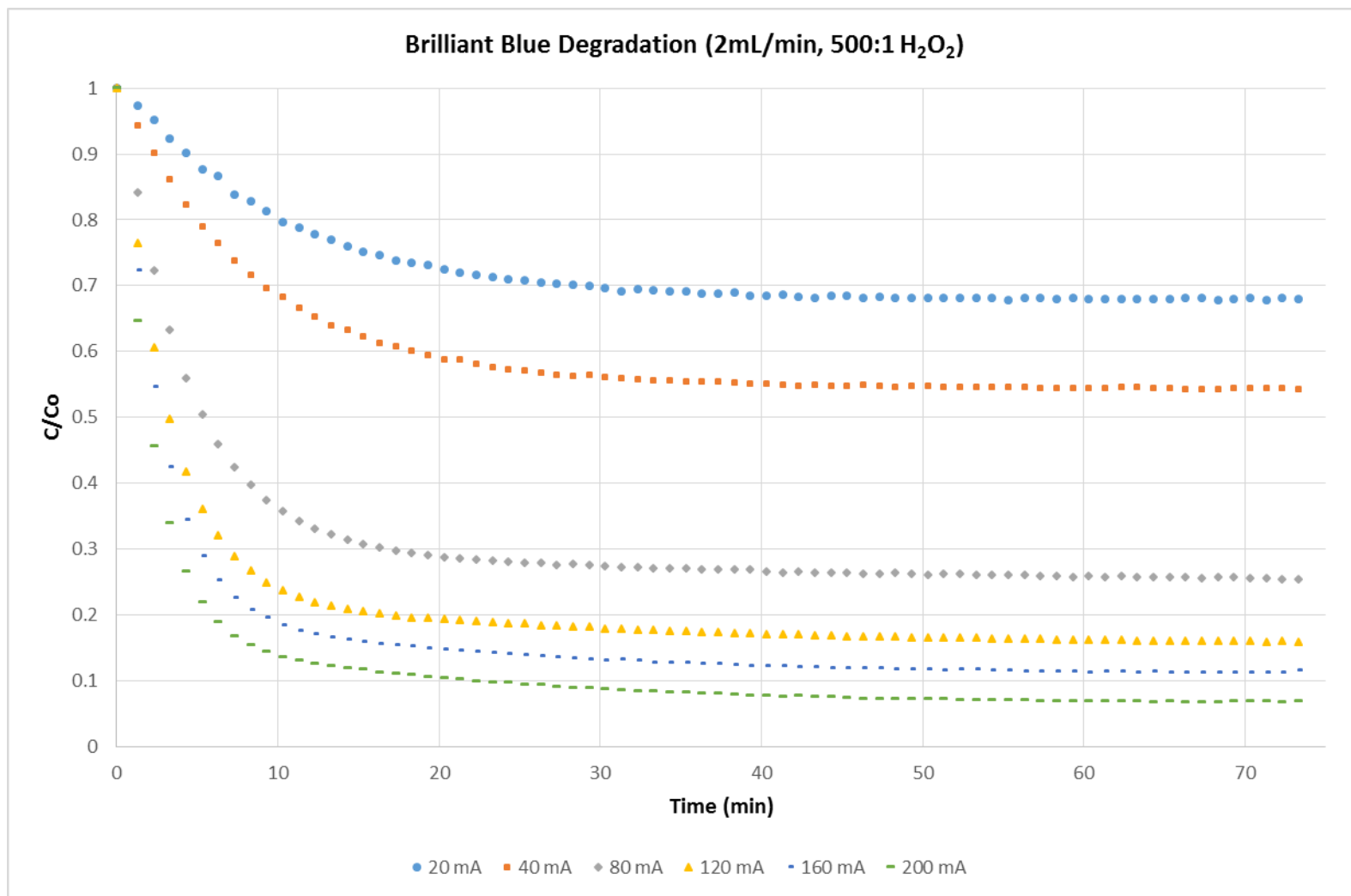


Figure A9. Brilliant Blue degradation as a function of drive current.

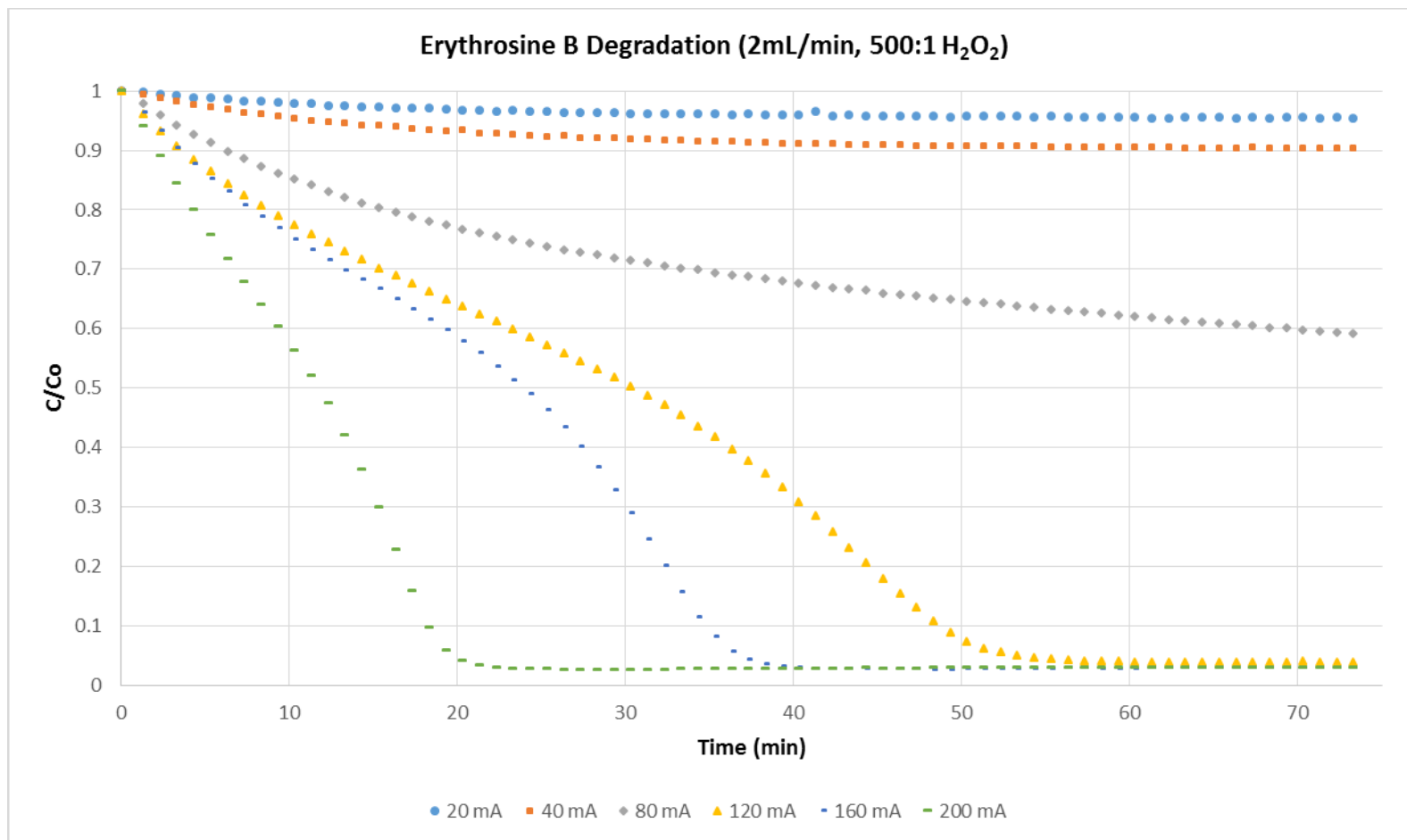


Figure A10. Erythrosine B degradation as a function of drive current.

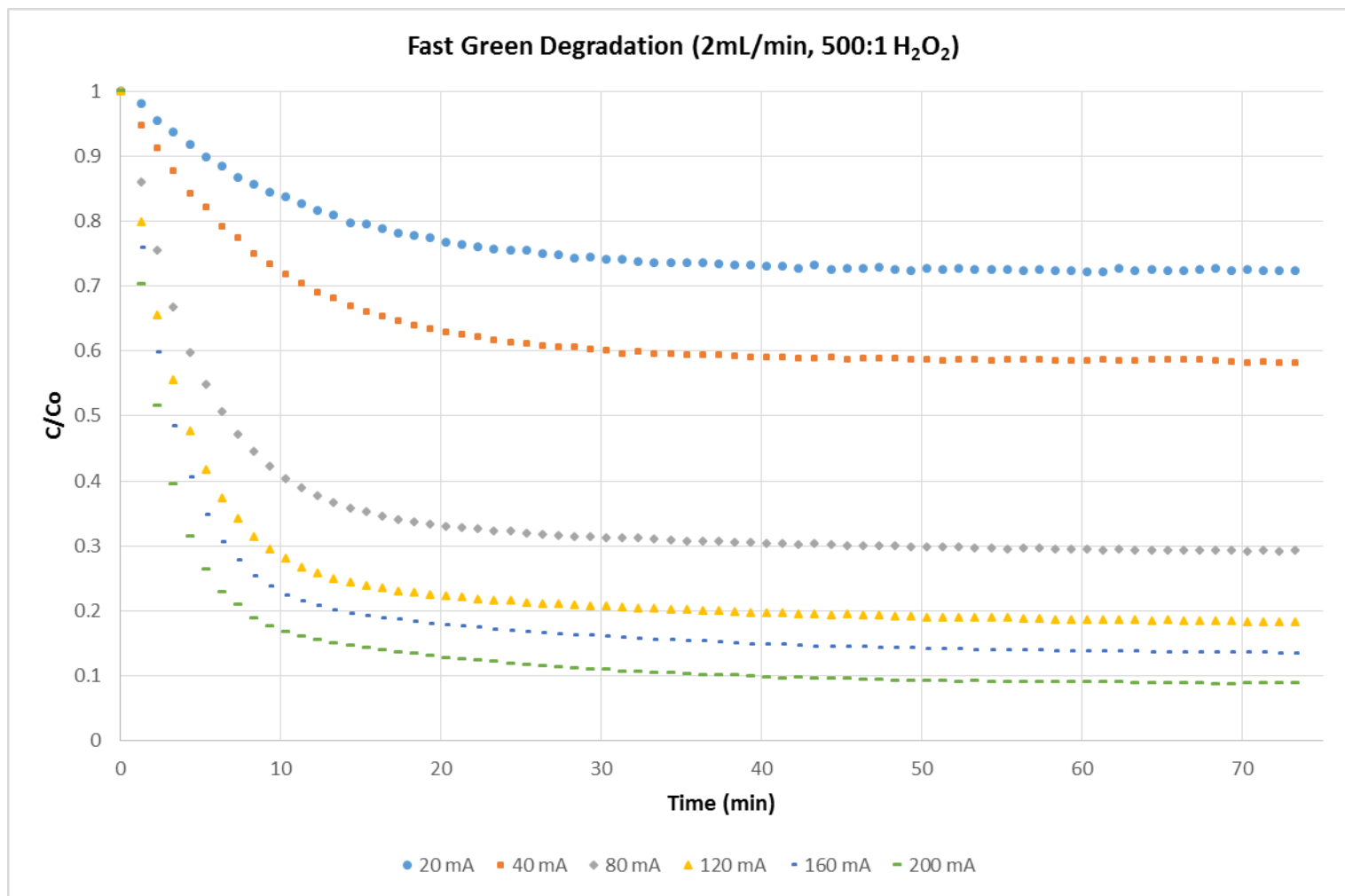


Figure A11. Fast Green degradation as a function of drive current.

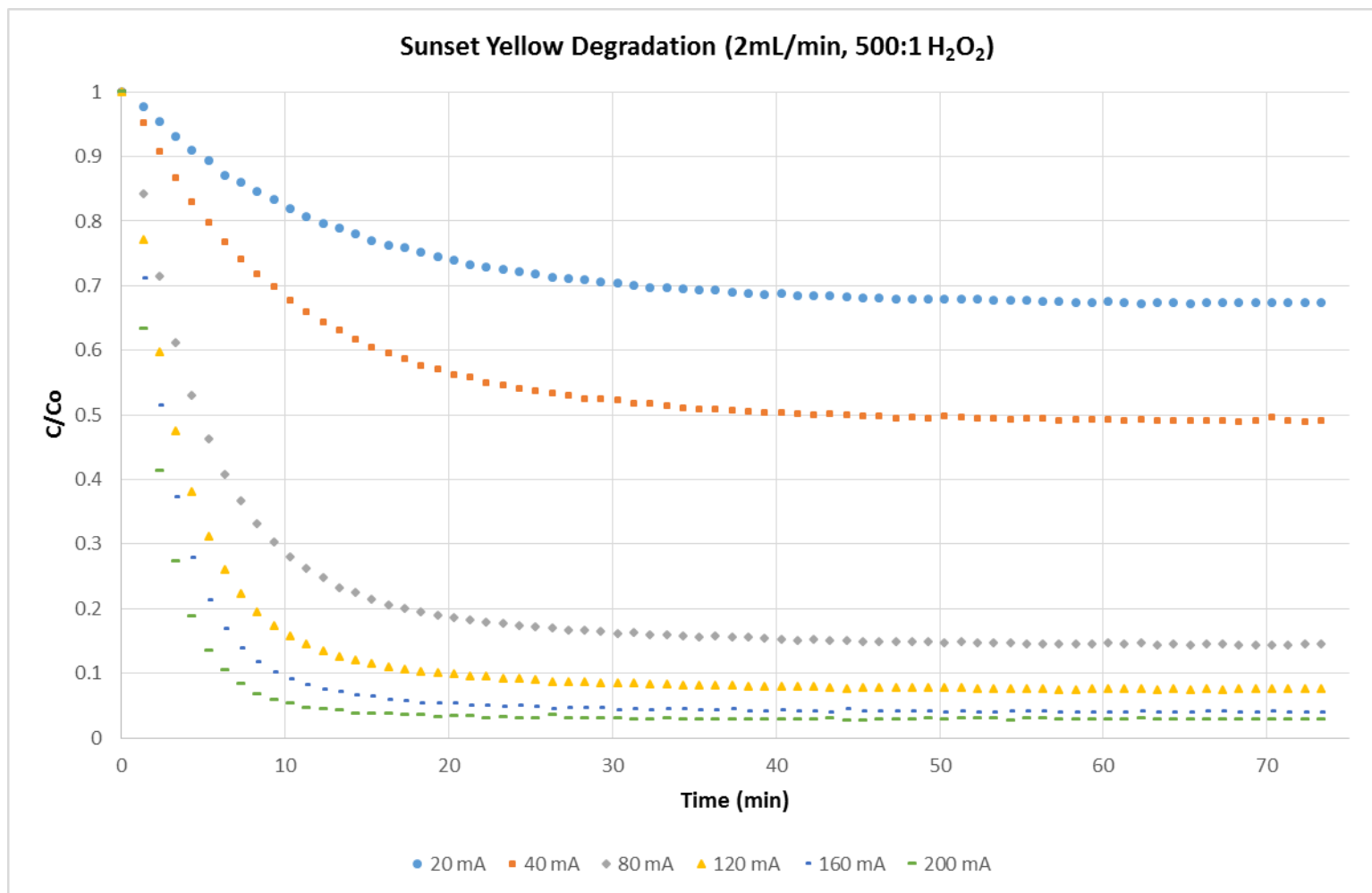


Figure A12. Sunset Yellow degradation as a function of drive current.

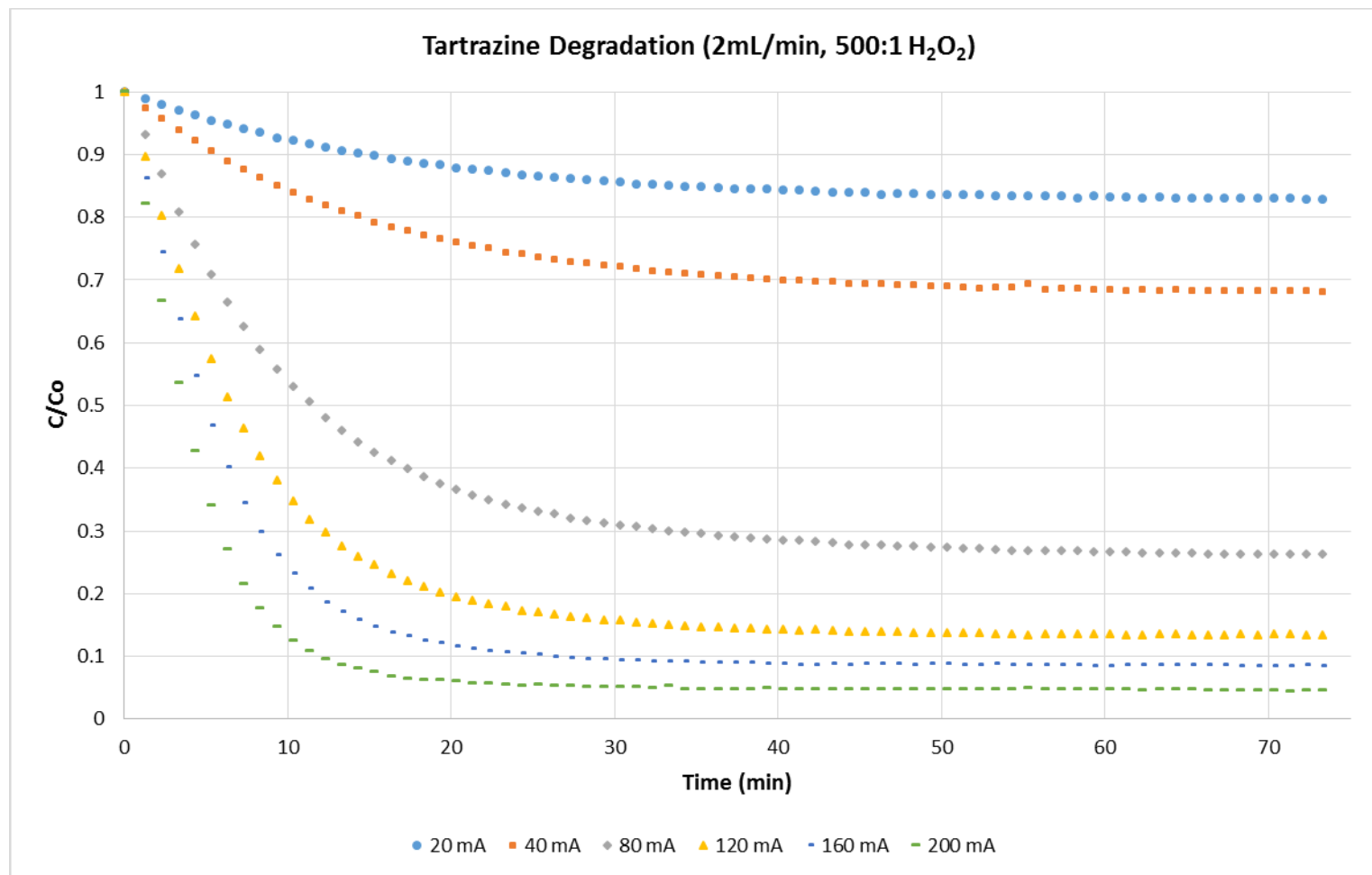


Figure A13. Tartrazine degradation as a function of drive current.

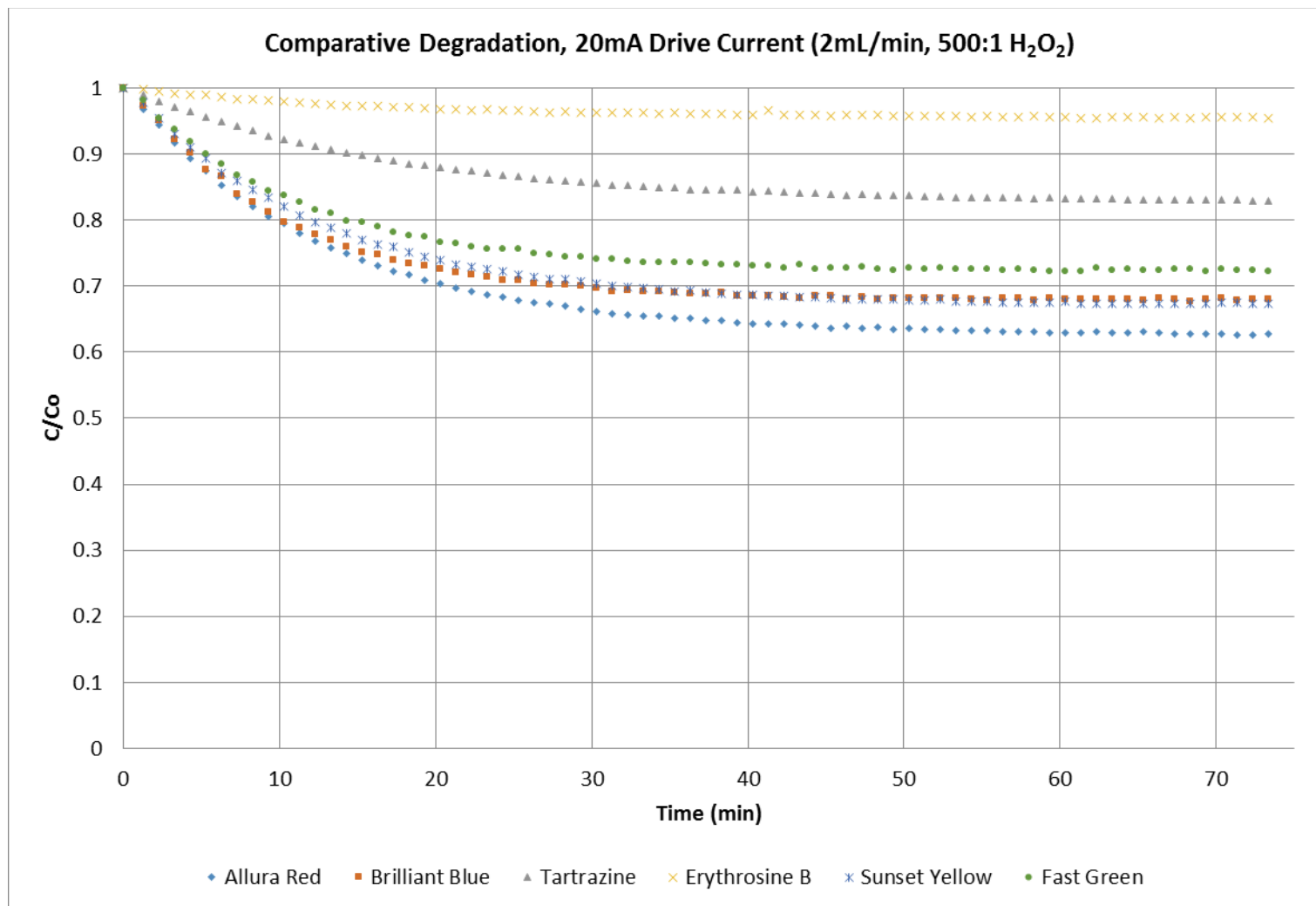


Figure A14. Comparative degradation of dyes at 20 mA drive current.

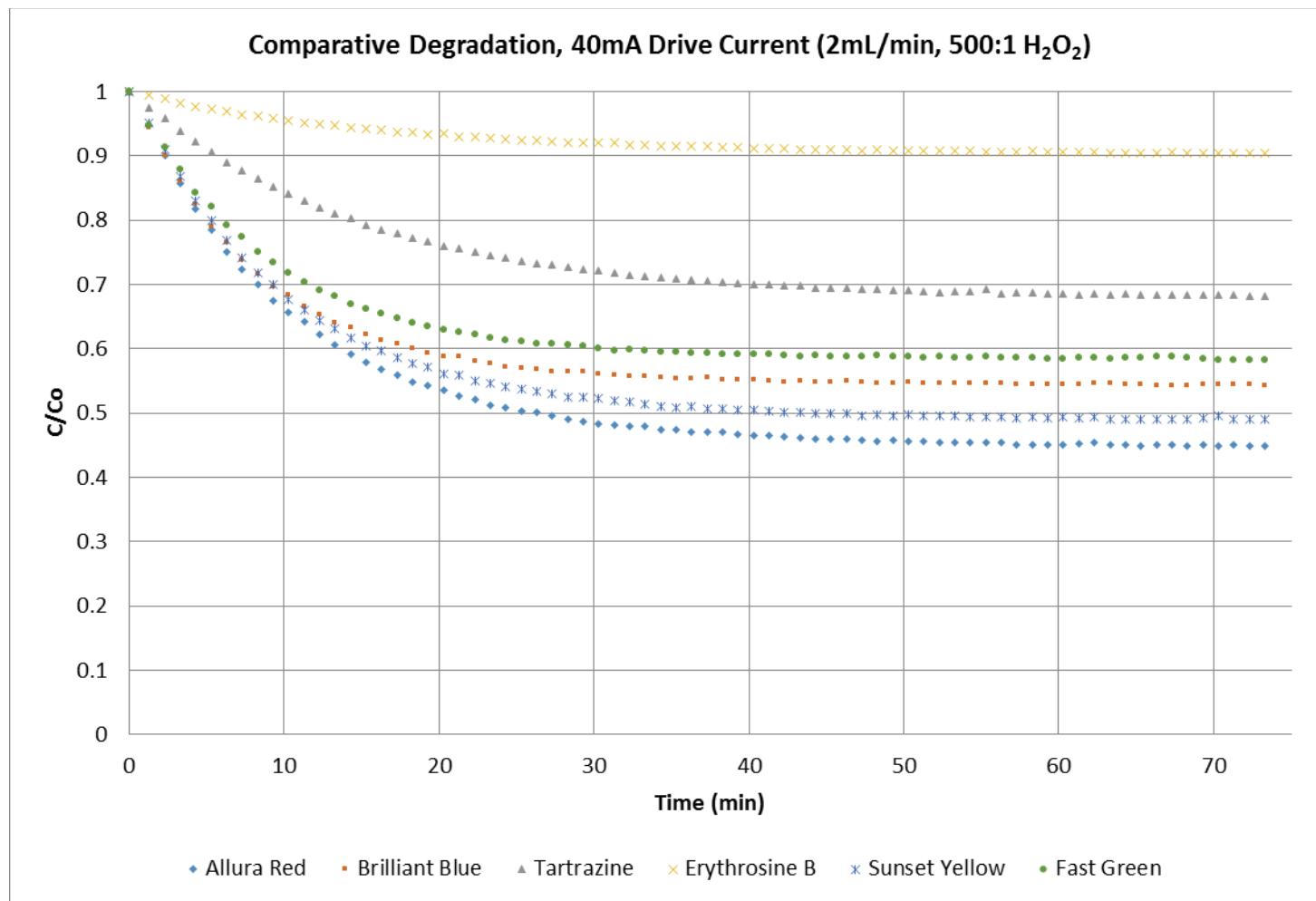


Figure A15. Comparative degradation of dyes at 40 mA drive current.

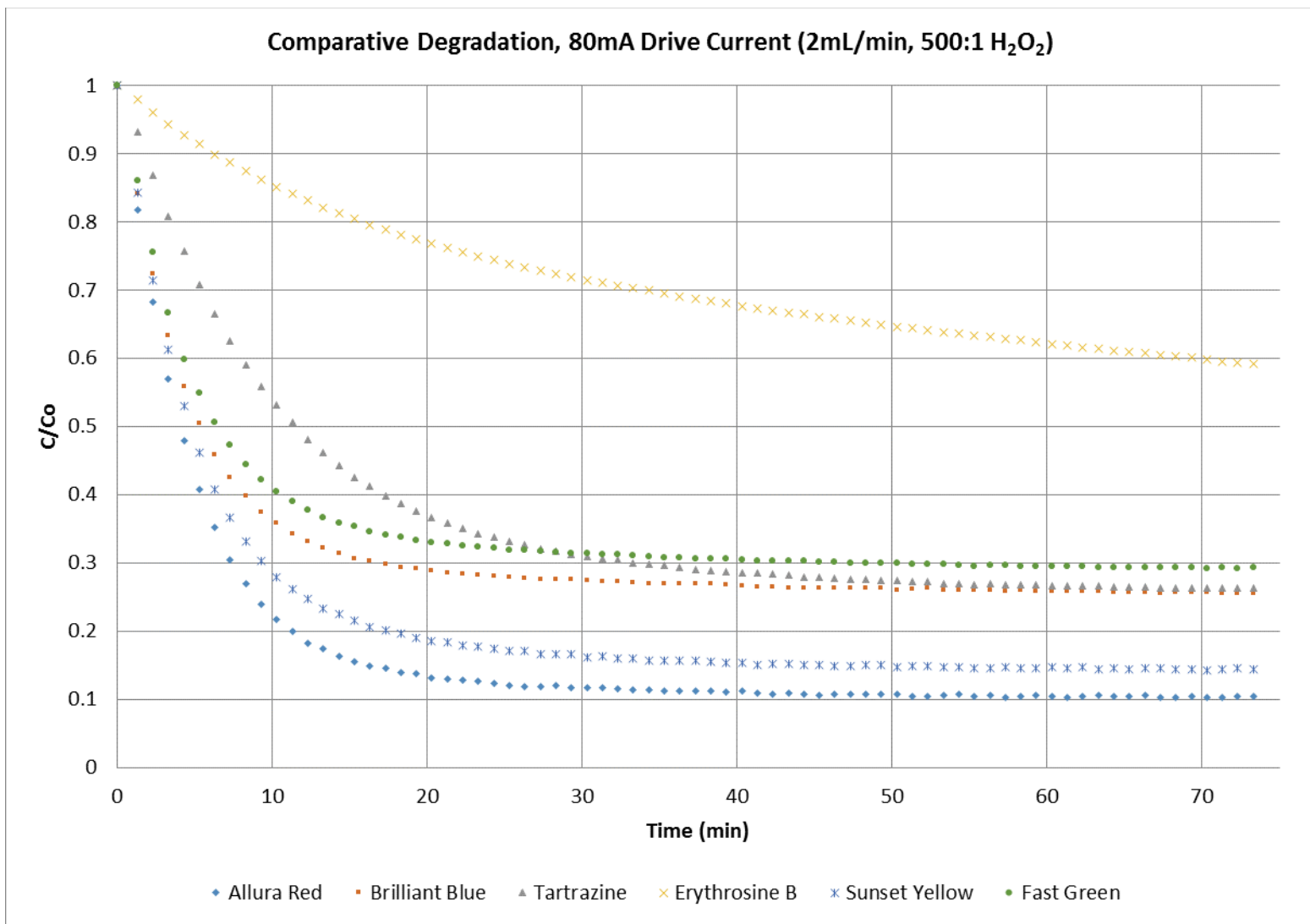


Figure A16. Comparative degradation of dyes at 80 mA drive current.

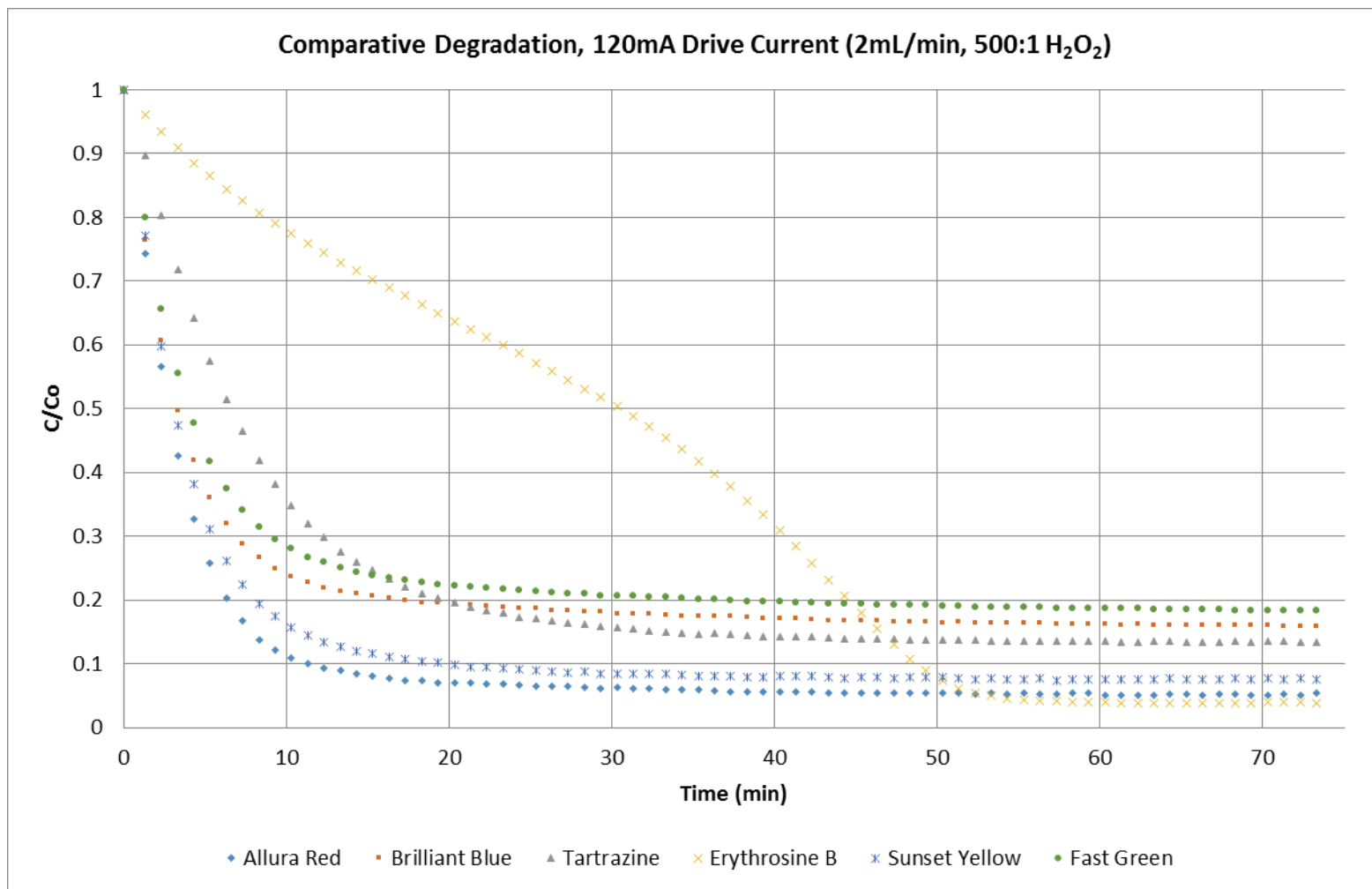


Figure A17. Comparative degradation of dyes at 120 mA drive current.

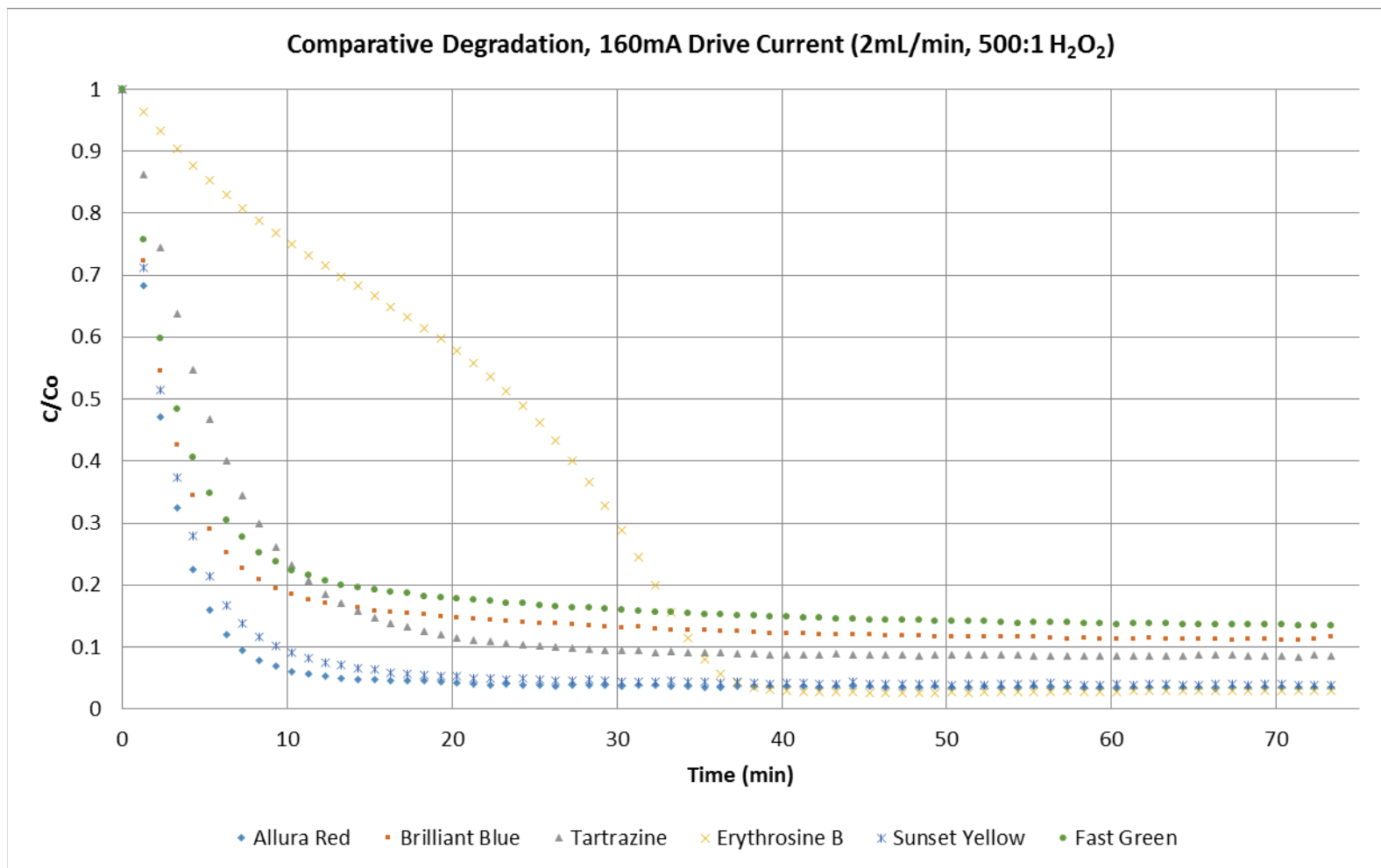


Figure A18. Comparative degradation of dyes at 160 mA drive current.

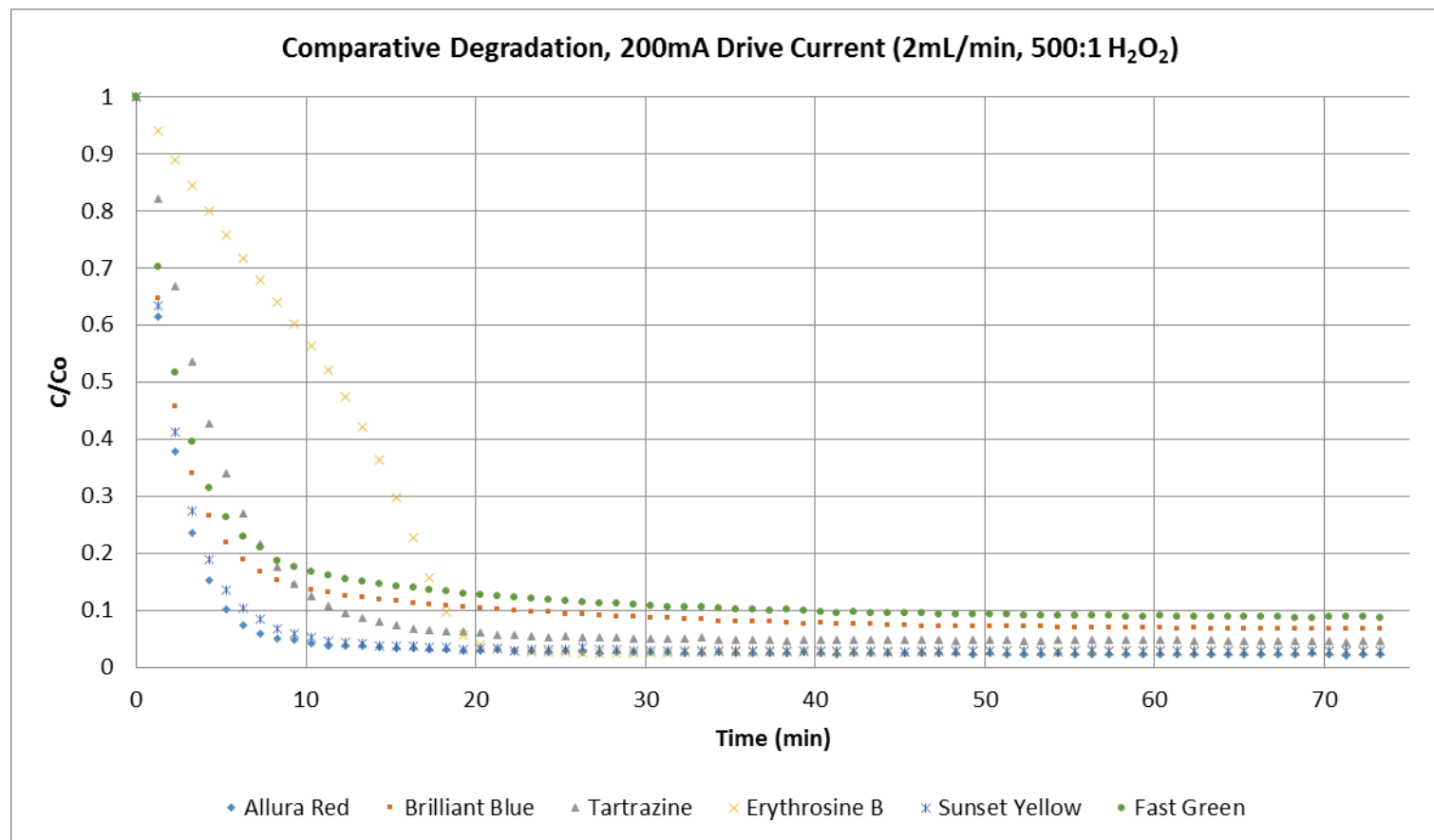


Figure A19. Comparative degradation of dyes at 200 mA drive current.

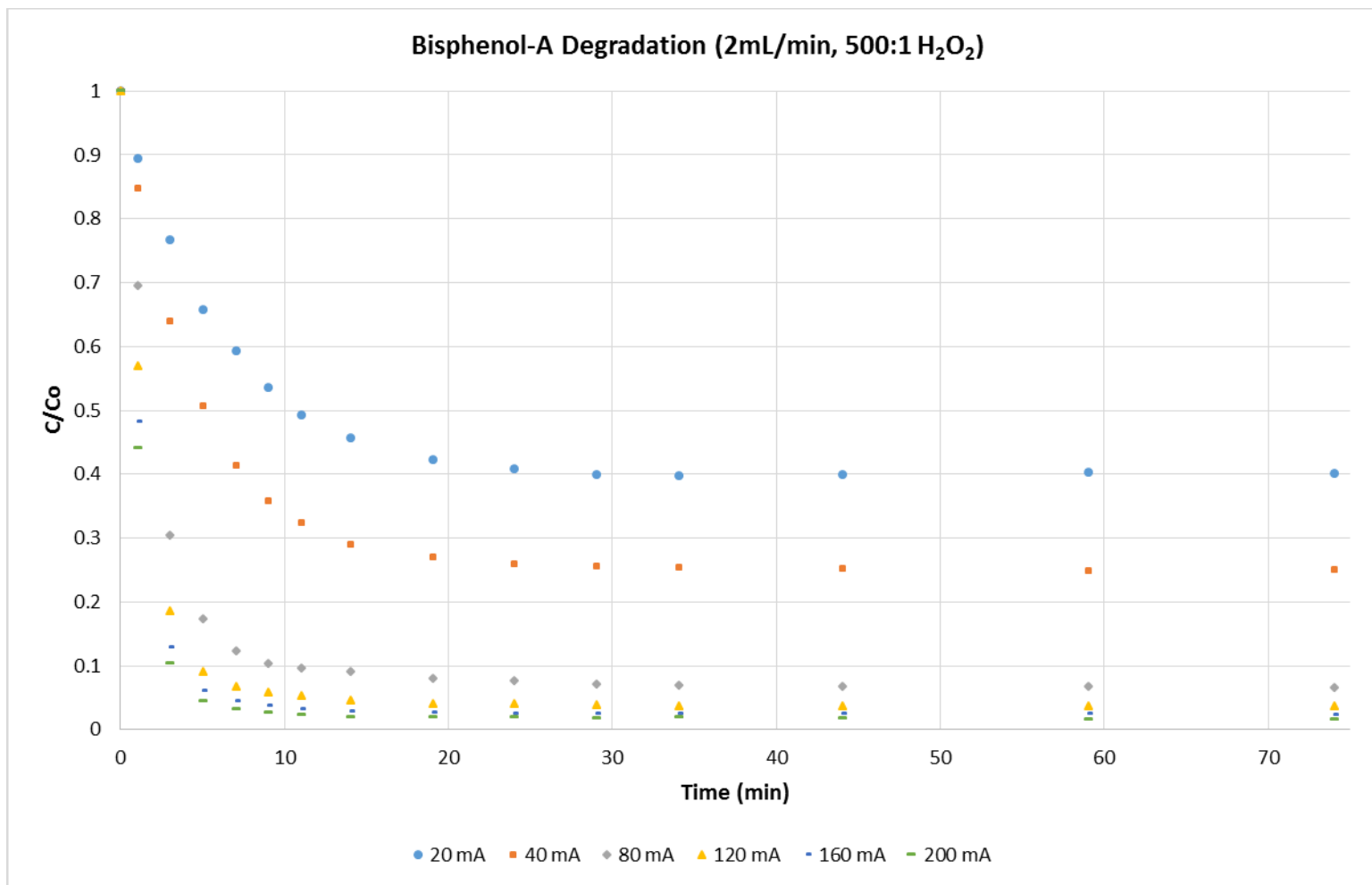


Figure A20. Bisphenol A degradation as a function of drive current.

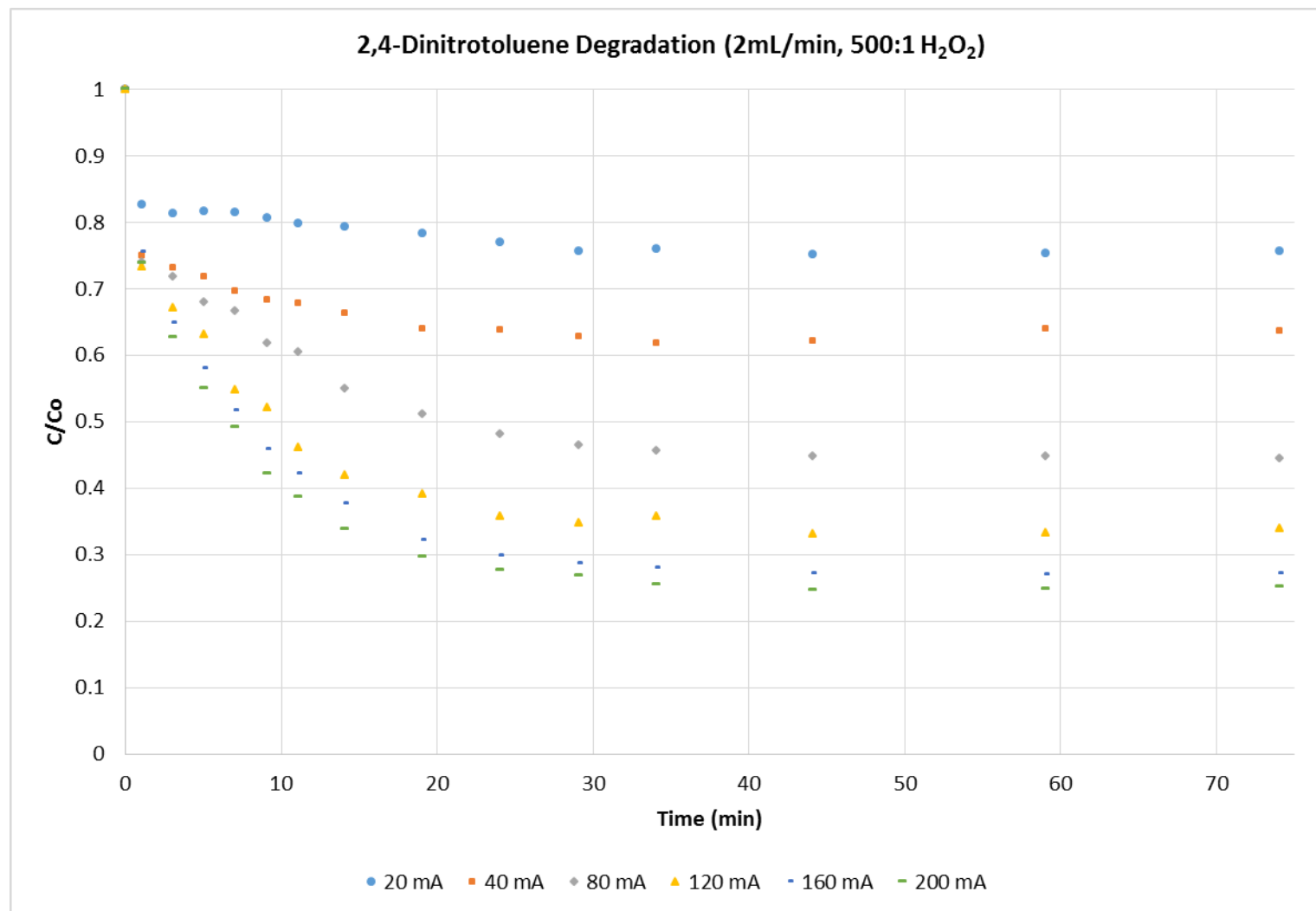


Figure A21. 2,4-Dinitrotoluene degradation as a function of drive current.

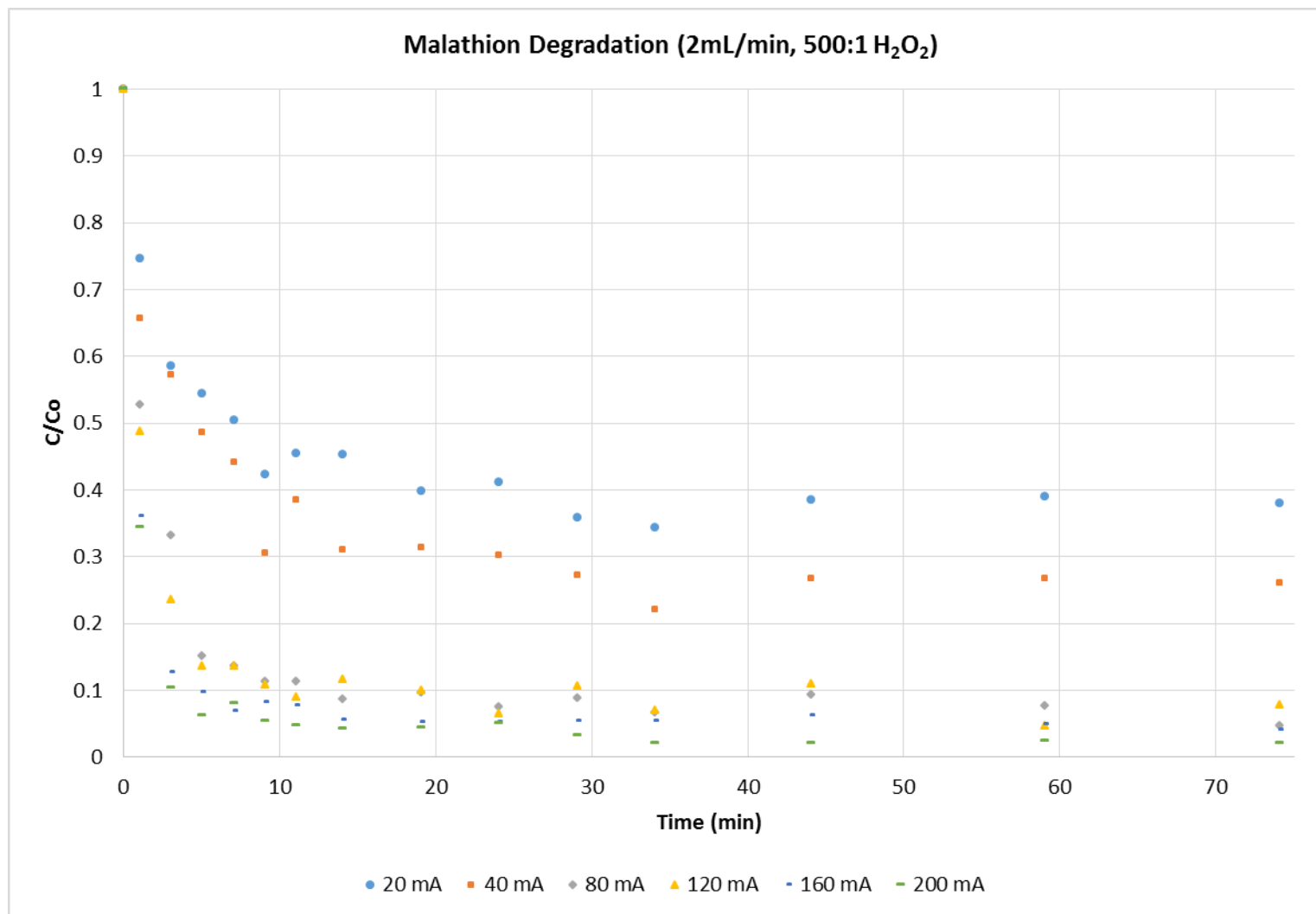


Figure A22. Malathion degradation as a function of drive current.

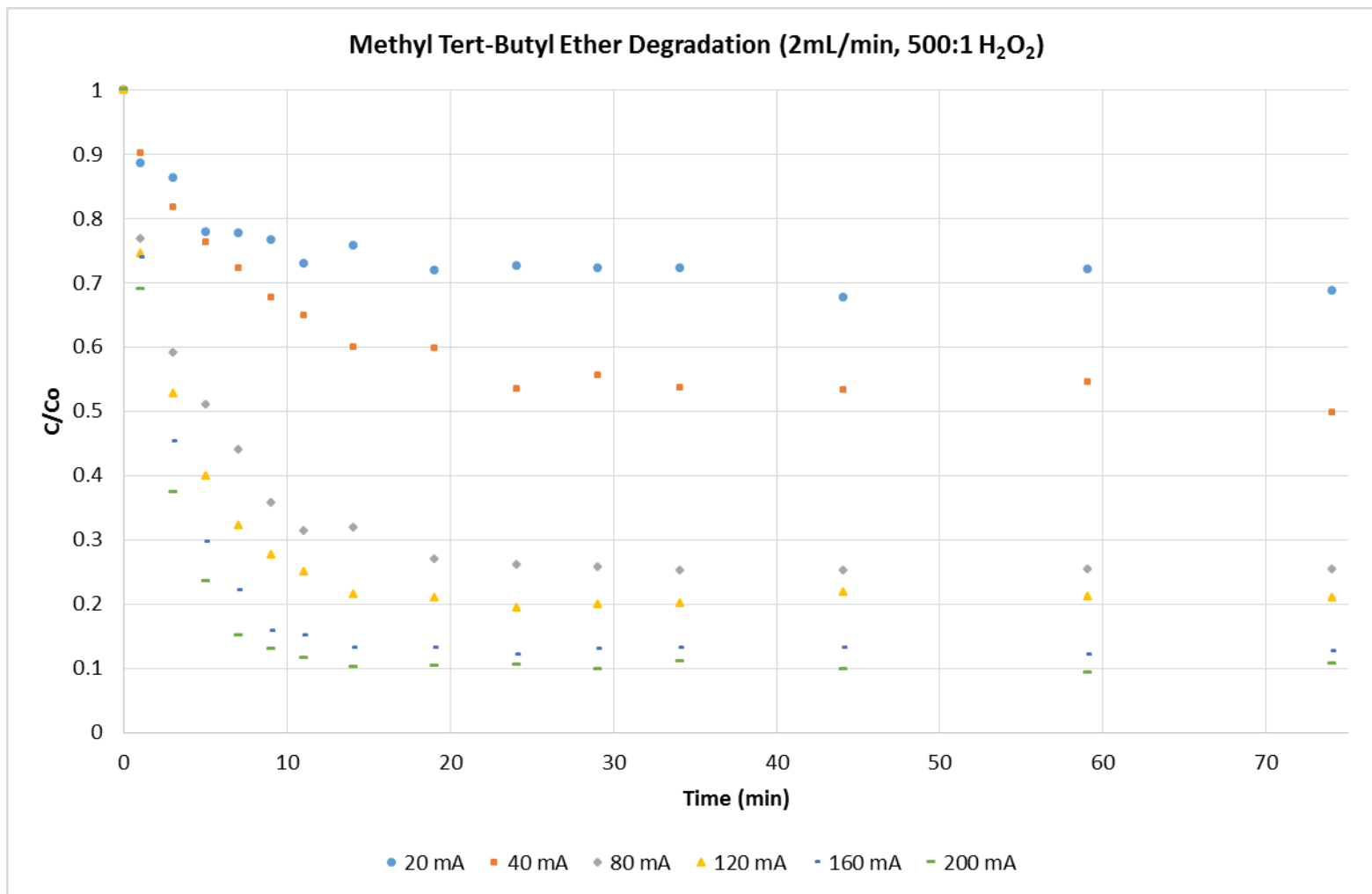


Figure A23. Methyl tert-butyl ether degradation as a function of drive current.

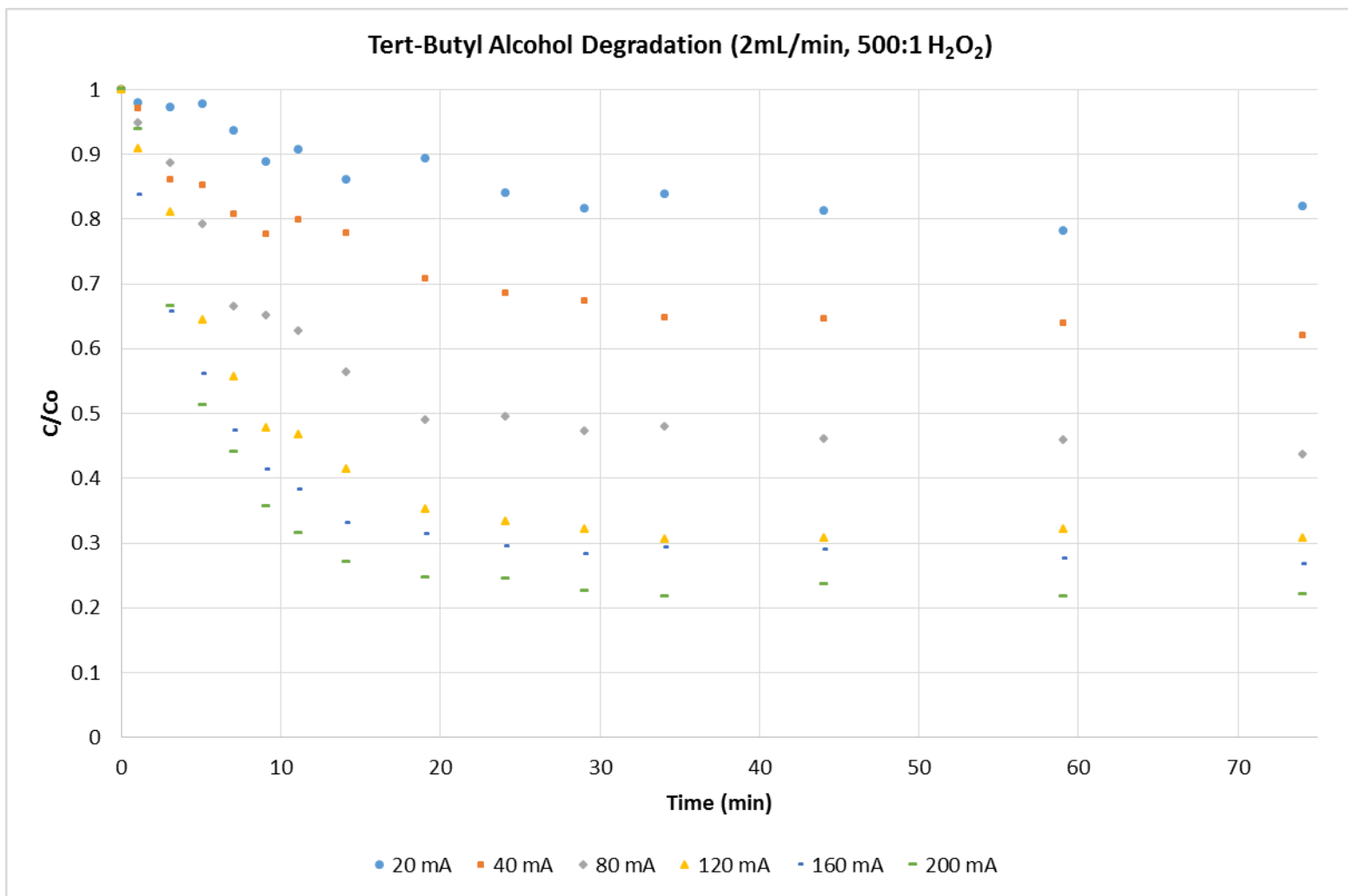


Figure A24. Tert-butyl alcohol degradation as a function of drive current.

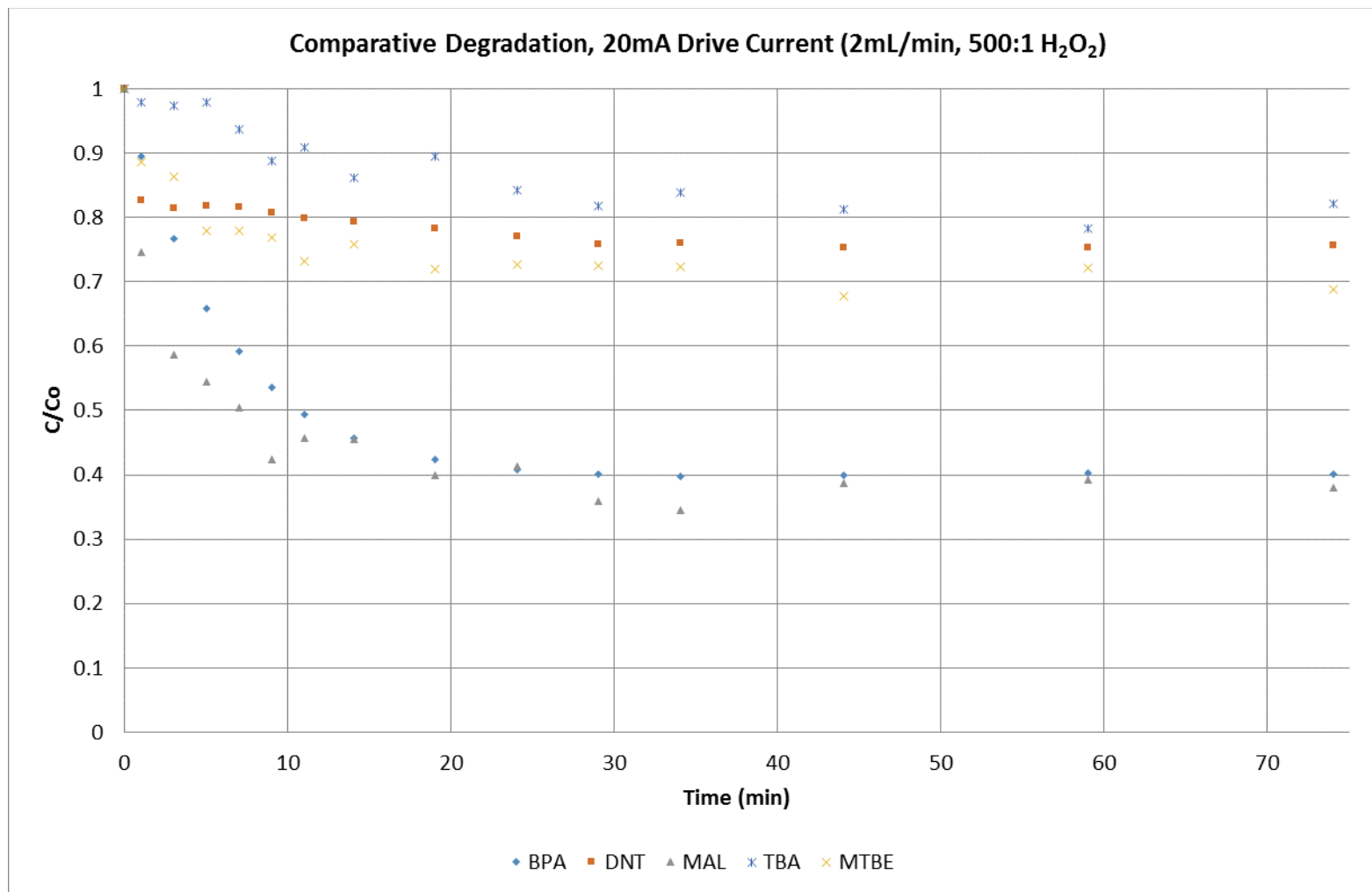


Figure A25. Comparative degradation of achromatic chemicals at 20 mA drive current.

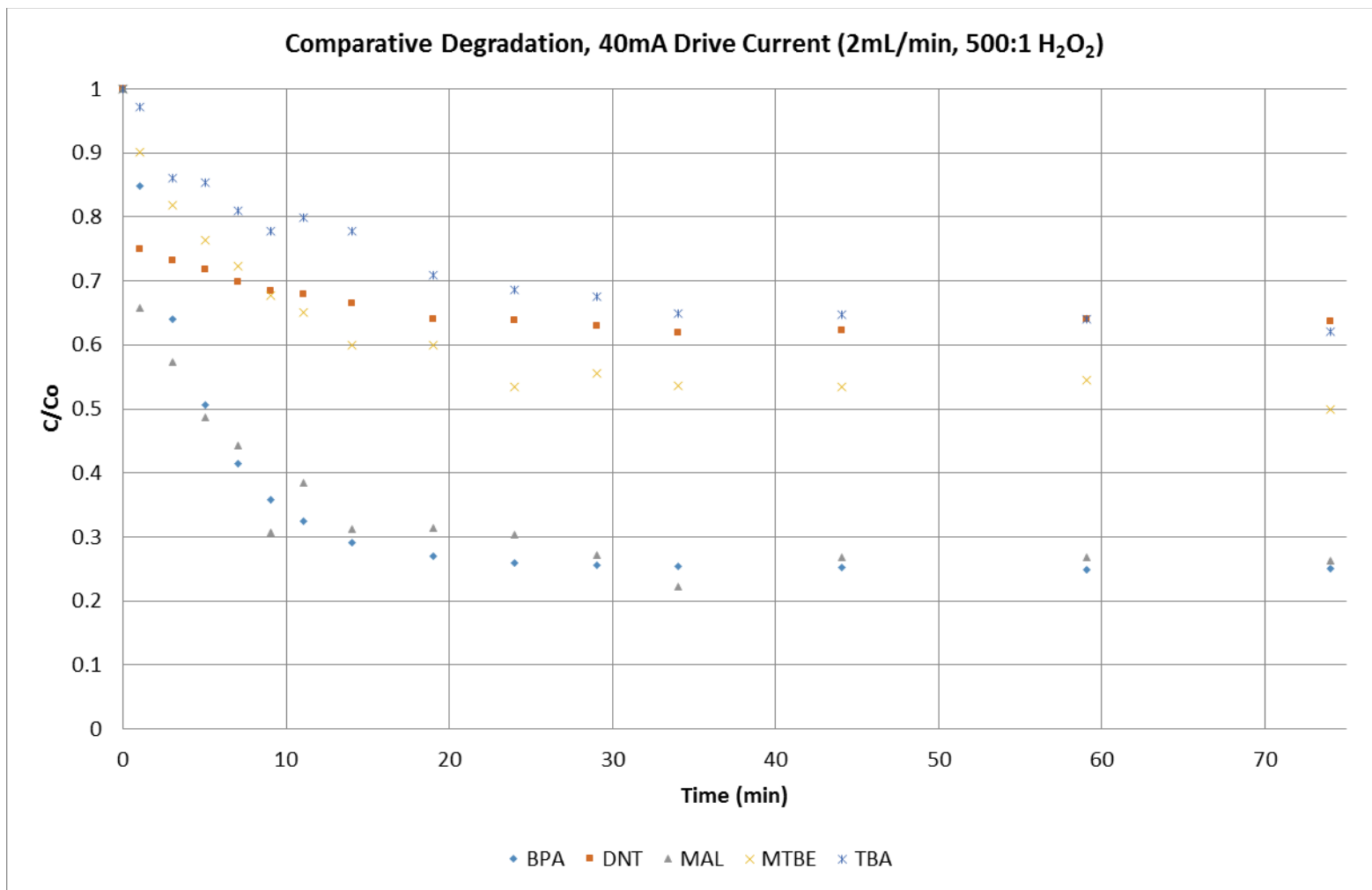


Figure A26. Comparative degradation of achromatic chemicals at 40 mA drive current.

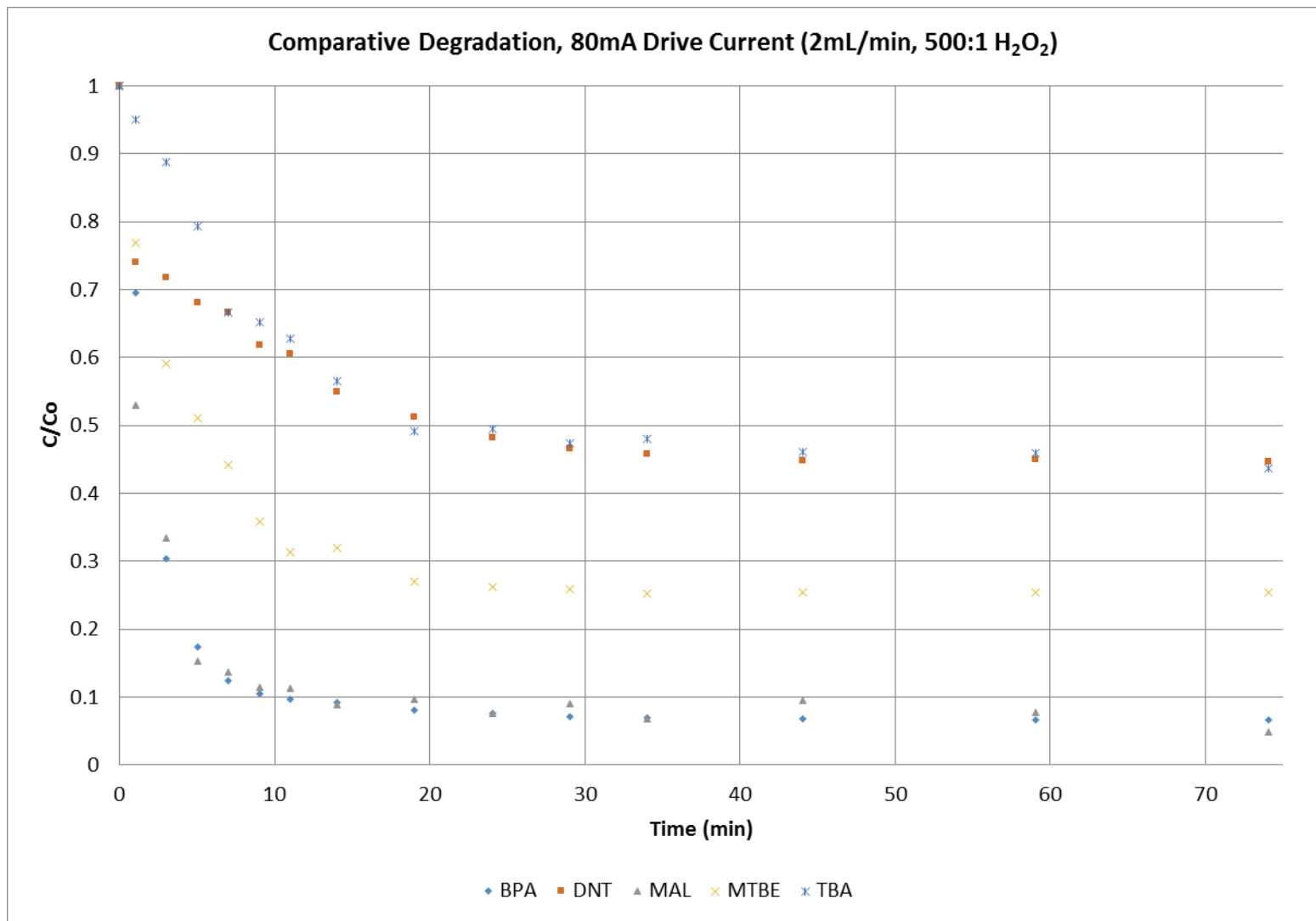


Figure A27. Comparative degradation of achromatic chemicals at 80 mA drive current.

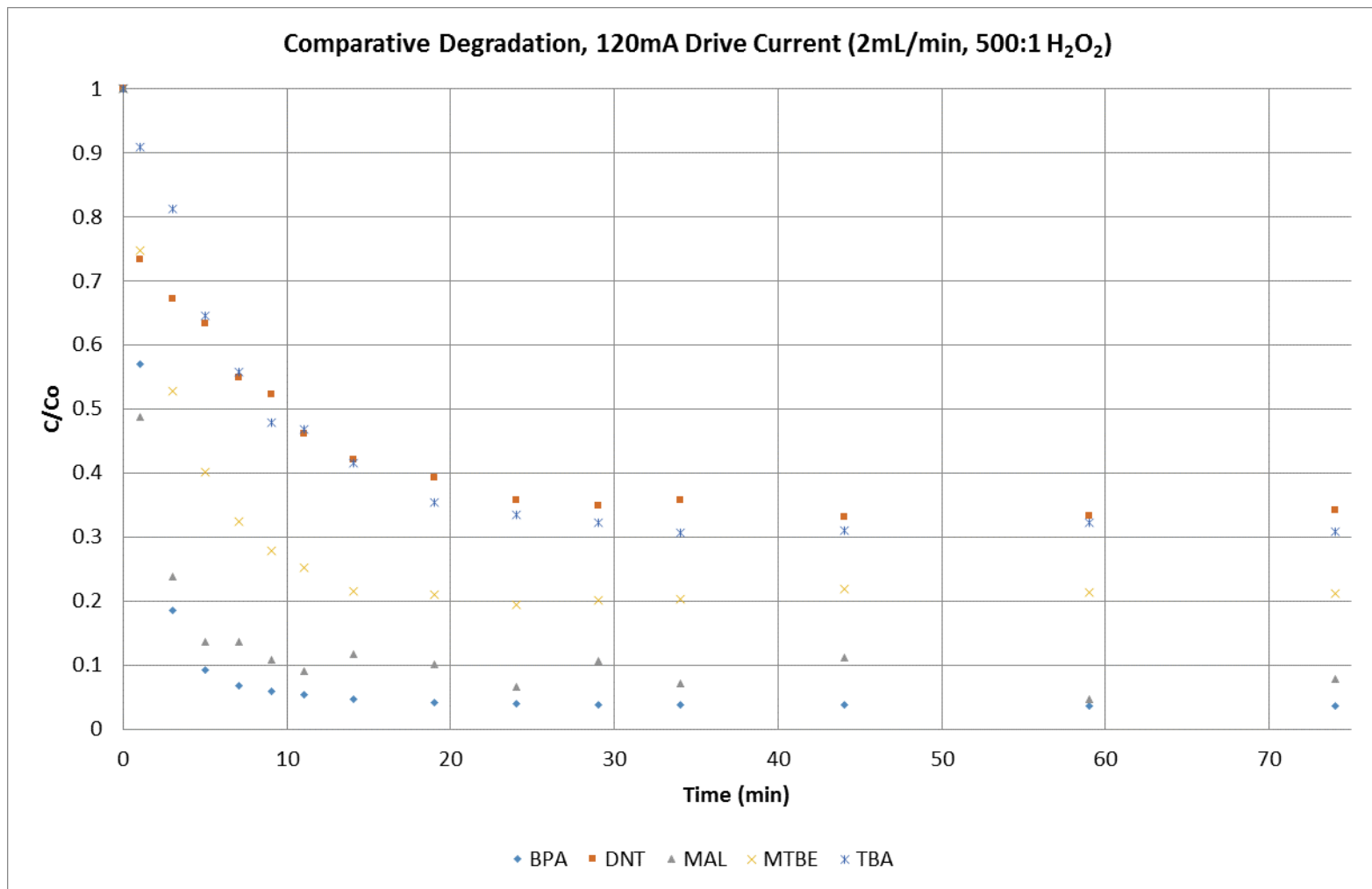


Figure A28. Comparative degradation of achromatic chemicals at 120 mA drive current.

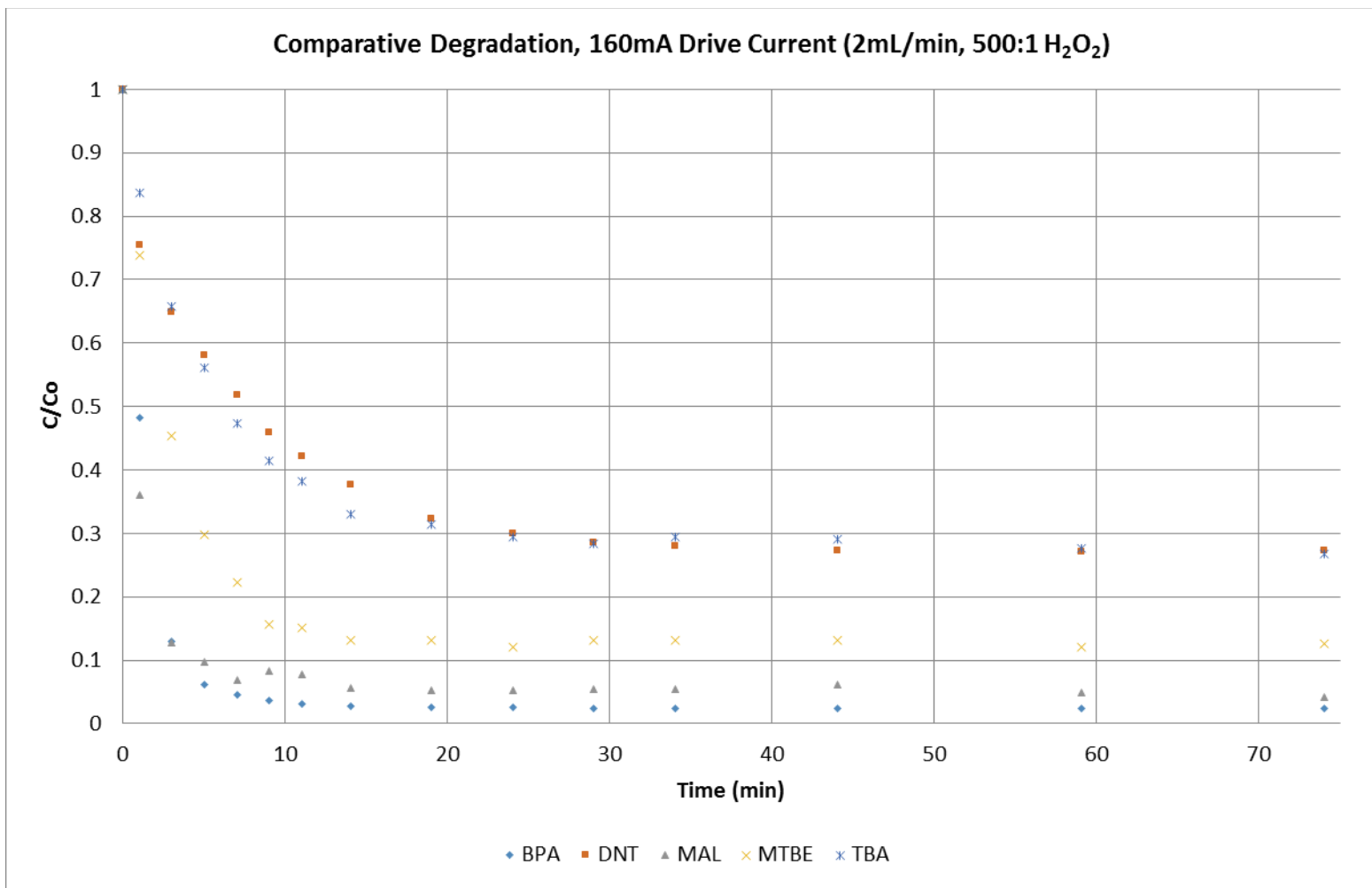


Figure A29. Comparative degradation of achromatic chemicals at 160 mA drive current.

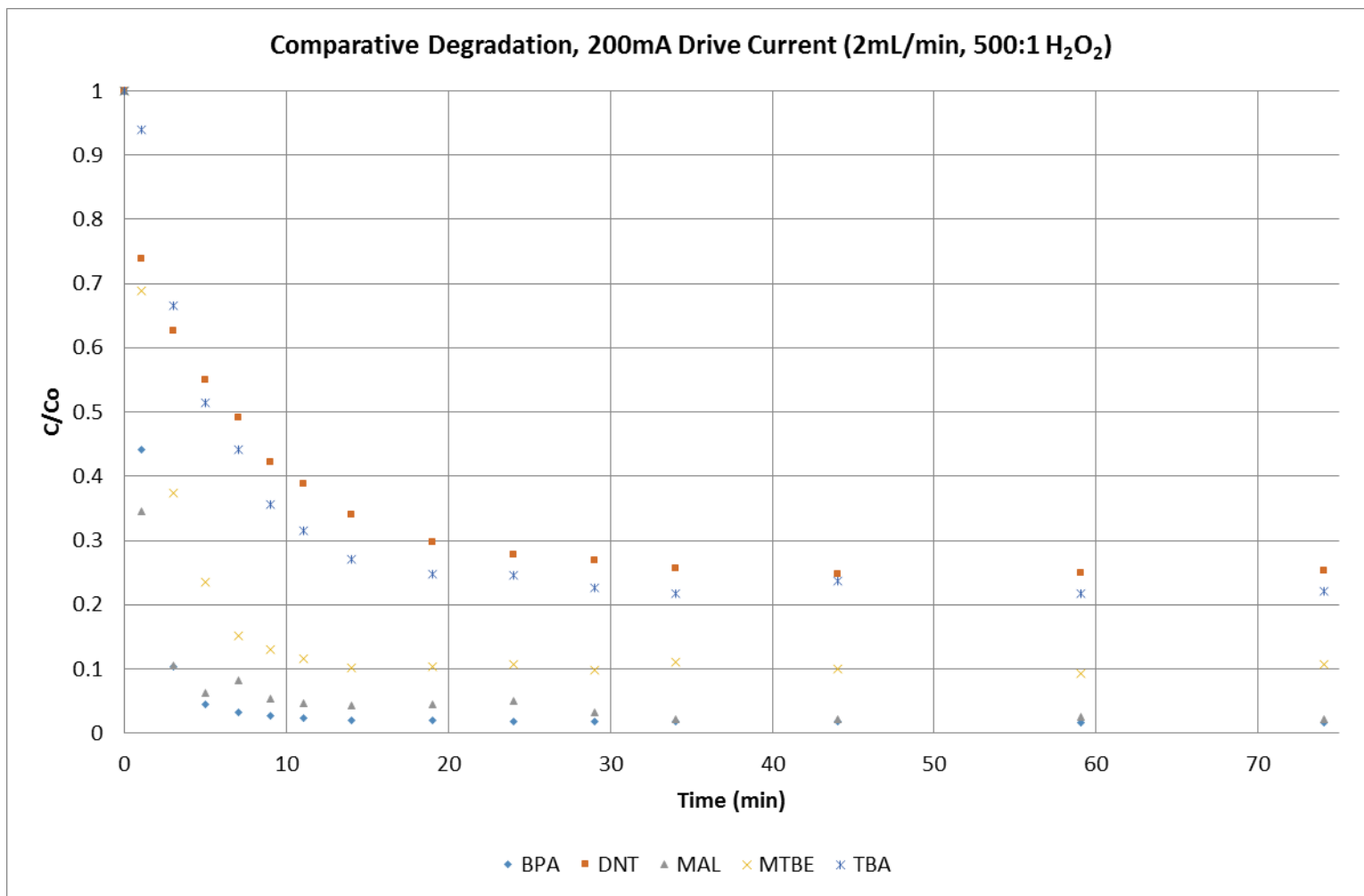


Figure A30. Comparative degradation of achromatic chemicals at 200 mA drive current.

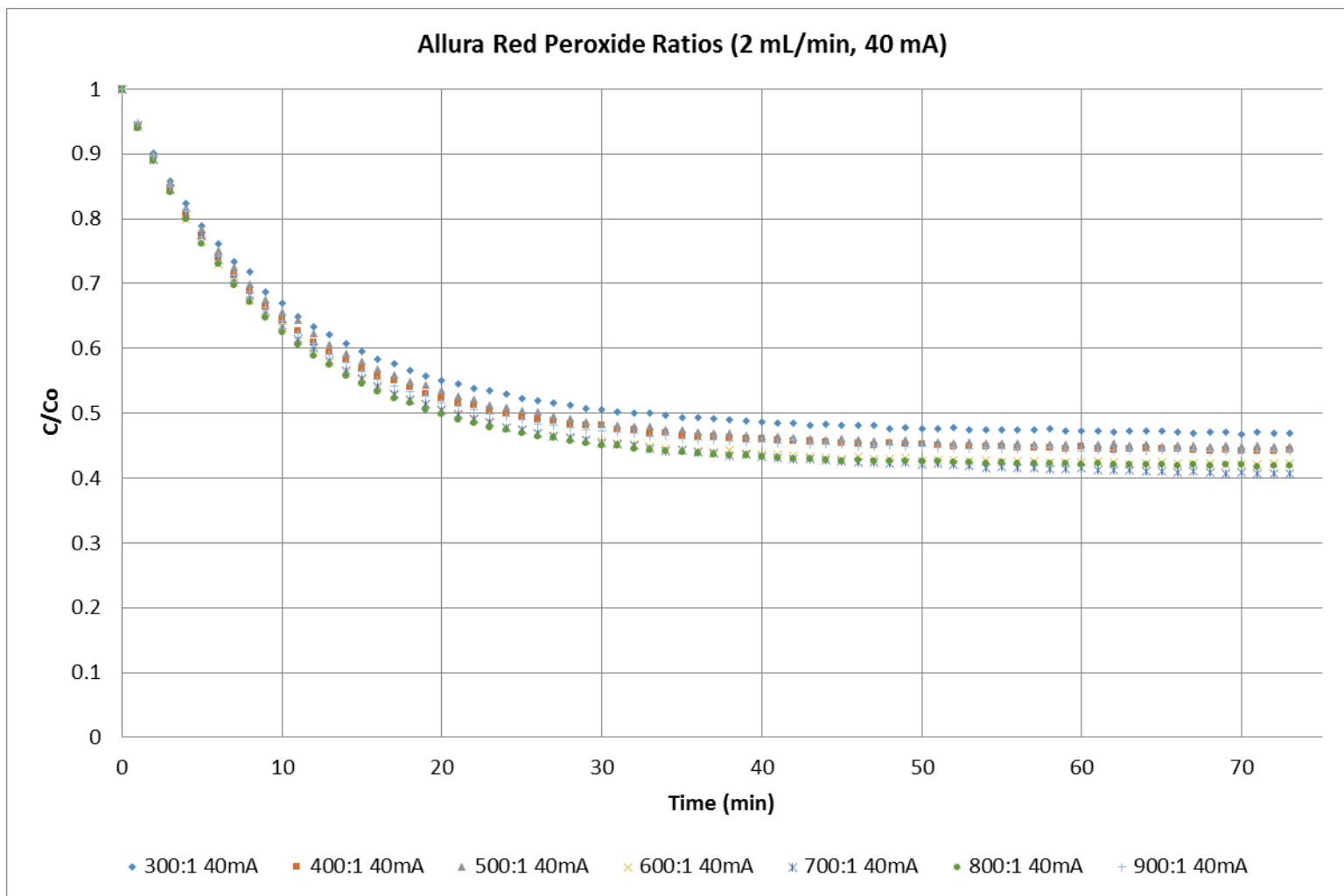


Figure A31. Allura Red degradation as a function of peroxide ratio, 40 mA.

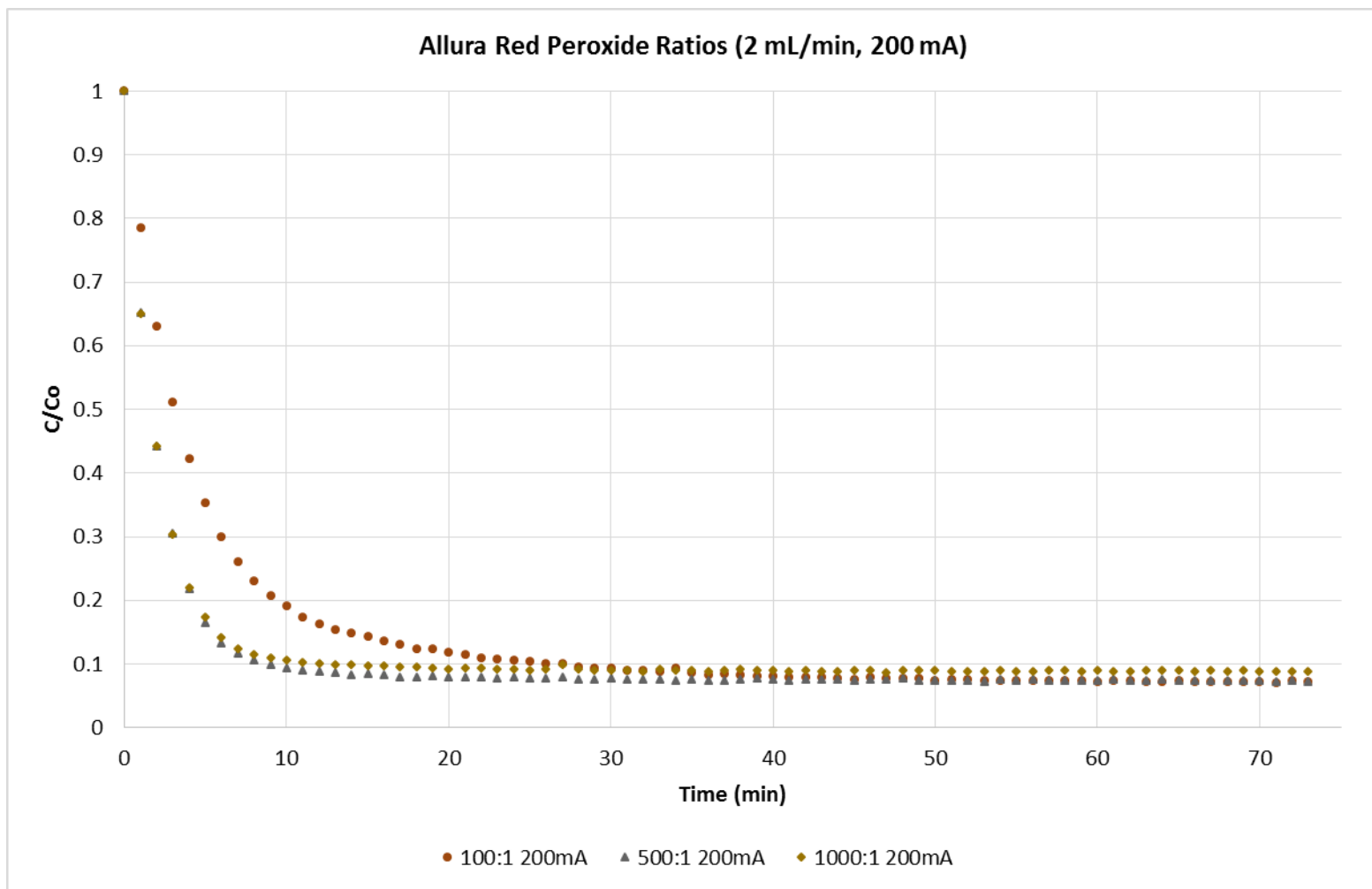


Figure A32. Allura Red degradation as a function of peroxide ratio, 200 mA.

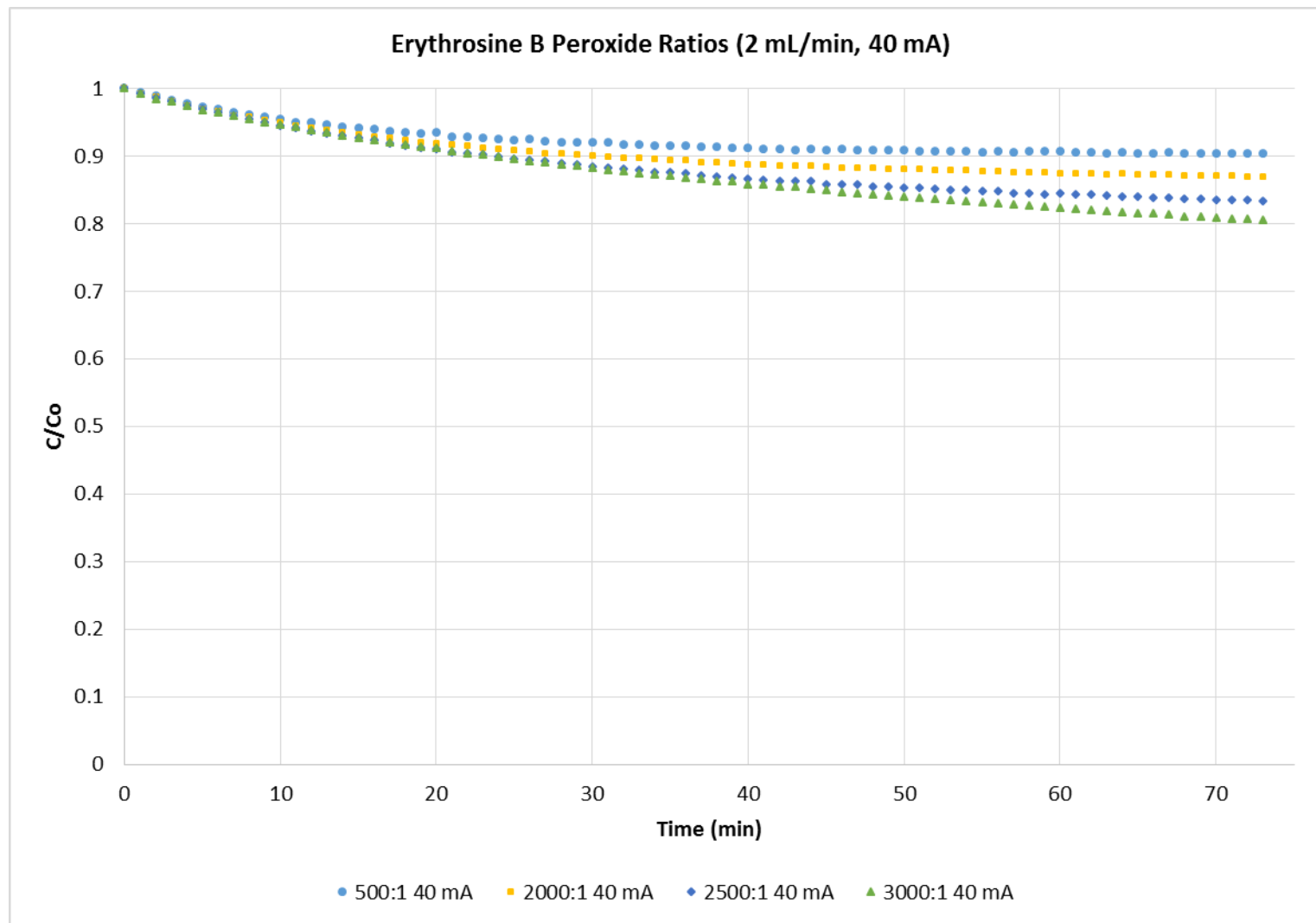


Figure A33. Erythrosine B degradation as a function of peroxide ratio, 40 mA.

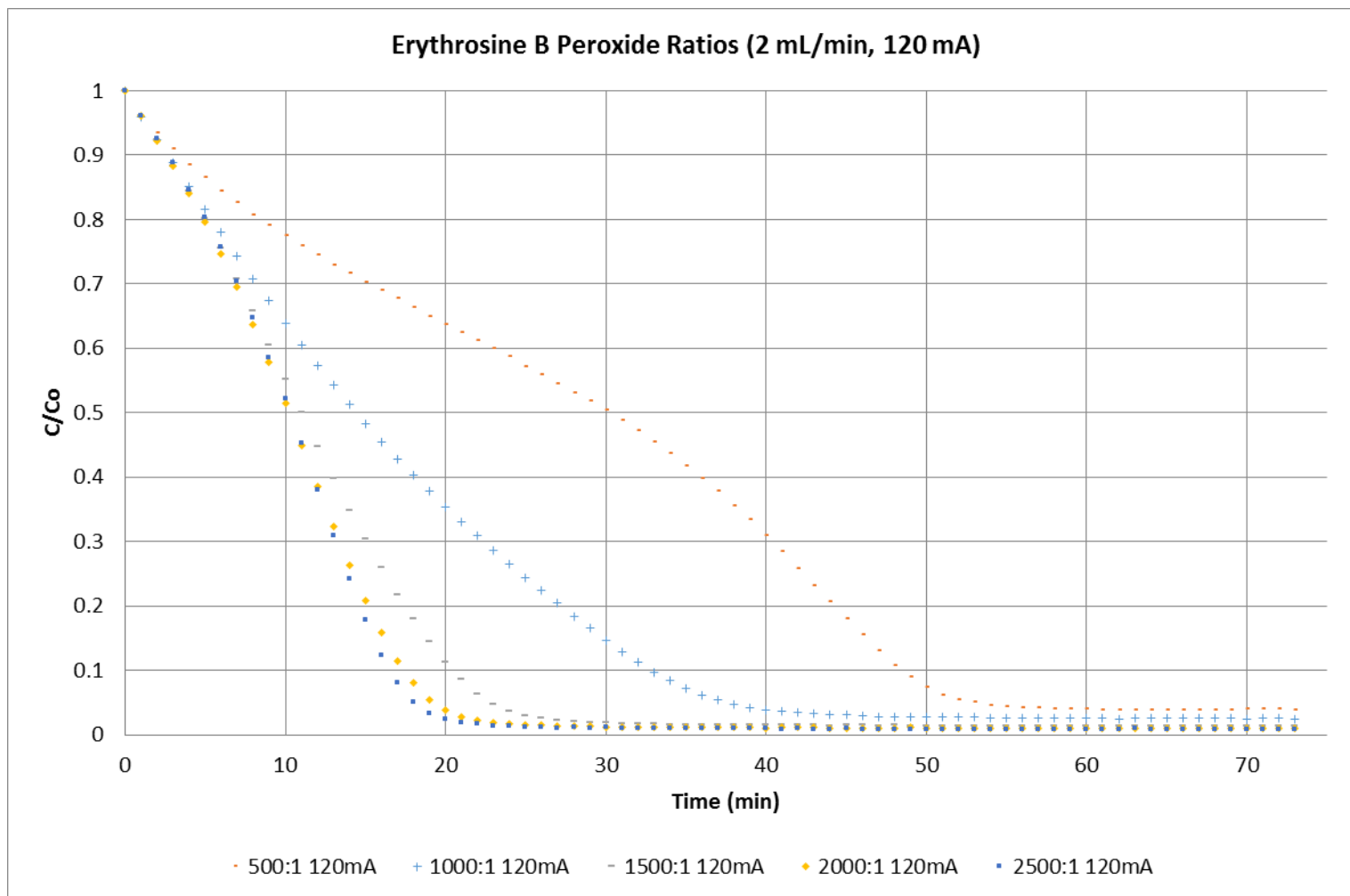


Figure A34. Erythrosine B degradation as a function of peroxide ratio, 120 mA.

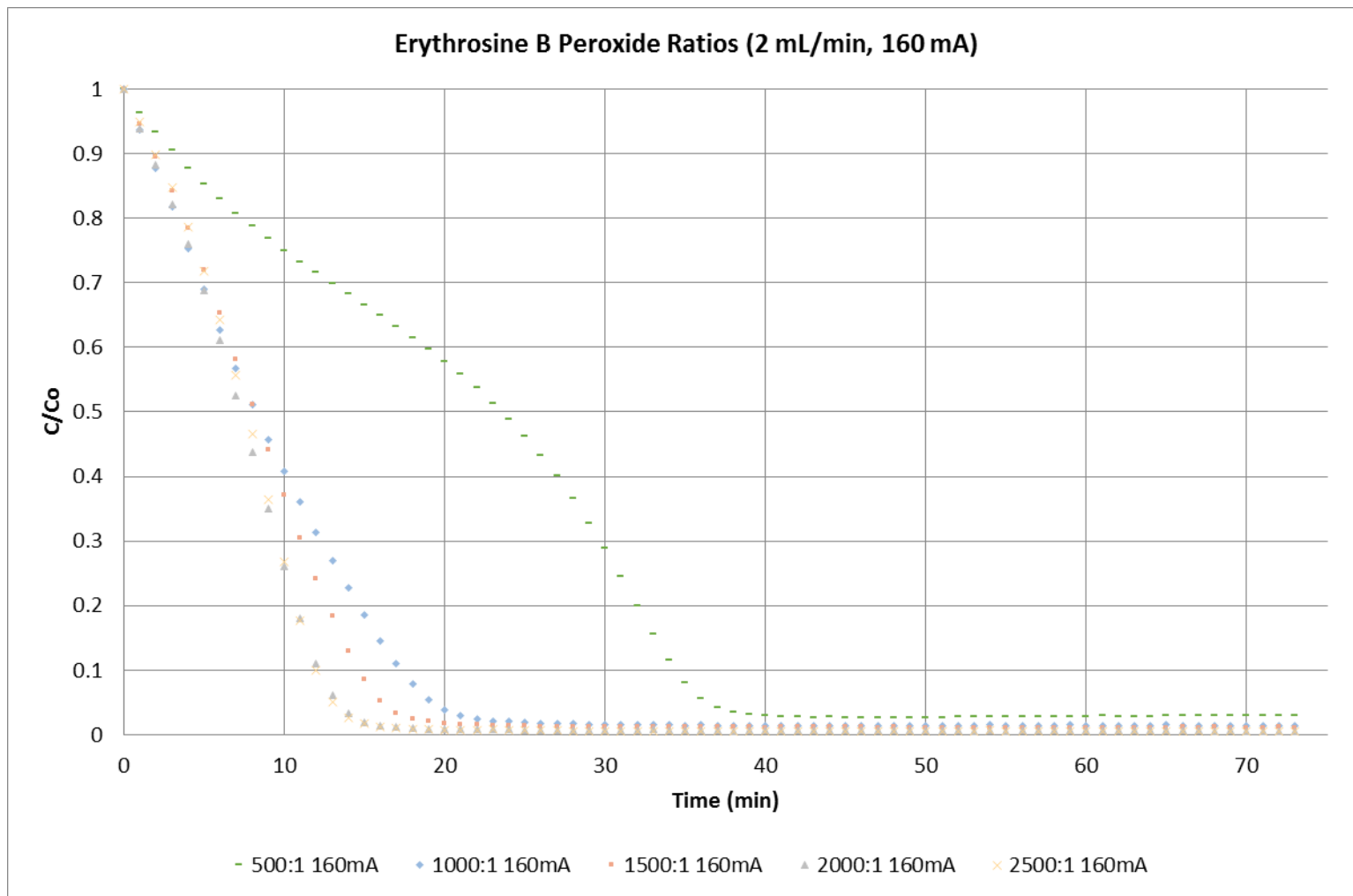


Figure A35. Erythrosine B degradation as a function of peroxide ratio, 160 mA.

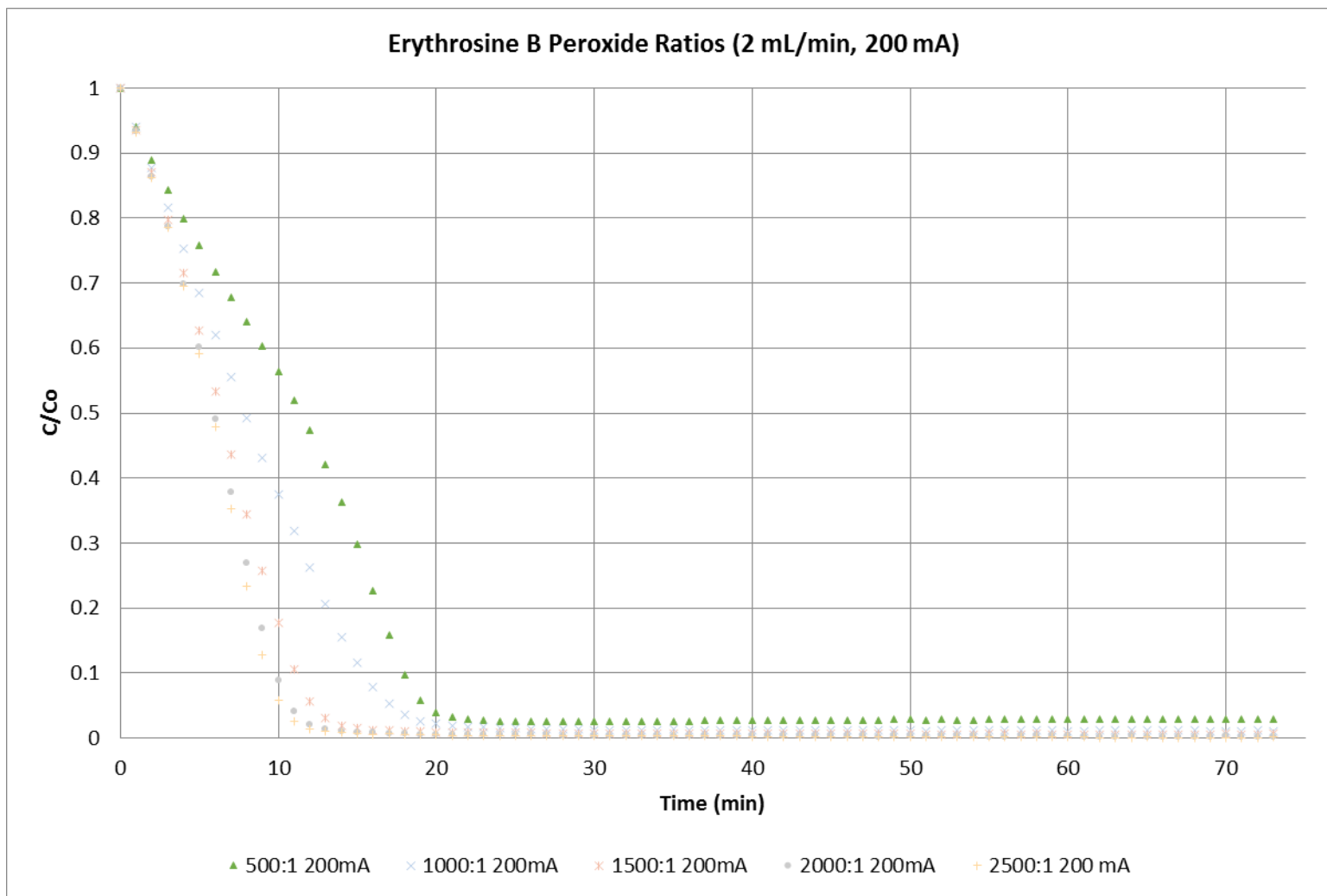


Figure A36. Erythrosine B degradation as a function of peroxide ratio, 200 mA.

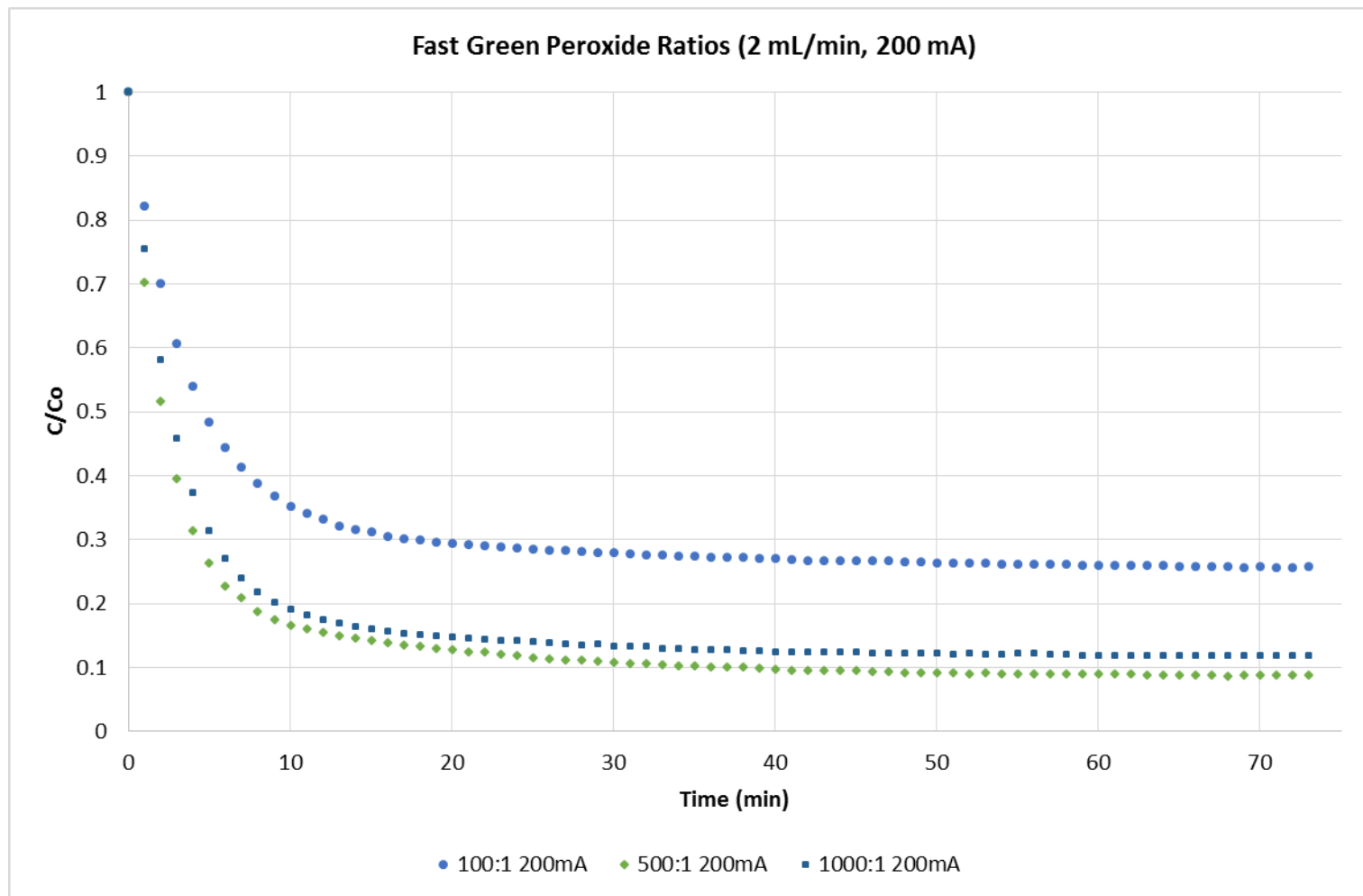


Figure A37. Fast Green degradation as a function of peroxide ratio, 200 mA.

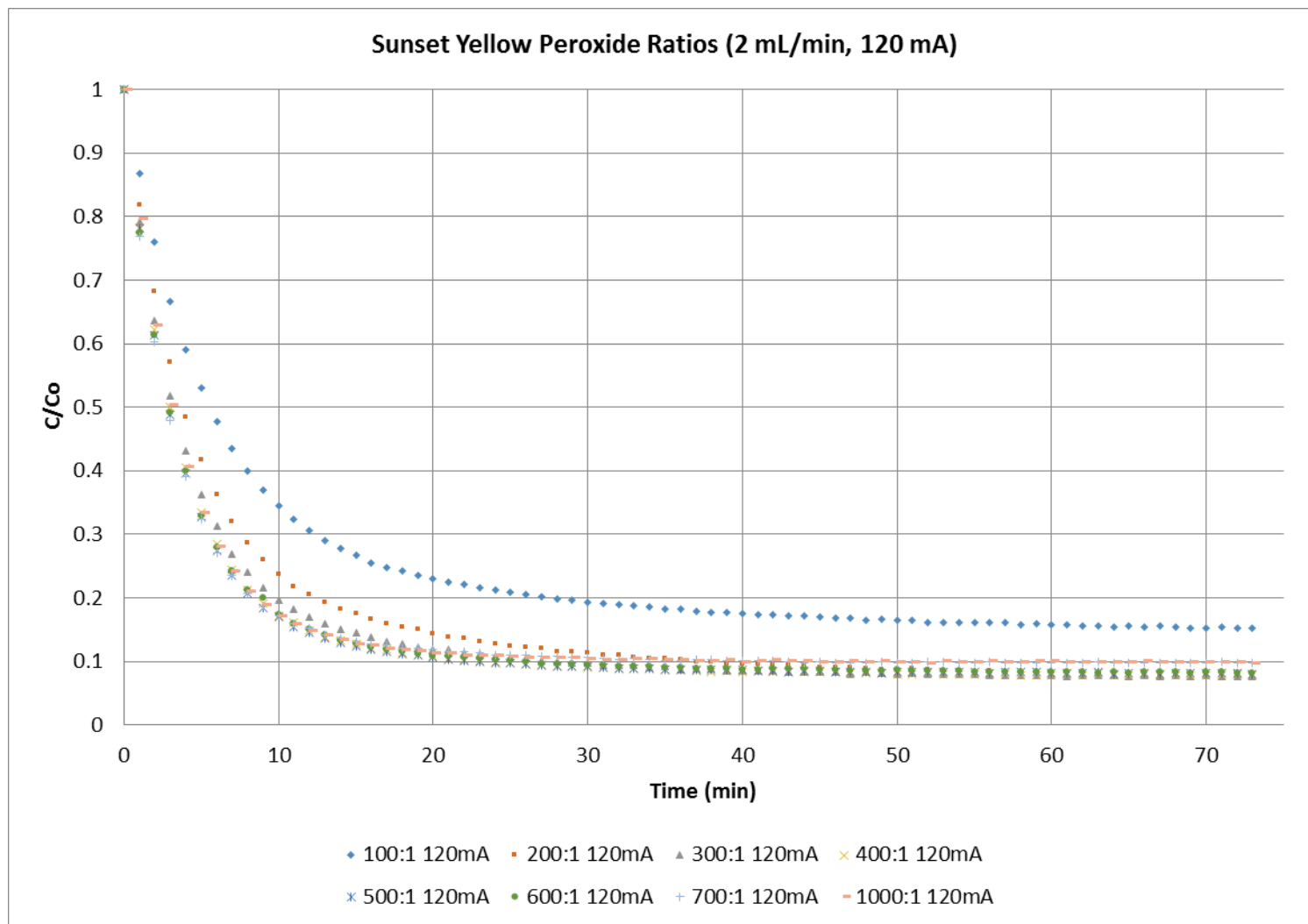


Figure A38. Sunset Yellow degradation as a function of peroxide ratio, 120 mA.

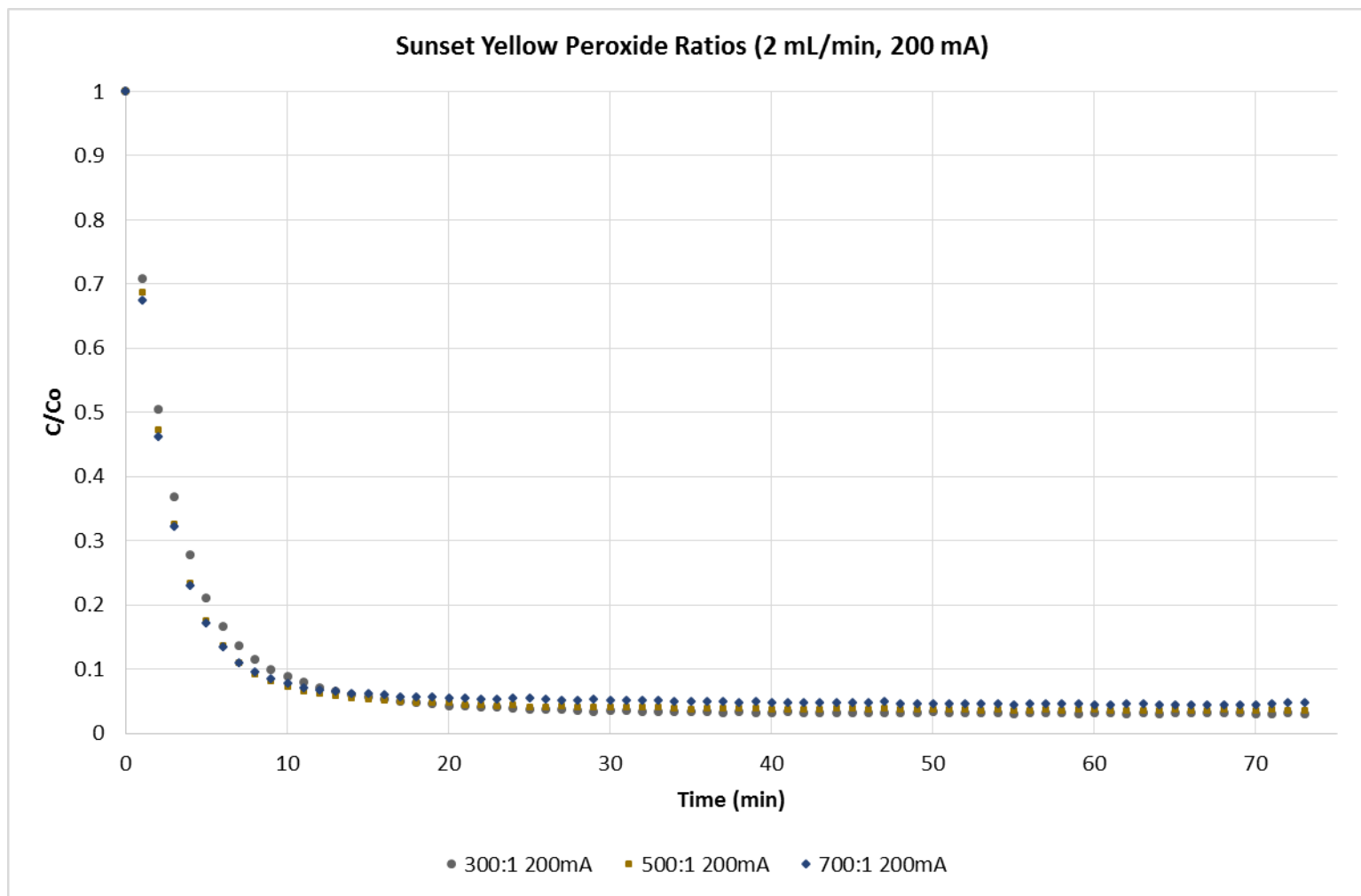


Figure A39. Sunset Yellow degradation as a function of peroxide ratio, 200 mA.

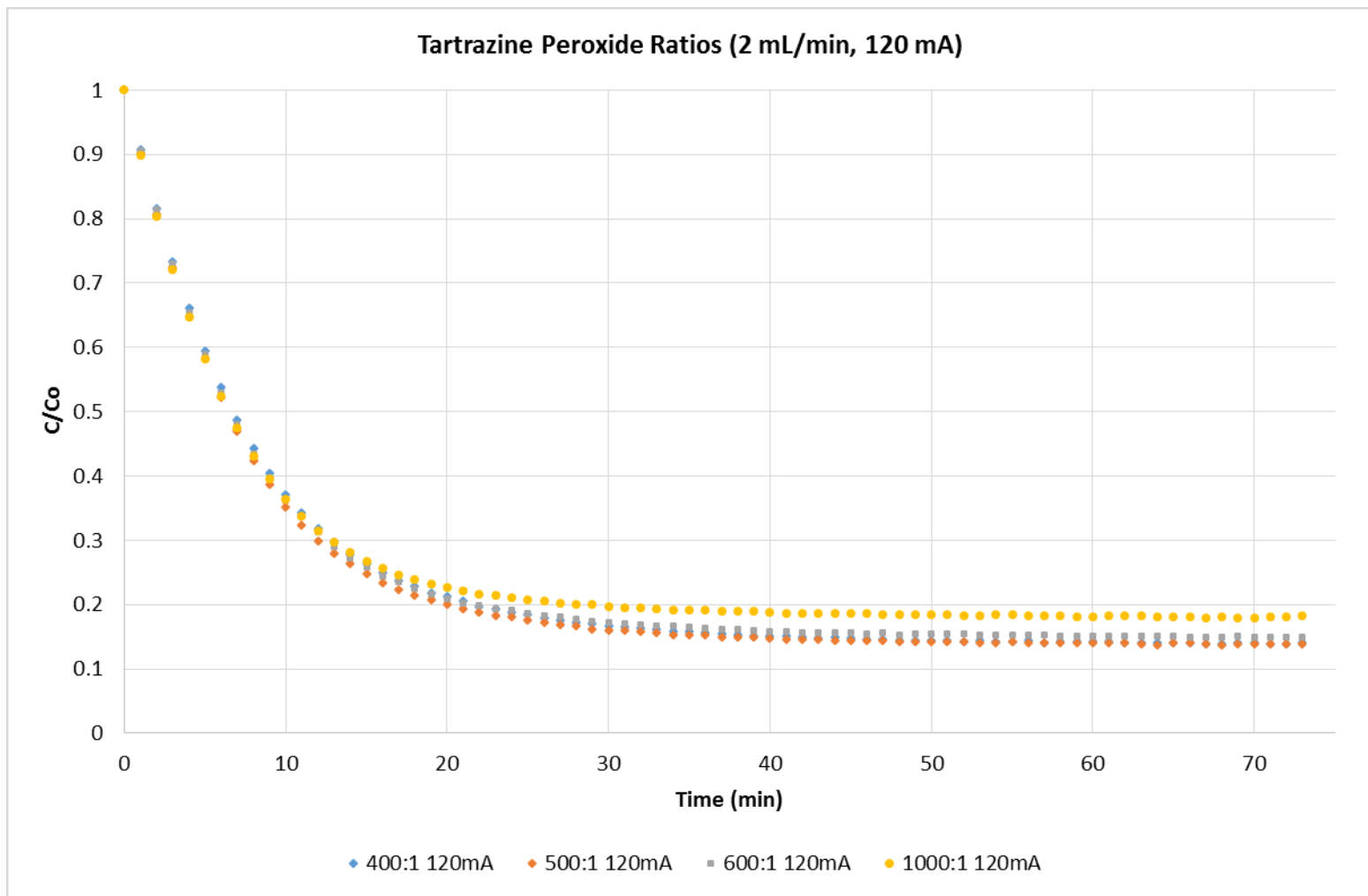


Figure A40. Tartrazine degradation as a function of peroxide ratio, 120 mA.

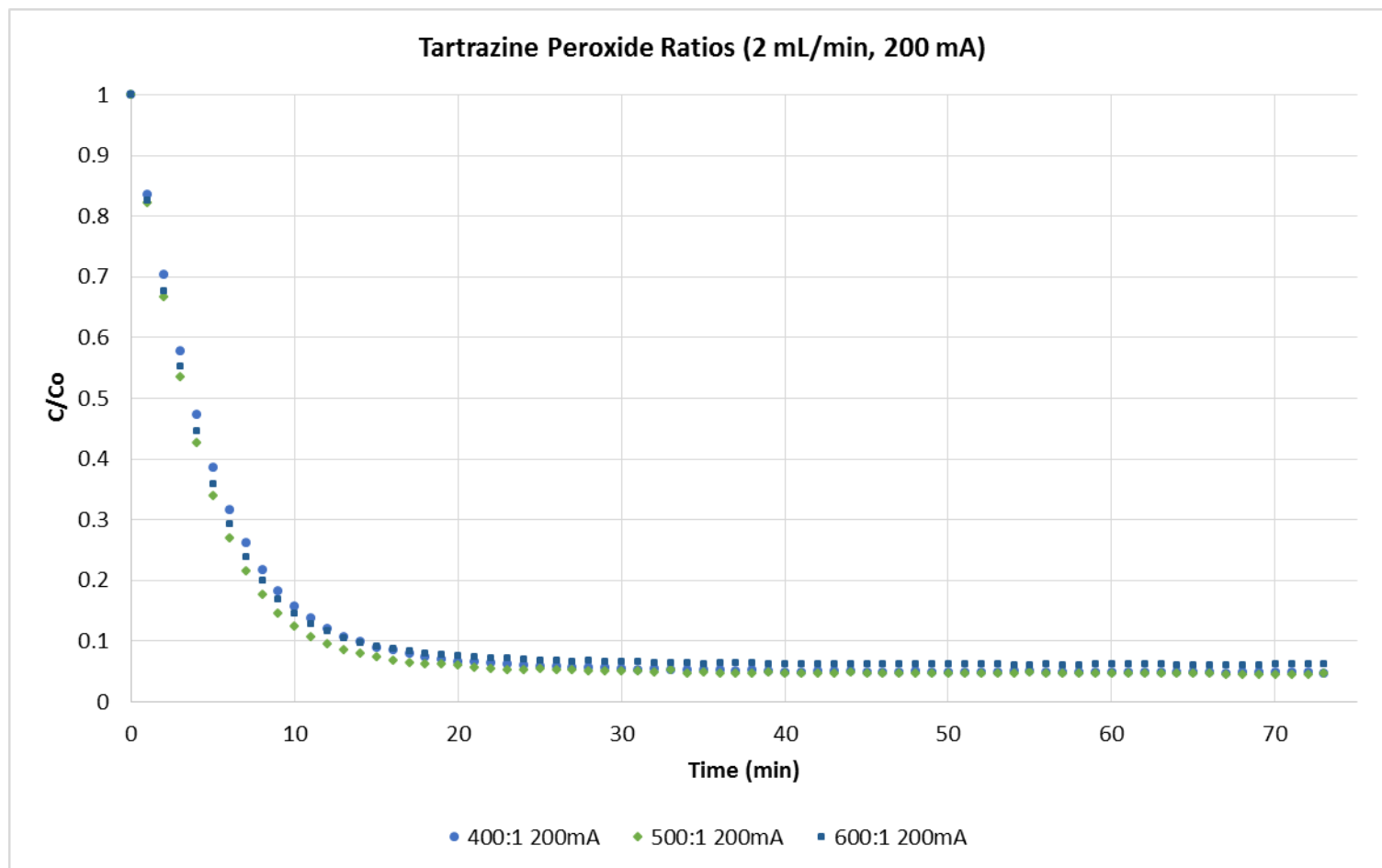


Figure A41. Tartrazine degradation as a function of peroxide ratio, 200 mA.

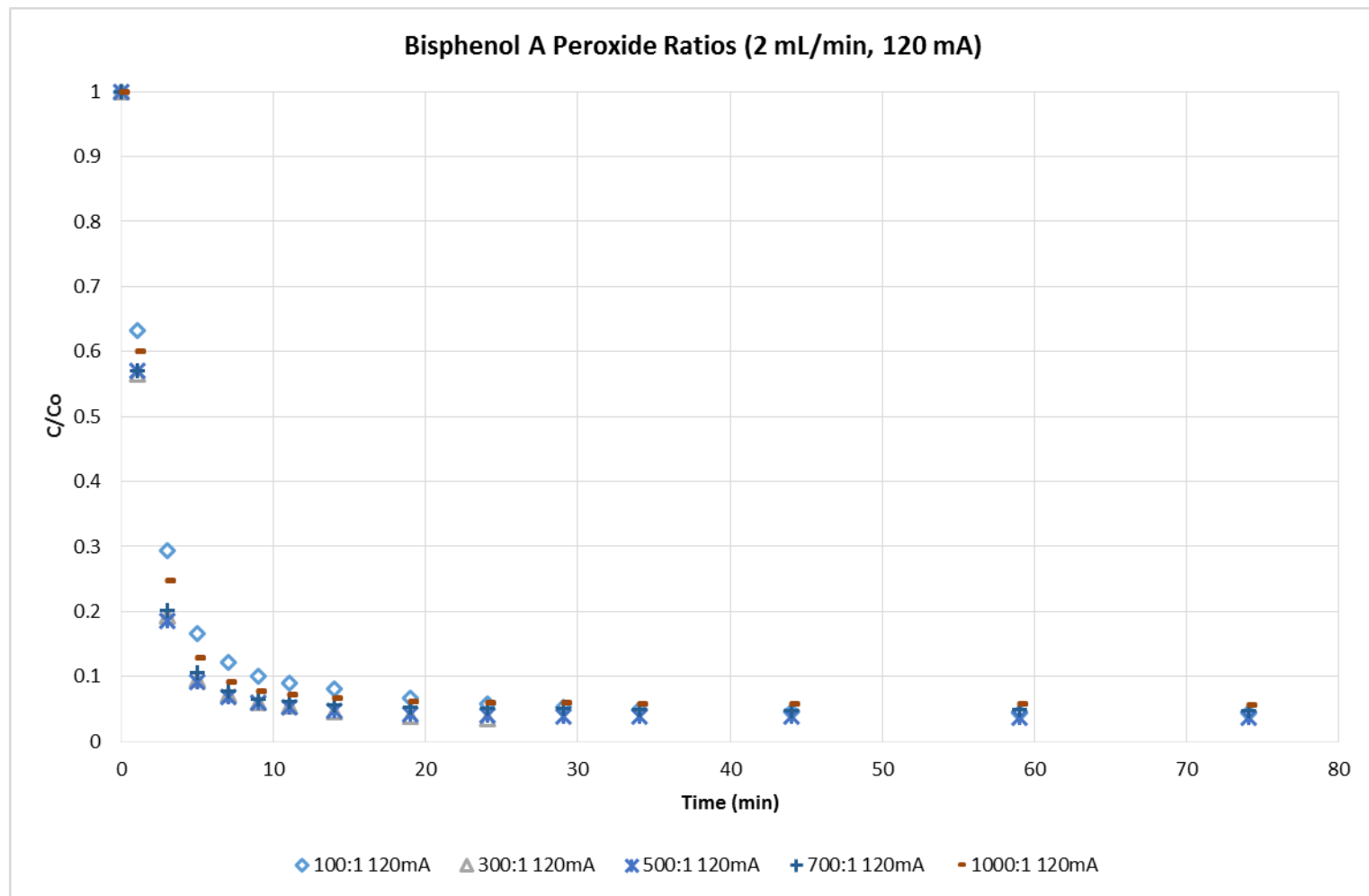


Figure A42. Bisphenol A degradation as a function of peroxide ratio, 120 mA.

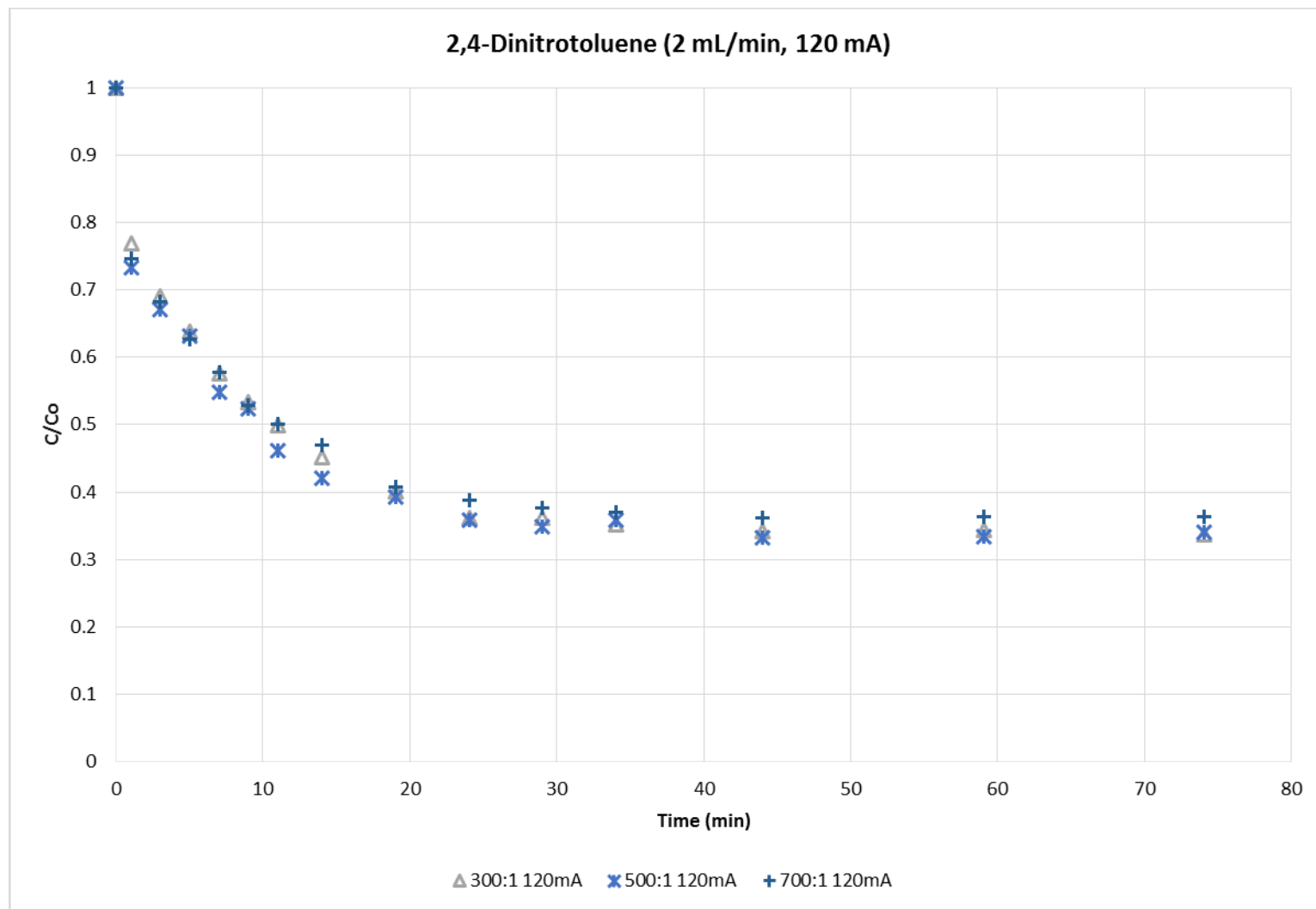


Figure A43. 2,4-DNT degradation as a function of peroxide ratio, 120 mA.

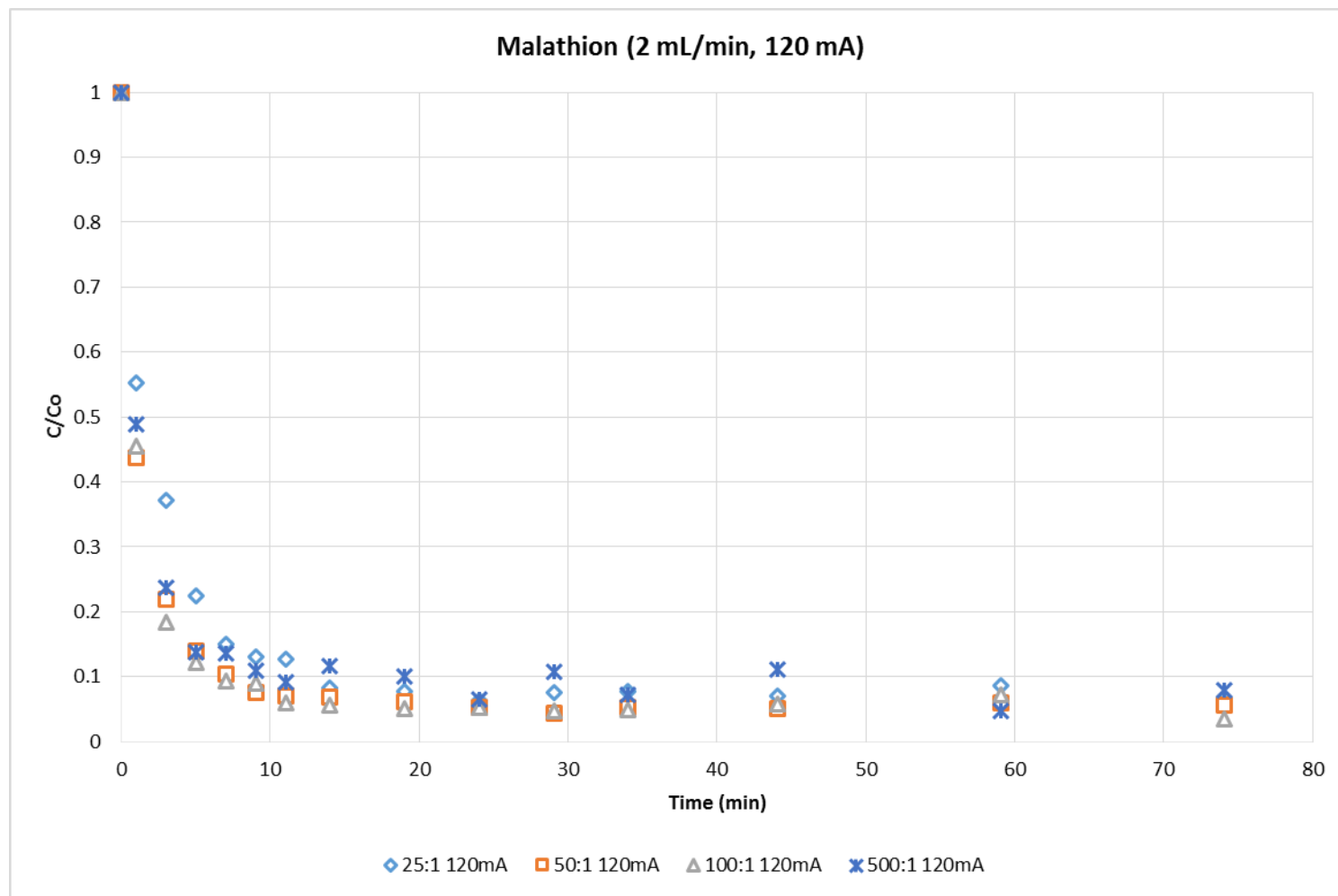


Figure A44. Malathion degradation as a function of peroxide ratio, 120 mA.

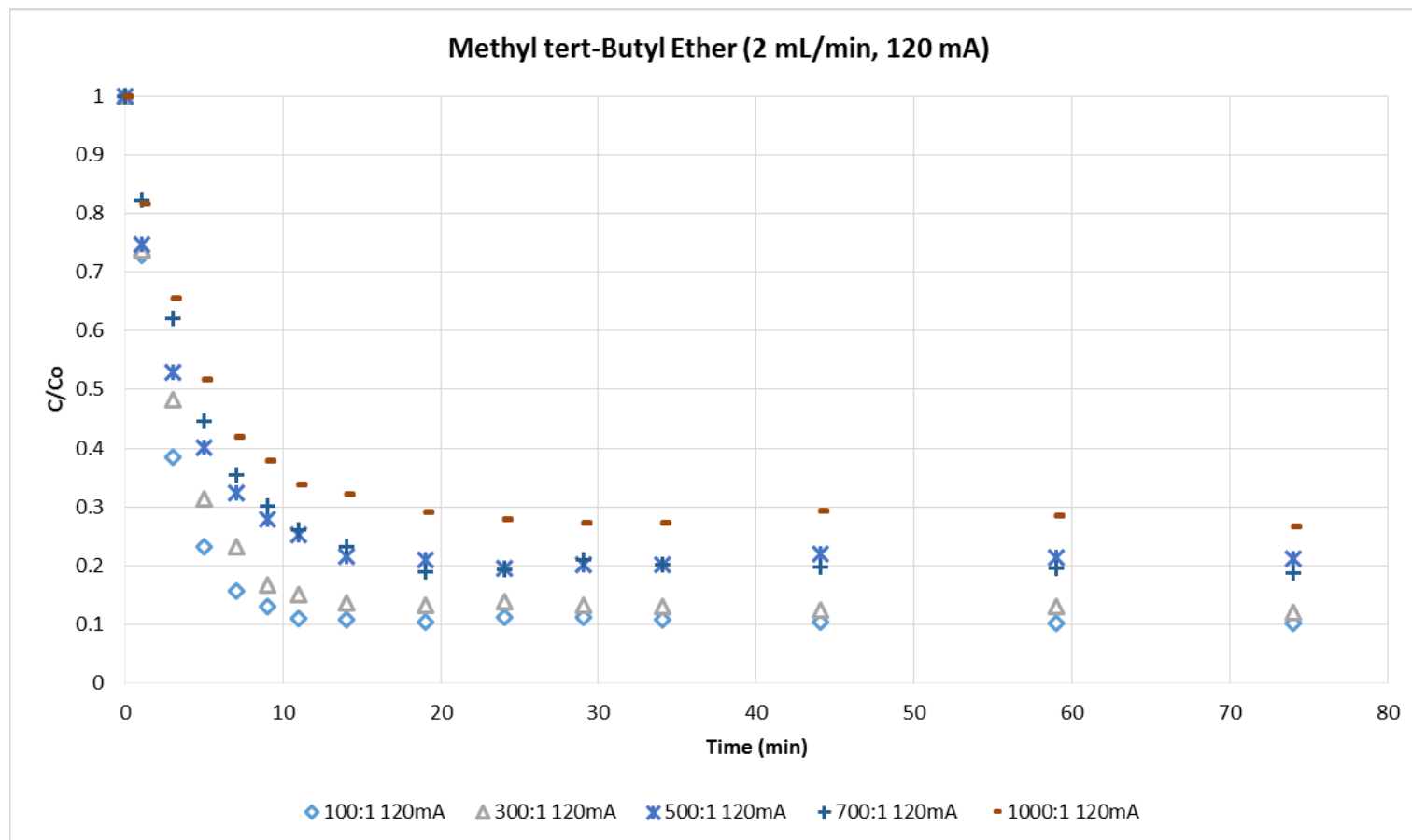


Figure A45. MTBE degradation as a function of peroxide ratio, 120 mA.

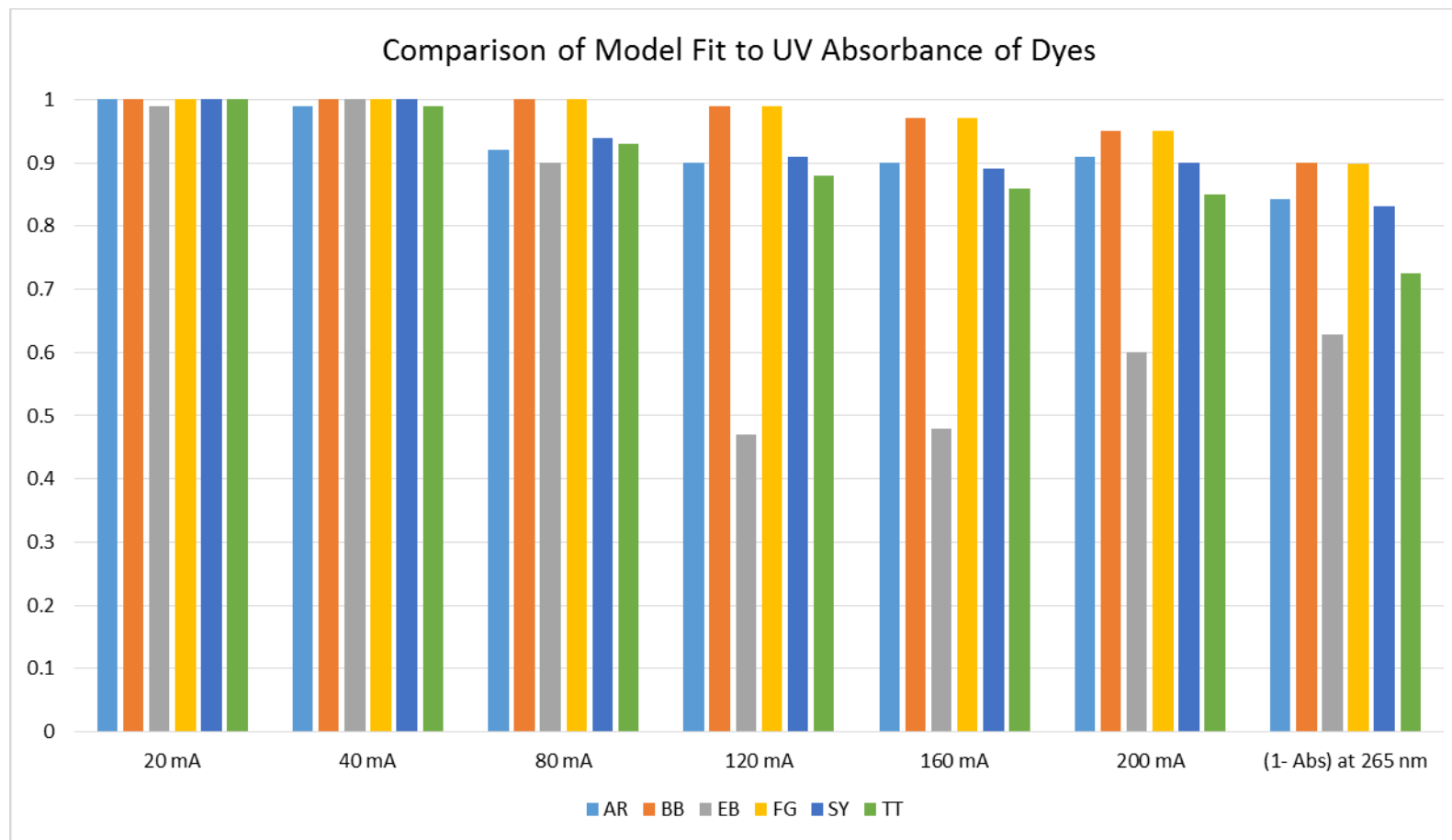


Figure A46. Comparative negative correlation between R^2 of model fit and absorptivity values.

VII. Appendix B

The table below and on subsequent pages contains an initial set of molecular descriptors generated from PubChem and Mold² for the dyes and achromatic chemicals utilized.

Descriptor	Description
PC1	Molecular Weight
PC2	Molecular Formula
PC3	XLogP3
PC4	Hydrogen Bond Donor Count
PC5	Hydrogen Bond Acceptor Count
PC6	Rotatable Bond Count
PC7	Exact Mass
PC8	Monoisotopic Mass
PC9	Topological Polar Surface Area
PC10	Heavy Atom Count
PC11	Formal Charge
PC12	Complexity
PC13	Isotope Atom Count
PC14	Defined Atom Stereocenter Count
PC15	Undefined Atom Stereocenter Count
PC16	Defined Bond Stereocenter Count
PC17	Undefined Bond Stereocenter Count
PC18	Covalently-Bonded Unit Count
D001	number of 6-membered aromatic rings (only carbon atoms)
D002	Number of 03-membered rings
D003	Number of 04-membered rings
D004	Number of 05-membered rings
D005	Number of 06-membered rings
D006	Number of 07-membered rings

D007	Number of 08-membered rings
D008	Number of 09-membered rings
D009	Number of 10-membered rings
D010	Number of 11-membered rings
D011	Number of 12-membered rings
D012	number of multiple bonds
D013	number of circuits structure
D014	number of rotatable bonds
D015	rotatable bond fraction
D016	number of double bonds
D017	number of aromatic bonds
D018	sum of conventional bond orders (H-depleted)
D019	number of Hydrogen
D020	number of Helium
D021	number of Lithium
D022	number of Beryllium
D023	number of Boron
D024	number of Carbon
D025	number of Nitrogen
D026	number of Oxygen
D027	number of Fluorine
D028	number of Neon
D029	number of Sodium
D030	number of Magnesium
D031	number of Aluminum
D032	number of Silicon
D033	number of Phosphorus
D034	number of Sulfur
D035	number of Chlorine

D036	number of Argon
D037	number of Potassium
D038	number of Calcium
D039	number of Scandium
D040	number of Titanium
D041	number of Vanadium
D042	number of Chromium
D043	number of Manganese
D044	number of Iron
D045	number of Cobalt
D046	number of Nickel
D047	number of Copper
D048	number of Zinc
D049	number of Gallium
D050	number of Germanium
D051	number of Arsenic
D052	number of Selenium
D053	number of Bromine
D054	number of Krypton
D055	number of Rubidium
D056	number of Strontium
D057	number of Yttrium
D058	number of Zirconium
D059	number of Niobium
D060	number of Molybdenum
D061	number of Technetium
D062	number of Ruthenium
D063	number of Rhodium
D064	number of Palladium

D065	number of Silver
D066	number of Cadmium
D067	number of Indium
D068	number of Tin
D069	number of Antimony
D070	number of Tellurium
D071	number of Iodine
D072	number of Xenon
D073	number of Cesium
D074	number of Barium
D075	number of Lanthanum
D076	number of Cerium
D077	number of Praseodymium
D078	number of Neodymium
D079	number of Promethium
D080	number of Samarium
D081	number of Europium
D082	number of Gadolinium
D083	number of Terbium
D084	number of Dysprosium
D085	number of Holmium
D086	number of Erbium
D087	number of Thulium
D088	number of Ytterbium
D089	number of Lutetium
D090	number of Hafnium
D091	number of Tantalum
D092	number of Tungsten
D093	number of Rhenium

D094	number of Osmium
D095	number of Iridium
D096	number of Platinum
D097	number of Gold
D098	number of Mercury
D099	number of Thallium
D100	number of Lead
D101	number of Bismuth
D102	number of Polonium
D103	number of Astatine
D104	number of Radon
D105	number of Francium
D106	number of Radium
D107	number of Actinium
D108	number of Thorium
D109	number of Protactinium
D110	number of Uranium
D111	number of Neptunium
D112	number of Plutonium
D113	number of Americium
D114	number of Curium
D115	number of Berkelium
D116	number of californium
D117	number of Einsteinium
D118	number of Fermium
D119	number of Mendelevium
D120	number of Nobelium
D121	number of Lawrencium
D122	Molecular weight

D123	Average of molecular weight
D124	number of atoms in each molecule
D125	number of none-Hydrogen atoms in each molecule
D126	number of bonds in each molecule
D127	number of none-Hydrogen bonds in each molecule
D128	number of rings in each molecule
D129	number of triple bonds in each molecule
D130	number of halogen atoms in each molecule
D131	molecular size index
D132	atomic composition index
D133	mean value of atomic composition index
D134	Branch index
D135	Molecular structure connectivity index
D136	Narumi-type topological index
D137	Harmonic topological index
D138	Geometric topological index
D139	Topological distance count order-3
D140	log of vertex distance path count
D141	average of vertex distance path count
D142	Balaban type of mean square vertex distance index
D143	sum of atomic Van Der Waals Carbon-scale
D144	mean atomic van der Waals Carbon-scale
D145	sum of atomic electronegativities Pauling-Scale on Carbon
D146	mean atomic electronegativities Pauling-scaled on Carbon
D147	sum of atomic electronegativities Sanderson-scaled on Carbon
D148	mean atomic electronegativity Sanderson-scaled on Carbon
D149	sum of atomic electronegativity Allred-Rochow-scaled on Carbon
D150	mean atomic electronegativity Allred-Rochow-scaled on Carbon
D151	sum of atomic polarizabilities scaled on Carbon-SP3

D152	mean atomic polarizability scaled on Carbon-SP3
D153	Zagreb order-1 index
D154	Zagreb order-1 index with value of valence vertex degrees
D155	Zagreb order-2 index
D156	Vertex degree topological index
D157	second Zagreb order-2 index with value of valence vertex degrees
D158	valence electrons of principal quantum index
D159	Schultz type Molecular Topological index
D160	Schultz type Molecular Topological Index of valence vertex degrees
D161	Molecular Topological Distance Index
D162	Molecular Topological Distance Index of valence vertex degrees
D163	Molecular size and branching index
D164	index of terminal vertex matrix
D165	Wiener index
D166	Average Path length in Wiener Index
D167	reciprocal index of Wiener distance matrix
D168	Harary index
D169	Index of Laplacian Matrix
D170	First No-Zero eigenvalue of Laplacian matrix
D171	Wiener-Path index
D172	reciprocal Wiener-Path index
D173	Mohar order-2 index
D174	Maximum Path Index
D175	Wiener Type Maximum Path Index
D176	reciprocal Wiener Type Maximum Path Index
D177	Minimum-Path/Maximum-Path Index
D178	All-Path Wiener - sum of the edges in the shortest paths between all pairs of non-hydrogen atoms
D179	Heteroatoms and Multiple bonds weighted Distance Matrix

D180	Mass Weighted Distance Matrix
D181	Index of Van Der Waals Weighted Distance Matrix
D182	Distance Matrix of Electronegativity Weighted with Electronegativities Pauling-Scale
D183	Distance Matrix of Electronegativity Weighted with Sanderson Electronegativities
D184	Distance Matrix of Electronegativity Weighted with Allred-Rochow Electronegativities
D185	Polarizability weighted distance matrix
D186	Average vertex distance connectivity index
D187	Balaban heteroatoms bonds weighted index
D188	Balaban mass weighted index
D189	Balaban van der Waals weighted index
D190	Balaban electronegativity weighted with Pauling-Scale index
D191	Balaban electronegativity weighted with Sanderson-Scale index
D192	Balaban electronegativity weighted with Allred-Rochow-Scale index
D193	Balaban-type polarizability weighted index
D194	maximal valence vertex electrotopological negative variation
D195	maximal valence vertex electrotopological positive variation
D196	Sum absolute electrotopological negative variation
D197	Electrotopological index
D198	sum electrotopological states index
D199	mean electrotopological states index
D200	vertex connectivity order-0 index
D201	vertex connectivity order-1 index
D202	vertex connectivity order-2 index
D203	vertex connectivity order-3 index
D204	vertex connectivity order-4 index
D205	vertex connectivity order-5 index
D206	average vertex connectivity order-0 index
D207	average vertex connectivity order-1 index
D208	average vertex connectivity order-2 index

D209	average vertex connectivity order-3 index
D210	average vertex connectivity order-4 index
D211	average vertex connectivity order-5 index
D212	valence vertex connectivity order-0 Index
D213	valence vertex connectivity order-1 Index
D214	valence vertex connectivity order-2 Index
D215	valence vertex connectivity order-3 Index
D216	valence vertex connectivity order-4 Index
D217	valence vertex connectivity order-5 Index
D218	average valence vertex connectivity order-0 Index
D219	average valence vertex connectivity order-1 Index
D220	average valence vertex connectivity order-2 Index
D221	average valence vertex connectivity order-3 Index
D222	average valence vertex connectivity order-4 Index
D223	average valence vertex connectivity order-5 Index
D224	principal quantum vertex connectivity order-0 Index
D225	principal quantum vertex connectivity order-1 Index
D226	principal quantum vertex connectivity order-2 Index
D227	principal quantum vertex connectivity order-3 Index
D228	principal quantum vertex connectivity order-4 Index
D229	principal quantum vertex connectivity order-5 Index
D230	aromaticity valence vertex connectivity order-1 index
D231	sum of valence vertex connectivity order-1 index
D232	reciprocal distance order-1 sum product index
D233	squared reciprocal distance order-1 sum product index
D234	Kier atom's 0-order path information index
D235	Kier 1-path index
D236	Kier 2-path index
D237	Kier 3-path index

D238	Molecular flexibility index
D239	atom's connectivity index in longest path
D240	sum of the longest path of the atom
D241	average longest path of the molecule
D242	average of deviation of average of longest path
D243	average of deviation of distance degree
D244	shortest path in the molecule
D245	shortest path centralization index
D246	maximum value of variation
D247	EXP2 of Path-distance / Walk-distance over all atoms
D248	EXP3 of Path-distance / Walk-distance over all atoms
D249	EXP4 of Path-distance / Walk-distance over all atoms
D250	EXP5 of Path-distance / Walk-distance over all atoms
D251	Petitjean index
D252	structure centric index
D253	structure lopping centric group index
D254	radial centric index
D255	vertex distance count equality index
D256	vertex distance count magnitude index
D257	total vertex distance count equality index
D258	total vertex distance count magnitude index
D259	mean of distance degree equality index
D260	mean of distance degree magnitude index
D261	information of vertex degree equality index
D262	information of bonds index
D263	vertex distance path count index
D264	complexity vertex distance path count index
D265	Vertex distance information index
D266	relative of vertex distance information index

D267	mean of vertex distance information index
D268	extended of vertex distance information index
D269	information content order-0 index
D270	information content order-1 index
D271	information content order-2 index
D272	information content order-3 index
D273	information content order-4 index
D274	information content order-5 index
D275	total information content order-0 index
D276	total information content order-1 index
D277	total information content order-2 index
D278	total information content order-3 index
D279	total information content order-4 index
D280	total information content order-5 index
D281	structural information content order-0 index
D282	structural information content order-1 index
D283	structural information content order-2 index
D284	structural information content order3 index
D285	structural information content order-4 index
D286	structural information content order-5 index
D287	Complementary information content order-0 index
D288	Complementary information content order-1 index
D289	Complementary information content order-2 index
D290	Complementary information content order3 index
D291	Complementary information content order-4 index
D292	Complementary information content order-5 index
D293	bond information content order-0 index
D294	bond information content order-1 index
D295	bond information content order-2 index

D296	bond information content order3 index
D297	bond information content order-4 index
D298	bond information content order-5 index
D299	The largest eigenvalue
D300	spanning tree with log value
D301	Maximum eigenvalue weighted by Heteroatoms and Multiple bonds Matrix
D302	Maximum eigenvalue weighted by mass distance matrix
D303	Maximum eigenvalue weighted by van der Waals distance matrix
D304	Maximum eigenvalue weighted by polarizability distance matrix
D305	Maximum eigenvalue weighted by electronegativity Pauling-Scale distance matrix
D306	Maximum eigenvalue weighted by electronegativity Sanderson-Scale weighted distance matrix
D307	Maximum eigenvalue weighted by electronegativity Allred-Rochow-Scale distance matrix
D308	Sum eigenvalue weighted by Heteroatoms and Multiple bonds Distance Matrix
D309	Sum eigenvalue weighted by mass distance matrix
D310	Sum eigenvalue weighted by van der Waals distance matrix
D311	Sum eigenvalue weighted by polarizability distance matrix
D312	Sum eigenvalue weighted by electronegativity Pauling-Scale distance matrix
D313	Sum eigenvalue weighted by electronegativity Sanderson-Scale distance matrix
D314	Sum eigenvalue weighted by electronegativity Allred-Rochow-Scale distance matrix
D315	Sum absolute eigenvalue weighted by Heteroatoms and Multiple bonds Distance Matrix
D316	Sum absolute eigenvalue weighted by mass distance matrix
D317	Sum absolute eigenvalue weighted by van der Waals distance matrix
D318	Sum absolute eigenvalue weighted by polarizability distance matrix
D319	Sum absolute eigenvalue weighted by electronegativity Pauling-Scale distance matrix
D320	Sum absolute eigenvalue weighted by electronegativity Sanderson-Scale distance matrix
D321	Sum absolute eigenvalue weighted by electronegativity Allred-Rochow-Scale distance matrix

D322	distance+detour path with ring index of order 3
D323	distance+detour path with ring index of order 4
D324	distance+detour path with ring index of order 5
D325	distance+detour path with ring index of order 6
D326	distance+detour path with ring index of order 7
D327	distance+detour path with ring index of order 8
D328	distance+detour path with ring index of order 9
D329	distance+detour path with ring index of order 10
D330	distance+detour path with ring index of order 11
D331	distance+detour path with ring index of order 12
D332	distance+detour path on ring index of order 3 (circuits)
D333	distance+detour path on ring index of order 4 (circuits)
D334	distance+detour path on ring index of order 5 (circuits)
D335	distance+detour path on ring index of order 6 (circuits)
D336	distance+detour path on ring index of order 7 (circuits)
D337	distance+detour path on ring index of order 8 (circuits)
D338	distance+detour path on ring index of order 9 (circuits)
D339	distance+detour path on ring index of order 10 (circuits)
D340	distance+detour path on ring index of order 11 (circuits)
D341	distance+detour path on ring index of order 12 (circuits)
D342	molecular topological path index of order 02
D343	molecular topological path index of order 03
D344	molecular topological path index of order 04
D345	molecular topological path index of order 05
D346	molecular topological path index of order 06
D347	molecular topological path index of order 07
D348	molecular topological path index of order 08
D349	molecular topological path index of order 09
D350	molecular topological path index of order 10

D351	molecular topological multiple path index of order 03
D352	molecular topological multiple path index of order 04
D353	molecular topological multiple path index of order 05
D354	molecular topological multiple path index of order 06
D355	molecular topological multiple path index of order 07
D356	molecular topological multiple path index of order 08
D357	molecular topological multiple path index of order 09
D358	molecular topological multiple path index of order 10
D359	molecular topological all path index
D360	conventional bond index
D361	ratio of convention bonds with total path counts
D362	ratio of difference of conventional bonds and total path counts
D363	Randic index
D364	Balaban All-Path index
D365	Balaban Short-Path index
D366	sum of topological distance between the vertices N and N
D367	sum of topological distance between the vertices N and P
D368	sum of topological distance between the vertices N and O
D369	sum of topological distance between the vertices N and S
D370	sum of topological distance between the vertices N and F
D371	sum of topological distance between the vertices N and Cl
D372	sum of topological distance between the vertices N and Br
D373	sum of topological distance between the vertices N and I
D374	sum of topological distance between the vertices O and O
D375	sum of topological distance between the vertices O and S
D376	sum of topological distance between the vertices O and P
D377	sum of topological distance between the vertices O and F
D378	sum of topological distance between the vertices O and Cl
D379	sum of topological distance between the vertices O and Br

D380	sum of topological distance between the vertices O and I
D381	sum of topological distance between the vertices S and S
D382	sum of topological distance between the vertices S and P
D383	sum of topological distance between the vertices S and F
D384	sum of topological distance between the vertices S and Cl
D385	sum of topological distance between the vertices S and Br
D386	sum of topological distance between the vertices S and I
D387	sum of topological distance between the vertices P and P
D388	sum of topological distance between the vertices P and F
D389	sum of topological distance between the vertices P and Cl
D390	sum of topological distance between the vertices P and Br
D391	sum of topological distance between the vertices P and I
D392	sum of topological distance between the vertices F and F
D393	sum of topological distance between the vertices F and Cl
D394	sum of topological distance between the vertices F and Br
D395	sum of topological distance between the vertices F and I
D396	sum of topological distance between the vertices Cl and Cl
D397	sum of topological distance between the vertices Cl and Br
D398	sum of topological distance between the vertices Cl and I
D399	sum of topological distance between the vertices Br and Br
D400	sum of topological distance between the vertices Br and I
D401	sum of topological distance between the vertices I and I
D402	walk count order-01
D403	walk count order-02
D404	walk count order-03
D405	walk count order-04
D406	walk count order-05
D407	walk count order-06
D408	walk count max-10 steps

D409	walk-returning count order-1
D410	walk-returning count order-2
D411	walk-returning count order-3
D412	walk-returning count order-4
D413	walk-returning count order-5
D414	walk-returning count order-6
D415	topological structure autocorrelation length-1 weighted by atomic masses
D416	topological structure autocorrelation length-2 weighted by atomic masses
D417	topological structure autocorrelation length-3 weighted by atomic masses
D418	topological structure autocorrelation length-4 weighted by atomic masses
D419	topological structure autocorrelation length-5 weighted by atomic masses
D420	topological structure autocorrelation length-6 weighted by atomic masses
D421	topological structure autocorrelation length-7 weighted by atomic masses
D422	topological structure autocorrelation length-8 weighted by atomic masses
D423	topological structure autocorrelation length-1 weighted by atomic van der Waals volumes
D424	topological structure autocorrelation length-2 weighted by atomic van der Waals volumes
D425	topological structure autocorrelation length-3 weighted by atomic van der Waals volumes
D426	topological structure autocorrelation length-4 weighted by atomic van der Waals volumes
D427	topological structure autocorrelation length-5 weighted by atomic van der Waals volumes
D428	topological structure autocorrelation length-6 weighted by atomic van der Waals volumes
D429	topological structure autocorrelation length-7 weighted by atomic van der Waals volumes
D430	topological structure autocorrelation length-8 weighted by atomic van der Waals volumes
D431	topological structure autocorrelation length-1 weighted by atomic Sanderson electronegativities

D432	topological structure autocorrelation length-2 weighted by atomic Sanderson electronegativities
D433	topological structure autocorrelation length-3 weighted by atomic Sanderson electronegativities
D434	topological structure autocorrelation length-4 weighted by atomic Sanderson electronegativities
D435	topological structure autocorrelation length-5 weighted by atomic Sanderson electronegativities
D436	topological structure autocorrelation length-6 weighted by atomic Sanderson electronegativities
D437	topological structure autocorrelation length-7 weighted by atomic Sanderson electronegativities
D438	topological structure autocorrelation length-8 weighted by atomic Sanderson electronegativities
D439	topological structure autocorrelation length-1 weighted by atomic polarizabilities
D440	topological structure autocorrelation length-2 weighted by atomic polarizabilities
D441	topological structure autocorrelation length-3 weighted by atomic polarizabilities
D442	topological structure autocorrelation length-4 weighted by atomic polarizabilities
D443	topological structure autocorrelation length-5 weighted by atomic polarizabilities
D444	topological structure autocorrelation length-6 weighted by atomic polarizabilities
D445	topological structure autocorrelation length-7 weighted by atomic polarizabilities
D446	topological structure autocorrelation length-8 weighted by atomic polarizabilities
D447	Geary topological structure autocorrelation length-1 weighted by atomic masses
D448	Geary topological structure autocorrelation length-2 weighted by atomic masses
D449	Geary topological structure autocorrelation length-3 weighted by atomic masses
D450	Geary topological structure autocorrelation length-4 weighted by atomic masses
D451	Geary topological structure autocorrelation length-5 weighted by atomic masses
D452	Geary topological structure autocorrelation length-6 weighted by atomic masses
D453	Geary topological structure autocorrelation length-7 weighted by atomic masses
D454	Geary topological structure autocorrelation length-8 weighted by atomic masses
D455	Geary topological structure autocorrelation length-1 weighted by atomic van der Waals volumes

D456	Geary topological structure autocorrelation length-2 weighted by atomic van der Waals volumes
D457	Geary topological structure autocorrelation length-3 weighted by atomic van der Waals volumes
D458	Geary topological structure autocorrelation length-4 weighted by atomic van der Waals volumes
D459	Geary topological structure autocorrelation length-5 weighted by atomic van der Waals volumes
D460	Geary topological structure autocorrelation length-6 weighted by atomic van der Waals volumes
D461	Geary topological structure autocorrelation length-7 weighted by atomic van der Waals volumes
D462	Geary topological structure autocorrelation length-8 weighted by atomic van der Waals volumes
D463	Geary topological structure autocorrelation length-1 weighted by atomic Sanderson electronegativities
D464	Geary topological structure autocorrelation length-2 weighted by atomic Sanderson electronegativities
D465	Geary topological structure autocorrelation length-3 weighted by atomic Sanderson electronegativities
D466	Geary topological structure autocorrelation length-4 weighted by atomic Sanderson electronegativities
D467	Geary topological structure autocorrelation length-5 weighted by atomic Sanderson electronegativities
D468	Geary topological structure autocorrelation length-6 weighted by atomic Sanderson electronegativities
D469	Geary topological structure autocorrelation length-7 weighted by atomic Sanderson electronegativities
D470	Geary topological structure autocorrelation length-8 weighted by atomic Sanderson electronegativities
D471	Geary topological structure autocorrelation length-1 weighted by atomic polarizabilities
D472	Geary topological structure autocorrelation length-2 weighted by atomic polarizabilities
D473	Geary topological structure autocorrelation length-3 weighted by atomic polarizabilities

D474	Geary topological structure autocorrelation length-4 weighted by atomic polarizabilities
D475	Geary topological structure autocorrelation length-5 weighted by atomic polarizabilities
D476	Geary topological structure autocorrelation length-6 weighted by atomic polarizabilities
D477	Geary topological structure autocorrelation length-7 weighted by atomic polarizabilities
D478	Geary topological structure autocorrelation length-8 weighted by atomic polarizabilities
D479	Moran topological structure autocorrelation length-1 weighted by atomic masses
D480	Moran topological structure autocorrelation length-2 weighted by atomic masses
D481	Moran topological structure autocorrelation length-3 weighted by atomic masses
D482	Moran topological structure autocorrelation length-4 weighted by atomic masses
D483	Moran topological structure autocorrelation length-5 weighted by atomic masses
D484	Moran topological structure autocorrelation length-6 weighted by atomic masses
D485	Moran topological structure autocorrelation length-7 weighted by atomic masses
D486	Moran topological structure autocorrelation length-8 weighted by atomic masses
D487	Moran topological structure autocorrelation length-1 weighted by atomic van der Waals volumes
D488	Moran topological structure autocorrelation length-2 weighted by atomic van der Waals volumes
D489	Moran topological structure autocorrelation length-3 weighted by atomic van der Waals volumes
D490	Moran topological structure autocorrelation length-4 weighted by atomic van der Waals volumes
D491	Moran topological structure autocorrelation length-5 weighted by atomic van der Waals volumes
D492	Moran topological structure autocorrelation length-6 weighted by atomic van der Waals volumes
D493	Moran topological structure autocorrelation length-7 weighted by atomic van der Waals volumes
D494	Moran topological structure autocorrelation length-8 weighted by atomic van der Waals volumes

D495	Moran topological structure autocorrelation length-1 weighted by atomic Sanderson electronegativities
D496	Moran topological structure autocorrelation length-2 weighted by atomic Sanderson electronegativities
D497	Moran topological structure autocorrelation length-3 weighted by atomic Sanderson electronegativities
D498	Moran topological structure autocorrelation length-4 weighted by atomic Sanderson electronegativities
D499	Moran topological structure autocorrelation length-5 weighted by atomic Sanderson electronegativities
D500	Moran topological structure autocorrelation length-6 weighted by atomic Sanderson electronegativities
D501	Moran topological structure autocorrelation length-7 weighted by atomic Sanderson electronegativities
D502	Moran topological structure autocorrelation length-8 weighted by atomic Sanderson electronegativities
D503	Moran topological structure autocorrelation length-1 weighted by atomic polarizabilities
D504	Moran topological structure autocorrelation length-2 weighted by atomic polarizabilities
D505	Moran topological structure autocorrelation length-3 weighted by atomic polarizabilities
D506	Moran topological structure autocorrelation length-4 weighted by atomic polarizabilities
D507	Moran topological structure autocorrelation length-5 weighted by atomic polarizabilities
D508	Moran topological structure autocorrelation length-6 weighted by atomic polarizabilities
D509	Moran topological structure autocorrelation length-7 weighted by atomic polarizabilities
D510	Moran topological structure autocorrelation length-8 weighted by atomic polarizabilities
D511	Molecular topological order-1 charge index
D512	Molecular topological order-2 charge index
D513	Molecular topological order-3 charge index

D514	Molecular topological order-4 charge index
D515	Molecular topological order-5 charge index
D516	Molecular topological order-6 charge index
D517	Molecular topological order-7 charge index
D518	Molecular topological order-8 charge index
D519	Molecular topological order-9 charge index
D520	Molecular topological order-10 charge index
D521	Mean molecular topological order-1 charge index
D522	Mean molecular topological order-2 charge index
D523	Mean molecular topological order-3 charge index
D524	Mean molecular topological order-4 charge index
D525	Mean molecular topological order-5 charge index
D526	Mean molecular topological order-6 charge index
D527	Mean molecular topological order-7 charge index
D528	Mean molecular topological order-8 charge index
D529	Mean molecular topological order-9 charge index
D530	Mean molecular topological order-10 charge index
D531	Sum of molecular topological mean charge index
D532	Lowest eigenvalue from Burden matrix weighted by masses order-1
D533	Lowest eigenvalue from Burden matrix weighted by masses order-2
D534	Lowest eigenvalue from Burden matrix weighted by masses order-3
D535	Lowest eigenvalue from Burden matrix weighted by masses order-4
D536	Lowest eigenvalue from Burden matrix weighted by masses order-5
D537	Lowest eigenvalue from Burden matrix weighted by masses order-6
D538	Lowest eigenvalue from Burden matrix weighted by masses order-7
D539	Lowest eigenvalue from Burden matrix weighted by masses order-8
D540	Lowest eigenvalue from Burden matrix weighted by van der Waals order-1
D541	Lowest eigenvalue from Burden matrix weighted by van der Waals order-2
D542	Lowest eigenvalue from Burden matrix weighted by van der Waals order-3

D543	Lowest eigenvalue from Burden matrix weighted by van der Walls order-4
D544	Lowest eigenvalue from Burden matrix weighted by van der Walls order-5
D545	Lowest eigenvalue from Burden matrix weighted by van der Walls order-6
D546	Lowest eigenvalue from Burden matrix weighted by van der Walls order-7
D547	Lowest eigenvalue from Burden matrix weighted by van der Walls order-8
D548	Lowest eigenvalue from Burden matrix weighted by electronegativities Sanderson-Scale order-1
D549	Lowest eigenvalue from Burden matrix weighted by electronegativities Sanderson-Scale order-2
D550	Lowest eigenvalue from Burden matrix weighted by electronegativities Sanderson-Scale order-3
D551	Lowest eigenvalue from Burden matrix weighted by electronegativities Sanderson-Scale order-4
D552	Lowest eigenvalue from Burden matrix weighted by electronegativities Sanderson-Scale order-5
D553	Lowest eigenvalue from Burden matrix weighted by electronegativities Sanderson-Scale order-6
D554	Lowest eigenvalue from Burden matrix weighted by electronegativities Sanderson-Scale order-7
D555	Lowest eigenvalue from Burden matrix weighted by electronegativities Sanderson-Scale order-8
D556	Lowest eigenvalue from Burden matrix weighted by polarizabilities order-1
D557	Lowest eigenvalue from Burden matrix weighted by polarizabilities order-2
D558	Lowest eigenvalue from Burden matrix weighted by polarizabilities order-3
D559	Lowest eigenvalue from Burden matrix weighted by polarizabilities order-4
D560	Lowest eigenvalue from Burden matrix weighted by polarizabilities order-5
D561	Lowest eigenvalue from Burden matrix weighted by polarizabilities order-6
D562	Lowest eigenvalue from Burden matrix weighted by polarizabilities order-7
D563	Lowest eigenvalue from Burden matrix weighted by polarizabilities order-8
D564	Highest eigenvalue from Burden matrix weighted by masses order-1
D565	Highest eigenvalue from Burden matrix weighted by masses order-2
D566	Highest eigenvalue from Burden matrix weighted by masses order-3

D567	Highest eigenvalue from Burden matrix weighted by masses order-4
D568	Highest eigenvalue from Burden matrix weighted by masses order-5
D569	Highest eigenvalue from Burden matrix weighted by masses order-6
D570	Highest eigenvalue from Burden matrix weighted by masses order-7
D571	Highest eigenvalue from Burden matrix weighted by masses order-8
D572	Highest eigenvalue from Burden matrix weighted by van der Walls order-1
D573	Highest eigenvalue from Burden matrix weighted by van der Walls order-2
D574	Highest eigenvalue from Burden matrix weighted by van der Walls order-3
D575	Highest eigenvalue from Burden matrix weighted by van der Walls order-4
D576	Highest eigenvalue from Burden matrix weighted by van der Walls order-5
D577	Highest eigenvalue from Burden matrix weighted by van der Walls order-6
D578	Highest eigenvalue from Burden matrix weighted by van der Walls order-7
D579	Highest eigenvalue from Burden matrix weighted by van der Walls order-8
D580	Highest eigenvalue from Burden matrix weighted by electronegativities Sanderson-Scale order-1
D581	Highest eigenvalue from Burden matrix weighted by electronegativities Sanderson-Scale order-2
D582	Highest eigenvalue from Burden matrix weighted by electronegativities Sanderson-Scale order-3
D583	Highest eigenvalue from Burden matrix weighted by electronegativities Sanderson-Scale order-4
D584	Highest eigenvalue from Burden matrix weighted by electronegativities Sanderson-Scale order-5
D585	Highest eigenvalue from Burden matrix weighted by electronegativities Sanderson-Scale order-6
D586	Highest eigenvalue from Burden matrix weighted by electronegativities Sanderson-Scale order-7
D587	Highest eigenvalue from Burden matrix weighted by electronegativities Sanderson-Scale order-8
D588	Highest eigenvalue from Burden matrix weighted by polarizabilities order-1
D589	Highest eigenvalue from Burden matrix weighted by polarizabilities order-2
D590	Highest eigenvalue from Burden matrix weighted by polarizabilities order-3

D591	Highest eigenvalue from Burden matrix weighted by polarizabilities order-4
D592	Highest eigenvalue from Burden matrix weighted by polarizabilities order-5
D593	Highest eigenvalue from Burden matrix weighted by polarizabilities order-6
D594	Highest eigenvalue from Burden matrix weighted by polarizabilities order-7
D595	Highest eigenvalue from Burden matrix weighted by polarizabilities order-8
D596	number of total primary C-sp3
D597	number of total secondary C-sp3
D598	number of total tertiary C-sp3
D599	number of total quaternary C-sp3
D600	number of ring secondary C-sp3
D601	number of ring tertiary C-sp3
D602	number of ring quaternary C-sp3
D603	number of unsubstituted aromatic C-sp2
D604	number of substituted aromatic C-sp2
D605	number of primary C-sp2
D606	number of secondary C-sp2
D607	number of tertiary C-sp2
D608	number of group allenes
D609	number of terminal C-sp
D610	number of non-terminal C-sp
D611	number of group cyanates (aliphatic)
D612	number of group cyanates (aromatic)
D613	number of group isocyanates (aliphatic)
D614	number of group isocyanates (aromatic)
D615	number of group thiocyanates (aliphatic)
D616	number of group thiocyanates (aromatic)
D617	number of group isothiocyanates (aliphatic)
D618	number of group isothiocyanates (aromatic)
D619	number of group carboxylic acids (aliphatic)

D620	number of group carboxylic acids (aromatic)
D621	number of group esters (aliphatic)
D622	number of group esters (aromatic)
D623	number of group primary amides (aliphatic)
D624	number of group primary amides (aromatic)
D625	number of group secondary amides (aliphatic)
D626	number of group secondary amides (aromatic)
D627	number of group tertiary amides (aliphatic)
D628	number of group tertiary amides (aromatic)
D629	number of group carbamates (aliphatic)
D630	number of group carbamates (aromatic)
D631	number of group acyl halogenides (aliphatic)
D632	number of group acyl halogenides (aromatic)
D633	number of group thioacids (aliphatic)
D634	number of group thioacids (aromatic)
D635	number of group dithioacids (aliphatic)
D636	number of group dithioacids (aromatic)
D637	number of group thioesters (aliphatic)
D638	number of group thioesters (aromatic)
D639	number of group dithioesters (aliphatic)
D640	number of group dithioesters (aromatic)
D641	number of group aldehydes (aliphatic)
D642	number of group aldehydes (aromatic)
D643	number of group ketones (aliphatic)
D644	number of group ketones (aromatic)
D645	number of group urea derivatives
D646	number of group urea derivatives (aromatic)
D647	number of group primary amines (aliphatic)
D648	number of group primary amines (aromatic)

D649	number of group secondary amines (aliphatic)
D650	number of group secondary amines (aromatic)
D651	number of group tertiary amines (aliphatic)
D652	number of group tertiary amines (aromatic)
D653	number of group N-hydrazines (aliphatic)
D654	number of group N-hydrazines (aromatic)
D655	number of group N-azo (aliphatic)
D656	number of group N-azo (aromatic)
D657	number of group nitriles (aliphatic)
D658	number of group nitriles (aromatic)
D659	number of group imines (aliphatic)
D660	number of group imines (aromatic)
D661	number of group ammonia groups (aliphatic)
D662	number of group ammonia groups (aromatic)
D663	number of group hydroxylamines (aliphatic)
D664	number of group hydroxylamines (aromatic)
D665	number of group oximes (aliphatic)
D666	number of group oximes (aromatic)
D667	number of group N-nitroso (aliphatic)
D668	number of group N-nitroso (aromatic)
D669	number of group nitroso (aliphatic)
D670	number of group nitroso (aromatic)
D671	number of group nitro (aliphatic)
D672	number of group nitro (aromatic)
D673	number of group imides
D674	number of group total hydroxyl groups
D675	number of group phenols
D676	number of group primary alcohols (aliphatic)
D677	number of group secondary alcohols (aliphatic)

D678	number of group tertiary alcohols (aliphatic)
D679	number of group ethers (aliphatic)
D680	number of group ethers (aromatic)
D681	number of group hypohalogenydes (aliphatic)
D682	number of group hypohalogenydes (aromatic)
D683	number of group water molecules
D684	number of group sulfoxides
D685	number of group sulfones
D686	number of group sulfates
D687	number of group thioles
D688	number of group thioketones
D689	number of group sulfides
D690	number of group disulfides
D691	number of group sulfonic acids
D692	number of group sulfonamides
D693	number of group phosphites
D694	number of group phosphates
D695	number of group phosphothionates
D696	number of group phosphodithionates
D697	number of group phosphothioates
D698	number of group CH ₂ X
D699	number of group CR ₂ HX
D700	number of group CR ₃ X
D701	number of group R=CHX
D702	number of group R=CRX
D703	number of group R#CX
D704	number of group CHRX ₂
D705	number of group CR ₂ X ₂
D706	number of group R=CX ₂

D707	number of group RCX3
D708	number of group X-C on aromatic ring
D709	number of group X-C- on ring
D710	number of group X-C= on ring
D711	number of group X-C on conjugated C
D712	number of group donor atoms for H-bonds (with N and O)
D713	number of group acceptor atoms for H-bonds (N O F)
D714	number of group CH3R and CH4
D715	number of group CH2R2
D716	number of group CHR3
D717	number of group CR4
D718	number of group CH3X
D719	number of group CH2RX
D720	number of group CH2X2
D721	number of group CHR2X
D722	number of group CHRX2
D723	number of group CHX3
D724	number of group CR3X
D725	number of group CR2X2
D726	number of group CRX3
D727	number of group CX4
D728	number of group =CH2
D729	number of group =CHR
D730	number of group =CR2
D731	number of group =CHX
D732	number of group =CRX
D733	number of group =CX2
D734	number of group #CH
D735	number of group #CR or R=C=R

D736	number of group #CX
D737	number of group R~CH~R
D738	number of group R~CR~R
D739	number of group R~CX~R
D740	number of group Al-CH=X
D741	number of group Ar-CH=X
D742	number of group Al-C(=X)-Al
D743	number of group Ar-C(=X)-R
D744	number of group R-C(=X)-X / R-C#X
D745	number of group X-C(=X)-X
D746	number of group H attached to C0(sp3) no X attached to next C
D747	number of group H attached to heteroatom
D748	number of group H attached to C0(sp3) with 1X attached to next C
D749	number of group H attached to C0(sp3) with 2X attached to next C
D750	number of group H attached to C0(sp3) with 3X attached to next C
D751	number of group H attached to C0(sp3) with 4X attached to next C
D752	number of group alcohol
D753	number of group phenol or enol or carboxyl OH
D754	number of group O=
D755	number of group Al-O-Al
D756	number of group Al-O-Ar or Ar-O-Ar or R-O-C=X
D757	number of group Al-NH2
D758	number of group Al2-NH
D759	number of group Al3-N
D760	number of group Ar-NH2 or X-NH2
D761	number of group Ar-NH-Al
D762	number of group Ar-NAI2
D763	number of group RCO-N< or >N-X=X
D764	number of group Ar2NH or Ar3N or Ar2N-Al

D765	number of group R#N or R=N
D766	r of group Ar-NO ₂ or RO-NO ₂
D767	number of group Al-NO ₂
D768	number of group Ar-N=X or X-N=X
D769	number of group R-SH
D770	number of group R ₂ S or RS-SR
D771	number of group R=S
D772	number of group R-SO-R
D773	number of group R-SO ₂ -R
D774	unsaturation index weighted by conventional bonds order
D775	hydrophilic factor index
D776	aromatic bonds ratio
D777	Molecular regression coefficients surface LogP index

Bibliography

- Air Force Civil Engineer Center. 2017. "US Air Force Civil Engineer Center." *Air Force PFOS/PFOA Snapshot*. June 22. Accessed June 29, 2017. <http://www.afcec.af.mil/WhatWeDo/Environment/Perfluorinated-Compounds/>.
- Anderson, Richard H, Janet K Anderson, and Paul A Bower. 2012. "Co-concurrence of 1,4-dioxane with Trichloroethylene in Chlorinated Solvent Groundwater Plumes at US Air Force Installations: Fact or Fiction." *Integrated Environmental Assessment and Management* 731-737.
- Andreozzi, R, V Caprio, A Insola, and R Marotta. 1999. "Advanced Oxidation Process (AOP) for Water Purification and Recovery." *Catalysis Today* 51-59.
- Apostol, Laura C, Camelia Smaranda, Mariana Diaconu, and Maria Gavrilescu. 2015. "Preliminary Ecotoxicological Evaluation of Erythrosin B and Its Photocatalytic Degradation Products." *Environmental Engineering and Management Journal* 465-471.
- Atlantium Technologies. 2017. *Medium Pressure and Low Pressure Lamps*. Accessed May 17, 2017. <http://www.atlantium.com/en/markets/aquaculture-eng/blog/medium-pressure-low-pressure-lamps.html>.
- Badawy, M, M Ghaly, and T Gad-Allah. 2006. "Advanced oxidation processes for the removal of organophosphorus pesticides from wastewater." *Desalination* 166-175.
- Bairagi, Rinku, and Rakshit Ameta. 2016. "Photocatalytic Degradation of Erythrosine by Using Manganese Doped TiO₂ Supported on Zeolite." *International Journal of Chemical Sciences* 1768-1776.
- Barry, Judith A. 2012. *Characterization of DoD Installation Wastewater Treatment*. Technical, Noblis Center for Sustainability.
- Beltran, Fernando J, Jose M Encinar, and Miguel A Alonso. 1998. "Nitroaromatic Hydrocarbon Ozonation in Water: Combined Ozonation with Hydrogen Peroxide or UV Radiation." *Industrial and Engineering Chemical Research* 32-40.
- Benjamin, Mark M, and Desond F Lawler. 2013. *Water Quality Engineering*. Hoboken: Wiley.

- Bohrerova, Z, G Bohrer, S Mohanraj, J Ducoste, and K Linden. 2005. "Experimental measurements of fluence distribution in a UV reactor using fluorescent microspheres." *Environmental Science and Technology* 8925-8930.
- Borhani, Tohid, Mohammadhossein Saniedanesh, Mehdi Bagheri, and Jeng S. Lim. 2016. "QSPR Prediction of the Hydroxyl Radical Rate Constant of Water Contaminants." *Water Research* 344-353.
- Buxton, G, C Greenstock, W Helman, and A Ross. 1988. "Critical review of rate constants for reactions of hydrated electrons, hydrogen atoms, and hydroxyl radicals in aqueous solution." *Journal of Physical and Chemical Reference Data* 513-531.
- Chang, M, C Chung, J Chern, and T Chen. 2010. "Dye decomposition kinetics by UV/H₂O₂: initial rate analysis by effective kinetic modeling methodology." *Chemical Engineering Science* 135-140.
- Chen, Jingwen, Degao Wang, Shuanglin Wang, Xianliang Qiao, and Liping Huang. 2007. "Quantitative structure–property relationships for direct photolysis of polybrominated diphenyl ethers." *Ecotoxicology and Environmental Safety* 348-352.
- Crittenden, J, S Hu, D Hand, and S Green. 1999. "A kinetic model for H₂O₂/UV process in a completely mixed batch reactor." *Water Research* 2315-2328.
- Dorfman, Leon M, and Gerald E Adams. 1973. *Reactivity of the Hydroxyl Radical in Aqueous Solutions*. Technical Report, Washington: National Bureau of Standards.
- Duckworth, Kelsey, Michael Spencer, Christopher Bates, Michael E. Miller, Catherine Almquist, Michael Grimaila, Matthew Magnuson, Stuart Willison, Rebecca Phillips, and LeeAnn Racz. 2015. "Advanced oxidation degradation kinetics as a function of ultraviolet LED duty cycle." *Water Science and Technology* 1375-1381.
- Edalatmanesh, M, R Dhib, and M Mehrvar. 2008. "Kinetic modeling of aqueous phenol degradation by UV/H₂O₂ process." *International Journal of Chemical Kinetics* 34-43.
- Englehardt, James D, Tingting Wu, Frederick Bloetscher, Yang Deng, Piet du Pisani, Sebastian Eilert, Samir Elmir, et al. 2016. "Net-Zero Water Management: Achieving Energy-Positive Municipal Water Supply." *Environmental Science: Water Research and Technology* 250-260.

- Famiglietti, Jay. 2014. "Epic California Drought and Groundwater: Where Do We Go from Here?" *Water Currents*.
- Ferguson, Grant, and Tom Gleeson. 2013. "Threats to Coastal Aquifers." *Nature Climate Change* 605-606.
- Fukui, Kenichi. 1981. "The role of frontier orbitals in chemical reactions - Nobel lecture." *Chemistry* 9-26.
- Gallucci, D. 2016. *Material and Design Considerations for a Portable Ultraviolet (UV) Light Emitting Diode (LED) Water Purification Device*. Masters Thesis, Wright-Patterson AFB: Air Force Institute of Technology.
- Ghafoorim, S, M Mehrvar, and P Chan. 2014. "Photoreactor scale-up for degradation of aqueous poly(vinyl alcohol) using UV/H₂O₂ process." *Chemical Engineering Journal* 133-142.
- Gillis, Regina. 2006. *US Air Force*. March 28. Accessed April 28, 2017. <http://www.af.mil/News/Article-Display/Article/131533/california-base-wins-water-recycling-award/>.
- Giri, R, H Ozaki, Y Takayanagi, S Taniguchi, and R Takanami. 2011. "Efficacy of ultraviolet radiation and hydrogen peroxide oxidation to eliminate large number of pharmaceutical compounds in mixed solution." *International Journal of Environmental Science and Technology* 19-30.
- Gligorovski, S, R Strekowski, S Barbati, and D Vione. 2015. "Environmental implications of hydroxyl radicals." *Chemical Reviews* 13051-13092.
- Grcic, I, S Papic, D Mesec, N Koprivanac, and D Vujevic. 2014. "The kinetics and efficiency of UV assisted advanced oxidation of various types of commercial organic dyes." *Journal of Photochemistry and Photobiology A: Chemistry* 49-58.
- Hartog, N, M Mahmoodlu, and S Hassanizadeh. 2015. "Bias by inappropriate use of the pseudo-first order approach to estimate second-order reaction rate constants: reply to the commentary by Tratnyek." *Science of the Total Environment* 724-725.
- Hong, H, Q Xie, W Ge, F Qian, F Fang, L Shi, Z Su, R Perkins, and W and Tong. 2008. "Mold2, molecular descriptors from 2D structures for chemoinformatics and toxicoinformatics." *Journal of Chemical Information and Modeling* 1337-1344.

- Hong, Huixiao, Svetoslav Slavov, Weigong Ge, Feng Qian, Zhenqiang Su, Hong Fang, Yiyu Cheng, Roger Perkins, Leming Shi, and Weida Tong. 2012. "Mold2 Molecular Descriptors for QSAR." In *Statistical Modelling of Molecular Descriptors in QSAR/QSPR*, by Matthias Dehmer, Kurt Varmuza and Danail Bonchev, 65-110. Weinheim: Wiley-Blackwell.
- Huang, Xiangfeng, Yi Feng, Cui Hu, Xiaoyu Xiao, Daliang Yu, and Xiaoming Zou. 2015. "Mechanistic QSAR models for Interpreting Degradation Rates of Sulfonamides in UV-Photocatalysis Systems." *Chemosphere* 183-189.
- Huber, Marc M, Silvio Canonica, Gun-Young Park, and Urs Von Gunten. 2003. "Oxidation of Pharmaceuticals During Ozonation and Advanced Oxidation Processes." *Environmental Science and Technology* 1016-1024.
- Ibrahim, MA, J MacAdam, O Autin, and B Jefferson. 2014. "Evaluating the Impact of LED Bulb Development on the Economic Viability of Ultraviolet Technology for Disinfection." *Environmental Technology* 400-406.
- Jenny, R, O Simmons, M Shatalov, and J Ducoste. 2014. "Modeling a continuous flow ultraviolet Light Emitting Diode reactor using computational fluid dynamics." *Chemical Engineering Science* 524-535.
- Jin, Xiaohui, Sigrid Peldszus, and Peter M Huck. 2015. "Predicting the Reaction Rate Constants of Micropollutants with Hydroxyl Radicals in Water Using QSPR Modeling." *Chemosphere* 1-9.
- Katsoyiannis, Ioannis A, Silvio Canonica, and Urs von Gunten. 2011. "Efficiency and Energy Requirements for the Transformation of Organic Micropollutants by Ozone, O₃/H₂O₂, and UV/H₂O₂." *Water Research* 3811-3822.
- Kim, I, N Yamashita, and H Tanaka. 2009. "Photodegradation of pharmaceuticals and personal care products during UV and UV/H₂O₂ treatments." *Chemosphere* 518-525.
- Kusic, Hrvoje, Bakhtiyor Rasulev, Danuta Leszczynska, Jerzy Leszczynski, and Natalija Koprivanac. 2009. "Prediction of rate constants for radical degradation of aromatic pollutants in water matrix: A QSAR study." *Chemosphere* 1128-1134.
- Lee, Yunho, and Urs von Gunten. 2012. "Quantitative structure–activity relationships (QSARs) for the transformation of organic micropollutants during oxidative water treatment." *Water Research* 6177-6195.

- Luo, Y.R. 2007. *Comprehensive Handbook of Chemical Bond Energies*. Boca Raton: CRC Press.
- Mandavgane, S, and M Yenkie. 2011. "Degradation of salicylic acid by UV, UV/H₂O₂, UV/O₃, photo-Fenton processes." *Journal of Chemistry* 640-647.
- Marcum, C. 2014. *Measurements of DNA Damage and Repair in Bacillus Anthracis Sterne Spores by UV Radiation*. Masters Thesis, Wright-Patterson AFB: Air Force Institute of Technology.
- Mariani, M, R Brandi, A Cassano, and C Zalazar. 2013. "A kinetic model for the degradation of dichloroacetic acid and formic acid in water employing the H₂O₂/UV process." *Chemical Engineering Journal* 423-432.
- Meylan, William M., and Philip H Howard. 2003. "A review of quantitative structure-activity relationship methods for the prediction of atmospheric oxidation of organic chemicals." *Environmental Toxicology and Chemistry* 1724-1732.
- Minakata, D, S Mezyk, J Jones, B Daws, and J Crittenden. 2014. "Development of Linear Free Energy Relationships for Aqueous Phase Radical-Involved Chemical Reactions." *Environmental Science and Technology* 13925-13932.
- Minakata, Daisuke, Ke Li, Paul Westerhoff, and John Crittenden. 2009. "Development of a Group Contribution Method to Predict Aqueous Phase Hydroxyl Radical Reaction Rate Constants." *Environmental Science and Technology* 6220-6227.
- Morckel, Victoria. 2017. "Why the Flint, Michigan, USA Water Crisis is an Urban Planning Failure." *Cities* 23-27.
- Mudimbi, P. 2015. *Pulsed Ultraviolet Light Emitting Diodes for Advanced Oxidation of Tartrazine*. Masters Thesis, Wright-Patterson AFB: Air Force Institute of Technology.
- Murcia, M, N Vershinin, N Briantceva, M Gomez, E Gomez, E Cascales, and A Hidalgo. 2015. "Development of a kinetic model for the UV/H₂O₂ photodegradation of 2,4-dichlorophenoxyacetic acid." *Chemical Engineering Journal* 356-367.
- Muruganandham, M, and M Swaminathan. 2004. "Photochemical oxidation of reactive azo dye with UV-H₂O₂ process." *Dyes and Pigments* 269-275.

- Narayansamy, L, and T Murugesan. 2014. "Degradation of Alizarin Yellow R using UV/H₂O₂ advanced oxidation process." *Environmental Progress and Sustainable Energy* 482-489.
- National Institutes of Health. 2016. "National Center for Biotechnology Information." *PubChem*. January 17. Accessed January 17, 2016. <https://pubchem.ncbi.nlm.nih.gov/#>.
- Oancea, P, and V Meltzer. 2013. "Kinetics of tartrazine photodegradation by UV/H₂O₂ in aqueous solution." *Chemical Papers* 105-111.
- O'Boyle, Noel M, Michael Banck, Craig A James, Chris Morley, Tim Vandermeersch, and Geoffrey R Hutchinson. 2011. "Open Babel: An Open Chemical Toolbox." *Journal of Chemoinformatics*.
- Ohura, Takeshi, Takashi Amagai, and Masakazu Makino. 2008. "Behavior and prediction of photochemical degradation of chlorinated polycyclic aromatic hydrocarbons in cyclohexane." *Chemosphere* 2110-2117.
- Oppenlander, T. 2003. *Photochemical Purification of Water and Air - Advanced Oxidation Processes (AOPs): Principles, Reaction Mechanisms, Reactor Concepts*. Darmstadt, Germany: Wiley-Vch.
- Pro-Act. 2000. *Spotlight On: Luke Air Force Base. Success Story*, San Antonio: Air Force Center for Environmental Excellence.
- Rahmani, Z, M Kermani, M Gholami, A Jafari, and N Mahmoodi. 2012. "Effectiveness of photochemical and sonochemical processes in degradation of Basic Violet 16 (BV16) dye from aqueous solutions." *Iranian Journal of Environmental Health Science and Engineering* 1-7.
- Rajagopalan, Balaji, Kenneth Nowak, James Prairie, Martin Hoerling, Benjamin Harding, Joseph Barsugli, Andrea Ray, and Bradley Udall. 2009. "Water Supply Risk on the Colorado River: Can Management Mitigate?" *Water Resources Research* 1-7.
- Rodriguez, Clemencia, Paul Van Buynder, Richard Lugg, Palenque Blair, Brian Devine, Angus Cook, and Philip Weinstein. 2009. "Indirect Potable Reuse: A Sustainable Water Alternative." *International Journal of Environmental Research and Public Health* 1174-1203.
- Rosario-Ortiz, F, E Wert, and S Snyder. 2010. "Evaluation of UV/H₂O₂ treatment for the oxidation of pharmaceuticals in wastewater." *Water Research* 1440-1448.

- Salinas, Alex. 2013. *Air Force directive prompts water conservation*. July 11. Accessed May 7, 2017. <http://www.jbsa.mil/News/News/Article/461563/air-force-directive-prompts-water-conservation/>.
- Sanches, S, Crespo MT Barreto, and VJ Pereira. 2010. "Drinking Water Treatment of Priority Pesticides Using Low Pressure UV Photolysis and Advanced Oxidation Processes." *Water Research* 1809-1818.
- Santoro, D, M Raisee, M Moghaddami, J Ducoste, M Sasges, L Liberti, and M Notarnicola. 2010. "Modeling hydroxyl radical distribution and trialkyl phosphates oxidation in UV - H₂O₂ photoreactors using computational fluid dynamics." *Environmental Science and Technology* 6233-6241.
- Scott, R, P Mudimbi, M.E. Miller, M Magnuson, S Willison, R Phillips, and Willie F Harper Jr. 2016. "Advanced oxidation of tartrazine and Brilliant Blue with pulsed ultraviolet light emitting diodes." *Water Environment Research* Vol 88.
- Scott, Robert W. 2015. *The Use of Ultra-violet (UV) Light Emitting Diodes (LEDs) in an Advanced Oxidation Process (AOP) with Brilliant Blue FCF as an Indicator*. Masters Thesis, Wright-Patterson AFB: Air Force Institute of Technology.
- Sharma, S. 2015. *Green Chemistry for Dyes Removal from Waste Water*. Hoboken: Wiley.
- Shu, Z, J Bolton, M Belosevic, and M Gamal El Din. 2013. "Photodegradation of emerging micropollutants using the medium-pressure UV/H₂O₂ Advanced Oxidation Process." *Water Research* 2881-2889.
- Singh, K, S Gupta, N Basant, and D Mohan. 2014. "QSTR Modeling for qualitative and quantitative toxicity predictions of diverse chemical pesticides in honey bee for regulatory purposes." *Chemical Research in Toxicology* 1504-1515.
- Stefan, Mihaela I, John Mack, and James R Bolton. 2000. "Degradation Pathways during the Treatment of Methyl tert-Butyl Ether by the UV/H₂O₂ Process." *Environmental Science and Technology* 650-658.
- Stewart, B. 2016. *Pulsed Ultraviolet Light Emitting Diodes for Advanced Oxidation of Tartrazine and Disinfection of Deployed Asset Drinking Water*. Masters Thesis, Wright-Patterson AFB: Air Force Institute of Technology.
- Stuart Computational Chemistry. 2016. *MOPAC*. Accessed July 21, 2016. <http://openmopac.net/index.html>.

- Sudhakaran, Sairam, and Gary Amy. 2013. "QSAR models for oxidation of organic micropollutants in water based on ozone and hydroxyl radical rate constants and their chemical classification." *Water Research* 1111-1122.
- Sudhakaran, Sairam, James Calvin, and Gary L. Amy. 2012. "QSAR models for the removal of organic micropollutants in four different river water matrices." *Chemosphere* 144-150.
- Sullivan, Abigail, Dave D White, Kelli L Larson, and Amber Wutich. 2017. "Towards Water Sensitive Cities in the Colorado River Basin: A Comparative Historical Analysis to Inform Future Water Sustainability Transitions." *Sustainability* 1-27.
- Tang, Water Z. 2004. *Physicochemical Treatment of Hazardous Wastes*. Boca Raton: Lewis Publishers.
- US Air Force. 2013. *US Air Force Energy Strategic Plan*. Washington: SAF/IE.
- US Army. 2015. *Army Techniques Publication 4-44, Water Support Operations*. Washington: Headquarters Dept of the Army.
- US Department of Energy. 2015. "US Department of Energy." *Federal Energy and Water Management Awards 2014*. January. Accessed May 3, 2017. https://energy.gov/sites/prod/files/2015/01/f19/fewma2014_usaf_hurlburt_field.pdf.
- US Food and Drug Administration. 2015. "US Food and Drug Administration." *Bioinformatics Tools: Mold2*. September 30. Accessed December 7, 2015. <https://www.fda.gov/ScienceResearch/BioinformaticsTools/Mold2/default.htm>.
- USEPA. 1999. *Alternative Disinfectants and Oxidants Guidance Manual*. Washington: Office of Water.
- . 2016. *Net Zero Concepts and Definitions*. September 16. Accessed February 18, 2017. https://19january2017snapshot.epa.gov/water-research/net-zero-concepts-and-definitions_.html.
- Vilhunen, S, and M Sillanpaa. 2009. "Ultraviolet light emitting diodes and hydrogen peroxide in the photodegradation of aqueous phenol." *Journal of Hazardous Materials* 1530-1534.

- Wang, Ya-nan, Jingwen Chen, Xuehua Li, Siyu Zhang, and Xianliannng Qiao. 2009. "Estimation of Aqueous-Phase Reaction Rate Constants of Hydroxyl Radical with Phenols, Alkanes and Alcohols." *QSAR and Combinatorial Science* 1309-1316.
- Wavefunction. 2017. "Wavefunction Inc." *Spartan Software*. Accessed May 12, 2017. <https://www.wavefun.com/products/spartan.html>.
- Wols, B, and C Hofman-Caris. 2012. "Review of photochemical reaction constants of organic micropollutants required for UV advanced oxidation in water." *Water Research* 2815-2827.
- Yee, Liew C, and Yap C Wei. 2012. "Current Modeling Methods Used in QSAR/QSPR." In *Statistical Modelling of Molecular Descriptors in QSAR/QSPR*, by Matthias Dehmer, Kurt Varmuza and Danail Bonchev, 1-31. Weinheim: Wiley-Blackwell.

Vita

Lieutenant Colonel John E. Stubbs was born and raised in North Carolina. After graduating from Saint Stephens High School in Hickory, NC in 1993, he attended North Carolina State University. He graduated Summa Cum Laude in 1998 with a bachelor's degree in Industrial Engineering.

In 1998, he started a brief career with Procter and Gamble where he worked as a process engineer dedicated to raw material supply chain management and quality control for antiperspirant and deodorant manufacturing. In 2001, an altruistic calling drove a desire for Lieutenant Colonel Stubbs to serve his country in the United States Air Force. He was selected for direct commissioning and entered the Bioenvironmental Engineering career field in January 2002.

After initial training, Lieutenant Colonel Stubbs was assigned to his first operational assignment with the Air Force Research Laboratory at Wright-Patterson AFB, Ohio as a principal investigator in the Human Effectiveness Directorate, Biodynamics and Acceleration Branch. There he was responsible for research programs related to aircrew seat system comfort, safety, and standardization and garnered \$1.2 million in research funding. He also served as the alternate Unit Environmental Coordinator for the Human Effectiveness Directorate, responsible for cradle-to-grave compliance with hazardous material and hazardous waste management.

In 2005, he was assigned to the 62nd Airlift Wing at McChord AFB, Washington where he was assigned to the 62nd Medical Operations Squadron, Bioenvironmental Engineering Element and was responsible for environmental, radiation safety, and

CBRNE response programs. During this time, he was deployed to Camp Lemonier, Djibouti in 2007 in support of the US Army's 350th CACOM Functional Specialty Team conducting medical and veterinary civil affairs programs in countries across the Horn of Africa.

In 2008, Lieutenant Colonel Stubbs was accepted to pursue a Master's Degree program at the Air Force Institute of Technology (AFIT) and returned to Wright Patterson AFB. There, he began a Master of Science in Industrial Hygiene, specializing in design of a novel noise delivery system for jet fuel aerosol ototoxicity studies.

Upon graduation from AFIT in 2010 he was assigned as chief of Bioenvironmental Engineering Education and Training Branch at the USAF School of Aerospace Medicine (USAFSAM) where he was responsible for all facets of curriculum development and maintenance for officer and enlisted courses. Additionally, he completed the USAF Basic Instructor Course and completed all required instructor internship hours to receive full instructor certification. While at USAFSAM, he was also assigned to the Air Force Radiation Assessment Team as Surveillance Team Chief and deployed to Japan in 2011 in support of Operation TOMODACHI, following the tsunami and subsequent nuclear reactor emergency.

In 2011, Lieutenant Colonel Stubbs moved to the 509th Bomb Wing at Whiteman AFB, Missouri. There he was assigned to the 509th Medical Operations Squadron as Bioenvironmental Engineering Flight Commander. He was responsible for all facets of bioenvironmental engineering programs in support of 3,000 personnel and four airframes. During this time, he was also deployed to Bagram Air Base, Afghanistan as

Bioenvironmental Engineering Element Chief, supporting a population of 30,000 personnel with all bioenvironmental engineering core competencies.

He returned to Wright Patterson AFB, Ohio in 2014 to begin his doctorate degree at AFIT. Upon graduation, he will be assigned to AFIT faculty in the Graduate School of Engineering and Management.

REPORT DOCUMENTATION PAGE				<i>Form Approved OMB No. 0704-0188</i>							
<p>The public reporting burden for this collection of information is estimated to average 1 hour per response, including the time for reviewing instructions, searching existing data sources, gathering and maintaining the data needed, and completing and reviewing the collection of information. Send comments regarding this burden estimate or any other aspect of this collection of information, including suggestions for reducing the burden, to Department of Defense, Washington Headquarters Services, Directorate for Information Operations and Reports (0704-0188), 1215 Jefferson Davis Highway, Suite 1204, Arlington, VA 22202-4302. Respondents should be aware that notwithstanding any other provision of law, no person shall be subject to any penalty for failing to comply with a collection of information if it does not display a currently valid OMB control number.</p> <p>PLEASE DO NOT RETURN YOUR FORM TO THE ABOVE ADDRESS.</p>											
1. REPORT DATE (DD-MM-YYYY) 14-09-2017		2. REPORT TYPE Doctoral Dissertation		3. DATES COVERED (From - To) August 2014 - September 2017							
4. TITLE AND SUBTITLE Dynamics of Chemical Degradation in Water Using Photocatalytic Reactions in an Ultraviolet Light Emitting Diode Reactor				5a. CONTRACT NUMBER							
				5b. GRANT NUMBER							
				5c. PROGRAM ELEMENT NUMBER							
6. AUTHOR(S) Stubbs, John E., Lieutenant Colonel, USAF				5d. PROJECT NUMBER							
				5e. TASK NUMBER							
				5f. WORK UNIT NUMBER							
7. PERFORMING ORGANIZATION NAME(S) AND ADDRESS(ES) Air Force Institute of Technology Graduate School of Engineering and Management (AFIT/EN) 2950 Hobson Way Wright-Patterson AFB OH 45433-7765				8. PERFORMING ORGANIZATION REPORT NUMBER AFIT-ENV-DS-17-S-052							
9. SPONSORING/MONITORING AGENCY NAME(S) AND ADDRESS(ES) Intentionally Left Blank				10. SPONSOR/MONITOR'S ACRONYM(S)							
				11. SPONSOR/MONITOR'S REPORT NUMBER(S)							
12. DISTRIBUTION/AVAILABILITY STATEMENT Distribution Statement A: Approved for Public Release; Distribution Unlimited.											
13. SUPPLEMENTARY NOTES This work is declared a work of the U.S. Government and is not subject to copyright protection in the United States.											
14. ABSTRACT This work examined ultraviolet (UV) light emitting diodes (LED) and hydrogen peroxide in an advanced oxidation process in support of a USAF installation net zero water initiative. A UV LED reactor was used for degradation of soluble organic chemicals. There were linear relationships between input drive current, optical output power, and first order degradation rate constants. When drive current was varied, first order degradation rates depended on chemical identities and the drive current. When molar peroxide ratios were varied, kinetic profiles revealed peroxide-limited or radical-scavenged phenomena. Molar absorptivity helped explain the complexity of chemical removal profiles. Degradation kinetics were used to compare fit of molecular descriptors from published quantitative structure property relationship (QSPR) models. A novel QSPR model was built using zero point energy and molar absorptivity as predictors. Finally, a systems architecture was used to describe a net zero water program and proposed areas for UV LED reactor integration. Facility-level wastewater treatment was found to be the most feasible near-term application.											
15. SUBJECT TERMS Ultraviolet, light emitting diodes, advanced oxidation process, chemical degradation, net zero water, systems architecture											
16. SECURITY CLASSIFICATION OF: <table border="1" style="width: 100%; border-collapse: collapse; margin-top: 5px;"> <tr> <td style="width: 33%; padding: 2px;">a. REPORT</td> <td style="width: 33%; padding: 2px;">b. ABSTRACT</td> <td style="width: 33%; padding: 2px;">c. THIS PAGE</td> </tr> <tr> <td style="text-align: center; padding: 2px;">U</td> <td style="text-align: center; padding: 2px;">U</td> <td style="text-align: center; padding: 2px;">U</td> </tr> </table>			a. REPORT	b. ABSTRACT	c. THIS PAGE	U	U	U	17. LIMITATION OF ABSTRACT UU		18. NUMBER OF PAGES 239
a. REPORT	b. ABSTRACT	c. THIS PAGE									
U	U	U									
			19a. NAME OF RESPONSIBLE PERSON Dr. Willie F. Harper, Jr., AFIT/ENV								
			19b. TELEPHONE NUMBER (Include area code) (937) 255-3636 x4528 willie.harper@afit.edu								